



Università
degli Studi
di Catania

DOTTORATO DI RICERCA IN SCIENZA DEI MATERIALI E
NANOTECNOLOGIE - XXXIII CICLO

In convenzione con



UNIVERSITÀ
DEGLI STUDI
DI PALERMO

LORENZO LISUZZO

—————

**Halloysite for smart nano-structured materials
in sustainable applications**

—————

Tutors:

Prof. Stefana Milioto

Prof. Giuseppe Lazzara

TESI PER IL CONSEGUIMENTO DEL TITOLO DI DOTTORE DI RICERCA

TABLE OF CONTENTS

Preface	III
Acknowledgements	IV
1. Eco-sustainable materials	1
1.1 Introduction	2
1.2 Nanoclays	3
1.3 Halloysite and Kaolinite	4
1.4 Sepiolite	6
1.5 Biopolymers	8
1.6 Chitosan.....	9
1.7 Alginate.....	10
1.8 Cellulose Nanofibers	10
1.9 Mater-Bi®	12
1.10 Biocompatible nanomaterials.....	13
1.11 Aims and objective of the study	14
2. Effect of the pressure on the loading mechanism of Halloysite	16
2.1 Loading and release optimization: a general overview	17
2.2 Water confinement within HNTs and the role of vacuum conditions	18
2.3 Targeting the site for drug loading into HNTs	25
3. Aqueous dispersions and targeted modifications	32
3.1 The importance of colloidal stability.....	33
3.2 Design of targeted functionalizations.....	34
3.3 Thermo-responsive characteristics of PNIPAAm/HNTs hybrid nanocarriers.....	34
3.4 Chitosan coating on HNTs for the controlled release of khellin	39
4. Biohybrid Gel beads	43
4.1 Design of gel beads based on biopolymers and HNTs	44
4.2 Physico-chemical characterization of Chitosan/HNTs/Alginate gel beads.....	44
4.3 Application of the alginate/chitosan/HNTs gel beads for controlled drug release	46
5. Bioplastics based on Halloysite	48
5.1 Design of plasticized bionanocomposites.....	49
5.2 Physico-chemical investigation of Mater-Bi/Nanoclays composite films.....	49
5.3 Effect of HNTs on the thermo-mechanical performances.....	52
6. Functional nano-engineered biohybrids for health applications	57
6.1 Design of new nanoarchitected materials.....	58
6.2 Layered composite based on HNTs and natural polymers: physico-chemical studies.....	58
6.3 Self-assembly of HNTs, Sepiolite and CNF: physico-chemical studies.....	62

6.4 Applications for health and drug delivery purposes.....	67
7. Pickering Emulsions based on Halloysite and wax for the consolidation of archeological wood.....	75
7.1 Pickering emulsions as green and ecofriendly materials	76
7.2 Wax/HNTs Pickering emulsions: preparation and characterization	77
7.3 Wax/HNTs Pickering emulsions: thermal properties	81
7.4 Treatment of archaeological woods by Wax/HNTs Pickering emulsions.....	84
8. Concluding remarks	87
9. References	91
10. Attached papers.....	96

Preface

This Ph.D. thesis entitled “Halloysite for smart nano-structured materials in sustainable applications” was initiated in November 2017 and finalized in September 2020. The study was mostly carried out at University of Palermo (Department of Physics and Chemistry - Emilio Segré) and some experiments were done at the Molecular Design Institute of the New York University (USA) during a scientific stage of 6 months as Fulbright Visiting Student Researcher. The thesis reports fundamental and precise physico-chemical insights on nanosized materials deriving from environmental friendly resources, such as nanoclays and biopolymers, with a special focus on Halloysite Nanotubes (HNTs). In detail, the thesis includes eight chapters. The first one summarizes the properties and the current applications of green materials (nanoclays, biopolymers and their composites). Chapter 2 provides the first thermodynamic demonstration of the water confinement within halloysite nanotubes and a proper description of their loading mechanism, thus allowing the optimization of the loading protocols and the targeting of the drug localization within the nanoclay. Chapters 3 and 4 are dedicated to the preparation and physico-chemical characterization of selectively functionalized HNTs and hybrid gel beads, respectively, with potential applications as smart and stimuli responsive delivery systems. The evaluation of the clays as nanofillers for the improvement of the thermal and mechanical performances of bioplastics was carried out in Chapter 5, in order to assess their effectiveness as biocompatible materials by correlating the macroscopic features to the microscopic properties. Chapter 6 shows the design of green and eco-compatible functional biohybrid materials. The preparation and physico-chemical characterization of the new nano-engineered architectures is reported, together with their employ in health and biomedical science. The experiments performed at New York University are reported in Chapter 7. Herein, a new protocol for the preparation of Pickering emulsions based on halloysite and wax is proposed and then employed for the consolidation of waterlogged archeological woods. Lastly, Chapter 8 outlines the most important insights and significant observations provided by this thesis. The details on the equipment used for the physico-chemical characterizations, on the preparation strategies and on the experimental data can be found in the attached related papers (Chapter 10).

Acknowledgements

I would like to thank all the people who assisted me during the PhD studentship period. In particular, I am grateful to the “Italy – USA Fulbright Commission” for choosing me as Member of the Fulbright Alumni Network and for giving me the great opportunity to visit the United States and to live the most fulfilling experience of my life. I am likewise grateful to Prof. Stefano Sacanna and his research group for hosting me at the Molecular Design Institute of the New York University and for all the stimulating discussions and sharing of perspectives we had. I gratefully acknowledge Prof. S. Milioto and Prof. G. Lazzara, who have been supervising me from my Bachelor’s Degree to my PhD, giving me the opportunity to work in their laboratories and, together with all the members of their group, to be part of such an amazing team. Also, I would like to thank all my co-authors for the valuable contributions they brought to our collaborations.

1. Eco-sustainable materials

1.1 Introduction

One of the major critical societal challenges in the 21st century is the strong demand in reducing the environmental degradation and the irresponsible consumption of the natural resources our Earth can actually offer. Pollution and climate change are the most urgent issues that science must tackle in the medium period. Hence, from both the scientific and the technological points of view, the need to exploit and strengthen all the possibilities to achieve this purpose is compelling.¹ Worldwide, scientists and researchers are making great efforts with the aim to provide new green tools to the society, thus ensuring a more respectful development model. Fossil fuels have been the most used source of energy that is being employed to meet the world's increasing energy demands and their use is undoubtedly associated with many different problems and harmful side effects. For instance, the disposal of plastic wastes by incineration increases carbon dioxide amounts in the ecosystem and, in some cases, generates toxic products which contribute to the global warming and the environmental pollution.² Petrochemical-based plastics are widely used due to their large availability, easy processing, low cost and good mechanical properties. Nevertheless, their use must be restricted because they pose some serious ecological concerns. The growing environmental attention requires a profound commitment and, in the most recent years, researchers have focused their attention on the design of new advanced and biodegradable materials with the purpose to replace traditional plastics and to encourage the eco-sustainable transition.³ Specifically, they tried to replace the petroleum-derivatives with eco-friendly, renewable and no toxic natural raw materials from agricultural or marine sources.⁴ Natural biopolymers that can be sustainably produced and are both biodegradable and biocompatible are good candidates but, despite their clear environmental benefits, their use shows major limitations as they generally possess limited mechanical performance due to their low stiffness and strength, weak physical and poor barrier properties and other features that make difficult their direct replacement and their use in commercial applications.⁵ In light of this, developing new environmental-friendly, green and eco-sustainable materials with specific and tailored physico-chemical properties is an ongoing challenge in the field. For instance, the biopolymer functionality can be tuned through its combination with additives, such as plasticizers and nanoparticles,^{6,7} thus representing an alternative to the conventional technologies for improving polymer properties, which may exhibit markedly advanced mechanical, thermal, optical, and physicochemical properties compared to those of the pure polymer.⁸ The class of materials resulting from the union of both organic and inorganic moieties converges in a wide family of so-called *organic-inorganic hybrid materials* that show the characteristic aspects of both the types of components and in some cases additional functionalities inherent to the new hybrid architecture.⁹ These materials represent a fast-growing subject dealing with very important

implications from the academic to the industrial point of view, covering areas of interest as important as biomedicine, pharmacy and health care, environmental science and technology, engineering and building materials, energy conversion and storage, among other crucial fields.¹⁰ The last generation of hybrids derives from nanosized or nanostructured raw materials, which show specific functionalities related to the chemical nature of the nanoparticles and organic species used for their preparation. In particular, nanoclays are really promising as inorganic nanoparticles that can be used for this purpose, thus leading to the design of clay-based hybrids and nanocomposites. More specifically, the organic moiety can be of biological origin and it can present an evolved functional activity. In this latter case, the materials are known as 'biohybrids'.¹¹ On this basis, nanoclays and biopolymers must be considered really interesting green materials for their environmental implications.

1.2 Nanoclays

Although nanoclays technology is a recent development, the science of clay has existed since the dawn of humanity. From prehistoric times, the use of clay is known in architecture, industry, and agriculture with the production of mural paintings, sun-dried or fired bricks, tiles for wall and floor, ceramics, etc. A common characteristic of clay minerals is their fine grained natural structure with sheet-like geometry. Indeed, the sheet-structured hydrous silicates are generally referred to as phyllosilicates. Clay minerals can be divided into four major groups in terms of the variation in the layered structure: the kaolinite group, the smectite group, the illite group, and the chlorite group.¹² The kaolinite group (e.g. kaolinite, nacrite, etc.) is characterized by $\text{Al}_2\text{Si}_2\text{O}_5(\text{OH})_4$ as unit formula. Some members of this group are polymorphs, meaning that they have the same formula but different structure, such as halloysite. Each member is composed of silicate sheets (Si_2O_5) bonded to aluminum oxide/hydroxide layers ($\text{Al}_2(\text{OH})_4$). Montmorillonite, talc and saponite are a few members of the larger smectite clay group. The general formula for this group is $(\text{Ca},\text{Na},\text{H})(\text{Al},\text{Mg},\text{Fe},\text{Zn})_2(\text{Si},\text{Al})_4\text{O}_{10}(\text{OH})_2 \cdot \text{H}_2\text{O}$. The structure contains silicate layers sandwiching an aluminum oxide/hydroxide sheet ($\text{Al}_2(\text{OH})_4$). The illite group is represented by the mineral illite, the only common clay type. The general formula is $(\text{K},\text{H})\text{Al}_2(\text{Si},\text{Al})_4\text{O}_{10}(\text{OH})_2 \cdot \text{H}_2\text{O}$. The structure of this group is similar to the montmorillonite group with silicate layers sandwiching an aluminum oxide/hydroxide sheet in the same stacking sequence. The chlorite group is relatively large and its members are not necessarily considered as clays, since some of them are different in formulas and structures.¹²

Overall, each layer in the structure is composed of two types of sheets: tetrahedral and octahedral. The former is composed of silicon-oxygen tetrahedra linked to the neighboring tetrahedra by sharing three corners, resulting in a hexagonal network. The remaining fourth corner of each tetrahedron forms a part to the adjacent octahedral sheet. The latter, instead, is usually composed of aluminum or magnesium in a six-fold coordination with oxygen from the tetrahedral sheet and with hydroxyl groups. The two sheets together form a layer, and several layers may be joined in a clay crystallite by the interlayer cations, Van der Waals force, electrostatic force, or by hydrogen bonding. The structure of clay minerals can be described in terms of arrangement of tetrahedral and octahedral sheets, allowing the classifications of the clays into three categories: 1:1, 2:1 and 2:1:1 phyllosilicates. The 1:1 phyllosilicates, like kaolinite and halloysite, have one tetrahedral and one octahedral sheet per clay layer whereas the 2:1 phyllosilicates contain two tetrahedral sheets and one octahedral sheet sandwiched between the two tetrahedral sheets (montmorillonite, laponite and illite are a few examples). For what concerns the 2:1:1 phyllosilicates, like cloisite, they are composed of an octahedral sheet adjacent to a 2:1 layer.¹³

Isomorphous substitution is the replacement of an element with another element in mineral crystal without modifying its chemical structure. For example, Al^{3+} can replace Si^{4+} in the tetrahedral coordination, and Al^{3+} can be replaced by Mg^{2+} or by Fe^{2+} and Mg^{2+} by Li^+ in the octahedral coordination. The presence of these substitutions can create charges that are counterbalanced by ions situated in the interlayer.

The term '*nanoclays*' is used here to denote clays whose particles have at least one dimension in the nanoscale range (1-100 nm).¹⁴ Due to their most peculiar features of morphology, tunable surface chemistry, hydrophilic character, surface area and aspect ratio, nanoclays have attracted growing interest in material science as raw materials for the design of smart functional new architectures to be used in many industrial and technological applications.¹⁵⁻¹⁸ Within this field, halloysite, kaolinite and sepiolite are new emerging clays with unique properties and appealing perspectives.

1.3 Halloysite and Kaolinite

Halloysite and Kaolinite are two 1:1 phyllosilicates, belonging to the same clay minerals group, with the chemical formula of $\text{Al}_2\text{Si}_2\text{O}_5(\text{OH})_4 \cdot n\text{H}_2\text{O}$. Despite the same chemical nature, the main difference between these two clays is their structural organization. Indeed, halloysite most characterizing feature is its typical hollow tubular morphology, being composed of a layer of Si–O–Si tetrahedrons overlapping Al–OH octahedrons that create a kaolinite-like sheet, which further rolls up forming hollow tubular nanoparticles (Figure 1.3.1).¹⁹ It is currently unclear the reason of

flat kaolinite rolling into Halloysite Nanotubes (HNTs).²⁰ We can suppose that a packing disorder is created by an interlayer of water molecules, thus causing the curvature and further rolling up of the two neighboring alumina and silica sheets, and forming the multilayer nanotubes. Herein, it is reported that the HNTs walls are formed by the rolling of 15-20 aluminosilicate layers.²¹ In particular, the “n” in the unit formula of halloysite represents the number of interlayer water molecules and it can be $n = 0$ and $n = 2$ for the hydrate or dehydrate nanoclay with a resulting interlayer distance of 0.7 nm and 1 nm, respectively.²² Contrarily to it, kaolinite morphology is a simple layered sheet.²³ Halloysite dimensions strongly depend on the natural deposit the raw clay is extracted from. The HNTs external diameter is 50–200 nm, while the internal diameter and the length are 15–50 nm and 1–2 μm , respectively.²⁴

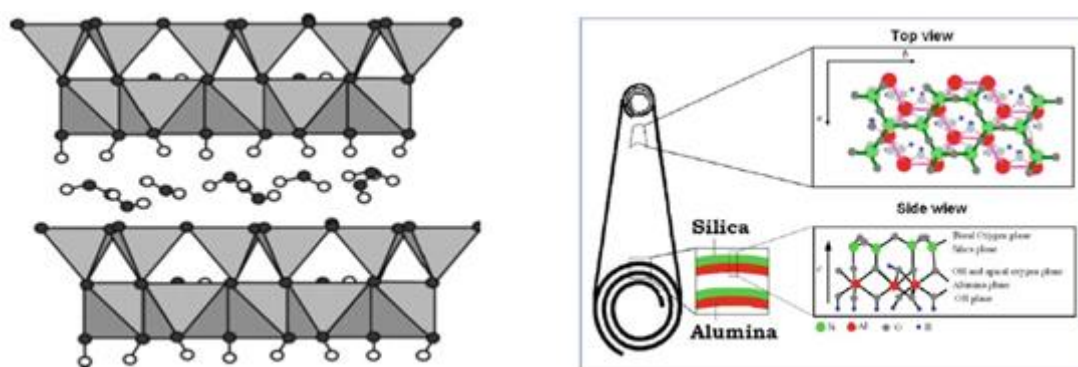


Figure 1.3.1. Crystalline structure of Halloysite (*Ref. 19,22*).

Interestingly, halloysite displays a positively charged lumen and a negatively charged outer surface in the pH range between 2 and 8. This characteristic is due to the different chemical compositions, since the external surface is composed of Si–O–Si groups while the inner surface consists of a gibbsite-like array of Al–OH groups.²⁵ Being a direct consequence of the clay morphology, this property can not be found in kaolinite sheets, which possess different charges in the opposite surfaces. For what concerns HNTs, therefore, this unique feature allows to operate a selective targeted modification of the inner/outer surfaces driven by electrostatic interactions.^{26,27} These groups allow the clays, both halloysite and kaolinite, to participate in electrostatic or hydrogen bonding in polar solvents and to interact favorably with the functional groups of a wide range of chemical species.²⁸ Moreover, HNTs are biocompatible as shown in several in vitro and in vivo studies.²⁹ Hence, due to various characteristics such as a nanoscale lumen, high aspect ratio, relatively low hydroxyl group density on the surface, etc., numerous advanced applications have been discovered for this unique, cheap, and abundant clay.^{30–32} Within this issue, the tubular shape represents an appealing characteristic providing an encapsulation site for active molecules inside the

lumen of the nanotubes, which can act as nanocarriers and delivery systems.^{33,34} In 2001 Price et al. firstly demonstrated that HNTs are proper nanocontainers for Tetracycline, Khellin, and Nicotinamide Adenine Dinucleotide.³⁵ Then, several smart materials have been prepared for the release of bioactive species and halloysite nanotubes based functional new architectures have received increasing attention as evidenced by research articles and reviews.^{36,37} For instance, Halloysite is a promising nanoclay in numerous applications, including drug delivery of antibiotics and non-steroidal anti-inflammatory drugs (NSAIDs),³⁸⁻⁴⁰ or catalytic applications such as metals immobilization onto its functionalized surfaces for the design of efficient catalysts or for hydrogen production and storage.⁴¹⁻⁴³ Moreover, there are many examples proving the importance of halloysite in addition to eco-compatible polymers as starting building blocks for the preparation of novel green materials with specific and technological functionalities.⁴⁴⁻⁴⁷ In particular, environmental remediation with the employ of HNTs as eco-friendly adsorbents for the capture of CO₂, oils adsorption and toxic chemicals entrapment;⁴⁸⁻⁵⁰ the preparation of bioplastics by filling halloysite into pectin matrix for food packaging applications and by combining lisozyme loaded nanotubes and poly (ϵ -caprolactone) (PCL) for the preparation of antimicrobial packaging membrane;⁵¹ the development of halloysite/keratin nanocomposites for the photoprotection of human air.⁵² Also, the addition of HNTs into cellulose and chitosan was exploited for the delivery of curcumin or tissue engineering applications, respectively, and to create membranes for bone regeneration using chitosan and PEO.^{53,54} Furthermore, other applications deal with the development of multilayered biocomposites composed by halloysite between biopolymers for medical or fire retardancy applications,⁵⁵ the design of sustainable cementitious materials for construction and building technology,⁵⁶ the creation of self-healing protective coatings by loading HNTs cavity with corrosion inhibitors and the employ of nanoclays for stabilizing dye formulations to create optically active nanopigments.⁵⁷⁻⁵⁹ Finally, the possibility to host a large variety of active species such as deacidifying (calcium hydroxide) and flame retardant agents (fluorinated surfactants) together with the tunable and controlled release of these molecules from the inner lumen of halloysite makes relevant its use for cultural heritage conservation and treatment.^{60,61}

1.4 Sepiolite

Sepiolite is a microcrystalline hydrated magnesium silicate with $\text{Si}_{12}\text{O}_{30}\text{Mg}_8(\text{OH},\text{F})_4(\text{H}_2\text{O})_4 \cdot 8\text{H}_2\text{O}$ as theoretical unit cell formula, showing a microfibrillar morphology with particle size typically in the 2-10 μm length range.⁶² Due to the similarity of OH and F in electronegativity and ionic radius, the substitution of fluorine for hydroxyl groups is plausible in sepiolite as in other clay minerals.⁶³

Structurally, it is formed by an alternation of blocks and cavities (tunnels) that grow up in the fiber direction (c-axis) (Figure 1.4.1).

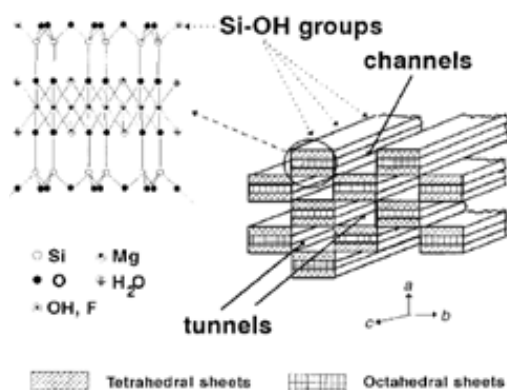


Figure 1.4.1. Schematic model representing the structure of sepiolite (*Ref. 60*).

Each structural block is composed of two tetrahedral silica sheets sandwiching a central sheet of magnesium oxide-hydroxide. Owing to the discontinuity of the silica sheets, silanol groups (Si-OH) are present on the “external surface” of the silicate particles.⁶⁴ These groups are located at the edges of the channels (i.e. those tunnels acceding to the external surface of the silicate) and are directly accessible to reagents allowing the preparation, for instance, of organic-inorganic materials derived from sepiolite with different surface organic functions. The dimensions of the cross-section of sepiolite tunnels are about $11 \times 4 \text{ \AA}^2$. They are filled by two types of water molecules: i) co-ordinated water molecules which are bonded to Mg^{2+} ions located at the edges of octahedral sheets, and ii) zeolitic water, associated by hydrogen bonding with the former. This latter type of water molecules is easily removed by exposure to vacuum or by thermal treatment at about $100 \text{ }^\circ\text{C}$, whereas the former needs more drastic conditions ($>350 \text{ }^\circ\text{C}$, dynamic vacuum) resulting in the complete dehydration of the silicate. The loss of these co-ordinated water molecules causes folding of the structure and the disappearance of the tunnels in agreement with XRD patterns.⁶² Sepiolite shows singular rheological and adsorption properties, as well as a large specific surface area ($\approx 300 \text{ m}^2\text{g}^{-1}$), which is related to the presence of pores of different sizes. The high density of hydroxyl groups is also advantageous to assemble different kinds of nanoparticles provided with diverse functionalities, leading therefore to the preparation of materials with predetermined properties useful for diverse potential applications.^{65,66} The reports from the International Agency for Research on Cancer (IARC) indicate that there is “inadequate evidence” in animals and humans to determine the carcinogenicity of sepiolite fibers of length inferior to $5 \text{ }\mu\text{m}$, whereas there is “limited evidence” in experimental animals for the carcinogenicity of longer sepiolite fibers. Moreover, literature reports that sepiolite exposure did not alter the cell cycle distribution and it triggers neither the

DNA damage response program nor apoptosis, suggesting that it does not significantly assault the genetic material in mammalian cells.⁶⁷ Furthermore, one of the most interesting features of sepiolite is its very high colloidal stability in aqueous media that has been exploited for stabilizing, among others, carbon nanotubes and graphene nanoplatelets suspensions.^{68,69} Bionanocomposites based on sepiolite involving different types of water-soluble polysaccharides (starch, chitosan, alginate, etc.), proteins (gelatin, collagen, wheat gluten), and other biomolecules have been reported as well as the development of biomimetic interfaces based on phospholipids as immobilization hosts for biological species.^{70,71} In some cases, these materials can exhibit enhanced mechanical properties compared to analogous materials based on layered silicates. This could be relevant in numerous applications, e.g., thermal and acoustic insulation, as well as in the packaging industry, environmental remediation, biomedical and biocatalytic applications. Darder and co-authors revealed that the association of sepiolite and chitosan resulted in a threefold improvement of the mechanical properties as compared with unmodified biopolymer films, and at the same time exhibited interesting functional properties allowing their application as components in electrochemical devices.⁷² In light of these properties and features, it is clear that sepiolite represents a very interesting starting building block for designing a wide class of smart materials.

1.5 Biopolymers

Biopolymers are natural-based polymers and an alternative to the petroleum-based materials. They gained recent research interest due to renewability, ecosystem friendliness, availability, sustainability, and degree of functionality. They are chain-like molecules made up of repeating and covalently bonded chemical blocks produced from renewable resources which could be degraded in the environment.⁷³ Biopolymers occupy a very small fraction in the polymer market, however, their place continues to grow year by year. These are the advantages of biopolymers: (1) they increase the soil organic content as well as water and nutrient retention, while reducing chemical inputs and suppressing plant disease, (2) the energy required to synthesize and manufacture most biopolymers is generally much lower compared to other species, and, (3) they offer environmental benefits by using renewable energy resources and reducing greenhouse gas emissions.⁷³ Biopolymers can be differently classified based various scales. Based on their origin, three types can be traditionally distinguished into natural, synthetic and microbial biopolymers. Also, they can be classified by their polymeric backbone, so we find polyesters, polysaccharides, polycarbonates, polyamides, and vinyl polymers. Depending on the type of monomers, we can find three groups: polysaccharides, proteins and nucleic acids. Another way to classify biopolymers is based on their response to heat so we find

elastomers, thermoplastics and thermosets. Generally, biopolymers offer strong development opportunities in a large number of technological sectors and they are widely used in everyday life: packaging, agriculture, medical science, automotive, construction, sports, adhesives, paints and others.⁷⁴ Interestingly, they can display some different features in relation with the natural source where the raw matter, used during the preparation procedure, is extracted.^{75,76} Mostly, organic raw materials are derived from agricultural or marine sources and can be functionalized in order to tune their main features such as the hydrophilic character, the thermal stability and the solubilization capability towards other compounds.⁷⁷

The biopolymers charge is one of the most important feature that affects their suitability in numerous applications and it represents a crucial parameter for their classification since they can be cationic (e.g. chitosan), anionic (e.g. pectin, alginate) or neutral species (e.g. amylose, starch and cellulose derivatives such as hydroxypropylcellulose).^{78,79} Among the others, chitosan, alginate and cellulose derivatives are very attractive due to the consequent differences in their interaction behavior and self-assembly with other building blocks.

1.6 Chitosan

Chitosan, a carbohydrate biopolymer, is a linear hetero-polysaccharide composed of D-glucosamine and N-acetyl-D-glucosamine connected by β -(1-4) linkage and it can present varying degree of deacetylation.⁸⁰ It is a cationic polysaccharide obtained from the alkaline deacetylation of the chitin using sodium hydroxide. After cellulose, chitin is the most profuse natural biopolymer found in the shells or exoskeletons of crustaceans, such as shrimps, crabs, lobsters, or in molluscs like bivalves, insects like cockroach, grasshopper, and in cell wall of some fungi.⁸¹ The presence of the amino (-NH₂) groups, in the glucosamine residues, renders chitosan extremely hydrophilic, capable of interacting with water and other polar compounds through strong interactions, such as hydrogen bonding.⁸² In addition, this process is responsible for allowing the dissolution of chitosan in acidified aqueous solutions, being chitosan virtually insoluble in neutral and alkaline aqueous solutions, as well as in nonpolar organic solvents. Being biodegradable, stable, non-toxic and biocompatible, this biopolymer has unique properties like excipient, but it also exhibits valuable properties that promote its diversity in biotechnology and biomedical fields like antimicrobial activity, mucoadhesion, well assessed chemistry, activation of macrophages and immunostimulation.⁸³ Indeed, chitosan carries a net positive surface charge at slightly acidic pH. For this special character, it can easily interact with the anionic mucin protein present in the mucus layer. The mucoadhesive property of chitosan allows intestinal and nasal cellular uptake and

provides an excellent platform for drug delivery. Mucoadhesion of chitosan is accomplished mainly by electrostatic interaction followed by hydrogen bonding and hydrophobic interaction.⁸⁴ Besides medical applications, chitosan can be used in many different domains, such as food packaging, removal of pollutants, membrane productions, etc.^{83,85,86}

1.7 Alginate

Alginic acid is a naturally occurring hydrophilic, β -1 \rightarrow 4-linked linear polymer built of D-mannuronic and L-guluronic acid.⁸⁷ It is found in cell walls of seagrass and brown algae, exerting a structural function by giving mechanical strength and flexibility. It can be also produced by some bacterial species: *Azotobacter vinelandii*, *Pseudomonas aeruginosa* and *Pseudomonas fluorescens*. The chain length and the order of blocks in the macromolecule may be different depending on the species and the harvest conditions, thus determining the chemical and physical properties of the alginates.⁸⁷ It has been extensively investigated within the polymeric biomaterials in virtue of its nontoxicity, biocompatibility and convenient source. Due to their negative charge, alginates can form hydrogels rapidly with multivalent cations, such as Ca^{2+} , Ba^{2+} or Fe^{3+} in mild condition via cross-linking, in which Ca^{2+} is more preferable due to low toxicity and low cost.⁸⁸ In light of its gelling ability under mild conditions and its stability, alginate allows the formation of materials, like hydrogels, microspheres, fibres and microcapsules, commonly used in biomedical applications such as wound healing, drug delivery, bone regeneration and tissue engineering.⁸⁹ The fact that alginate is a biocompatible polymer, it does not present toxicity and it is biodegradable, makes it ideal for human body direct applications.⁹⁰ Besides, it has also been used in cosmetic, food and pharmaceutical industries as stabilizer, emulsifier and humectant.⁹¹ Also, alginates can be used for the removal of heavy metals from wastewater.⁹²

1.8 Cellulose Nanofibers

Cellulose is the most abundant renewable biopolymer, which is primarily present in wood biomass. For the past few decades, cellulose has attracted attention as one of the promising polysaccharides for accomplishing highly engineered nanoparticles, which can be applied in many areas. It is a linear chain of ringed glucose molecules and it has a flat ribbon-like conformation.⁹³ The repeated unit is composed of two anhydroglucose rings, $(\text{C}_6\text{H}_{10}\text{O}_5)_n$; $n = 10000$ to 15000 , where n depends on the cellulose source, linked together through an oxygen covalently bonded to C1 of one glucose ring and C4 of the adjoining ring (1-4 linkage) and so called β 1-4 glucosidic bond.⁹⁴ The intra-

chain hydrogen bonding between hydroxyl groups and oxygen atoms of the adjoining ring molecules stabilizes the linkage resulting in the linear configuration of the cellulose chain (Figure 1.8.1).

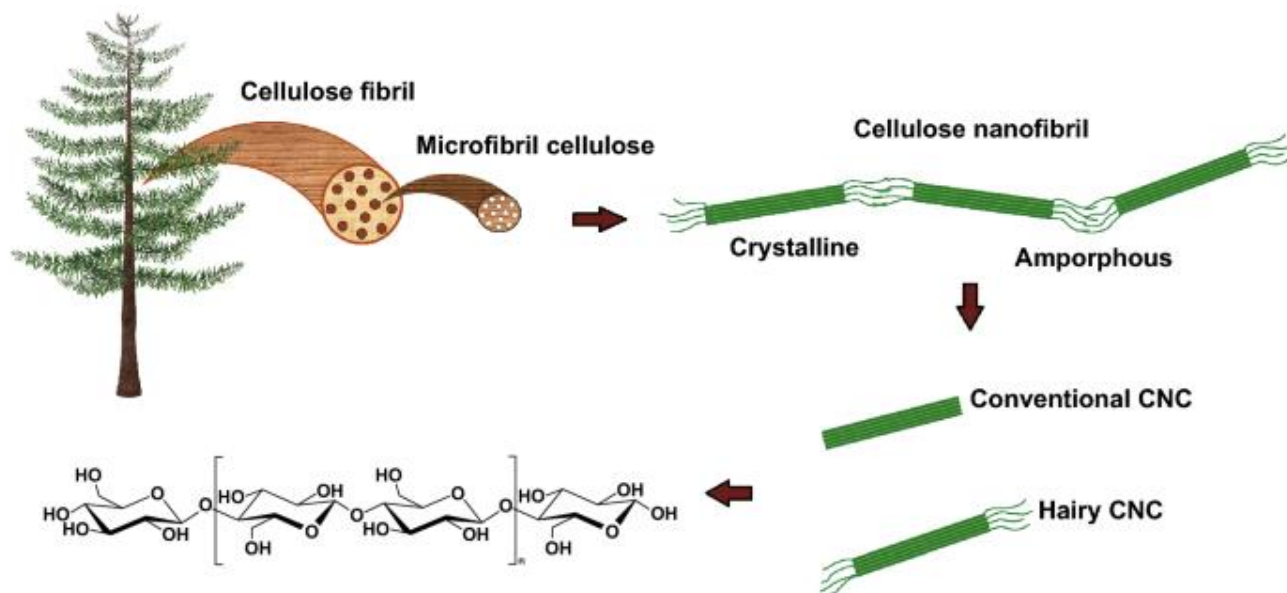


Figure 1.8.1. Schematic representation of cellulose structures from resources to molecular level (Ref. 92).

During biosynthesis, Van der Waals and intermolecular hydrogen bonds between hydroxyl groups and oxygen atoms of adjacent molecules promote parallel stacking of multiple cellulose chains forming elementary fibrils that further aggregate into larger microfibrils (5–50 nm in diameter and several microns in length). The intra- and inter-chain hydrogen bonding network makes cellulose a relatively stable polymer, and gives the cellulose fibrils high axial stiffness. Within these cellulose fibrils there are regions where the cellulose chains are arranged in a highly ordered (crystalline) structure, and regions that are disordered (amorphous-like).⁹⁴ By applying mechanical, chemical, physical, or biological methods, cellulosic fibers can be disintegrated into cellulose substructures with microsized or nanosized dimensions.⁹⁵ The term “nanocellulose” refers to a family of nanomaterials achieved by different chemical and mechanical methodologies that provoke a defibrillation process in raw cellulosic materials (e.g., wood, cotton, etc.).⁹⁶ They are usually classified into three main groups: (i) cellulose nanofibrils (CNFs), (ii) cellulose nanocrystals (CNCs), and (iii) bacterial cellulose (BC).⁹⁷ The main nanomaterials obtained from those processes are CNF and cellulose nanocrystals.⁹⁸ CNF are physically entangled in a wet gel. Once that water is evaporated, fiber–fiber bonding due to secondary attraction forces, including hydrogen bonds, are formed between the CNF. Because of their high aspect ratio (CNFs have an average length of around 1 μm and an average diameter of 2–5 nm), chemically modifiable surface, high Young’s

modulus resulting from high crystallinity and relatively inexpensive production methods, nanocellulose exhibits a great potential as a sustainable nanomaterial for the fabrication of many functional structures.⁹⁹ In recent years, nanocellulose based materials are the focus of every active research with the aim to develop a wide variety of applications in fields as energy storage and conversion, water treatment, biomedicine, packaging, fire retardancy, support for metal and metal oxide nanoparticles in catalysis and electronics.^{100,101} In this context, the concept of “nanopaper” refers to the use of cellulose nanofibers for making paper employing this nanomaterial instead of conventional cellulose.¹⁰² Such nanopapers show improved mechanical properties, optical transparency, and a smooth surface together with the possibility of combination with other kind of nanoparticles, as well as the incorporation of different functional groups on their surface.¹⁰³

1.9 Mater-Bi[®]

Mater-Bi is a biodegradable material based on plasticized starch that is commercially purchased by Novamont, an innovation-oriented company generally recognized as a pioneer in the field of bioplastics in Italy with a capacity of 60,000 tons per annum.¹⁰⁴ Starch is an inexpensive, abundant, annually renewable material derived from corn and other crops. The biodegradation of starch products recycles atmospheric CO₂ trapped by starch-producing plants. All starches contain amylose and amylopectin at ratios that vary with the natural source, thus providing a natural mechanism for regulating the properties of this material.

For industrial applications, starch is preferably used in its thermoplastic form, namely the Thermoplastic Starch (TPS), rather than in its native form, because the plasticized granules of native starch allow the formation of a continuous and viscous phase, which can be easily processed by traditional plastics processing technologies.¹⁰⁵ However, the development of TPS-based materials is still limited due to its fragility, low water resistance and dependence of the thermo-mechanical properties on the environmental moisture. This is why TPS has also been blended with other polymers in order to widen its range of applications and to improve its physico-chemical properties.¹⁰⁶ In this context Mater-Bi is one of the most popular commercial TPS, which have been marketed in accordance with the specifications of its use due to the fact that it is derived from a natural raw material and it has a low impact on the environment. Mater-Bi products constitute a wide family of biodegradable materials exhibiting different microstructures, from a droplet-like to a layered one, probably as a result of hydrophobic and hydrophilic interactions between the natural and the synthetic components.¹⁰⁷ Under the Mater-Bi trademark, Novamont today produces different classes of biodegradable materials, all based on starch and varying in synthetic

components. Although the exact composition of Mater-Bi is not known, the literature provides some indications.¹⁰⁸ Thus, it is possible to find: (i) Mater-Bi[®] Y, composed of starch and cellulose acetate blends, whose properties resemble those of polystyrene (PS); (ii) Mater-Bi[®] A, constituted by a strong complex between TPS and copolymers of polyvinyl alcohol (PVA); (iii) Mater-Bi[®] V, having a TPS content greater than 85% and a high solubility in water ; (iv) Mater-Bi[®] Z, having a poly(-caprolactone) (PCL) matrix; and (v) Mater-Bi[®] N whose polymeric matrix is based on polybutylene adipate-co-terephthalate (PBAT).¹⁰⁹ Since it is fully biodegradable and compostable and, as such, it can be disposed of together with organic waste, Mater-bi can be used in various commercial and industrial contexts: packaging of fresh and dry food as well as non-food products, carrier and shopping bags, foodservice (e.g. plates, glasses, cutlery, bowls, straws, ice cups, etc.), agriculture and many others.

1.10 Biocompatible nanomaterials

It is now clear the importance of green and eco-sustainable materials in facing and tackling both technological and societal challenges. Starting from the most diverse types of raw materials and building blocks, several laboratories have been developing various strategies to improve the key properties of the resulting novel platforms by exploiting the proper features of the initial components and also by taking advantage of new synergistic effects arising after their manipulation. However, within the field of environmental-friendly nanomaterials, many different architectures have been proposed. Polymers and biopolymers have been employed for the preparation of films which have been reinforced and optimized by adding nanoparticles, thus creating the so-called *nanocomposite films*. The resulting materials may exhibit markedly improved mechanical, thermal, optical, gas barrier and physicochemical properties compared to those of the pure polymer or conventional (microscale) composites.¹¹⁰ Therefore, the design of bioplastics plays a major role in replacing the petroleum-derived products in order to promote a green transition. The matrix-filler compatibility must be addressed during the fabrication of bionanocomposite films, since the introduction of inorganic fillers such as silica, alumina, or metals may detrimentally impact the recyclability of biopolymers.¹¹¹ Furthermore, biohybrid materials have been prepared and used in the form of powdery materials, taking advantage of their nanoscaled dimensions and colloidal stability, and exploiting the electrostatic, Van der Waals and covalent interactions between the inorganic species and the organic moieties (e.g. clays and surfactants).¹¹² Besides, since their discovery, hydrogels have received attention from the scientific community due to the wide range of applications they can be used for. In particular, with the evolution of nanotechnology, the

challenge to design and prepare hydrogels with specific and requested features at the nano-scale led to the development of nanohydrogels. Among the different polymeric species that can be used to achieve this aim, polysaccharides cover a marked importance, especially in the preparation of the so-called “polysaccharide-based natural hydrogels”, for some of their most peculiar properties such as water solubility and swelling capacity, biocompatibility and biodegradability, self-healing, pH sensitivity and also due to the adaptability of their networks that is crucial for their use and for the development of eco-friendly *hydrogel beads*.^{113,114} Also emulsions, either in the form of water-in-oil (W/O) or oil-in-water (O/W), play important roles within the domain of green and eco-sustainable materials for their application in the field of pharmaceutical, food, personal care products, and petrochemical industries.¹¹⁵ In particular, conventional emulsions were generally stabilized by surfactants, which induced several drawbacks including environmental problems and difficulty in recovery but, recently, the solid particles as alternatives of traditional emulsifiers have drawn much attention because of their low toxicity, low cost, and remarkable resistance against coalescence, leading to the formation of the *Pickering emulsions*.¹¹⁶ These emulsions exhibit many unique advantages including enhanced stability, improved biocompatibility, and environmental friendliness.

1.11 Aims and objective of the study

The work of this thesis was addressed to the creation and development of innovative and eco-friendly functional hybrid materials based on nanoclays, as inorganic solid counterpart, and polymers or biopolymers as organic moieties. Firstly, an extended physico-chemical study on the thermodynamics of water confinement within the inner lumen of halloysite nanotubes was conducted in order to provide valuable insights on the loading mechanism of guest molecules and to optimize the encapsulation efficiency into HNTs from aqueous solutions (attached paper I). Then, a study was carried out by focusing the confinement effect of an organic solvent. Being the loading efficiency as important as the release kinetics for all those applications in which halloysite nanotubes can be used, the purpose of this study concerned the possibility to target the loading site of the guest molecules and to control, above all, the releasing profiles from the nanomaterials to the solution (submitted paper). Hence, we tried to design and develop selectively functionalized HNTs by using temperature-responsive PNIPAAms in order to generate smart hybrid nanoparticles. To do so, Van der Waals and electrostatic interactions between the clay and the macromolecules were exploited and the effect of the thermodynamic behavior after functionalization and therefore the temperature responsive features of the resulting hybrid material were investigated (attached paper

II). The electrostatic interactions between oppositely charged counterparts (i.e. chitosan and halloysite) were also exploited with the aim to propose a novel strategy for the preparation of biohybrids with tunable and controlled release properties by varying the coating efficiency onto HNTs surfaces (attached paper III). We also prepared and characterized novel green and eco-sustainable gel beads based on biopolymers, namely chitosan and alginate, and halloysite. In particular, the aim of this work was to design hydrogels with a specific layered structure, with a chitosan/halloysite rich core and an alginate external coating, which could be used as drug carrier and delivery system (attached paper IV). Since the addition of nanofillers to a polymeric matrix is a well-known method to improve the mechanical properties of the resulting nanocomposite materials, we also prepared novel bioplastics based on Mater-Bi and nanoclays. For this purpose, we firstly used sepiolite, laponite and halloysite in order to explore the effect of the addition of the nanoclays on the mechanical behavior of the Mater-Bi based films and to assess which clay improved the most the overall features of the resulting samples (attached paper V). In light of this, we also studied the influence of HNTs concentration on both the thermal and mechanical properties of the prepared bioplastics, with the aim to provide an easy preparation protocol for the design of Mater-Bi/Halloysite nanocomposite films that could be used for several technological applications (attached paper VI). At this point, we used the attained knowledge with the aim to design new nano-engineered materials to be employed in different fields such as health and pharmaceutical sciences, cosmetics or food storage. Hence, we studied the preparation of a novel functional architecture composed of a layered tablet made of chitosan and halloysite which was sandwiched between two alginate layers (attached paper VII). We also designed a new biohybrid material made of halloysite, sepiolite and cellulose nanofibers that was developed in order to exploit the proper components features together with other arising synergistic properties (attached paper VIII). Both the two materials were tested for the controlled and sustained release of bioactive species by assessing their applicability through the simulation of the human gastro-intestinal path most typical conditions and by testing the bactericidal and antiseptic activity through in vitro antibacterial assay, with the aim to open a versatile path for developing other related materials of potential interest in different technological fields. Finally, we focused on the preparation of Pickering Emulsions based on halloysite and wax. In particular, we tried to develop a new strategy for the development of pickering emulsions using water as the unique solvent and we studied the possibility to tune the particles dimensions as a function of the clay content (paper in preparation). The proposed protocol was exploited for the treatment of waterlogged archaeological woods, thus opening new perspectives also for the consolidation of shipwrecks of big dimensions.

2. Effect of the pressure on the loading mechanism of Halloysite

2.1 Loading and release optimization: a general overview

The possibility to load the inner volume of halloysite nanotubes is a crucial factor and it represents an emerging issue because of its implications on the both fundamental sciences and nanotechnologies, as previously discussed in the introduction chapter.^{117–119} For instance, HNTs can act as nanocontainers for biologically and chemically active molecules, whose sustained release from the confined space can extend their action time, thus allowing to exploit these systems for specific pharmaceutical, medical, food packaging and many other technological purposes.¹²⁰ Therefore, the importance to load the inner volume of the nanotubes together with the possibility to control and to optimize this mechanism are two very crucial aspects.

The confinement effect of a liquid into a very narrow space inside of nanoparticles whose aspect ratio is very high plays a major role within this issue. Indeed, literature reports that the encapsulation of molecules inside carbon nanotubes from aqueous media strictly depends on the particular evaporation process occurring in the confined space.¹¹⁷ As far as HNTs are concerned, similar observations were made, proving that by subjecting the drug/clay dispersion to a vacuum pumping step, where the pressure is lower than the standard atmospheric value, the drug loading efficiency is greatly enhanced for comparison with encapsulation protocols carried out without any particular pressure control.³⁵ In light of this, the most used protocol for the HNTs loading is composed of three steps: (1) mixing of the clay dry powder with a saturated solution of the guest molecules; (2) sonication and stirring of the HNTs/guest molecules dispersion; (3) vacuum pumping in/out operations for 1–5 h and then cycling it back to the atmospheric conditions. Generally, this last operation is repeated for 3 times. However, the specific influence of the vacuum pumping on the filling mechanism of HNTs lumen was still unclear. The only macroscopic effect was represented by a slight fizzing of the suspension and, at first, this observation was related to the air removal from the inner lumen of halloysite improving the filling of the internal empty space.¹²¹ Recently, instead, it has been hypothesized that the lower pressure conditions increase the loading efficiency because of the water removal from the nanotubes.¹²² Hence, in this chapter we demonstrate the confinement of water within the inner lumen of halloysite and we provide a clear and unequivocal description of the HNTs filling mechanism from aqueous solutions of guest molecules, searching a correlation with the optimization of the loading efficiency (attached paper I). Afterwards, we investigate the confinement effect of an organic solvent, namely ethanol, in order to understand its influence on the loading mechanism and to exploit the possibility to target the drug localization in the nanomaterials depending on the loading protocol (submitted paper). Above all, our aim is to investigate about the possibility to have control both on the filling efficiency and on the releasing kinetics.

2.2 Water confinement within HNTs and the role of vacuum conditions

According to the Gibbs-Thomson effect, the curvature of halloysite inner surface increases the water vapor pressure and, consequently, the evaporation process is faster. Namely, the increase of the vapor pressure is related to the surface/volume ratio and it is enhanced for water confined within the HNTs pores. In general, the dependence of the vapor pressure $P(r)$ of a liquid on the curvature of the pores is expressed by the Kelvin equation:¹²³

$$P(r) = P^\infty \exp(\gamma/r \cdot \rho \cdot k_B \cdot T) \quad (2.2.1)$$

where P^∞ is the vapour pressure of the bulk liquid, γ is the surface tension, r is the pore radius, ρ is the density, k_B is the Boltzmann constant and T is the temperature.

With the aim to demonstrate the water confinement inside the cavity of halloysite nanotubes, Knudsen thermogravimetry (KTG) tests were conducted in isothermal conditions (temperature was fixed at 30 °C). Herein, by replacing the standard open pan with the Knudsen cell, which possesses an orifice, it is possible to properly investigate the interactions between water and nanoclays.¹²⁴

KTG measurements were conducted on aqueous dispersions of clay samples, and namely: kaolinite, pristine HNTs and HNT/NaL, which are nanotubes with hydrophobically modified inner lumen. Figure 2.2.1 shows the morphology of the nanoclays used in this work.

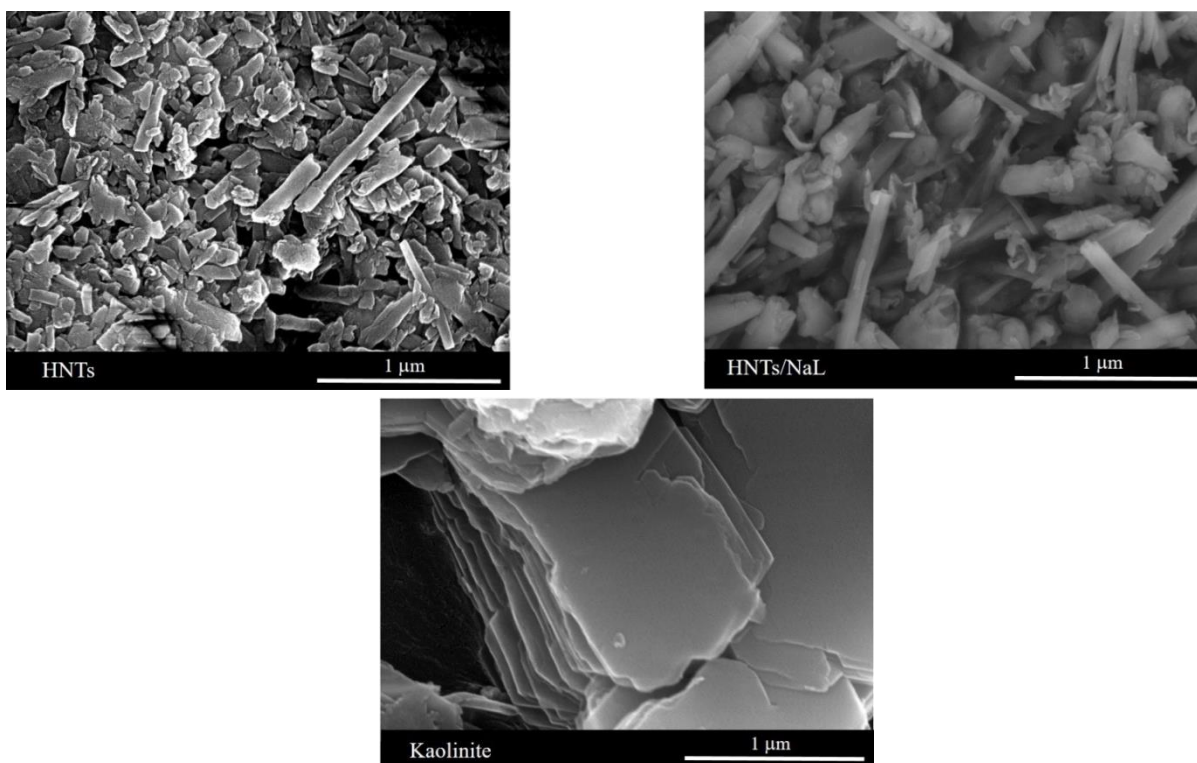


Figure 2.2.1. FESEM images for HNTs, HNTs/NaL and kaolinite.

KTG measurements allowed us to study the isothermal water evaporation from wet nanoclays by focusing the evolution of the thermodynamic water activity (a_w) during the evaporation according to the following equation:

$$(dm/dt)_n/(dm/dt)_w \approx (P_{int})_n/(P_{int})_w = a_w \quad (2.2.2)$$

being $(dm/dt)_n$ and $(dm/dt)_w$ the mass loss rates for the nanoclay aqueous dispersion and pure water, respectively. $(P_{int})_w$ represents the relative vapor pressure for pure water, while $(P_{int})_n$ is the vapor pressure of water contained in the nanoclay dispersion. Therefore, the thermodynamics of water evaporation from halloysite nanotubes and kaolinite was explored by KTG experiments in order to investigate the effect of the nanoclay morphology. Based on this analysis, the dependence of the water evaporation rate on the moisture content (M_w), calculated from the ratio between the masses of water and dry nanoclay, for HNTs, HNTs/NaL and kaolinite dispersions is reported in Figure 2.2.2.

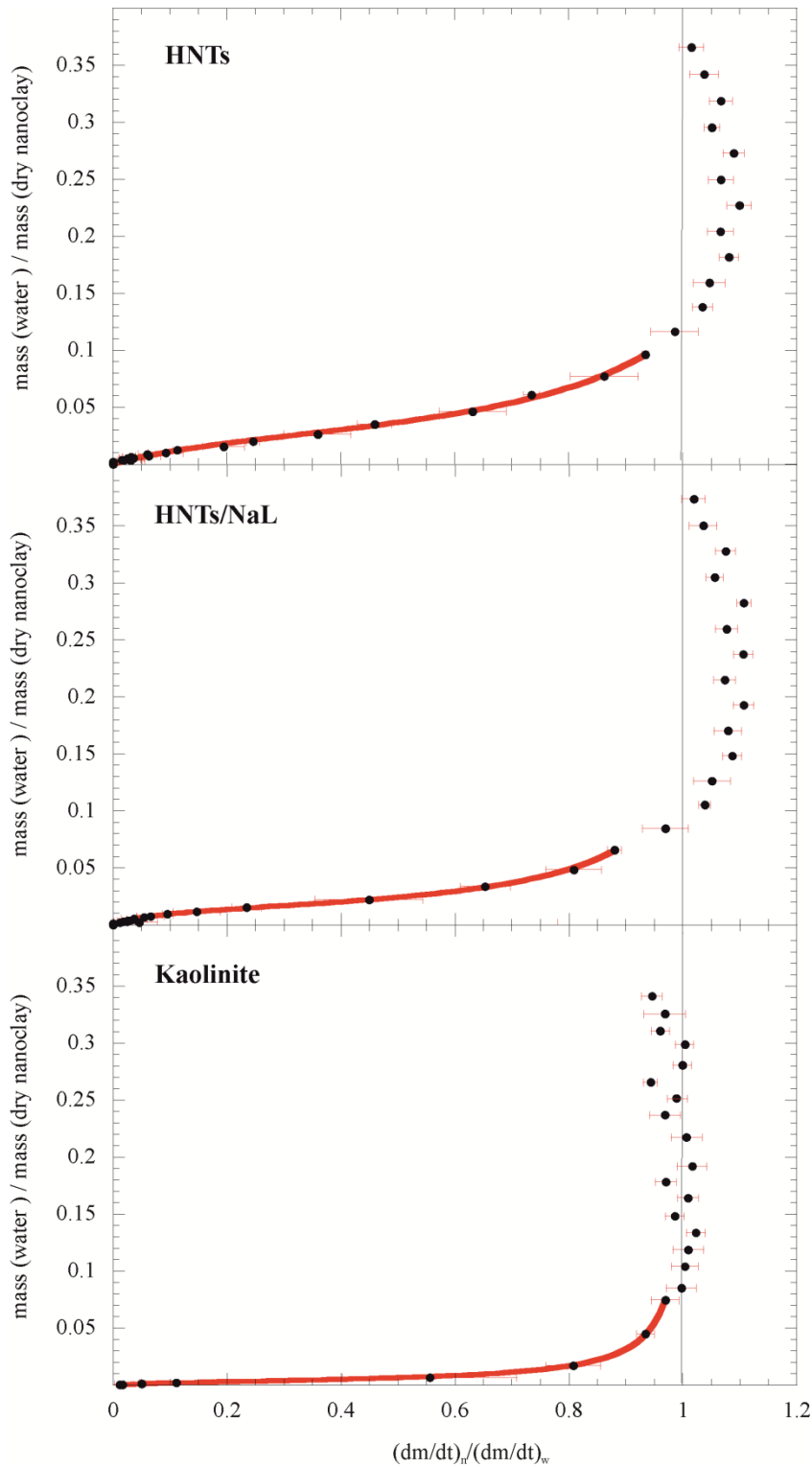


Figure 2.2.2. Mass loss rates for the nanoclay aqueous dispersions normalized for pure water evaporation as a function of the mass ratio between water and dry nanoclay. The experimental data in the water activity range between 0.05 and 0.95 were fitted according to the GAB model (red solid line).

In the reported graphs, it is possible to classify the evaporating water in three categories: 1) bulk water with $(dm/dt)_n / (dm/dt)_w = 1$; 2) confined water with $(dm/dt)_n / (dm/dt)_w > 1$; and 3) adsorbed water with $(dm/dt)_n / (dm/dt)_w < 1$. It is noteworthy that the interlayer water molecules proper of

halloysite nanotube can not be detected at these conditions, since they leave the inorganic solid at ca. 500 °C. The presence of evaporating water in both pure and surfactant modified halloysite is an indication that its vapor pressure is greater than that of bulk water, due to the confinement of water molecules within HNTs inner lumen, in agreement with the Gibbs-Thomson effect. Hence, the confined water can evaporate faster than the bulk water due to its higher vapor pressure and this aspect represents the main driving force for filling the cavity of HNTs cavity. It was also observed that the hydrophobic functionalization of the halloysite lumen did not alter the water confinement, meaning that the chemical nature of the inner surface does not influence the confinement process. On the other hand, no confined water is detected for kaolinite nanoclay, since all the evaporating water possesses $(dm/dt)_n/(dm/dt)_w$ values ≤ 1 . This is most likely due to the proper morphology of kaolinite sheets that do not provide any confinement site for the solvent. These observations are sketched in Figure 2.2.3.

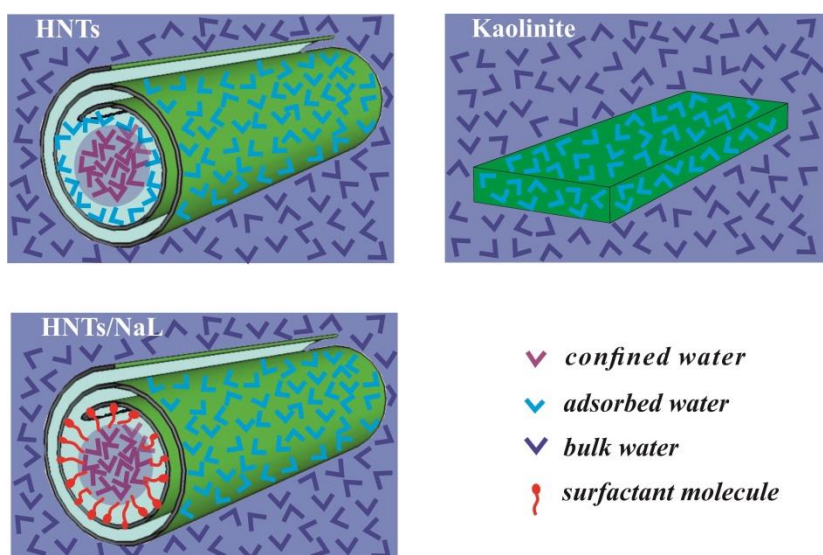


Figure 2.2.3. Schematic representation of the water interactions with clay nanoparticles.

If we focus on the adsorbed water molecules, with $(dm/dt)_n/(dm/dt)_w < 1$, other observations can arise. As shown in Figure 2.2.2, the desorption isotherms were successfully fitted by using the Guggenheim-Anderson-de Boer (GAB) model,¹²⁵ which is valid for $0.05 \leq a_w \leq 0.95$ and, based on this, the specific surface area (SSA) for water sorption was determined and reported in Table 2.2.1 for each investigated sample.

Table 2.2.1. Specific surface area of the nanoclays determined by the fitting of water desorption isotherms.

Nanoclay	SSA / m ² g ⁻¹
HNTs	96 ± 4
HNTs/NaL	51.9 ± 1.3
Kaolinite	13.4 ± 0.3

According to the morphological characteristics, kaolinite possesses a smaller SSA compared to halloysite. Namely, the rolling of kaolinite plates into halloysite nanotubes generates an enhancement of the surface area because of geometrical considerations. Similarly, HNTs/NaL has a smaller specific surface area than pure HNTs, due to the surfactant modification of the inner lumen. Indeed, this difference can not be ascribed to structural or geometrical variations since, even after the chemical functionalization, the hollow tubular morphology is preserved (as shown in FESEM images in Figure 2.2.1). Therefore, pristine HNTs possess a hydrophilic lumen that allows for the water adsorption onto the internal surface whereas water molecules cannot be adsorbed within the hydrophobically modified cavity of HNTs/NaL. In light of this, HNTs exhibits two hydrophilic adsorption sites (outer and inner surfaces), while the water sorption is limited to the HNTs/NaL outer shell. These difference are also enlighten in Figure 2.2.3.

Afterwards, we investigated the effect of pressure conditions on the guest molecules loading within HNTs lumen. For this purpose, we used different bioactive species, namely: metoprolol tartrate (MT), salicylic acid (SA) and malonic acid (MA). In particular, the atmospheric pressure was changed by means of a vacuum jar and the loading procedure was carried out by exposing the aqueous solution at ambient pressure ($P = 1$ atm) as well as under forced reduced pressure ($P = 0.01$ atm). Thermogravimetry (TGA) was used to determine the loading efficiency.

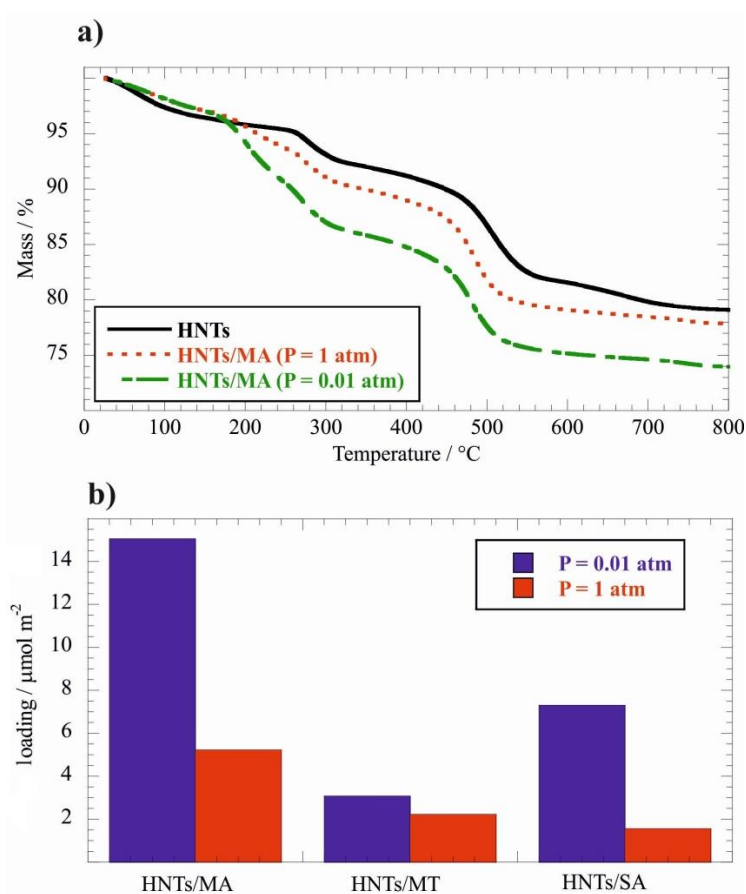


Figure 2.2.4. (a) Thermogravimetric curves for HNTs and HNTs loaded with malonic acid. (b) Loadings for HNTs filled with malonic acid, metoprolol tartrate and salicylic acid.

In Figure 2.2.4(a), the thermograms of pristine halloysite and HNTs filled with malonic acid are reported as an example. It is clear that the presence of organic moieties reduced the residual mass at high temperature because of their decomposition from 200 to 400 °C. More interestingly, the residual mass is lower when the loading procedure is conducted under vacuum conditions (0.01 atm) compared to the filling protocol carried out at room pressure (1 atm), highlighting the better loading efficiency at reduced pressure.

In light of this, we calculated the amount of guest molecules encapsulated inside the nanotubes (as μmol of guest molecule per m^2 of halloysite surface), by using the rule of mixtures (figure 2.2.4(b)). Specifically, the amount of guest molecule incorporated within the nanotubes increased by 38, 188 and 369 % for MT, MA and SA, respectively, as a consequence of the pressure reduction, confirming that the vacuum pumping plays a major role in favoring the filling of HNTs. Besides, morphological investigations of loaded HNTs confirmed that a lower pressure increases the filling of the halloysite lumen. In this regards, Figure 2.2.5 shows FESEM images of HNTs/MA samples prepared at different pressure conditions.

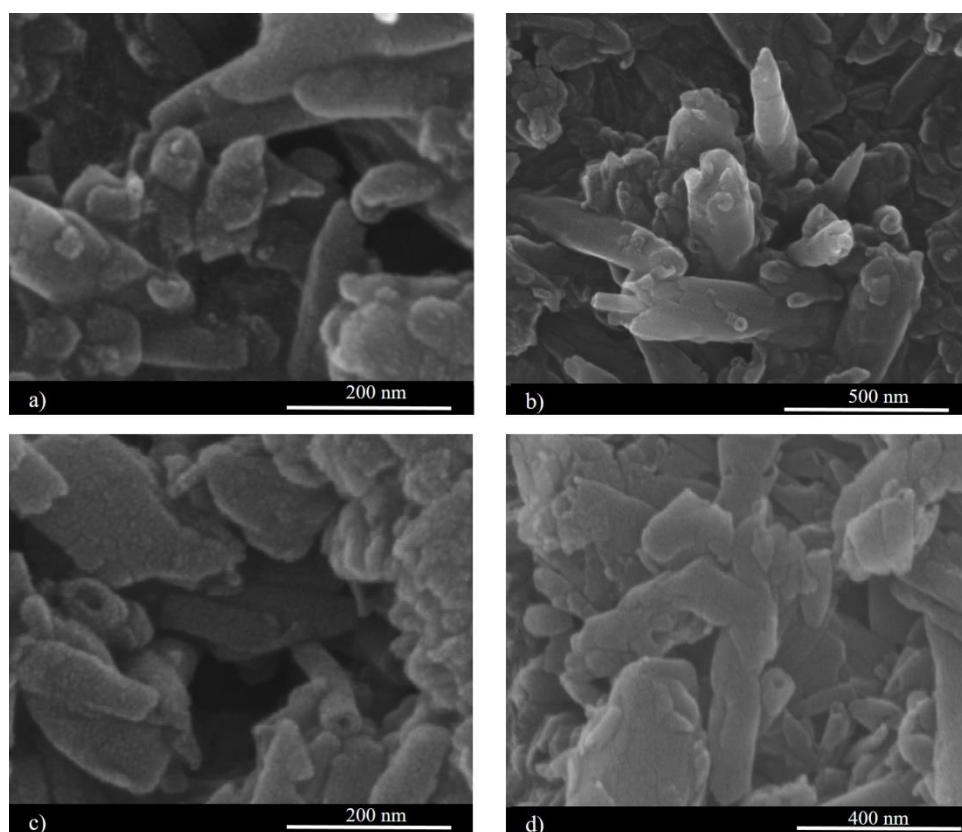


Figure 2.2.5. FESEM images for HNTs/MA prepared at $P = 0.01$ atm (a,b) and 1 atm (c,d).

Clearly, the loading procedure did not change the halloysite peculiar tubular morphology but, more importantly, halloysite loaded at $P = 0.01$ atm (Figures 2.2.5(a,b)) evidenced several nanotubes fully closed with some spherical nanoparticles at the lumen entry as a consequence of the MA filling. This observation was not made for the loading protocol carried out at $P = 1$ atm (Figures 2.2.5(c,d)), indicating a lower loading efficiency. Then, the influence of the pressure conditions on the loading mechanism of halloysite is strictly correlated to the water confinement within HNTs cavity, proved by Knudsen thermogravimetry, and the thermodynamic evidence of the water confinement is the starting point for a proper description of the loading mechanism of HNTs cavity from aqueous solutions of guest molecules (Figure 2.2.6).

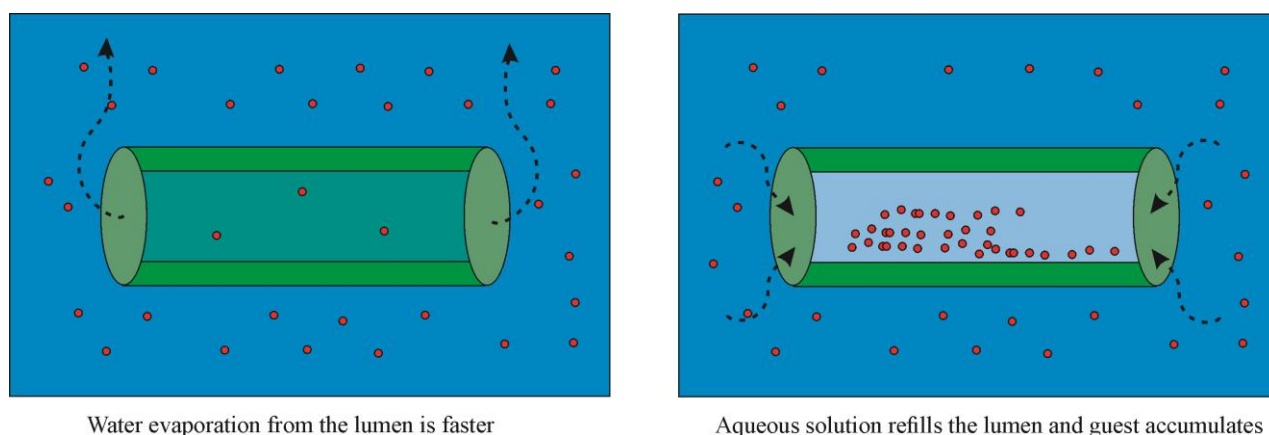


Figure 2.2.6. Schematic representation on the filling process of halloysite nanotubes.

As sketched, the different volatility of confined and bulk water is the key factor for filling the nanotubes. In particular, the fraction of water confined into the lumen exhibits a larger vapor pressure compared to that of the bulk water generating a faster evaporation, attributed to the Gibbs-Thomson effect. During the water evaporation, the active compounds precipitate inside the lumen and, when the vacuum is broken, a flux of fresh aqueous solution from the bulk phase to the HNTs cavity is formed, thus increasing the amount of entrapped guest molecules. By repeating the vacuum pumping operations several times, the loading efficiency is highly enhanced. Hence, the replacement of the aqueous solution inside the halloysite lumen is facilitated under low-pressure conditions because the water vapor pressure is approached. As a consequence, the solvent volatilization rate increases.

In conclusion, this work represents the first thermodynamic demonstration of the water confinement within the cavity of HNTs and it describes physico-chemical aspects of halloysite filling. The attained knowledge represents a fundamental step for the development of loading protocols into confined spaces of tubular nanoparticles.

2.3 Targeting the site for drug loading into HNTs

In this paragraph we study the confinement effect of another solvent, namely the ethanol, and its influence on the loading mechanism. More importantly, we investigate the possibility to specifically target the drug site into halloysite nanotubes and, as a consequence, to control the releasing kinetics of active species from the inner lumen. Indeed, this seems to be the most important aspect concerning the use of halloysite as controlled and tunable delivery system.

With this in mind, the encapsulation of two different model drugs, salicylic acid and diclofenac, within the halloysite cavity was performed by ethanol suspensions. Here again, two protocols have

been carried out for the loading of HNTs at $P = 0.01$ atm and $P = 1$ atm, respectively. The same procedure was repeated using kaolinite instead of halloysite.

To investigate the effect on the filling efficiency, TGA measurement were performed and, using the rule of the mixtures, the loading amounts were determined (Figure 2.3.1).

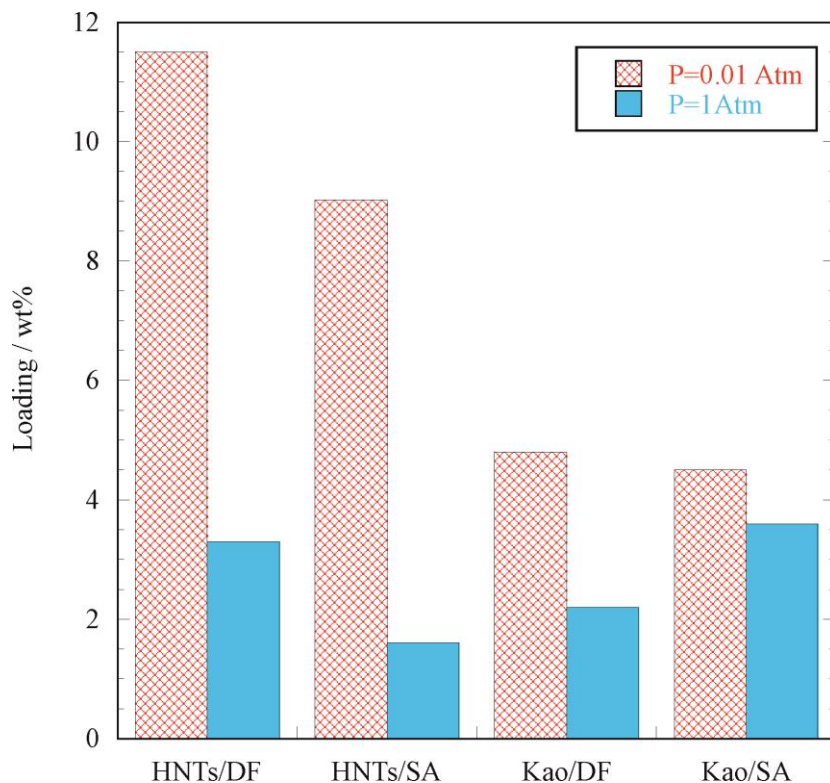


Figure 2.3.1. Loading efficacy for nanoclay/drug systems prepared at different pressure conditions.

It is clear that the pressure conditions play a major role in controlling the loading efficiency of halloysite nanotubes, thus confirming the results discussed in the previous paragraph. In particular, the reduced pressure enhances the amount of guest molecules encapsulated into HNTs by a factor of 4 and 6 for diclofenac (DF) and salicylic acid (SA), respectively, whilst the dependence on the external conditions is less crucial for kaolinite (Kao) although the reduced pressure generated an increase up to a factor 2 in the loading amount of diclofenac.

In order to investigate the morphological features of halloysite and to enlighten any possible difference in the loading site, Transmission Electron Microscopy (TEM) was carried out. Figure 2.3.2 shows the images for pristine nanotubes and HNTs/DF and HNTs/SA samples prepared at $P=0.01$ and $P=1$ atm, respectively.

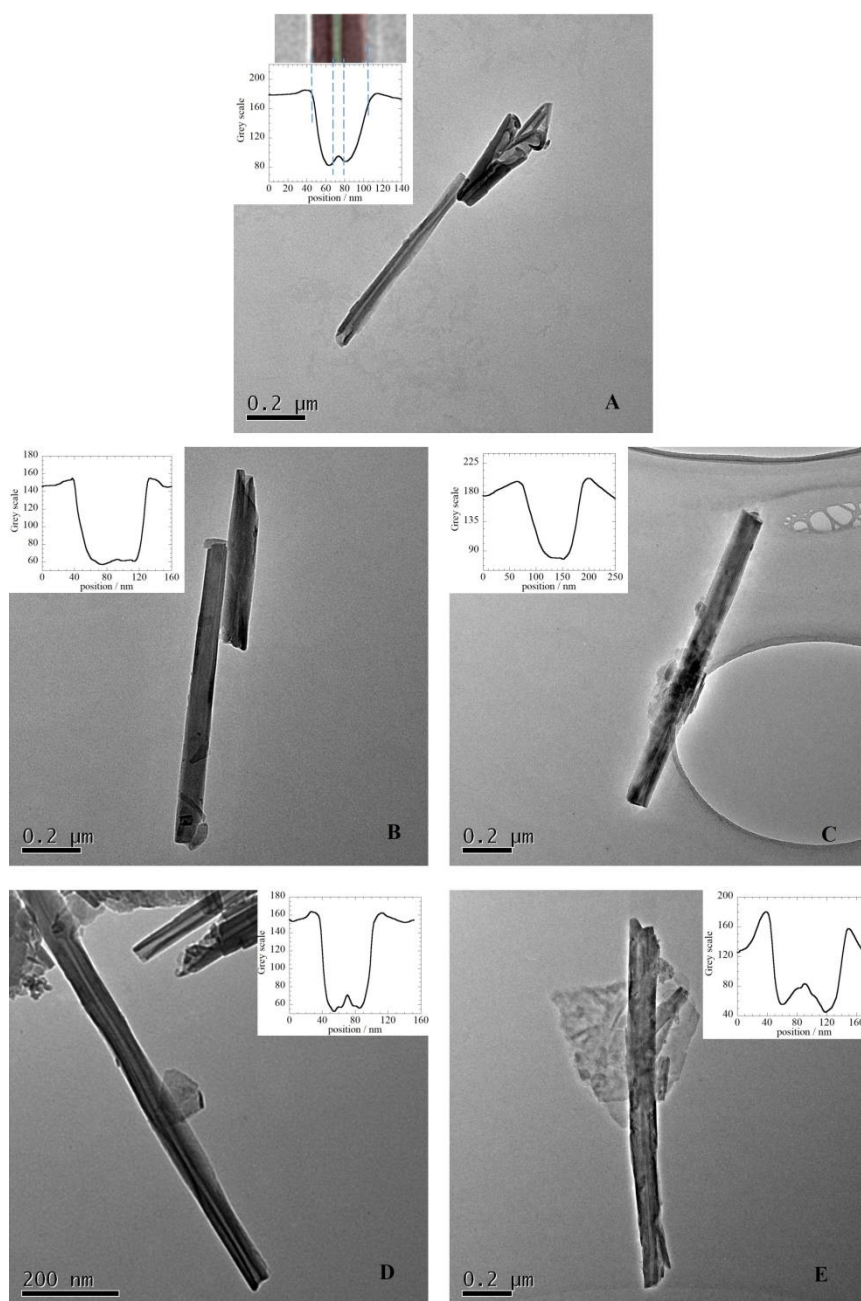


Figure 2.3.2. TEM images for pristine HNTs (A), HNTs/SA (P = 0.01 atm) (B), HNTs/DF (P = 0.01 atm) (C), HNTs/SA (P=1 atm) (D) and HNTs/DF (P=1 atm) (E).

Aimed at a better visualization of the HNTs cavity, an averaged grey scale profile was plotted along the perpendicular direction of the main nanotube axis for each case (see insets in TEM images from Figure 2.3.2), evidencing the empty cavity of ca. 10 nm with wall thickness of 20 nm. It is noteworthy that the cavity appears full filled when the loading is conducted under reduced pressure for both DF and SA. However, some additional organic material can be imaged on the outer surface of the nanotube. For what concerns the preparation carried out by mixing at ambient pressure, a larger accumulation of the drugs outside the nanotubes is provided and the lumen appears to be empty. Undoubtedly, these findings are in agreement with the TGA data reporting an increase of the

drug loading at $P=0.01$ atm and they clearly highlight the key role of the vacuum in favoring the halloysite lumen filling. In light of this, the solvent confinement within the cavity and its different volatility, combined with a larger vapor pressure compared to the bulk phase, deeply affect the drug localization in halloysite.

Therefore, the possibility to target the drug localization within the nanoclay is a promising result for attaining tunable release based on different preparation protocols. Drug release experiments were performed for salicylic acid and diclofenac encapsulated into halloysite and kaolinite under variable pressure. Release profiles of diclofenac from both the nanoclays are reported in Figure 2.3.3.

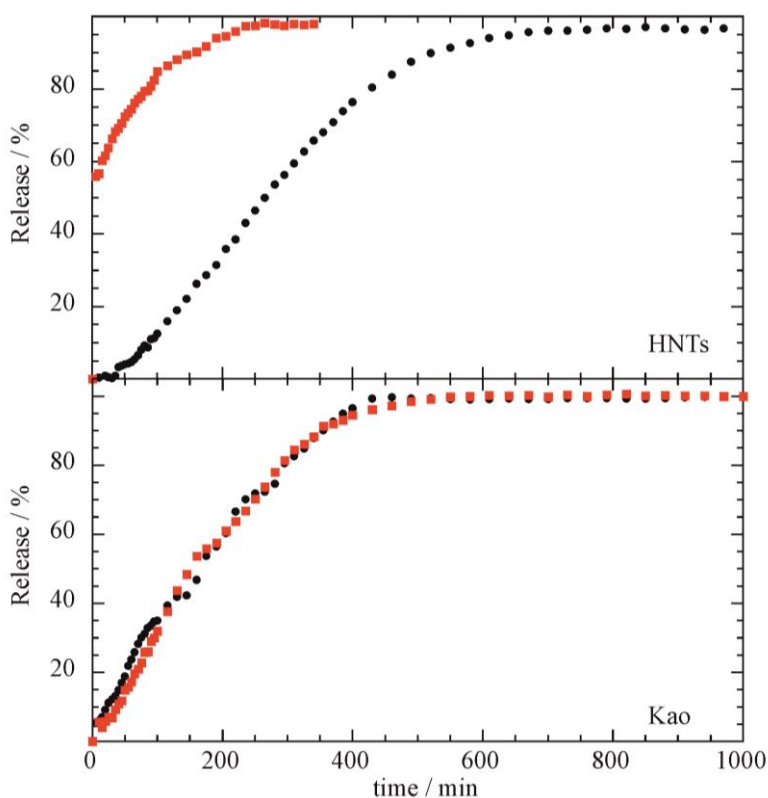


Figure 2.3.3. Diclofenac release as a function of time from halloysite and kaolinite based systems. Drug loading was performed at $P=1$ atm (red squares) and $P=0.01$ atm (black circles).

As observed, the loading protocol has a profound effect on the release profile for halloysite nanotubes based systems. Indeed, it emerges that the kinetics is lower for the sample obtained with HNTs by carrying out the loading procedure at reduced pressure, compared to the corresponding system obtained at ambient pressure. This result reflects the drug localization driven by the loading protocol as evidenced by TEM images. It should be noted that the incorporation into the halloysite lumen generates a sustained release profile due to confinement effect and the diffusion mechanism inside the lumen: these aspects are less relevant when the drug is mainly outside the nanotubes. Similar findings arise for both the investigated drugs. Figure 2.3.4 reports the release profiles of salicylic acid from halloysite and kaolinite.

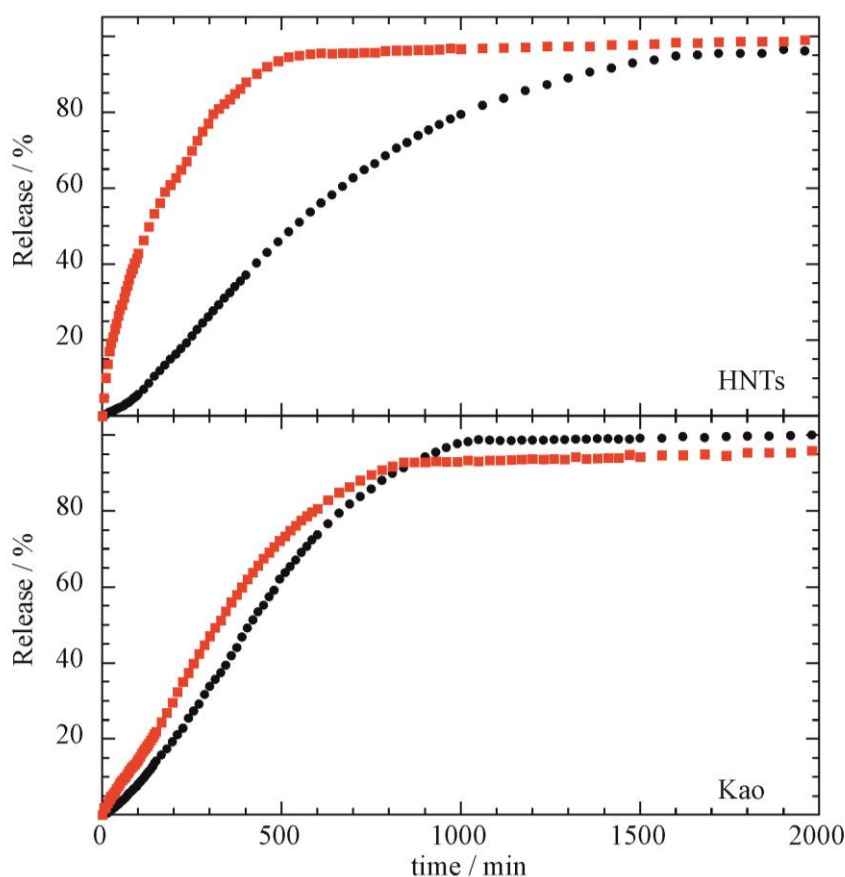


Figure 2.3.4. Salicylic acid release as a function of time from halloysite and kaolinite based systems. Drug loading was performed at $P=1$ atm (red squares) and $P=0.01$ atm (black circles).

Then, the release experiments for kaolinite have been also considered to corroborate this hypothesis. It is very interesting to note that the release is not influenced by the loading protocol. Indeed, in the case of the diclofenac release from kaolinite, the release profile did not change at all, despite the different pressure conditions during the experimental phase. The curves, instead, are completely overlapped. This result is in agreement with the morphological planar structure of kaolinite that, differently than halloysite, does not possess a cavity to be preferentially filled under reduced pressure conditions. For a clear quantitative evaluation, the time necessary for the release of 50 % ($t_{50\%}$) of the payload is reported in Table 2.3.1 for all the systems.

Table 2.3.1. Release kinetics data for 50% of the loading amount.

		$t_{50\%}/\text{min}$	
		HNT	
		P=0.01 atm	P=1 atm
DF		270±30	4.7±0.2
SA		570±60	135±3
		Kao	
		P=0.01 atm	P=1 atm
DF		160±20	163±12
SA		425±20	330±20

Based on $t_{50\%}$ values one can state that the preparation protocol can tune the release time even by an order of magnitude in the case of halloysite nanotubes whilst its effect is almost negligible for flat kaolinite clay mineral.

As we discussed for water in the previous paragraph, the influence of the pressure conditions on the loading is strictly correlated to the solvent confinement and in particular to its faster evaporation from the confined space compared to the bulk one. To verify this interpretation also for ethanol, the evaporation rate in the presence of halloysite nanotubes and kaolinite was explored by Knudsen Thermogravimetry. The results are discussed in terms of relative vapour pressure after the normalization for the bulk ethanol evaporation (P/P°) as a function of the ethanol/clay mass ratio ($R_{\text{EtOH:Clay}}$), Figure 2.3.5.

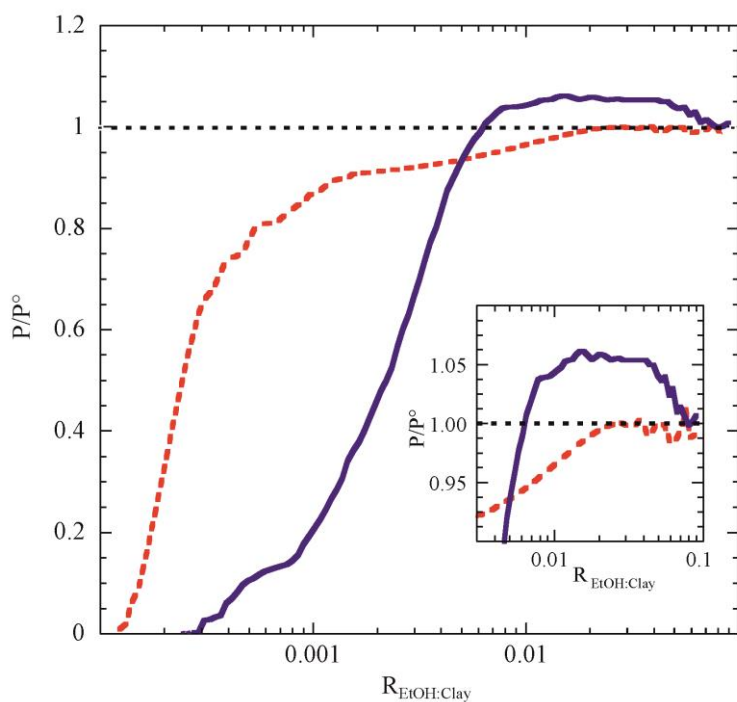


Figure 2.3.5. Relative vapor pressure for ethanol as a function of the ethanol to clay mass ratio for kaolinite (red broken line) and halloysite (full blue line) system.

The graph in Figure 2.3.5. evidenced that bulk solvent evaporates like the pure one in high solvent to clay mass ratios, whilst in the clay rich domain the adsorption phenomenon strongly lowers the ethanol vapor pressure. Interestingly, for the $R_{\text{EtOH:clay}}$ included between 6×10^{-3} and 6×10^{-2} in the presence of Halloysite the ethanol evaporation is faster ($P/P^\circ > 1$) than bulk solvent. This peculiarity is due to the hollow tubular morphology of the halloysite. Contrarily, kaolinite does not show such an effect. In conclusion, this work represents a fundamental step for the basic understanding of drug loading mechanism into confined spaces of clay minerals. The loading of halloysite nanotubes is typically conducted under reduced pressure and this work clarifies the advantage of these conditions: improved loading efficiency, targeting of the specific drug localization, better control of the release kinetics.

3. Aqueous dispersions and targeted modifications

3.1 *The importance of colloidal stability*

The colloidal stability of HNTs is a crucial aspect that has been investigated with the aim of improving nanoparticles use and applicability in different domains (as discussed in the attached papers IX and X). Hence, different strategies for the manipulation of the physico-chemical properties into both aqueous and apolar media are pursued considering the most appropriate functionalization of halloysite internal or external surface by electrostatic interactions with differently charged molecules

For instance, the adsorption of anionic surfactants (e.g. sodium alkanoates) occurs onto the inner surface and it increases the net negative charge of the nanotubes enhancing the electrostatic repulsions and consequently the dispersion stability.¹²³ Variations of ζ potential, which becomes more negative, predict a better colloidal stability for the modified nanoparticles compared to the pristine nanotubes due to their lower tendency to aggregate and, thus, the sedimentation is strongly slowed down.²⁶ Most likely, the enhanced colloidal stability is due to the neutralization of the inner positive charge, leading to an increase of the net negative charge and particle–particle repulsions. Amphiphilic molecules are typically used to stabilize nanoparticles dispersions due to their surface active features. Regarding halloysite nanotubes, the choice of the surfactant in terms of the headgroup charge is a key factor and it has a profound effect on their colloidal stability. Such a peculiarity is due to the charge separation in the inner and outer surface of halloysite regardless the surfactants loading degree onto the nanotubes surfaces. In this case, the sedimentation process is also slowed down by the surfactants.²⁸ Moreover, the solubilization capacity of these inner functionalized nanotubes toward hydrophobic compounds has been demonstrated. Accordingly, the surfactant/HNTs hybrids can be considered as inorganic micelles useful for the solubilization of pollutants and delivery of compounds from different origin.

According to the DLVO (Derjaguin-Landau-Verwey-Overbeek) theory, colloidal stability depends on the balance between attractive van der Waals forces and electrostatic repulsions caused by the double layer surrounding each particle. Therefore, both ζ -potential and width of the electric double layer contribute to the total repulsive force. This theory also envisages that a large ionic strength generates a screening of the electrostatic repulsions because of the reduction of the double layer.¹²⁶

Literature also reports another easy strategy to obtain stable colloidal dispersions and it deals with the preparation of inorganic reverse micelles in non-aqueous media based on halloysite nanotubes and cationic surfactants.¹²⁷ A “reverse micelle” is a well-known structure possessing a hydrophilic core and a hydrophobic shell that delineates a nanoscale droplet of aqueous phase into a nonpolar medium. Because of their positive headgroup, the cationic surfactants are selectively adsorbed onto

the HNTs external surface endowing to the formation of tubular nanoparticles with a hydrophobic shell and a hydrophilic cavity. Besides, the charge of the modified HNTs is strongly dependent on the hydrocarbon length chain of the surfactant. In particular, the ζ potential of the hybrids increases with the tails length of the adsorbed surfactant.¹²⁸

Furthermore, also biopolymers can be used for the design of stable nanoparticle colloidal dispersions. Indeed, the dispersion stability is dependent on particle dimensions, charge (e.g. positive chitosan, negative pectins or neutral cellulose derivatives), viscosity of the medium, and interactions between components (HNTs/polymer) and it is controlled by both electrostatic interactions and steric effects.¹²⁹

3.2 Design of targeted functionalizations

A part of the PhD thesis work was aimed to design, prepare and characterize HNTs functionalized with stimuli-responsive macromolecules to generate smart nanohybrids. Indeed, PNIPAAMs with opposite charge were selected because their targeted adsorption is driven by electrostatic interactions with HNT surfaces, and namely the negatively charged Poly(N-isopropylacrylamide)-co-methacrylic acid (PNIPAAM-co-MA) and the positively charged amino-terminal PNIPAAM (PNIPAAM-NH₂). The former was selectively adsorbed into the halloysite lumen by exploiting electrostatic interactions whereas the latter selectively interacts with the outer surface of the nanotubes due to its charge (attached paper II).

The selective modification of the outer and inner halloysite surfaces was deeply investigated. An extended physico-chemical study was performed with the aim of studying the effect of the functionalization on the thermodynamic behavior and therefore temperature responsive features of the hybrid material. The drug release kinetics was investigated by using diclofenac as a non-steroidal anti-inflammatory drug model.

Similarly, a novel strategy to prepare hybrid nanostructures with controlled release properties towards khellin by exploiting the electrostatic interactions between chitosan and halloysite nanotubes was also developed (attached paper III). Herein, the effect of the ionic strength on the coating efficiency of chitosan onto HNTs surfaces has been also investigated.

3.3 Thermo-responsive characteristics of PNIPAAM/HNTs hybrid nanocarriers

The physico-chemical characterization of the PNIPAAM/HNTs aqueous dispersions was carried out by using different techniques, such as Dynamic light scattering (DLS) and Micro differential scanning calorimetry (micro-DSC), and also by focusing their colloidal stability, thermodynamics,

and structural properties. Herein, the effect of the site adsorption on the PNIPAAm/HNT hybrids thermo-responsive behavior was explored.

The trends of the hydrodynamic radius for both pure polymers and the hybrids are reported in Figure 3.3.1 as a function of temperature.

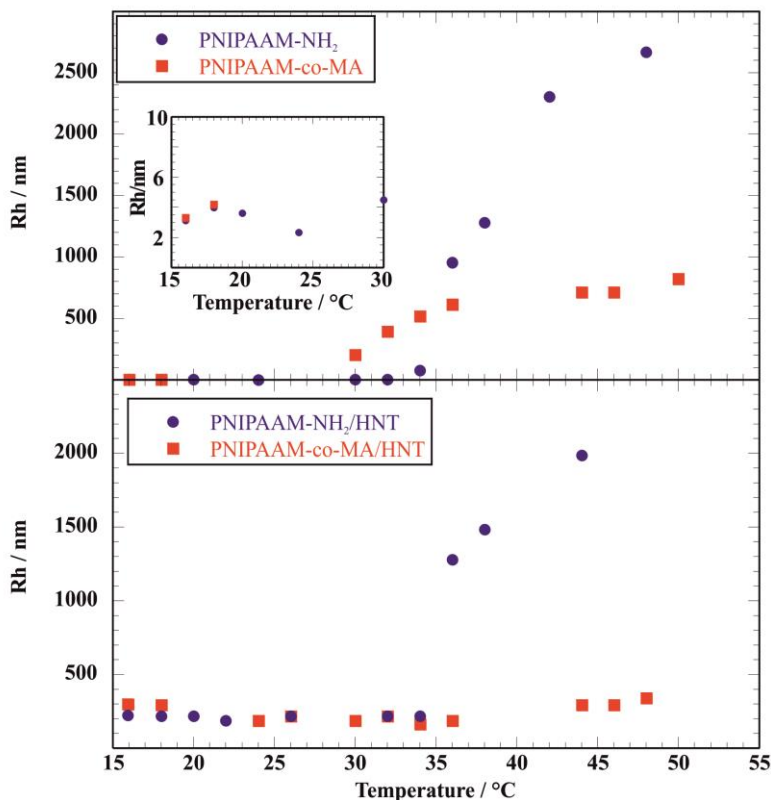


Figure 3.3.1. Hydrodynamic radius as a function of temperature.

Both pure PNIPAAm-NH₂ and PNIPAAm-co-MA show small Rh values, ca. 3 and 4 nm, below the LCST (see inset in Figure 3.3.1). The Rh values significantly increased, instead, for temperature > LCST, reaching 2000 nm and 800 nm for PNIPAAm-NH₂ and PNIPAAm-co-MA, respectively, as a consequence of the polymer aggregation, coalescence and phase separation. In particular, the Rh value of PNIPAAm-co-MA is smaller than that of PNIPAAm-NH₂ above the LCST and it is most likely due to the repulsive electrostatic effect caused by large negative charges related to the methacrylic groups, that hinder any further aggregation. Moreover, no temperature effect is observed in the PNIPAAm-co-MA/HNTs hybrids, whose Rh remains actually constant (200-300 nm), thus reflecting the diffusion behavior of pristine halloysite. This effect is probably due to the negative polymer incorporation into the positively charged lumen of HNTs. Contrarily, the PNIPAAm-NH₂/HNTs nanohybrid shows a strong Rh increase (from 200 to 2000 nm), when the LCST is reached, due to the collapsing of the polymeric chains and to the aggregation driven by the hydrophobic interactions between the nanotubes, which bear PNIPAAm-NH₂ on their external

surface. In light of these findings, the peculiar effect of the temperature increase on the nanostructure of the PNIPAAm/HNTs hybrids is sketched in Figure 3.3.2.

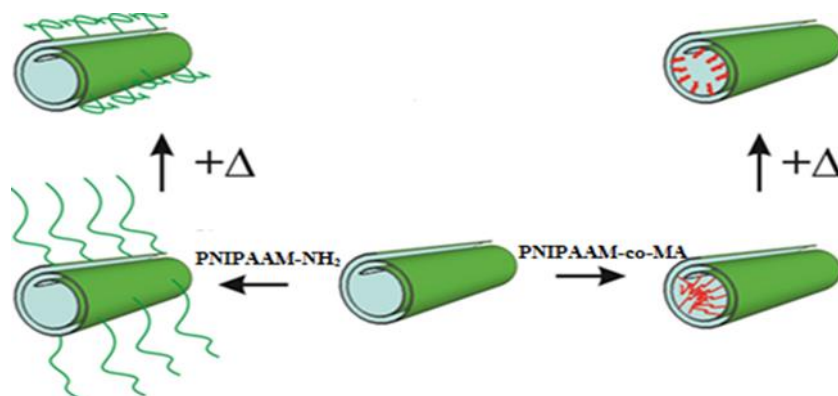


Figure 3.3.2. Schematic representation of PNIPAAm-NH₂ and PNIPAAm-co-MA interactions with HNTs surfaces and effect of temperature increase on the nanostructures of the PNIPAAm/HNT hybrids.

Thereafter, DSC experiments were carried out to study the specific correlation between the PNIPAAms adsorption site onto Halloysite and the thermo-responsiveness of the hybrids, being focused on the hydration/dehydration processes induced by temperature for polymers dispersed in water. Figure 3.3.3 reports the thermograms for pure PNIPAAms and PNIPAAm/HNTs mixtures.

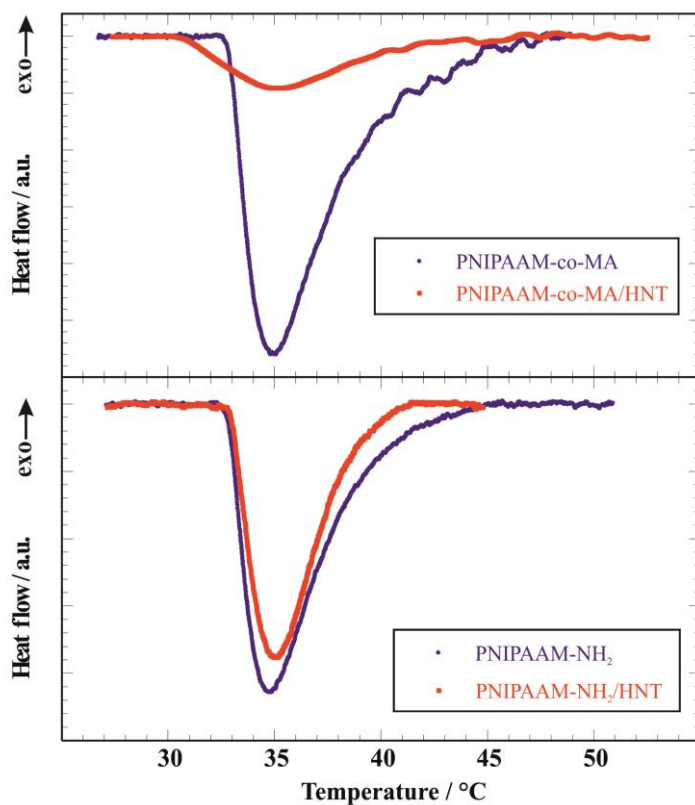


Figure 3.3.3. DSC thermograms for pure PNIPAAms and PNIPAAms/ HNTs nanohybrids.

As a general trend, the endothermic signals can be attributed to the polymers dehydration. The enthalpy (ΔH) of the PNIPAAm dehydration is provided by their integration, whereas the peak temperature corresponds to the LCST value. These data are collected in Table 3.3.1, where ΔH is expressed as kJ per mole of PNIPAAm by considering the stoichiometric polymer amount in solution.

Table 3.3.1. Enthalpy of PNIPAAm dehydration and LCST provided by micro-DSC.

	LCST / °C	ΔH / kJ mol ⁻¹
PNIPAAm-NH ₂	34.4	95.8
PNIPAAm-NH ₂ /HNTs	34.6	70.2
PNIPAAm-co-MA	34.4	145.8
PNIPAAm-co-MA/HNTs	34.4	30.9

According to the reported data, the LCST did not change as a consequence of the nanoclay addition either for PNIPAAm-NH₂ or for PNIPAAm-co-MA. Contrarily, the polymer adsorption onto the HNTs surfaces induced a reduction of ΔH thus highlighting some variations in the thermodynamics of the hydration/dehydration process. Therefore, lateral interactions between the polymeric chains play a major role since they probably provide a partial dehydration of the PNIPAAms when they adsorb onto halloysite surface, yet below the LCST. Besides, the PNIPAAm-co-MA undergoes a larger ΔH reduction after the interaction with HNTs in the hybrid compared to the PNIPAAm-NH₂, in agreement with the different adsorption site. Being encapsulated inside the nanotubes lumen, after its interaction with their inner surface, both curvature and confining effect must be considered in the dehydration mechanism of PNIPAAm-co-MA since lateral interactions between the polymer molecules are promoted. On the other side, PNIPAAm-NH₂ is adsorbed onto the external surfaces and the lateral interactions between the organic moieties are generated at a smaller extent.

Once the physico-chemical characterization was completed, the applicability of the functionalized halloysite nanotubes was estimated by investigating their employ as carriers for diclofenac. Hence, HNTs were firstly loaded with the drug and then the release kinetics was studied at variable temperatures in order to evaluate the efficiency of the hybrids as thermo-responsive nanocarriers. To this purpose, UV-vis spectrophotometry analysis was performed at 25 °C and 50 °C, below and above the LCST value, to assess the temperature effect. The release profiles (Figure 3.3.4) were fitted according to the Korsmeyer–Peppas equation:¹³⁰

$$R\%(t) = kt^n \quad (3.3.1)$$

where $R\%(t)$ is the percentage of diclofenac released at time t , k is the kinetics constant and n is the release exponent, which depends on the release mechanism as well as on the specific geometry of the matrix.

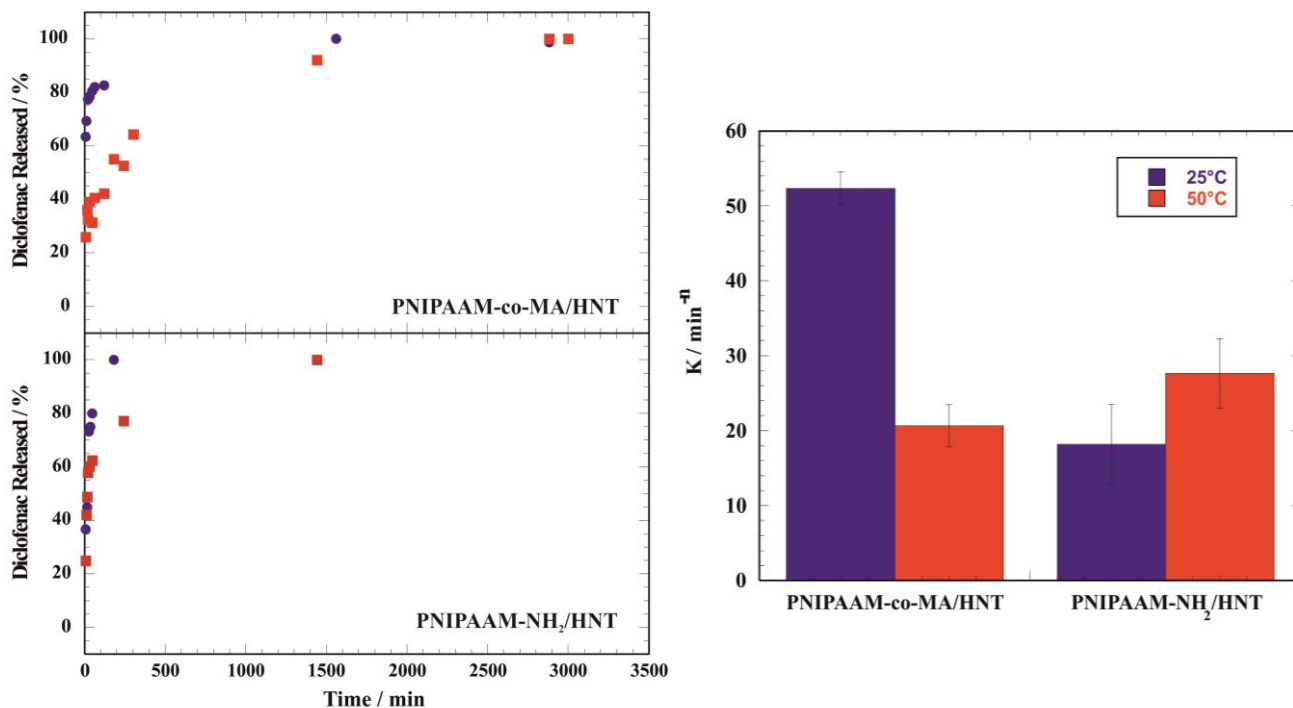


Figure 3.3.4. (right) Release profiles of diclofenac from hybrid systems at 25 °C (blue) and 50 °C (red). (left) Kinetics constants of release from PNIPAAm-co-MA/HNT and PNIPAAm-NH₂/HNT.

Release experiments allowed to determine that the diclofenac loadings are 4.7 and 5.3 mg g⁻¹ for PNIPAAm-co-MA/HNTs and PNIPAAm-NH₂/HNTs, respectively. As long as the release kinetics are concerned, it was found that they are effectively influenced by the specific adsorption site of the polymers.

If the values of k at the two different temperature conditions are considered, it is clear that the diclofenac release from the PNIPAAm-co-MA/HNTs hybrid is strongly slowed down by the temperature increase, in agreement with the confinement of the polymer within the halloysite cavity. Namely, the hydrated PNIPAAm-co-MA at 25 °C allows for a fast release of the drug from the lumen, whereas after it transition to the completely dehydrated and collapsed state at 50 °C, the drug release is slowed down by the shrinking thus determining a reduction of k . Instead, this effect is not observed for the PNIPAAm-NH₂/HNTs hybrid as a consequence of the selective adsorption of the polymer on the halloysite outer surface. Based on these results, it is possible to conclude that the PNIPAAms/HNTs nanocarriers are smart stimuli-responsive systems whose release is strongly

dependent on their specific nanoarchitecture and it can be controlled by varying the temperature conditions.

3.4 Chitosan coating on HNTs for the controlled release of khellin

In order to prepare new hybrid nanostructures based on halloysite nanotubes coated with chitosan, the electrostatic interactions between the two components have been exploited. Firstly, HNTs were loaded with the bioactive molecule to be used for the drug delivery applications, namely khellin. Then, the coating procedure was carried out both in water and in NaCl aqueous solution, in order to explore the effect of the ionic strength on the chitosan coating efficiency. The physico-chemical characterization of the prepared materials was conducted, among other techniques, by ζ potential and contact angle (θ_i) measurements. Table 3.4.1 reports the values for the analyzed samples.

Table 3.4.1. ζ potential and contact angle values.

Material	ζ potential (mV)	θ_i (°)
HNTs	-20.0 ± 0.6	30.5 ± 1.1
HNTs/khellin	-21.5 ± 0.3	30.9 ± 1.2
Chitosan/HNTs/khellin (NaCl)	$+23.5 \pm 0.8$	80 ± 3
Chitosan/HNTs/khellin	-18.5 ± 0.4	75 ± 2

As shown, the khellin loading into halloysite nanotubes did not significantly affect the ζ potential of the clay. This finding is in agreement with the hydrophobic character of khellin, which is encapsulated within the HNTs cavity as a consequence of the solvent confinement. Also, the confinement of the bioactive molecule was confirmed by water contact angle experiments, which evidenced that the θ_i values for HNTs and HNTs/khellin tablets did not change. These results indicate that the khellin loading did not alter the hydrophilic character of halloysite outer surface demonstrating that the hydrophobic drug is mostly confined into its lumen. As concerns the chitosan/HNTs/khellin hybrid nanostructures, the ζ potential values are strongly affected by the presence of NaCl during the nanotubes coating step with the biopolymer. In particular, an inversion from negative to positive was detected. Hence, it is possible to assert that some electrostatic attractions between cationic chitosan and the HNTs outer surface take place. On the other side, the coating procedure in water generated a slight decrease of the HNTs surface charge, thus highlighting that the chitosan coating efficiency is remarkably improved in aqueous medium with higher ionic strength. Besides, the chitosan coating generated the hydrophobization of the HNTs

outer surface as evidenced by the significant enhancements of the contact angle values (both in water and NaCl solution). In light of these observations, both a contribution from the electrostatic interactions and from the mobility of the polymeric chains exist. Lvov et al. evidenced that the addition of electrolytes is used in the layer by layer technique because of the “rod-to-coil” transition of polyelectrolytes in solution.¹³¹ Additionally, it is reported that the increase of the ionic strength enhances the chitosan flexibility.¹³²

By using thermogravimetric analysis and applying the rule of mixtures, the loading of khellin into halloysite nanotubes was determined to be 1.03 ± 0.02 wt%. Similarly, the chitosan coating efficiencies were also calculated and it was estimated that the biopolymer amount in the chitosan/HNT/khellin nano hybrid prepared in water is 2.38 ± 0.03 wt% whereas it increased up to 31.4 ± 0.3 wt% by dispersing chitosan in NaCl aqueous. As aforementioned, these results could be related to the effect of the electrolytes on the chitosan chains flexibility.

At this point, the possibility to use the chitosan/HNTs hybrid as nanocarrier for khellin was highlighted by the release experiments conducted at variable pH simulating the typical conditions along the human gastro-intestinal path, which moves from acidic (stomach) to basic (colon) conditions. Figure 3.4.1 shows the khellin release profiles under neutral conditions (pH=7) from HNTs and chitosan coated HNTs.

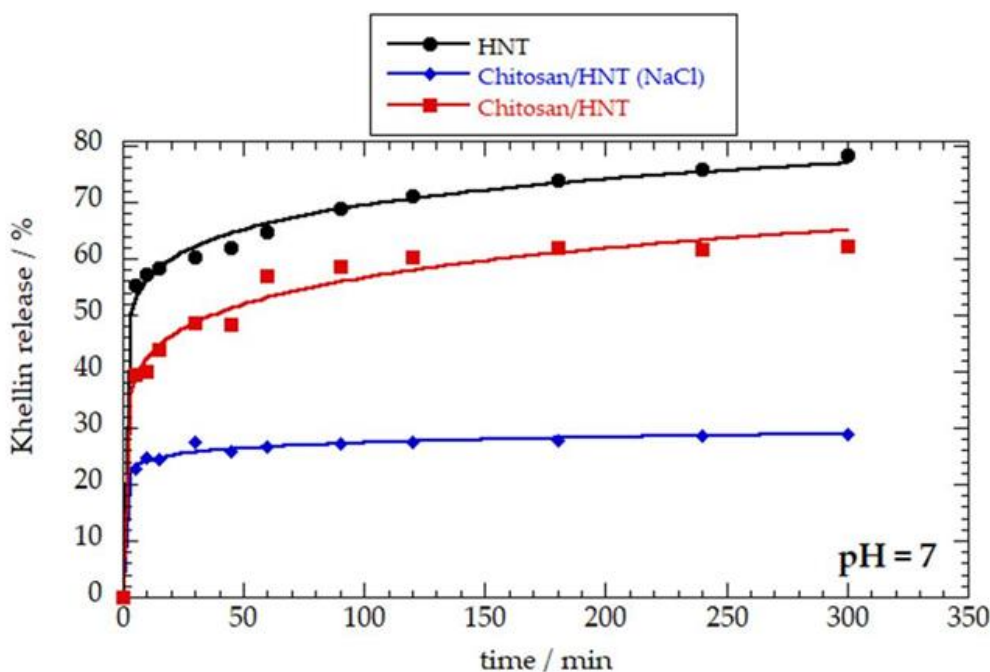


Figure 3.4.1. Khellin release as a function of time in water under neutral conditions (pH = 7). Solid lines represent the fitting according to the Korsmeyer–Peppas model (equation 3.3.1).

Overall, the adsorption of chitosan onto the HNTs outer surface slowed down the khellin release. For instance, the amount of khellin released after 6 hours was 78 % for uncoated nanotubes. This percentage was reduced in the chitosan/HNT nanocarriers (62 and 28% for the composites prepared in water and NaCl solution, respectively). These results are consistent with the previous data, which evidenced that the higher ionic strength improved the coating efficiency, with a delaying effect on the drug exit from the inner lumen. The khellin release profiles were analyzed using the Korsmeyer–Peppas model, which allowed to confirm that the retarding effect is stronger for the coated nanotubes obtained in NaCl aqueous solution.

Furthermore, the influence of pH was also explored at two different conditions for the chitosan/HNTs hybrid nanocarriers (Figure 3.4.2).

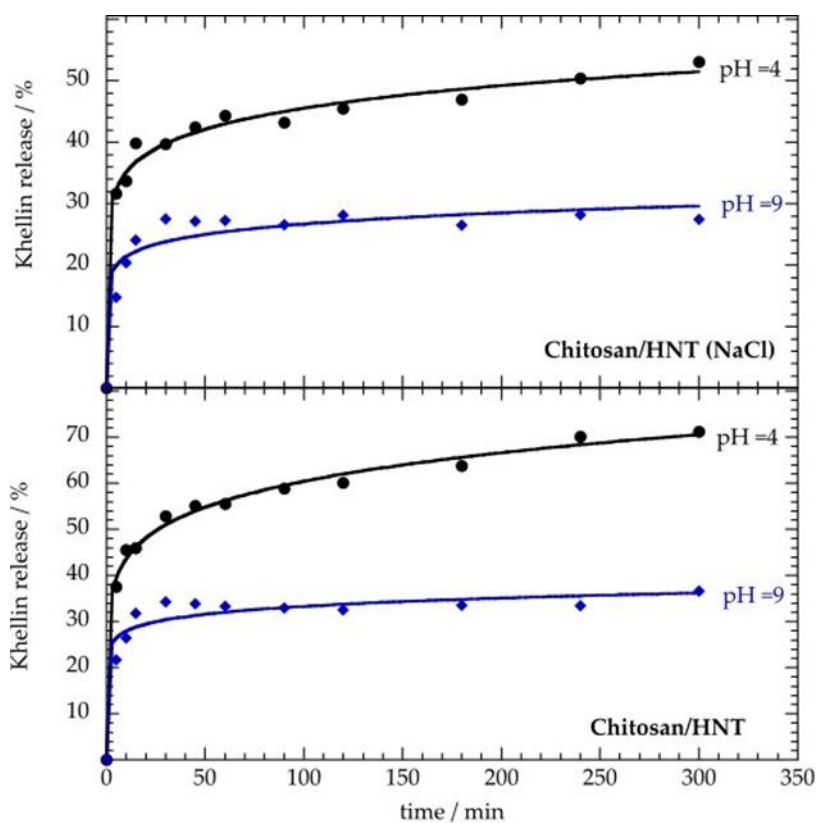


Figure 3.4.2. Khellin release as a function of time in water under acidic (pH = 4) and basic (pH = 9) conditions. Solid lines represent the fitting according to the Korsmeyer–Peppas model (equation 3.3.1).

Herein, it was found that the chitosan retarding effect was reduced under acidic conditions with respect to those obtained at pH = 9. These results can be attributed to the enhanced chitosan solubility in water at $\text{pH} \leq 4$.¹³³ We observed that the chitosan coated nanotubes in NaCl solution are more effective in controlling the khellin release compared to those coated without NaCl. This observation is valid at pH = 7 as well under acidic/basic conditions. These results could be related

to the larger amount of biopolymer onto the nanoclays as a consequence of the influence of the electrolyte on the flexibility of the polymeric chains. Specifically, the increase of the solvent ionic strength makes chitosan more flexible in agreement with the reduction of the repulsive interactions between the polymeric chains, as previously discussed. We can hypothesize that chitosan coating layer onto HNTs is thicker in NaCl solution and, consequently, the controlling efficiency on the khellin release is more effective. Based on these considerations, we can conclude that the preparation of these new biohybrid nanostructures represents a suitable strategy to obtain drug delivery systems with tunable properties.

4. Biohybrid Gel beads

4.1 Design of gel beads based on biopolymers and HNTs

Hydrogels are defined by the existence of a three-dimensional network, formed by the cross-link of polymeric chains, that possesses the capability to swell thanks to the presence of hydrophilic groups and to maintain a very high amount of water in its structure.¹³⁴ While working at this thesis, we decided to use natural polymers and nanoclays with the aim to develop novel eco-friendly smart gel beads (attached paper IV). Therefore, hydrogel beads based on chitosan with uniformly dispersed halloysite nanotubes were obtained by a dropping method and alginate was used to generate an external coating layer by diffusion and immersion of the beads in a sodium alginate solution (Figure 4.1.1). The physico-chemical characterization and the study of the applicability of such systems as drug carrier are reported in the following paragraphs.

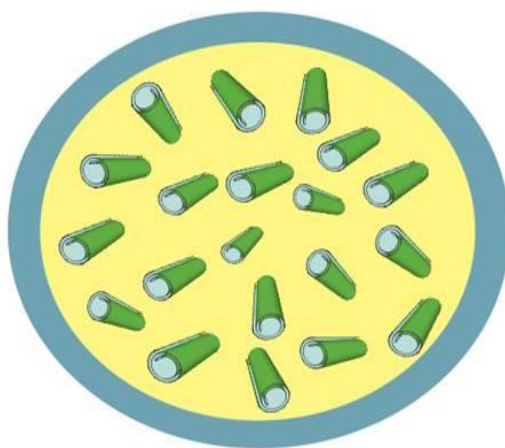


Figure 4.1.1. Representation of the designed bio-hybrid gel beads.

4.2 Physico-chemical characterization of Chitosan/HNTs/Alginate gel beads

The chitosan/HNTs gel beads covered with a calcium alginate layer are showed in Figure 4.2.1. The optical image enlightens they have an average diameter of 3.5 mm that shrunk to 0.8 mm after drying. The morphology was studied by scanning electron microscopy in order to investigate the clay nanotubes distribution into the polymeric matrix.

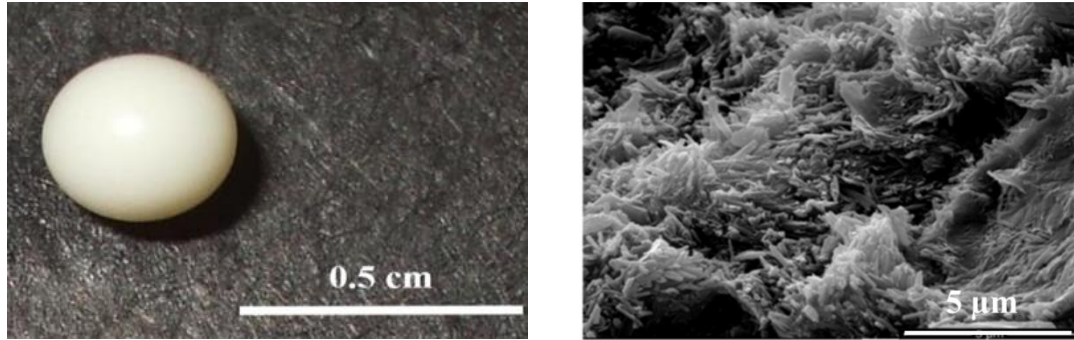


Figure 4.2.1. (a) Optical image of wet alginate/chitosan/halloysite nanotubes (HNTs) gel beads and (b) SEM image of the inner part of the dried gel beads.

It is observed that HNTs are homogeneously distributed and randomly oriented within the polymeric matrix. This finding can be explained by the affinity between chitosan and halloysite, that are oppositely charged, and also by the colloidal stability of the nanoclay in the polymer solution. Moreover, the halloysite cavity did not interact with the positive chitosan since the inner surface of the nanotubes is positively charged as well. In light of this, the HNTs lumen was preserved for drug loading and further release of active molecules.

Therefore, since neither optical images nor SEM micrographs were able to identify the alginate location in the beads, it was labeled with 5-(4,6-dichlorotriazinyl) aminofluorescein (DTAF), a fluorescent probe that shows fluorescent emission when excited at 490 nm, and Laser Scanning Confocal Microscopy was used (Figure 4.2.2).

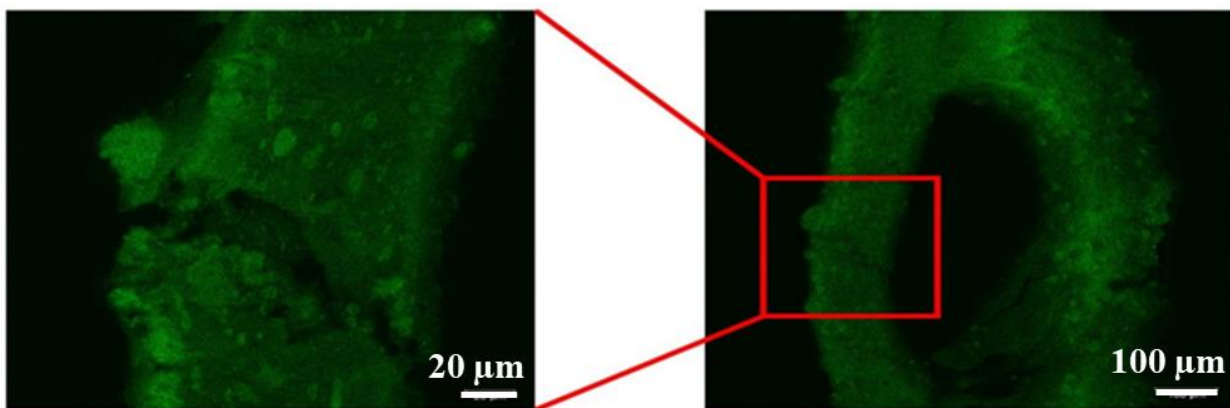


Figure 4.2.2. Laser scanning confocal microscopy images of alginate/chitosan/HNTs gel beads with DTAF labeled alginate.

At first, a blank experiment resulted in negligible fluorescence on the chitosan/halloysite gel beads. Once the most external layer of calcium alginate is formed, instead, the laser scanning confocal microscopy images on the full components beads clearly showed a fluorescent layer with an average thickness of $\approx 130 \mu\text{m}$. This is due to the diffusion of alginate into the chitosan/halloysite

inner part only to a certain extent whilst the core of the beads was completely alginate free. In light of this, it can be concluded that the preparation protocol allowed to develop a controlled and complex architecture in the mesoscopic scale. It might be suitable for the fabrication of functional carriers in advanced health applications.

4.3 Application of the alginate/chitosan/HNTs gel beads for controlled drug release

Doxycycline, an antibiotic of the tetracycline class, was used as the model drug and it was loaded into the halloysite cavity by using the IN/OUT vacuum pumping procedure to optimize the encapsulation efficiency as previously discussed. Thermogravimetric experiments allowed to determine that the drug loading was 4.2 wt %. Then, UV-VIS analysis was carried out to provide the release profiles of doxycycline from halloysite nanotubes, chitosan/HNTs dried beads and alginate/chitosan/HNTs dried beads in water (Figure 4.3.1).

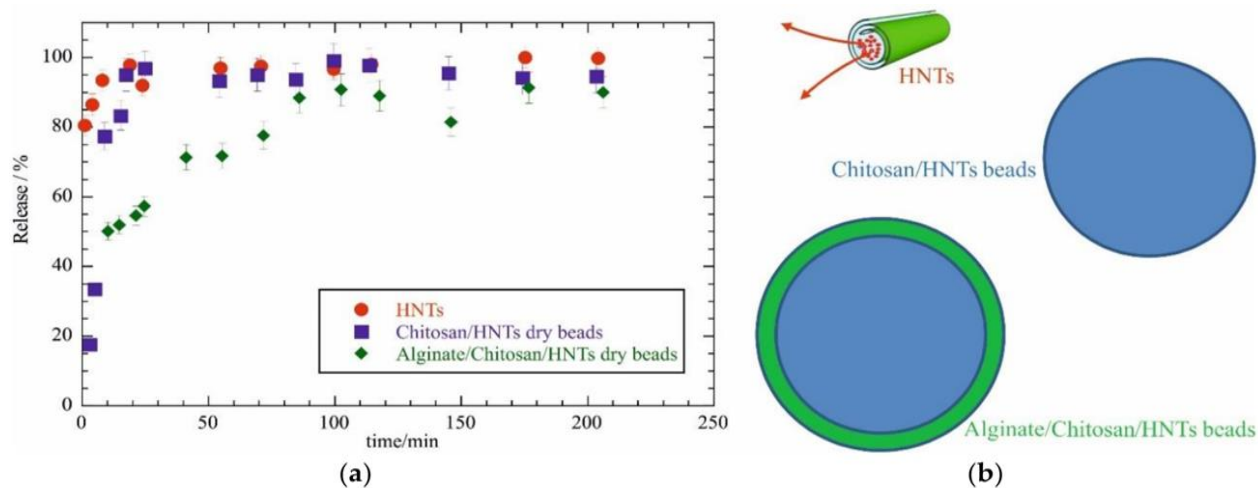


Figure 4.3.1. (a) Doxycycline chlorohydrate release as a function of time for different carriers. (b) Representation of the different release systems.

It can be observed that no much difference exists between the drug loaded pristine nanotubes and the chitosan/HNTs gel beads, thus meaning that halloysite incorporation within the chitosan matrix did not have any profound effect on the drug release and the particular morphology did not prevent the doxycycline from being completely available in the solvent media after 20 min. More interestingly, the presence of alginate in the alginate/chitosan/HNTs system significantly affected the release kinetics. For instance, only 50% of the drug was released into the solvent medium after 20 min whereas a full release occurs in more than 80 min. Hence, the presence of an alginate coating significantly slowed down the doxycycline release from the hybrid beads. This is most

likely due to the drug exit from the inner lumen of halloysite, its diffusion through the chitosan matrix and, then, the interaction with the outer alginate layer. The latter, in combination with the oppositely charged chitosan could create a highly viscous shell thus provoking a further delay, acting as a barrier, for the drug diffusion from the beads to the solvent. Thus, this work represents a promising step for the development of hybrid hydrogels with oppositely charged biopolymers and inorganic nanoclay with specific architecture and morphology for controlled drug release.

5. Bioplastics based on Halloysite

5.1 Design of plasticized bionanocomposites

The addition of inorganic fillers to a biopolymeric matrix represents an efficient strategy to fabricate composite materials with improved performance, which are suitable for numerous technological applications. In this chapter we focus on the preparation of new bioplastics based on halloysite nanotubes. Firstly, we investigated the possibility to use different clays as nanofillers for Mater-Bi, which is a commercial bioplastic extensively used within food packaging applications. Sepiolite nanofibers, laponite nanodisks and halloysite nanotubes were selected for this purpose and the preparation of Mater-Bi/nanoclay nanocomposite films was easily achieved by using the solvent casting method from dichloroethane (attached paper V).

Hence, the bioplastics were characterized by dynamic mechanical analysis (DMA) in order to explore the effect of the addition of the nanoclays on the mechanical behavior of the Mater-Bi-based films thus providing the tensile properties as well as the thermo-mechanical properties of the prepared films.

Since the results showed that halloysite is the most promising in inducing significant improvement of the mechanical performances of Mater-Bi, we also investigated the influence of HNTs content on both the mechanical and thermal features of the bionanocomposites in order to determine an effective protocol for the development of Mater-Bi/Halloysite hybrid films with proper characteristics for packaging purposes (attached paper VI).

5.2 Physico-chemical investigation of Mater-Bi/Nanoclays composite films

The preparation method used for the design of Mater-Bi/clays nanocomposites is the solvent casting procedure from dichloroethane, by maintaining the nanoclay content at 30 wt %.

Stress vs strain curves for both pure Mater-Bi and Mater-Bi/nanoclays bioplastics are reported in Figure 5.2.1.

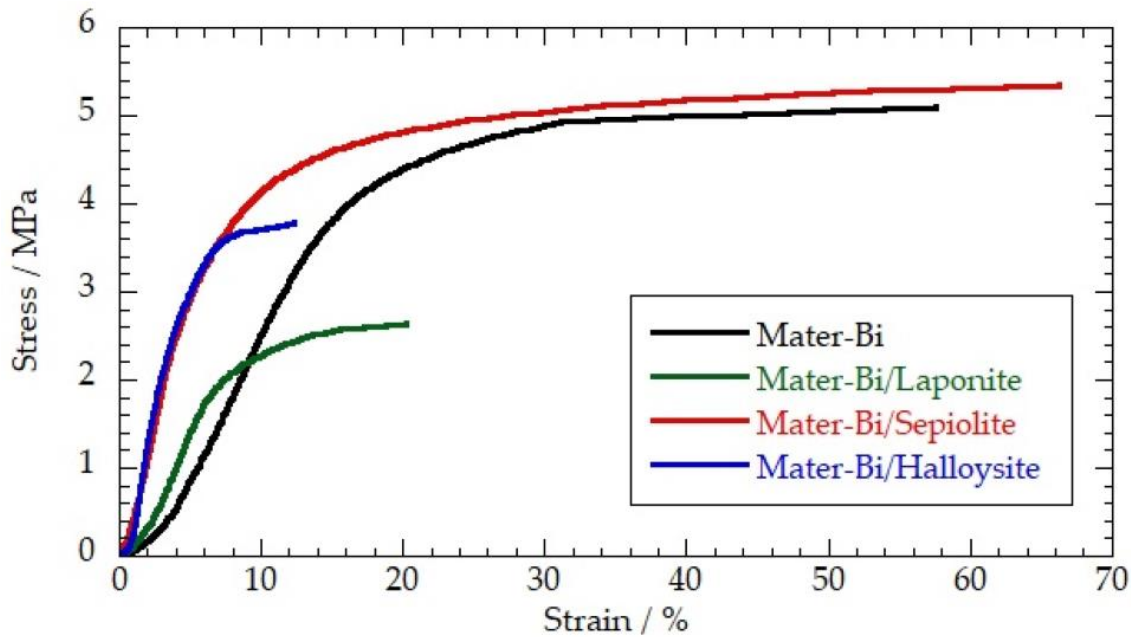


Figure 5.2.1. Stress–strain curves for pure Mater-Bi and Mater-Bi/nanoclays bioplastics. The nanoclay content was fixed at 30 wt %.

The analysis of the stress–strain profiles allowed to completely describe the mechanical features of the prepared bionanocomposites by deriving the data collected in Table 5.2.1.

Table 5.2.1. Tensile properties of Mater-Bi and Mater-Bi/nanoclay films.

Film	Elastic Modulus / MPa	Stress at Yielding Point/MPa	Elongation at Yielding Point/%	Stress at Breaking Point/MPa	Elongation at Breaking Point/%
Mater-Bi	32 ± 3	3.8 ± 0.5	15.4 ± 1.8	5.0 ± 0.6	57 ± 6
MaterBi/HNTs	109 ± 8	2.8 ± 0.4	4.6 ± 0.5	3.8 ± 0.5	12 ± 2
MaterBi/Sepiolite	79 ± 7	3.4 ± 0.4	6.3 ± 0.6	5.3 ± 0.6	63 ± 6
MaterBi/Laponite	38 ± 4	1.98 ± 0.19	7.1 ± 0.6	2.6 ± 0.4	20 ± 2

It is observed that the addition of nanoclays affects the tensile properties of the polymer in the hybrid systems. In particular, the elastic modulus exhibits a relevant increase after the inorganic particles incorporation with a maximum for the halloysite based film, thus meaning that the nanotubular morphology is the most suitable to generate an improvement in the film rigidity, being the Young modulus variations 240% and 146% for halloysite and sepiolite, respectively, and negligible for laponite nanodisks. As far as the yielding point is concerned, instead, the nanoclays addition to the polymeric matrix reduced both the stress and the elongation. Furthermore, the stress at breaking point and the maximum elongation decreased in the Mater-Bi/HNTs and Mater-

Bi/laponite nanocomposites, contrarily to the Mater-Bi/sepiolite system where the clay did not alter these properties. This is most likely due to the peculiar morphology and structure of each nanoclay. For instance, the nanotubes and nanodisks do not allow the polymeric chains to slide against each other after their interactions with the inorganic surfaces whereas it is possible when they interact with long and microfibrillar particles.

Moreover, the mechanical performance were also studied as a function of the temperature of the bionanocomposites by using the DMA in the oscillatory regime and by heating the films from 40 to 100 °C at a heating rate of 5 °C min⁻¹. In particular, it was possible to determine the thermal effect on the viscoelastic properties, which are described by the storage and the loss moduli, G' and G'' respectively. The G''/G' ratio, that is reported as tanδ, is shown in Figure 5.2.2 for both the pure Mater-Bi and Mater-Bi/sepiolite.

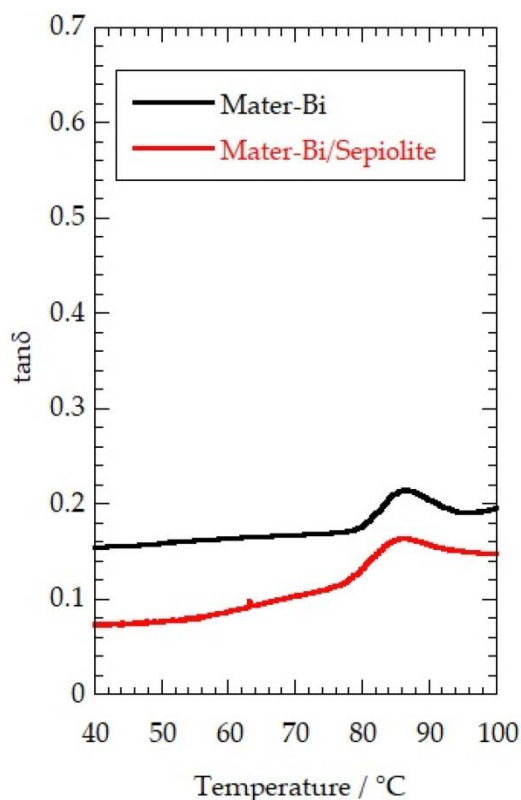


Figure 5.2.2. Dependence of tanδ on the temperature of Mater-Bi and Mater-Bi/sepiolite.

As observed, the curve of Mater-Bi exhibits a peak at ca. 85 °C that represents the glass transition of the polymer. The same peak is likewise shown for the nanocomposite film based on sepiolite and, similarly to it, on halloysite and laponite as well. In light of these findings, we can assess that the addition of inorganic nanoparticles did not alter the transition temperature of the materials, despite their different morphology.

5.3 Effect of HNTs on the thermo-mechanical performances

Once we observed that HNTs are the most promising nanoclays for the preparation of Mater-Bi based bioplastics, we focused on the influence of their content on both the mechanical and thermal features of the nanocomposites, which could be employed as effective alternatives to the petroleum derived products. To do so, the same solvent casting method was used to prepare the materials at variable halloysite content (from 0 to 30 wt%) and the mechanical behaviour and the thermal properties were investigated. Figure 5.3.1 reports the stress vs. strain curves for both the Mater-Bi and Mater-Bi/HNTs films.

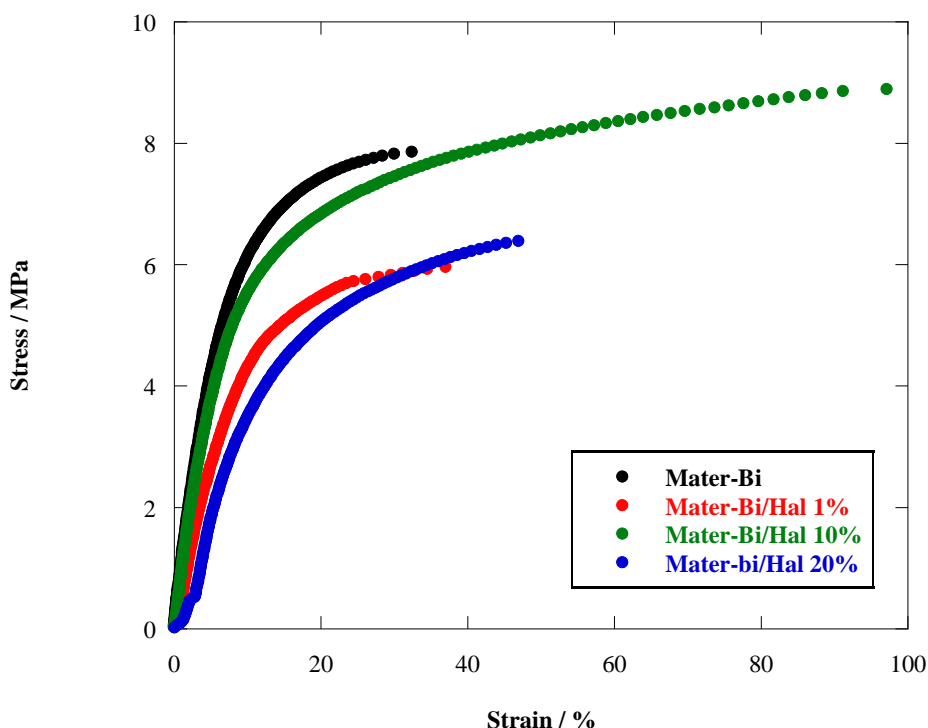


Figure 5.3.1. Stress vs. strain curves for pure Mater-Bi and Mater-Bi/Halloysite films as a function of the nanoclay content.

It is clear that all the samples, whatever the HNTs content is, show an initial elastic behavior and then they convert into plastic material. Indeed, the stress increases linearly with the strain and, once the yielding point is reached, every deformation becomes irreversible.

Thereafter, the elongation at break and the stored energy were also investigated and they are reported in Figure 5.3.2.

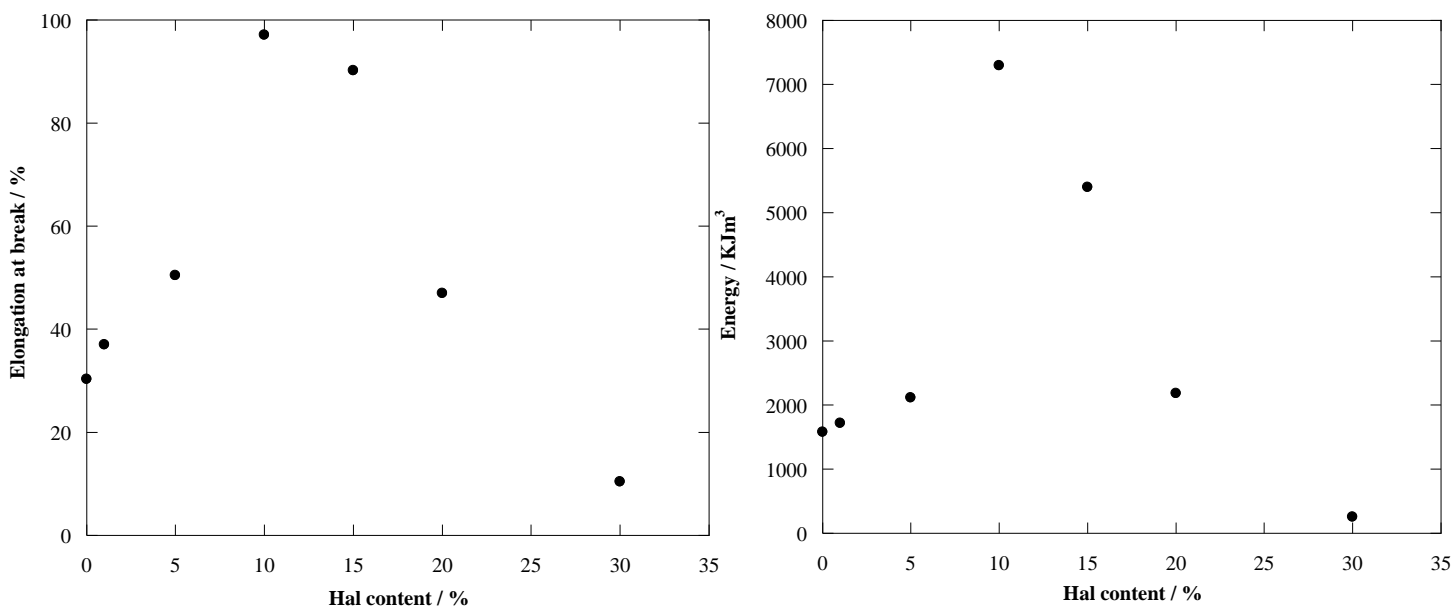


Figure 5.3.2. Elongation at break (*right*) and stored energy up to breaking (*left*) for Mater-Bi/Halloysite composite films as a function of the nanoclay content. The relative error is 2%.

It is clearly observed that the concentration of nanoclays influences the strain at break of Mater-Bi based films. For instance, the ultimate elongation percentage increases from 30% for the pure Mater-Bi film reaching 100%, its highest value, for the Mater-Bi/HNTs 10 wt% nanocomposite. Then, the deformation at breaking shows a constant decrease for any further addition of nanotubes down to ca. 10% for the composite material with the largest HNTs content (30 wt%). Similar findings are also reported in literature and they are most likely due to the interactions existing between the clay nanoparticles and the organic matrix, which avoid the sliding of the polymeric chains, as already observed in the previous study.¹³⁵

Similar effects were also observed for the stored energy at breaking (Figure 5.3.2). Specifically, the pure Mater-Bi film shows a stored energy of 1718 kJ m^{-3} and it is significantly enhanced up to 7300 kJ m^{-3} in the Mater-Bi/HNTs 10% nanocomposite, whereas the Mater-Bi/HNTs 30 wt% exhibited a much lower stored energy (254 kJ m^{-3}).

Besides, we also carried out thermogravimetric analysis in order to investigate the thermal properties, i.e. stability and degradation, of the Mater-Bi/HNTs bioplastics. Figure 5.3.3 reports thermograms and differential curves for both the pure polymer and the Mater-Bi/HNTs 10% samples.

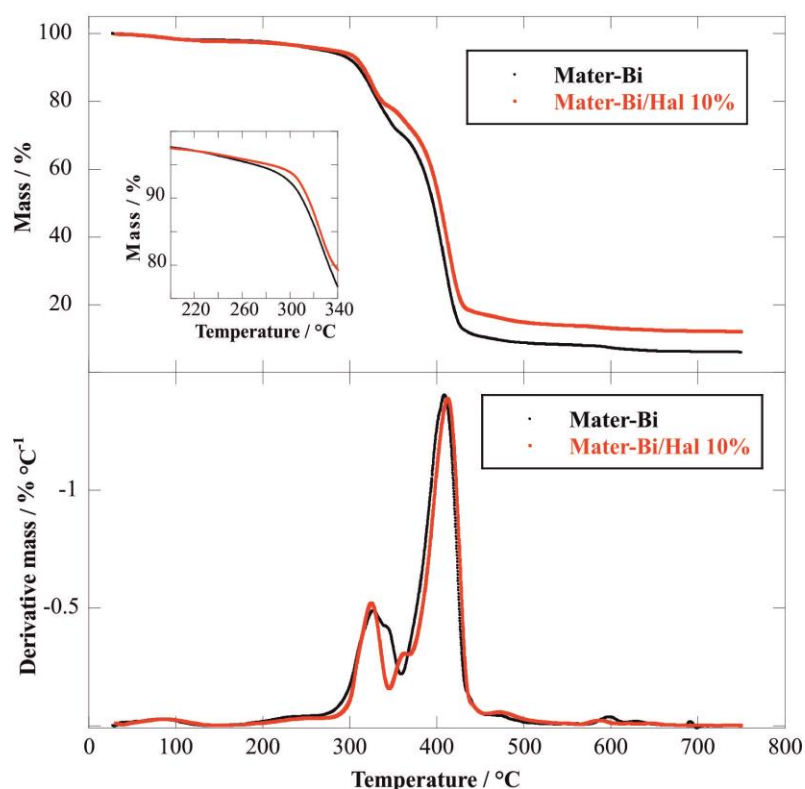


Figure 5.3.3. Thermogravimetric (up) and differential thermogravimetric (bottom) curves for Mater-Bi and Mater-Bi/HNTs 10 wt% samples. The inset shows the thermogravimetric curves within the temperature range between 200 and 340 °C.

First of all, it can be observed that the mass residue at 700 °C is higher for the Mater-Bi/HNTs 10% nanocomposite, compared to the pure polymeric film. This is due to the presence of inorganic particles which do not completely degrade at this conditions. Obviously, this observation has a specific trend if all the different halloysite contents employed during the preparation procedure are considered (Table 5.3.1)

Table 5.3.1. Thermogravimetric parameters for Mater Bi and Mater-Bi/Halloysite nanocomposites.

Material	ML ₁₅₀ ^a / wt%	MR ₇₀₀ ^b / wt%
Mater Bi	1.98	6.19
Mater-Bi/Hal 1 wt%	2.21	6.97
Mater-Bi/Hal 5 wt%	1.92	9.04
Mater-Bi/Hal 10 wt%	2.22	12.17
Mater-Bi/Hal 15 wt%	1.49	16.99
Mater-Bi/Hal 20 wt%	1.73	21.44
Mater-Bi/Hal 30 wt%	1.86	30.27

^aMass loss between 25 and 150 °C; ^bResidual mass at 700 °C.

These results evidenced that the samples with higher nanotubes contents possess larger residual masses at 700 °C. Moreover, the mass loss at 150 °C can be attributed to the moisture content of the bioplastics. Both the Mater-Bi and Mater-Bi/HNTs 10 wt% thermograms exhibited two different degradation steps in the 300–400 °C range as highlighted by the differential thermogravimetric curves showing two correspondent peaks (Figure 5.3.3.). Hence, with the aim to investigate these aspects we derived the onset temperatures for each curve, which is obtained by the intersection of a line tangent to the baseline the with a line tangent to the inflection point of the thermogravimetric curve. In particular, the onset temperature describes the initial degradation of the sample and it is referred to the temperature where the Mater-Bi starts to decompose. Figure 5.3.4 reports the onset temperatures for all the prepared samples.

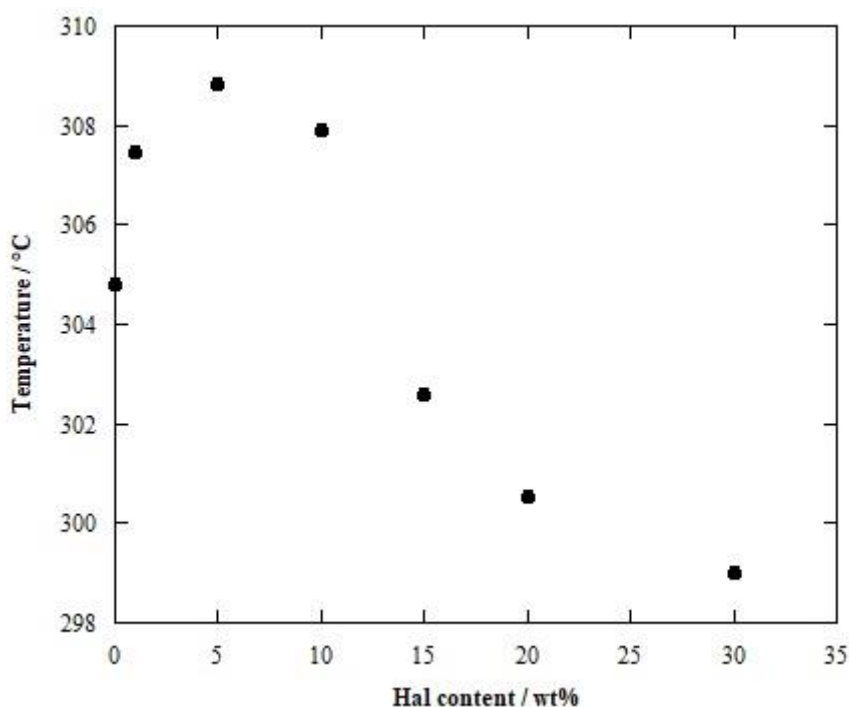


Figure 5.3.4. Onset temperature values for pure Mater-Bi and Mater-Bi/Halloysite composite films as a function of the nanoclay content. The relative error is 2%.

As far as it is concerned, trends similar to those observed for the mechanical properties are also reported for the onset temperature. In particular, the maximum is measured for the Mater-Bi/HNTs 10% with an increase of 4 °C and, then, the values show a decrease for any further nanoclay addition.

In light of this, it is possible to conclude that small amounts of halloysite induced a slight thermal stabilization effect whereas larger filler contents (> 10 wt%) induced a worsening of the polymer thermal stability. This effect is probably related to the morphological features of the nanocomposites and to their specific composition. Indeed, Scanning Electron Microscopy showed

that the clay nanoparticles are randomly and homogeneously distributed within the polymeric matrix of Mater-Bi for halloysite contents ≤ 10 wt% (Figure 5.3.5) thus enhancing the thermal stability as a consequence of the barrier effect towards the volatile products of the polymer degradation, as reported in literature.¹³⁶

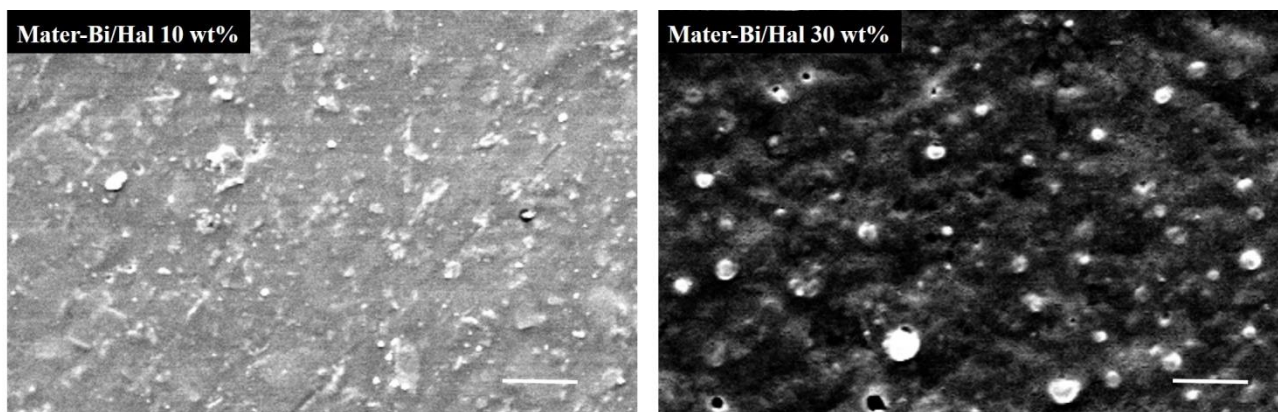


Figure 5.3.5. Scanning Electron Microscopy images of the Mater-Bi/Halloysite nanocomposites at variable composition. The scale bar is 10 μm .

On the contrary, the decrease of the onset temperature for halloysite contents ≥ 10 wt% can be related to the separation between the polymeric phase and the nanotubes, which are not homogeneously distributed. Therefore, HNTs form aggregates and they can not effectively play a role as a barrier towards the volatile products of degradation, thus decreasing the thermal stability. For instance, Figure 5.3.5 shows that the Mater-Bi/HNTs 30 wt% nanocomposite has a rough surface with several holes and clusters indicating that the nanotubes are not homogeneously dispersed in the polymeric matrix.

Thus, the preparation of Mater-Bi/halloysite 10 wt% allowed the achievement of the strongest enhancements in both the thermal stability and in the tensile properties, with a worsening for any further addition of nanoclays. The attained knowledge represents the starting step and a very promising point for the development of green and eco-compatible films for packaging and in numerous industrial and technological applications that could replace the traditional petroleum plastics.

6. Functional nano-engineered biohybrids for health applications

6.1 Design of new nanoarchitected materials

Following the preparation of plasticized bionanocomposites that can be used for industrial applications, as discussed in the previous chapter, this part of the work was dedicated to the design of novel hybrid materials to be employed in different domains such as biomedical and pharmaceutical sciences, cosmetics or food storage. Hence, we report the preparation of a new functional nanoarchitecture resulting in a layered tablet with a chitosan/halloysite nanocomposite film sandwiched between two alginate layers (attached paper VII). Besides, we also discuss the design of a biohybrid material that was prepared by co-assembling the three following components in aqueous dispersions: nanotubular halloysite, microfibrinous sepiolite, and cellulose nanofibers, with the aim to exploit the most profitable features of each component (attached paper VIII).

In both cases, the prepared functional hybrids were used for the controlled and sustained release of bioactive species by simulating the most typical conditions of the human gastro-intestinal path or testing the bactericidal and antiseptic activity through in vitro antibacterial assay. The results demonstrated that the proposed organic–inorganic nanoarchitectures are suitable as functional materials with tunable delivery capacity, opening a versatile path for developing other related materials of potential interest in different technological fields.

6.2 Layered composite based on HNTs and natural polymers: physico-chemical studies

Firstly, we report the design of a new material with a peculiar architecture. For instance, it is constituted by a chitosan/halloysite (CHI/HNTs) nanocomposite film, prepared by solvent casting method, covered on both (top and bottom) sides with alginate (ALG) layers in order to generate a compact tablet (Figure 6.2.1)

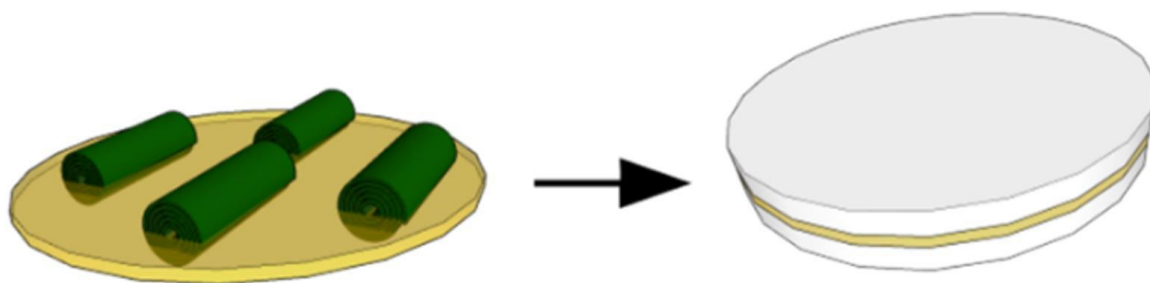


Figure 6.2.1. Schematic representation of the biohybrid tablet.

The amount of alginate was systematically changed to prepare tablets with variable thickness, thus allowing the control and regulation of active species release kinetics. Indeed, Table 6.2.1 lists the

prepared layered tablets with variable alginate/chitosan–HNTs mass ratios ($R_{\text{Alg/Film}}$) also providing the corresponding thicknesses, measured using a micrometer, of both the inner film and the whole sandwiched tablet. Nevertheless, in this paragraph we will focus on the physico-chemical characterization, since the assembly of the raw components and the final structure of the hybrid tablet have been highlighted by investigating the morphological and wettability properties. Figure 6.2.2 shows the optical photographs of the tablet by observing also the details of the cross sections of all the prepared samples.

Table 6.2.1. Composition and thicknesses of the layered hybrid tablets.

$R_{\text{Alg/Film}}$ (wt%)	CHI-HNTs thickness (μm)	Tablet thickness (mm)
20	58 ± 1	1.114 ± 0.001
25	44 ± 1	1.423 ± 0.001
30	60 ± 1	1.710 ± 0.001

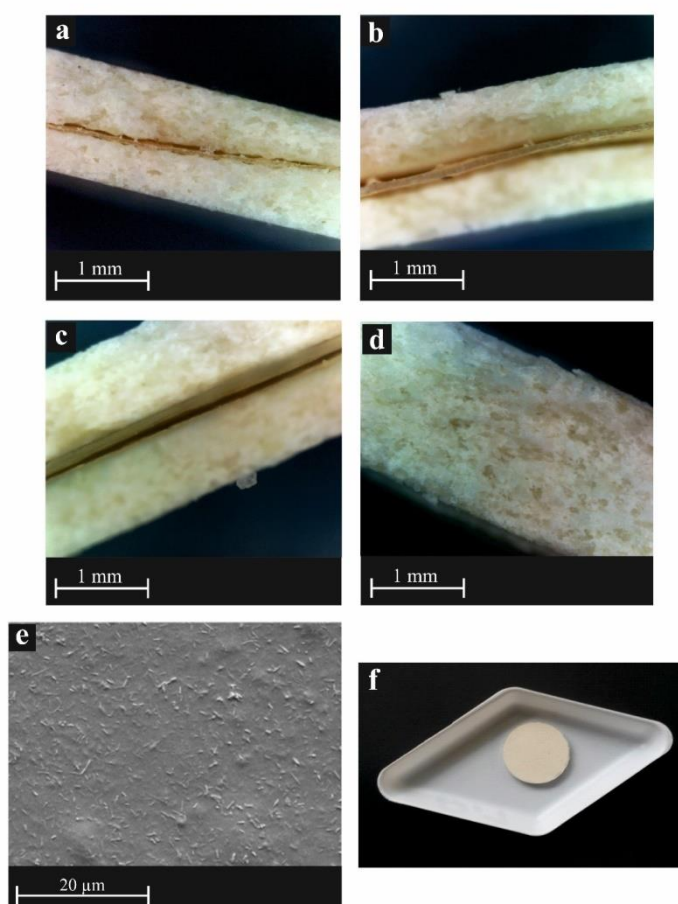


Figure 6.2.2. Cross section optical photographs of (a) $R_{\text{Alg/Film}} = 20$, (b) $R_{\text{Alg/Film}} = 25$, (c) $R_{\text{Alg/Film}} = 30$ and (d) pure alginate prepared tablets; (e) SEM image of the CHI-HNTs nanocomposite film with drug loaded nanotubes; (f) optical photograph of the tablet with $R_{\text{Alg/Film}} = 20$.

As shown in Figure 6.2.2(a-c) the ALG/CHI–HNTs/ALG hybrid materials possess a very peculiar architecture. For instance, they have a sandwich-like structure and the inner CHI-HNTs film is always visible in the cross section images. The two alginate outer layers of each tablet have a homogeneous aspect and morphology and, obviously, their dimensions depend on the amount of polymer used for the preparation. Indeed, an increase in the alginate/nanocomposite ratios (the $R_{\text{Alg/Film}}$ parameters reported in Table 6.2.1 determined an enhancement of the tablet thickness.

Figure 6.2.2(d) shows the pure alginate tablet for comparison, whereas Figure 6.2.2(e) is a SEM image of the CHI-HNTs film with drug loaded nanotubes showing their homogeneous and random dispersion within the chitosan matrix, a crucial property for the drug delivery purposes. Therefore, we carried out contact angle measurements in water to investigate the wettability of the biohybrid tablets. Figure 6.2.3 reports the θ values as a function of time for the sample with $R_{\text{Alg/Film}} = 30$, as an example.

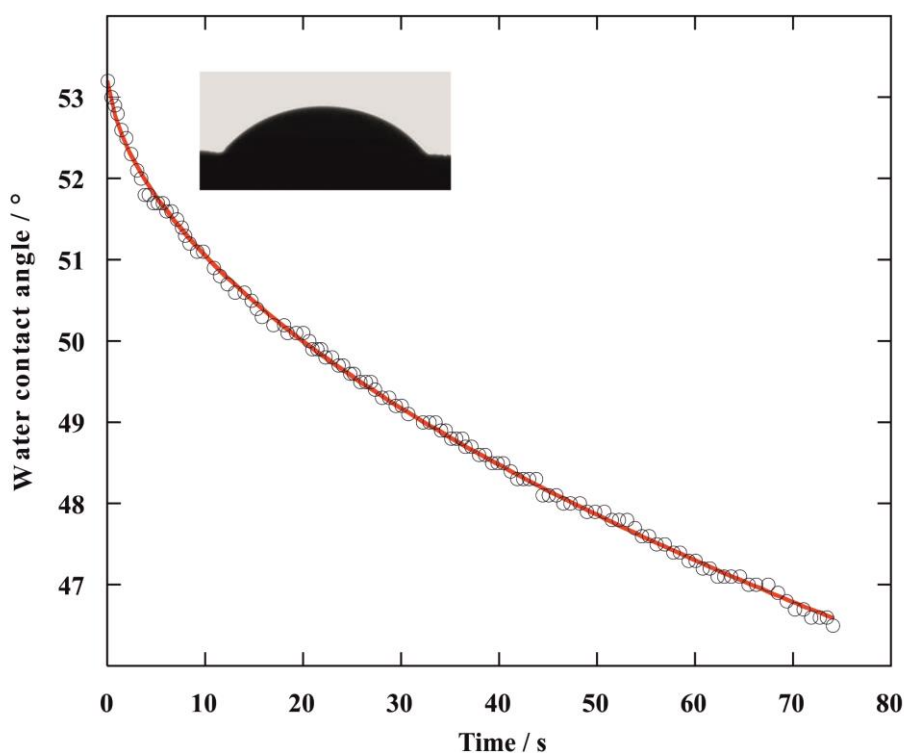


Figure 6.2.3. Contact angle values as a function of time for $R_{\text{Alg/Film}} = 30$ tablet. The inset displays the image of the water droplet just after surface deposition. The solid red line represents the fitting based on equation (6.2.1).

Contact angle values over time were fitted by the following equation:¹³⁷

$$\theta = \theta_i * \exp(-k_\theta * t^n) \quad (6.2.1)$$

where θ_i represents the initial value, and k_θ and n are characteristic coefficients related to the process rate and mechanism. In particular, n ranges between 0 and 1 depending on the absorption

and spreading contributions to the kinetics, being 0 for the former and 1 for the latter, respectively. The value of θ_i , k_θ and n resulting from fitting the curves are reported in Table 6.2.2.

Table 6.2.2. Parameters of wettability obtained by fitting the contact angle vs. time curves for tablets with variable composition.

Sample	θ_i (°)	k_θ	N
Alginate	59	0.0366	0.31
$R_{\text{Alg}/\text{Film}} = 20$	64	0.1242	0.16
$R_{\text{Alg}/\text{Film}} = 25$	58	0.0242	0.51
$R_{\text{Alg}/\text{Film}} = 30$	53	0.0115	0.57

Errors: 1% for θ_i and k_θ , 3% for n .

It is clear that all the prepared biohybrid materials are hydrophilic, since the θ_i values are always lower than 90. Moreover, the wettability degree is not noticeably altered by the sandwich-like structure and by the thickness variation of the prepared hybrid tablets, if compared to the pure alginate sample. The contact angle values measured for all samples are always lower than that of the chitosan/HNTs nanocomposite film, which was experimentally measured to be 79 °C. As concerns k_θ , the hybrid tablets showed lower values compared to that of pristine alginate. Accordingly, we can state that the kinetics of the contact angle evolution was slowed down by the peculiar sandwich like structure of the hybrid tablets. For what concerns n , instead, it is 0.31 for the pure alginate tablet, indicating a major role of the spreading contribution. Then, the n values ranged from 0.16 for the $R_{\text{Alg}/\text{Film}} = 20$ tablet, to 0.51 for the $R_{\text{Alg}/\text{Film}} = 25$ sample, then reaching 0.57 for the $R_{\text{Alg}/\text{Film}} = 30$ tablet, thus depending on both spreading and adsorption mechanisms. More interestingly, we observed that the increase of the alginate amount in the hybrid systems determined an enhancement of the absorption contribution. In light of these findings, we studied the possibility to use the prepared materials for biomedical applications. These aspects will be highlighted in paragraph 6.4.

6.3 Self-assembly of HNTs, Sepiolite and CNF: physico-chemical studies

Here, it is reported the development of an alternative strategy for the preparation of a new type of multicomponent hybrid nanopaper constituted by the co-assembling in water of cellulose nanofibers (CNF), sepiolite (SEP) and halloysite nanotubes (HNTs). The aim of this choice is to exploit the most peculiar features of each starting building block in order to overcome their individual limitations and to prepare homogeneous and flexible nanopapers with good mechanical properties, which can be used for biomedical and pharmaceutical applications as well. Most importantly, the main focus of this work is the design of a material with different chemical surfaces. To achieve this purpose, the ratio (w/w) of HNT, SEP, and CNF was fixed at 1 : 1 : 1 and the films were prepared by using the solvent casting method followed by drying in a controlled atmosphere to obtain reproducible hybrid nanopapers. The schematic representation of the procedure to prepare the material is shown in Figure 6.3.1.

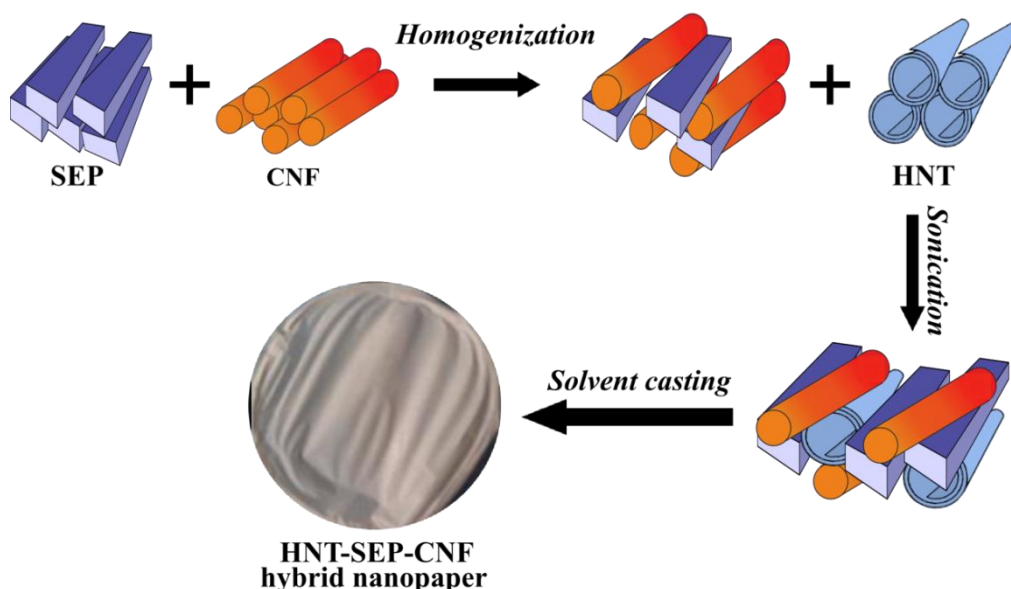


Figure 6.3.1 Scheme of the procedure followed for the integration the three components leading to HNT–SEP–CNF hybrid nanopapers.

The physico-chemical characterization was carried out by means of different techniques, such as: Scanning Electron Microscopy and Atomic Force Spectroscopy to observe the pure components and the hybrid nanopapers morphological organization, X-ray diffraction to investigate the microstructure and any possible preferential orientation/order, FTIR to elucidate the interactions between components, Dynamo-Mechanic Analysis to evaluate the mechanical performances of the prepared samples.

Therefore, we investigated the morphology and the microscopic features of the three starting building blocks. Figure 6.3.2(a) shows the peculiar hollow nanotubular shape of pristine HNTs with ca. 50–200 nm external diameter and 100–3000 nm length. Also, some kaolinite particles are contained in the samples, in their typical hexagonal sheets structure (arrows in figure). The morphology of sepiolite microfibers with a length of 0.5–2 μm and a thickness of ca. 30–50 nm is examined in Figure 6.3.2(b). For what concerns the CNFs, instead, the characteristic fibrous morphology consisting of 2–4 nm thick fibers whose length is in the 300–600 nm range is reported in Figure 6.3.2(c). Here, the semi-flexibility of the fibers is revealed by the kinks between the crystalline domains (arrows in figure).

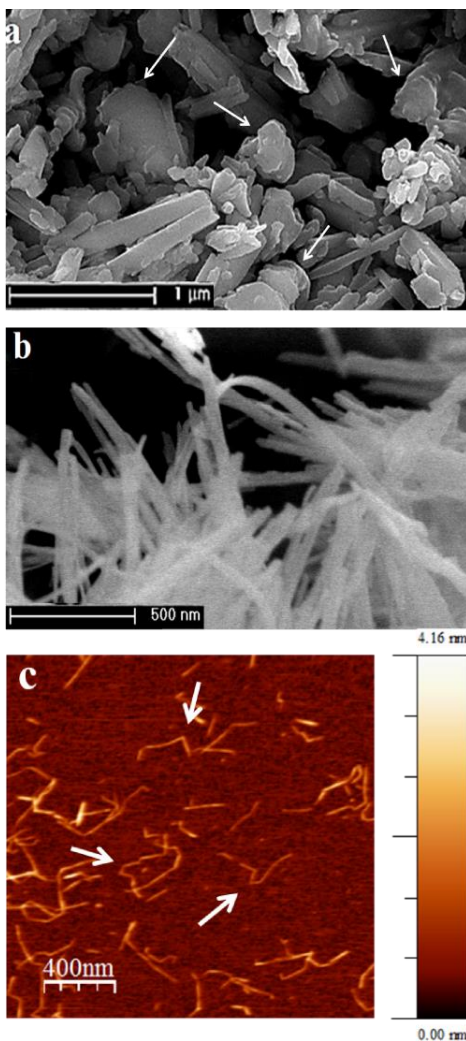


Figure 6.3.2. SEM micrographs of (a) pristine HNTs (white arrows represent the hexagonal kaolin sheets), (b) pristine sepiolite and (c) the AFM image of CNF (white arrows represent the fiber kinks).

The HNT–SEP–CNF hybrid nanopaper was examined from both the surface and the cross section, as reported in the FE-SEM images. In particular, it is possible to observe the three components, even though HNTs are more clearly recognized due to their unique shape whereas SEP and CNF are

not easily distinguished since they are both composed of microfibers (see Figure 6.3.3(a)). It is noteworthy that both nanotubes and fibers shows a preferential orientation on the surface of the film which is also visible within the film fracture. Indeed, if the cross sections is focused, it resembles the layered stratified structured typically observed in materials resulting from solvent casting procedures (Figure 6.3.3(b)).¹³⁸ This is most likely due to the density of carboxylate groups along the CNF fiber length that leads to a certain degree of lateral alignment. Since the groups density varies between the crystalline and disordered regions of the fibers, which possess also flexibility, the formation of hydrogen bonds is allowed not only with the –OH groups on the side facets of other CNFs but, more importantly, also with the Si–OH groups at the edges of sepiolite.

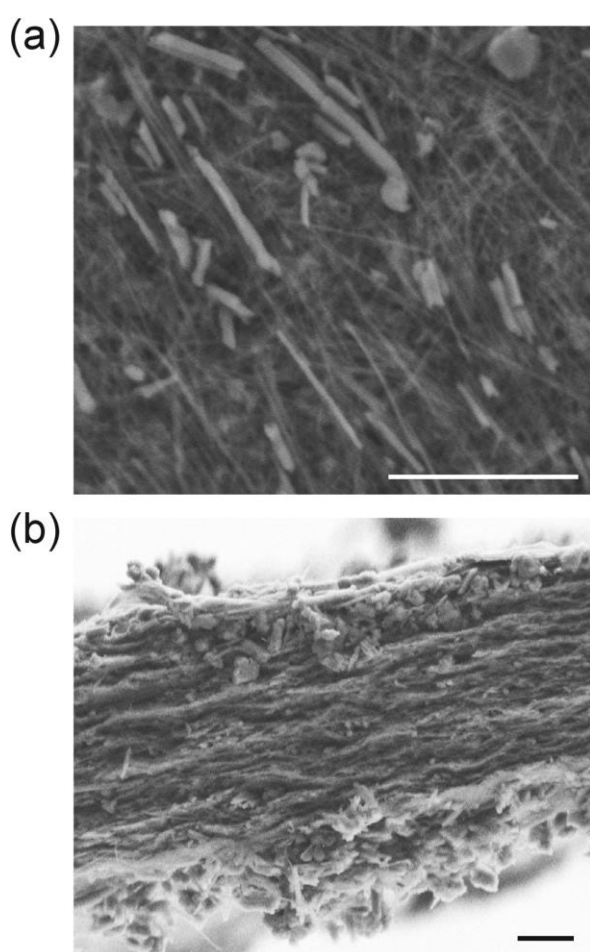


Figure 6.3.3. SEM micrographs of (a) the surface and (b) the cross section of the HNT–SEP–CNF hybrid nanopaper. The scale bars refer to 2 μm .

Thereafter, we tried to understand the role of each component by investigating the nanopaper formation. To do it, we used the raw materials in pairs (at a 1 : 1 w/w ratio) or all together during the preparation procedure. For instance, the sample containing only halloysite and sepiolite was not a film but a powdery material (Figure 6.3.4(b)), the hybrid with CNF and HNTs rendered a self

supported film with many defects (Figure 6.3.4(c)) and, on the other hand, the combination of SEP and CNF ratio produced homogeneous films (Figure 6.3.4(d)). In light of these observations, CNF probably plays a major role in providing consistency and mechanical integration to the samples thus deeply affecting the macroscopic aspect, while the sepiolite improves the dispersions of the components. However, only the multicomponent HNT–SEP–CNF hybrid nanopaper gave better results considering the macroscopic aspect, film consistency and homogeneity (Figure 6.3.4(a))

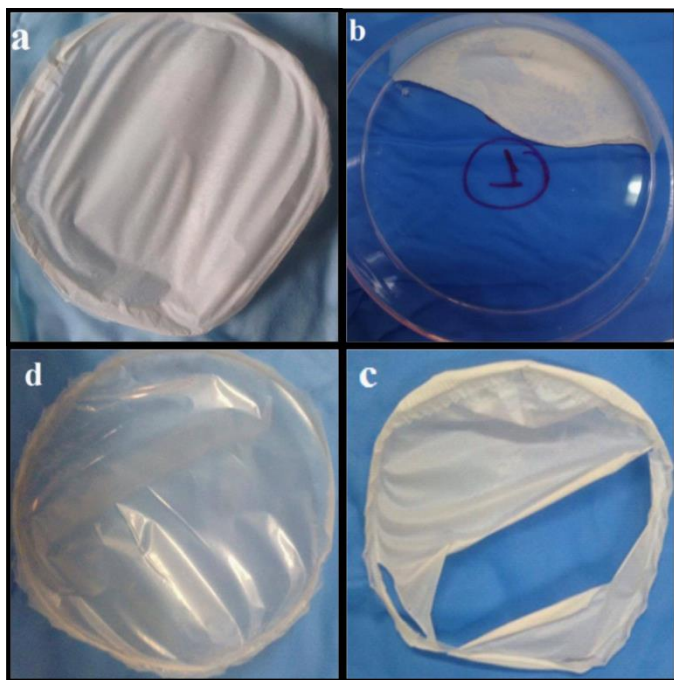


Figure 6.3.4. Macroscopic aspect of various hybrid films prepared by combining HNTs, SEP and CNF at different compositions: (a) 1 : 1 : 1 HNT–SEP–CNF nanopaper, (b) 1 : 1 HNT–SEP, (c) 1 : 1 HNT–CNF, and (d) 1 : 1 SEP–CNF.

In order to study any preferential orientation of the components within the nanopapers and to corroborate the possible intercalation inside the inter-layer volume of halloysite nanotubes, X-ray diffraction (XRD) was employed (Figure 6.3.5).

It was found that the (001) reflection of halloysite at $12.0^\circ 2\theta$ is not displaced in the HNT–SEP–CNF hybrid nanopaper, confirming that that no intercalation occurred during the film formation. Moreover, while the most typical reflections of halloysite and sepiolite are present, the low intensity reflections of the CNF are absent in the multicomponent nanopaper, and it can be attributed to the relatively low crystallinity of the cellulose nanofibers. More interestingly, the intensity ratio of the $7.4^\circ 2\theta$ and $13.4^\circ 2\theta$ reflections in the patterns of neat sepiolite and of the HNT–SEP–CNF hybrid film decreased from 15.9 to 2.4.

It is well-known that a change in the relative intensity of peaks in a XRD is strictly related to the particular orientation of the crystals. In this case, the interactions between CNF and sepiolite can

lead to preferential orientations of the fibers and to this significant variation in the ratio of the (110) and (003) reflections intensity, thus suggesting that the sepiolite has a preferred orientation within the hybrid nanopaper, well accommodated within the plane of the film.

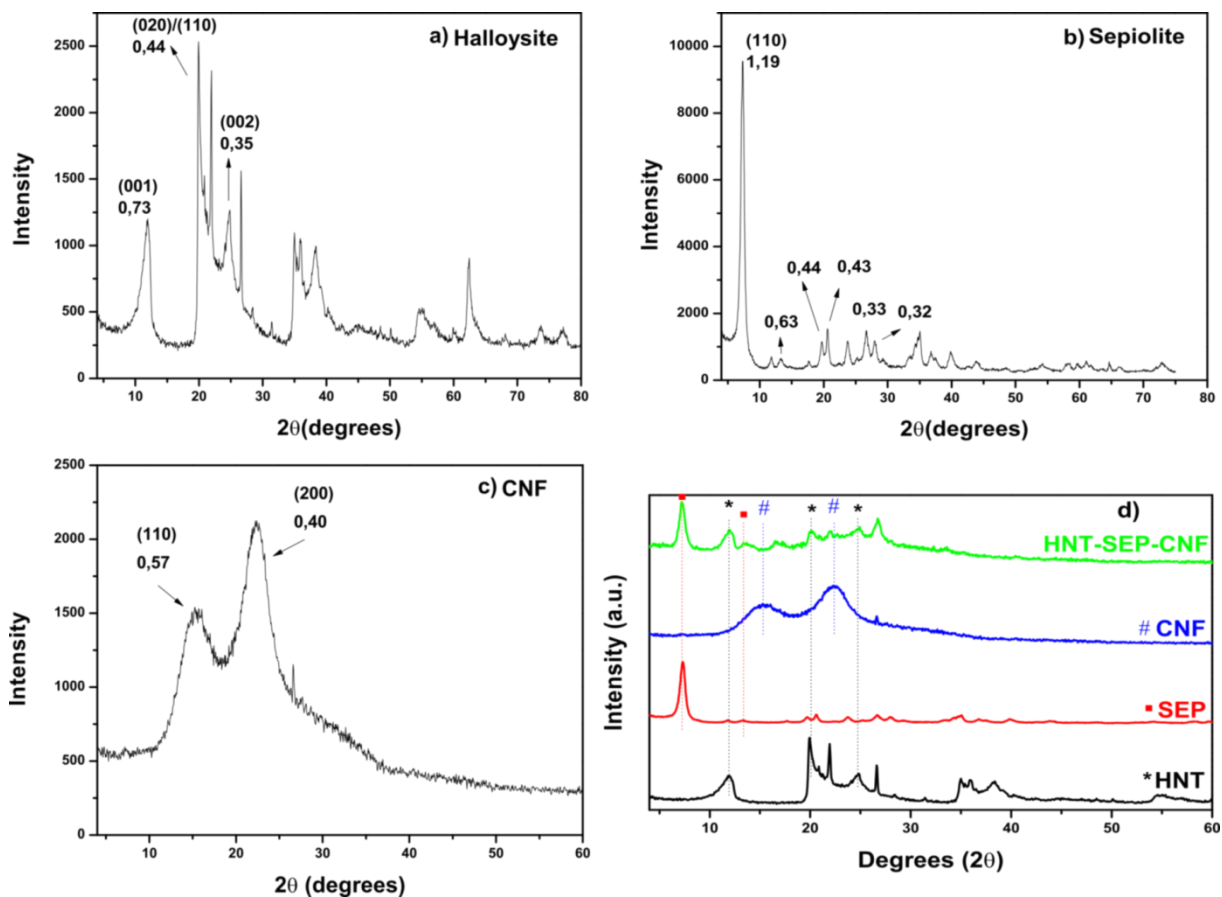


Figure 6.3.5. X-ray diffractograms of pure (a) halloysite, (b) sepiolite, (c) cellulose nanofibers and (d) HNT-SEP-CNF hybrid nanopaper.

Then, stress vs. strain measurements were carried out to evaluate the mechanical properties of the HNT-SEP-CNF hybrid nanopapers (Figure 6.3.6). The incorporation of sepiolite is responsible for a decrease in the Young's modulus of the CNF nanopaper from 3.8 GPa to 1.8 GPa but the presence of halloysite nanotubes into the SEP-CNF films significantly enhanced the elastic modulus up to 3.2 GPa, thus improving the rigidity and the overall mechanical performance. This finding confirm the observations we made in the previous chapters about the role that HNTs play in the variation of the tensile properties. More specifically, the good mechanical features open the possibility to use the prepared hybrid material in technological applications.

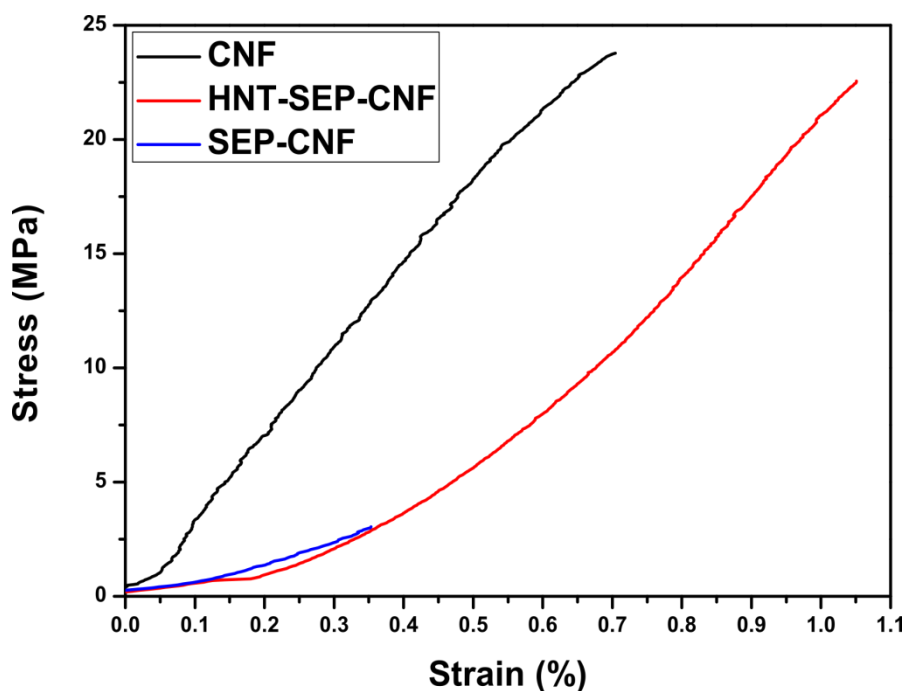


Figure 6.3.6. Stress vs. strain curves measured for CNF, SEP-CNF and HNT-SEP-CNF hybrid nanopapers.

6.4 Applications for health and drug delivery purposes

After the preparation of both the biohybrid ALG/CHI-HNTs/ALG tablets and the HNTs-SEP-CNF nanopapers and their physico-chemical characterizations, which allowed a full and deep comprehension of the most important aspects and advantages in using these new platforms (morphological features, mechanical properties, chemistry of the different surfaces, wettability), we tried to investigate about the possibility to employ these materials for health applications.

Therefore, with the aim to exploit the prepared tablets as smart carriers, we loaded halloysite with a model drug, namely the diclofenac.

Preliminarily, we determined the amount of diclofenac encapsulated within the halloysite lumen via thermal analysis by comparing the thermograms of neat HNTs, the pure drug and the loaded nanotubes, reported in Figure 6.4.1. According to the rule of mixtures, the drug loading was determined to be ≈ 10 wt% before the incorporation of the nanotubes within chitosan film and, then, as inner layer of the tablets.

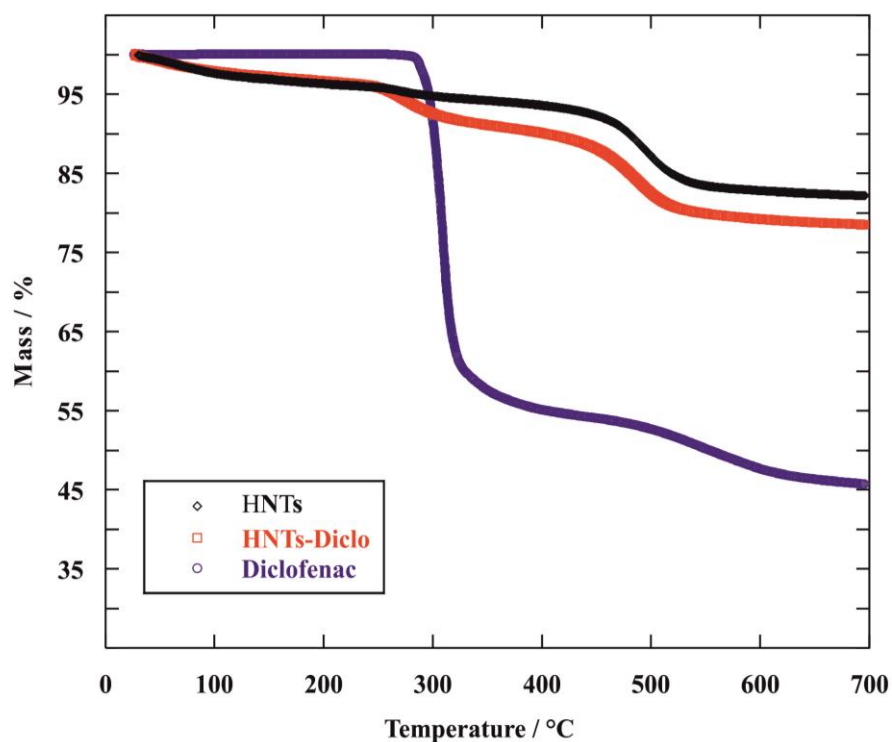


Figure 6.4.1. Thermograms of HNTs, pure diclofenac and drug loaded HNTs.

Thereafter, we studied the release from the pristine HNTs, the CHIT-HNTs hybrid nanocomposite and from the biohybrid tablets by using the UV-VIS spectrophotometry.

Release profiles at pH=7.8 for drug loaded HNTs and CHIT-HNTs nanocomposite films are shown in Figure 6.4.2.

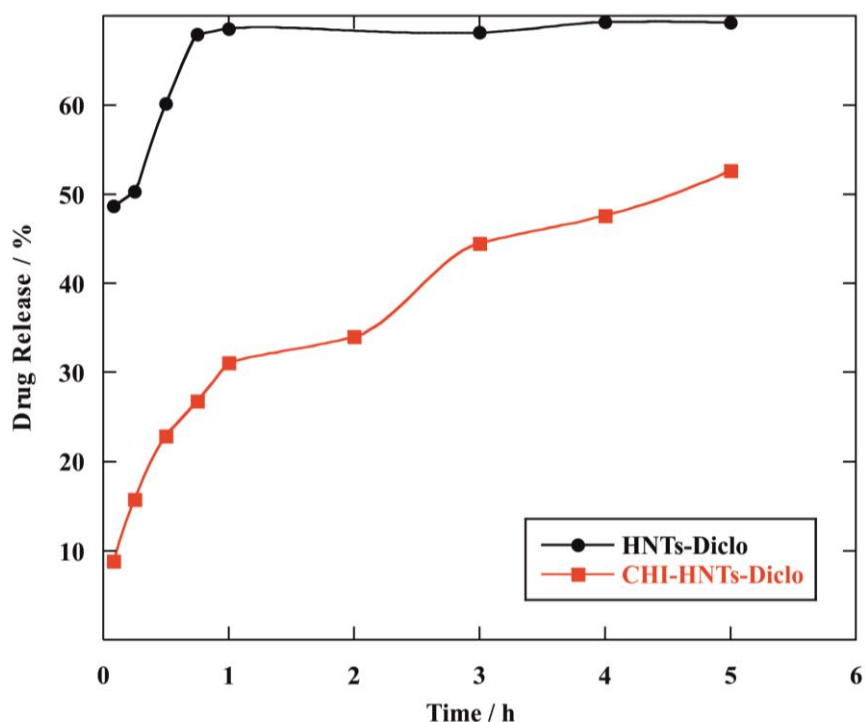


Figure 6.4.2. Release profiles for HNT–Diclo powder and CHI–HNT–Diclo nanocomposite films as a function of time.

It is clear that the incorporation of halloysite nanotubes within the polymeric matrix slows down the release kinetics. For instance, 45% of diclofenac is detected in the medium after 5 minutes for drug loaded HNTs and then a plateau is reached after 45 minutes with 70% as maximum release. On the other side, only 9% of the drug is released by the chitosan based nanocomposite film after 5 minutes and just 52% after 5 hours. This is most likely due to the barrier effect of the polymeric matrix, which can delay the drug release from the halloysite cavity.

The release kinetics for the biohybrid tablets with variable thickness are reported in Figure 6.4.3. It is noteworthy that we also investigate the dissolution process of the alginate from the material.

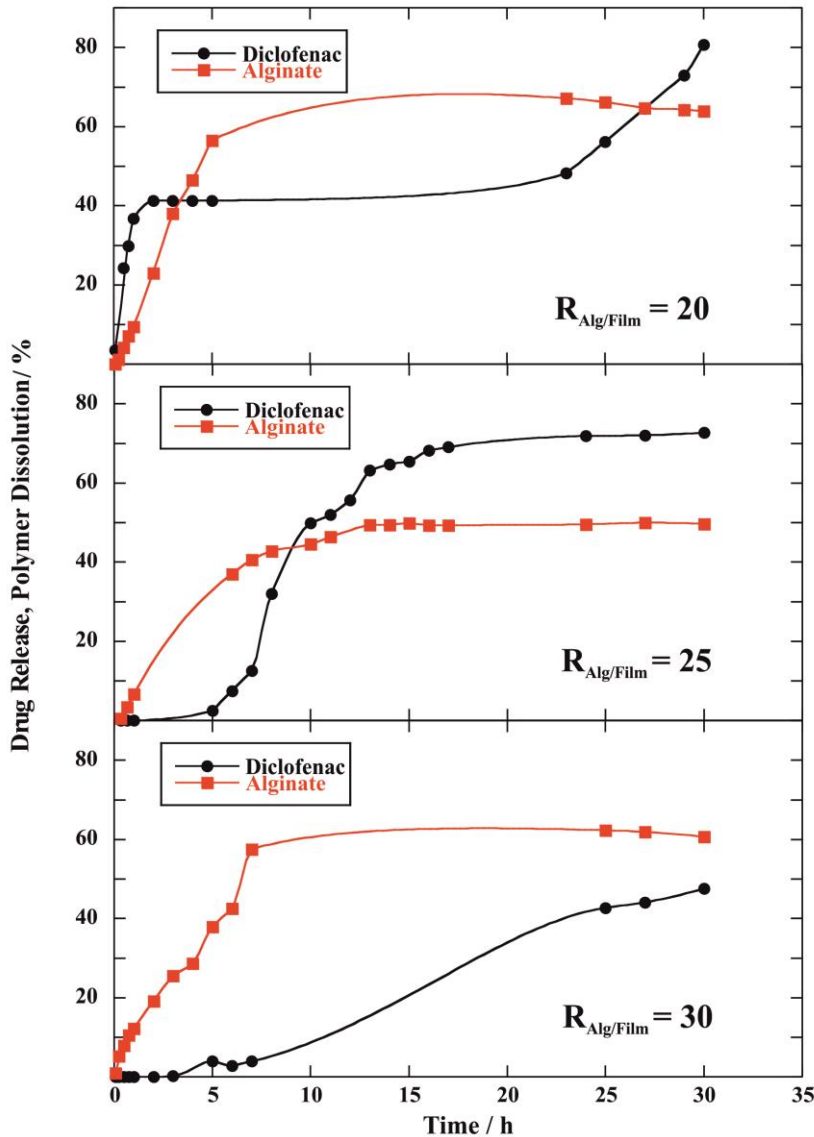


Figure 6.4.3. Release profiles for the three prepared tablets as a function of time.

As a general result, we observed that the presence of the external alginate layers slows down the drug release kinetics. In particular, the tablets with $R_{\text{Alg/Film}} = 20$ released 3% and 40% of the drug after 5 minutes and 2 hours, respectively. At this point, the diclofenac solubilization was interrupted as the alginate dissolution started and it resumed after ca. 5 hours, once the biopolymeric dissolution was completed. On the other side, the tablet with $R_{\text{Alg/Film}} = 25$ showed an induction time of ca. 5 hours where no diclofenac was released. In this timeframe, the external layers of alginate started their dissolution reaching a constant value (45%) after 5 hours and, at this point, the drug release registered a burst up to 50 and 70% after 10 and 24 hours, respectively. Similarly, the hybrid with $R_{\text{Alg/Film}} = 30$ showed a longer induction time (ca. 7 hours) where actually no drug was released. After, once the alginate concentration was found to be constant (57 % released), the

diclofenac was delivered reaching 42% in 24 hours and 47% in 30 hours. This finding enlighten that the alginate outer layers have an important effect on the release kinetics. This is most likely due to the water absorption causing the polymer swelling and the formation of a gel phase, thus delaying the drug delivery until the biopolymer dissolution is achieved. More interestingly, the kinetics of this mechanism is also influenced by the different thickness of the prepared materials, with a general increase of the induction time, from 0 to 7 hours, as a function of the biopolymeric amount and a decrease of the total delivery efficiency: 80, 65 and 45% after 30 hours for tablets with $R_{\text{Alg/Film}} = 20, 25$ and 30 , respectively.

In addition, a simulation of the typical conditions of the human gastro-intestinal path was carried out at variable pH (3, 5.7, and 7.8 that correspond to stomach, duodenum/ileum and colon, respectively) and at 37 °C using the hybrid tablet with $R_{\text{Alg/Film}} = 25$. The release profile is shown in Figure 6.4.4.

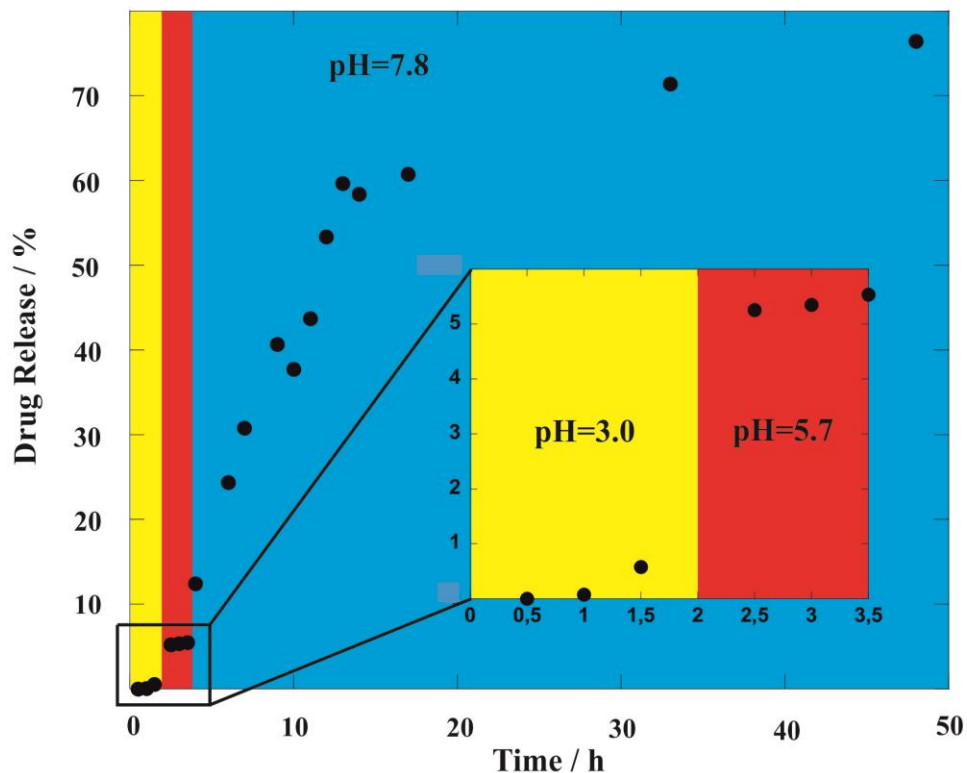


Figure 6.4.4. Release profile for the $R_{\text{Alg/Film}} = 25$ tablet measured by simulating the human body gastrointestinal path's most typical pH conditions, as a function of time.

Firstly, the biohybrid tablet was put in a strongly acidic solution with pH=3 and only a negligible amount of diclofenac was release ($< 1\%$). Thereafter, we put the material in mild conditions, namely pH = 5.7 for 1.5 hours, and only 5% of the drug release was registered. Finally, the tablet was kept in condition simulating the colon (pH = 7.8) and, suddenly, an exponential trend was observed. Herein, the released jumped to 12% after 4 hours (total timeframe) then reaching 75%

after 50 hours. According to these results, the alkaline conditions promote the diclofenac release and one can state that the sandwich like structure of the hybrid tablet is efficient in controlling the drug release with a dependence on both the material structural features and the pH conditions of the physiological aqueous medium.

Besides, owing to their hierarchical porosity and the diverse surface characteristics of the HNTs-SEP-CNF nanopapers, these hybrids can be also used in diverse biomedical applications. To prove this point, we loaded halloysite nanotubes with model drugs: ibuprofen (IBU) and salicylic acid (SA). The former is a hydrophobic, non-steroidal, anti-inflammatory drug (NSAID) that is administered for the relief of moderate pain and inflammation and the latter was tested for its bactericidal and antiseptic properties, and is used in a wide range of pharmaceutical formulations and as an additive for food and cosmetics.

The loading efficiency into HNTs was estimated to be 8.4 wt% for SA and 5.1 wt% for IBU, respectively. Moreover, N₂ adsorption/desorption isotherms were collected in order to verify the encapsulation of the drugs in the HNT lumen. After the loading procedures were carried out, a noticeable reduction in the BET surface area, pore surface area, and pore volume was observed for the drug loaded halloysite compared to the pristine HNTs (Table 6.4.1)

Table 6.4.1. The BET surface area, pore surface area, S_{mes} , and pore volume, V_{mes} , of pristine HNTs and drug loaded HNTs.

	S_{BET} ($m^2 g^{-1}$)	S_{mes} ($m^2 g^{-1}$)	V_{mes} ($cm^3 g^{-1}$)
HNTs	27.3	23.2	0.062
HNT + SA	20.2	17.8	0.054
HNT + IBU	24.6	21.9	0.057

For instance, the BET surface area dropped from 27.3 to 20.2 $m^2 g^{-1}$, the mesopore area from 23.2 to 17.8 $m^2 g^{-1}$ and the mesopore volume was reduced from 0.062 to 0.054 $cm^3 g^{-1}$. These effects can be due to the entrapment of the drug inside the halloysite inner volume, thus causing a partial blockage at the entry of the pores. It is interesting to note that the variation of these parameters is greater for the salicylic acid than the ibuprofen loading, perhaps reflecting the higher SA uptake.

Figure 6.4.5 reports the release profile from HNTs and the HNTs–SEP–CNF hybrid nanopapers.

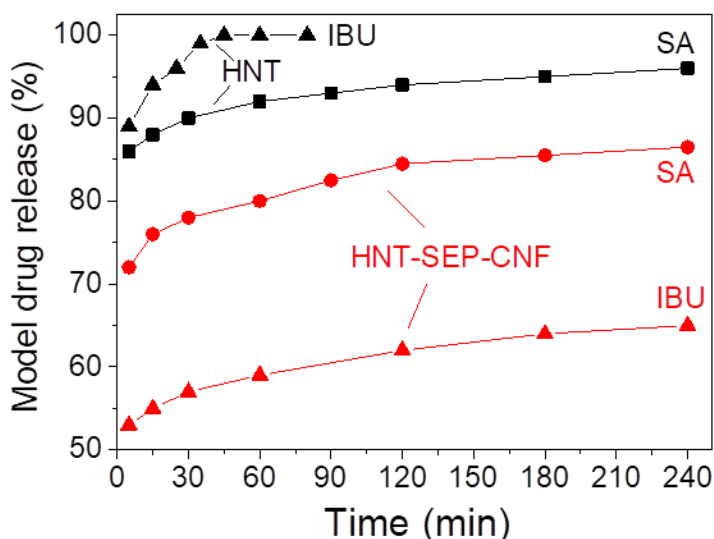


Figure 6.4.5. Release profiles of salicylic acid (SA) and ibuprofen (IBU) from the loaded HNTs and loaded HNT–SEP–CNF hybrid nanopaper.

Therefore, more than 90% of salicylic acid was released from HNTs after 60 min while less than 80% was released from the HNT–SEP–CNF hybrid nanopaper. Similarly, 100% of ibuprofen leaves the halloysite lumen after 1 hour but less than 60% is detected in water after the nanotubes incorporation in the multicomponent matrix. Hence, the kinetics is faster for IBU compared to SA when the drugs are released by the untreated clay but it is slower if the releasing material is the HNT–SEP–CNF film. These findings could be explained by taking into account the water solubility of each drug (100 mg mL^{-1} for IBU and 50 mg mL^{-1} for SA). Moreover, the release rate of the drugs is always lower for the HNT–SEP–CNF hybrid nanopapers, compared to the neat HNTs, due to the multicomponent nature of the material and the co-assembly of different building blocks. The particular diffusion mechanism of the drugs inside the nanotubes lumen and through the nanocomposite matrix plays an important role. Once the drugs leave halloysite lumen, they find the fibrous matrix of sepiolite and CNFs and some interactions can arise. For instance, strong interactions exist between IBU and nanocellulose which could explain the slower IBU release from hybrid nanopaper compared to the SA.¹³⁹ Also, the nanotubes gates could be partially obstructed by the particular texture of the film and its morphological organization at a micro- and nanoscopic level.

Finally, *in vitro* antibacterial assays from salicylic acid loaded HNT–SEP–CNF hybrid nanopapers were conducted in order to evaluate the applicability of this new type of material for topical applications. With this aim, we employed Gram-negative *E. coli* and Gram-positive *S. aureus* bacteria under neutral and acidic ($\text{pH} = 5.5$) conditions SA by means of the disk diffusion method. It was found that the SA loaded in HNT and then incorporated into the HNT–SEP–CNF nanopaper

expresses very good antimicrobial activity when it is used against *S. aureus* at pH = 5.5. The result of the trials is shown in Figure 6.4.6, with the formation of a clear inhibition zone whose average diameter is ca. 16 mm and in the same order of magnitude of other salicylic acid loaded pectin-HNT bionanocomposites,¹⁴⁰ thus confirming the activity of the drug loaded HNT-SEP-CNF hybrid nanopapers and their potential use in controlled and smart delivery applications.

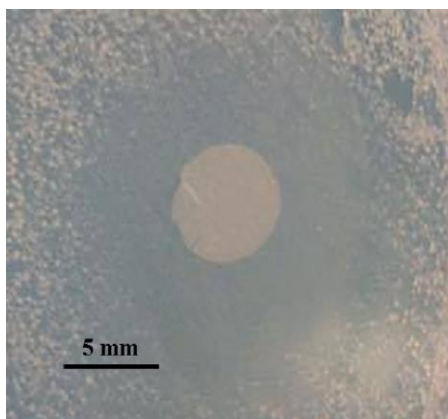


Figure 6.4.6. Inhibition zone of the salicylic acid loaded HNT-SEP-CNF hybrid nanopaper against Gram-positive *S. aureus* at pH = 5.5.

7. Pickering Emulsions based on Halloysite and wax for the consolidation of archeological wood

7.1 Pickering emulsions as green and ecofriendly materials

It is well-known that an emulsion is a multiphase system composed of two immiscible liquids where one of them is dispersed into the other in the form of droplets. Being thermodynamically unstable due to the high surface energy of the liquid/liquid interface, emulsions are usually stabilized by surfactants or amphiphilic species that decrease the oil/water interfacial tension thus avoiding coalescence and agglomeration.¹⁴¹ The interface of a multiphase system can also be stabilized by colloidal particles, thus leading to the preparation of the so-called Pickering emulsion, as reported by the pioneering studies of Ramsden and Pickering.¹¹⁶ In particular, the mechanism of stabilization is referred to a kinetic barrier that avoids the coalescence and agglomeration due to steric hindrance and volume exclusion.¹⁴² Recently, several biopolymers have been employed for the design of Pickering emulsions, and namely polysaccharides, proteins, lipids, cellulose micro- and nano-fibrils or nanocrystals.¹⁴³ Hence, Pickering emulsions meet the current demand for green and ecofriendly materials using particles derived from renewable and eco-sustainable sources.

In this chapter, we propose a new protocol for the preparation of halloysite based Pickering emulsion using wax as the inner phase of the oil-in-water droplets. The physico-chemical characterization was carried out by optical microscopy coupled with Scanning Electron Microscopy and by Differential Scanning Calorimetry in order to assess whether the thermal properties of the wax are affected after its interaction with HNTs. Finally, the pickering emulsions were employed for the treatment of waterlogged archeological woods (paper in preparation).

7.2 Wax/HNTs Pickering emulsions: preparation and characterization

At the beginning of this work, the microscopic characterization of both the starting building blocks was carried out, as reported in Figure 7.2.1.

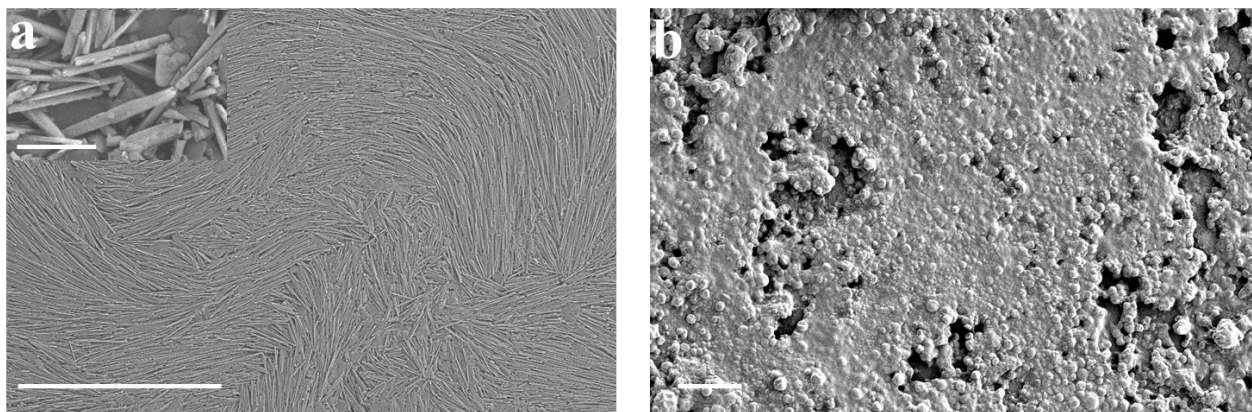


Figure 7.2.1. SEM images of pristine Halloysite Nanotubes and paraffin-in-water system. The scale bars are 20 μm for figures (a) and (b) and 1 μm for the inset in figure (a), respectively.

It is noteworthy that the nanotubes appear to have some particular orientations on the plane of the stage after drying the pristine clay aqueous suspension and many distinct domains can be recognized in Figure 7.2.1(a). Moreover, in absence of halloysite, the paraffin creates a continuous matrix where only a few spherical particles can be observed (Figure 7.2.1(b)), thus confirming the major role played by the clay in the formation of the pickering emulsions by preventing agglomeration/coalescence and oil phase separation.

Therefore, halloysite nanotubes were added to the wax at different concentrations, and namely: 0.05, 0.1, 0.25, 0.5, 0.75 and 1% w/w. Figure 7.2.2 reports the optical images of the wax/HNTs emulsions.

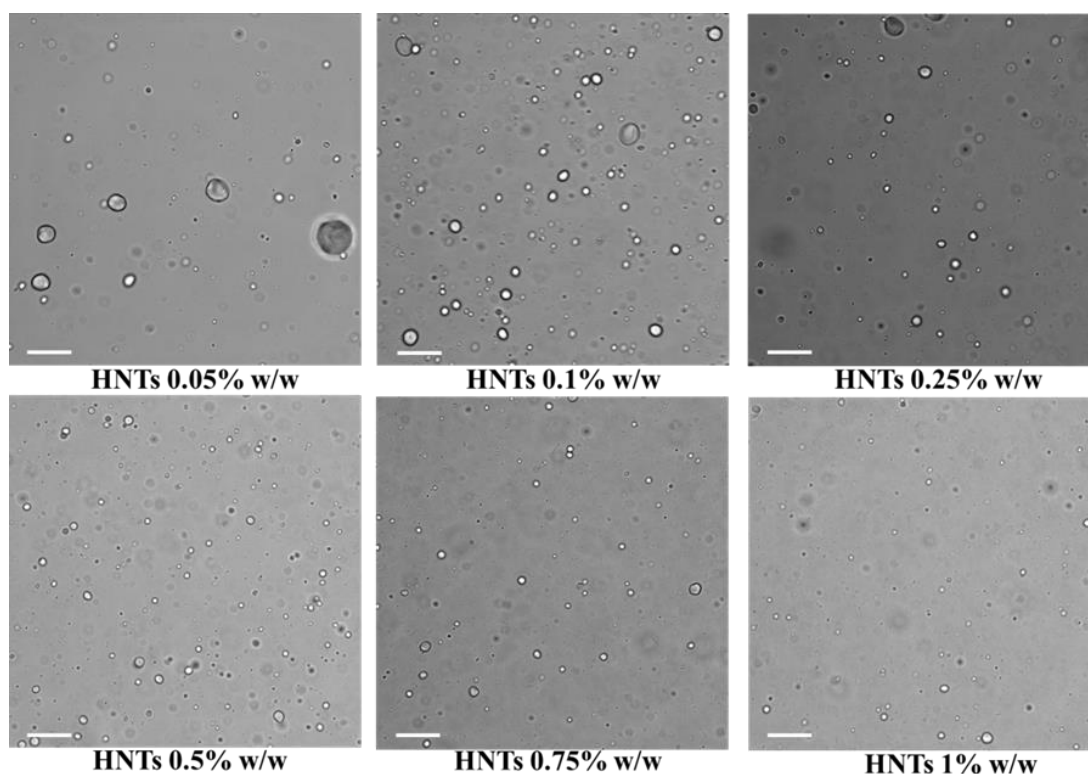


Figure 7.2.2. Optical images of wax/HNTs Pickering emulsions as a function of halloysite concentration. Scale bars are 50 μm .

The presence of the spherical pickering emulsions is clear. It is noteworthy that the dimensions of the prepared systems seem to decrease as the halloysite concentration increases. To investigate this aspect, SEM analysis were carried out with the aim to reach a higher quality morphological and structural characterization of the pickering emulsion at a nanoscopic level (Figure 7.2.3).

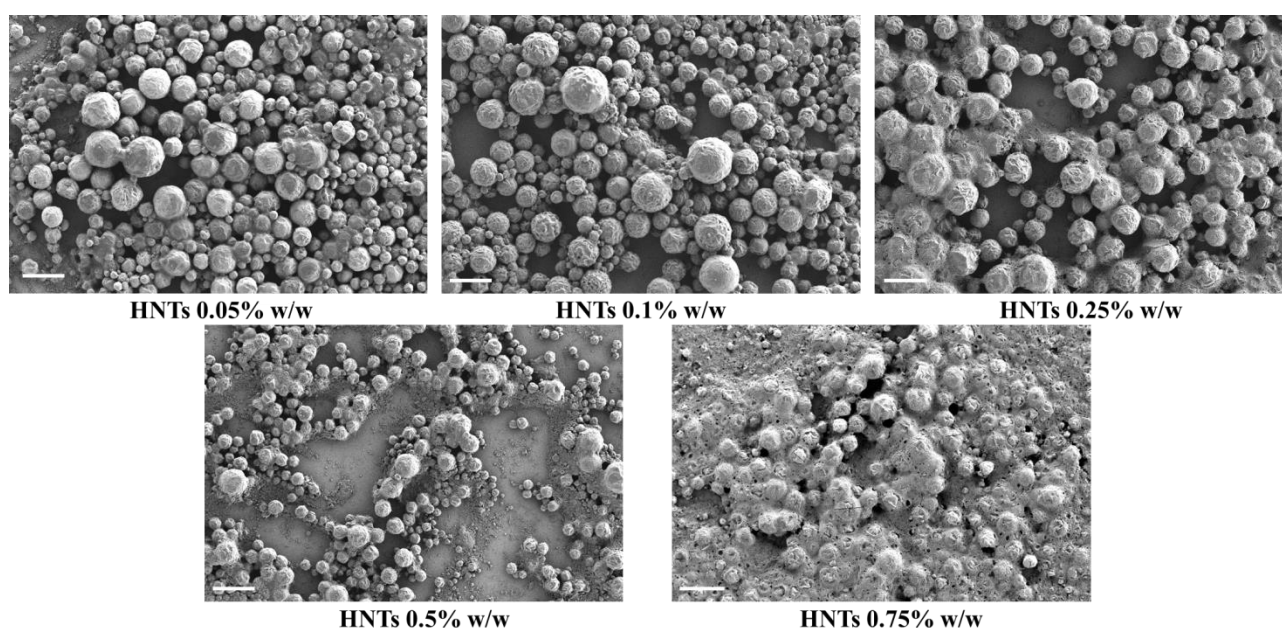


Figure 7.2.3. SEM images of Wax/HNTs pickering emulsions with an increasing concentration of Halloysite. The scale bars represent 60 μm .

As shown, the development and design of this new preparation protocol allowed the preparation of a quantitative amount of paraffin/halloysite pickering emulsions by keeping constant the concentration of wax and increasing the amount of added HNTs from 0.01 to 0.75 % w/w. Since some roughness at a certain extent can be observed at the outer surface of each spherical-shaped pickering emulsion, SEM images at a higher magnification are reported in Figure 7.2.4 for each sample, in order to better visualize this aspect and to have more precise insights.

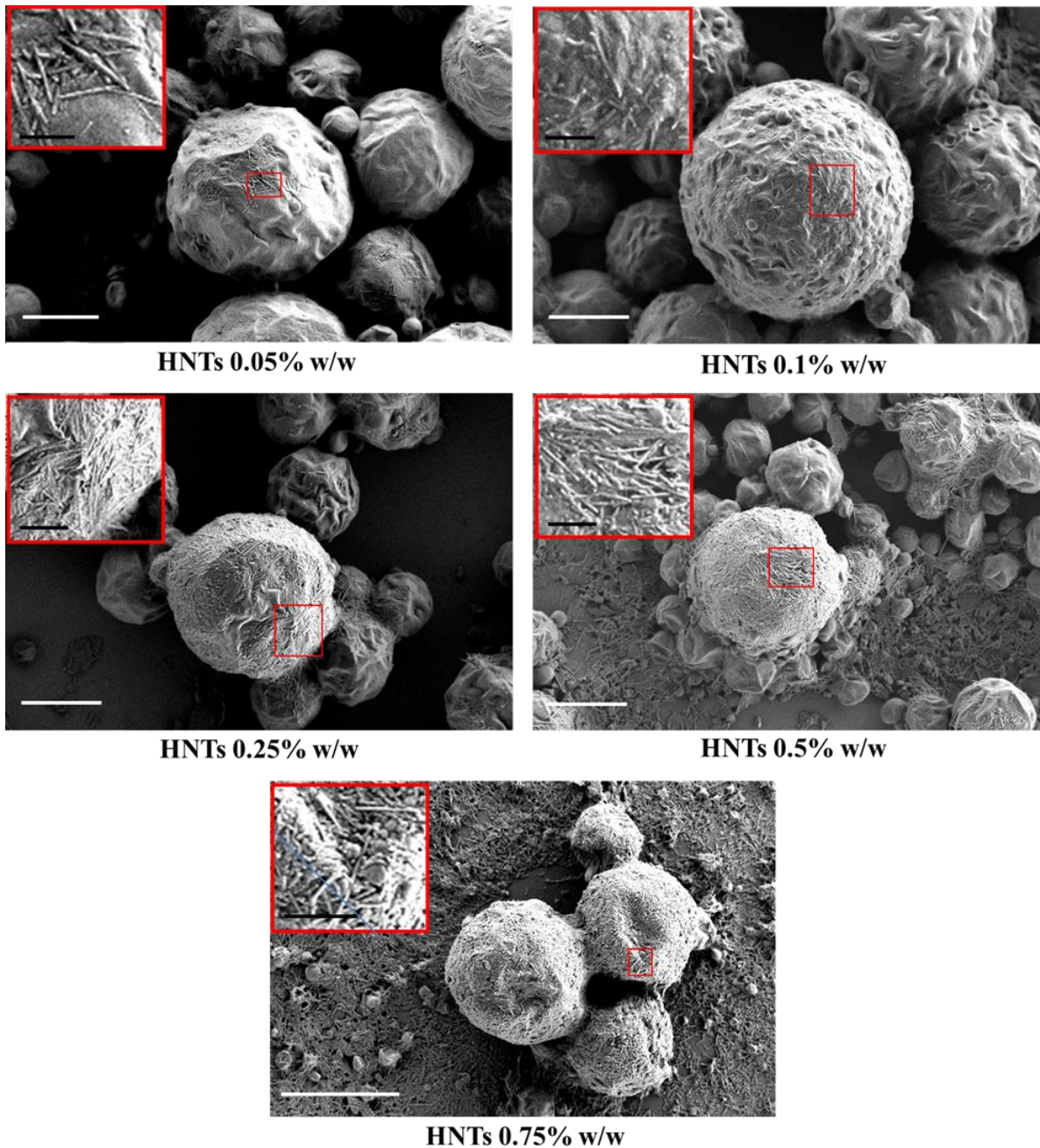


Figure 7.2.4. Higher magnification SEM images of Wax/HNTs pickering emulsions with an increasing concentration of Halloysite. The scale bars are 20 μm for the images and 3 μm for the insets.

Herein, halloysite nanotubes can be observed in their peculiar hollow tubular shape at the external surface of the pickering emulsions. Interestingly, the coverage degree strictly depends on the amount of HNTs added during the preparation procedure, the coverage being higher the higher is the concentration of nanoclays. This is most likely due to the particular temperature responsive behaviour of paraffin that, after melting and while cooling down, catches the nanotubes in the surrounding proximity. In light of this, the quantity of halloysite stabilizing the systems is a function of its overall concentration. Moreover, a concentration effect of HNTs is also registered on the general dimensions of the different wax/clay systems. The result of a statistical study on the lower magnification images is shown in Figure 7.2.5.

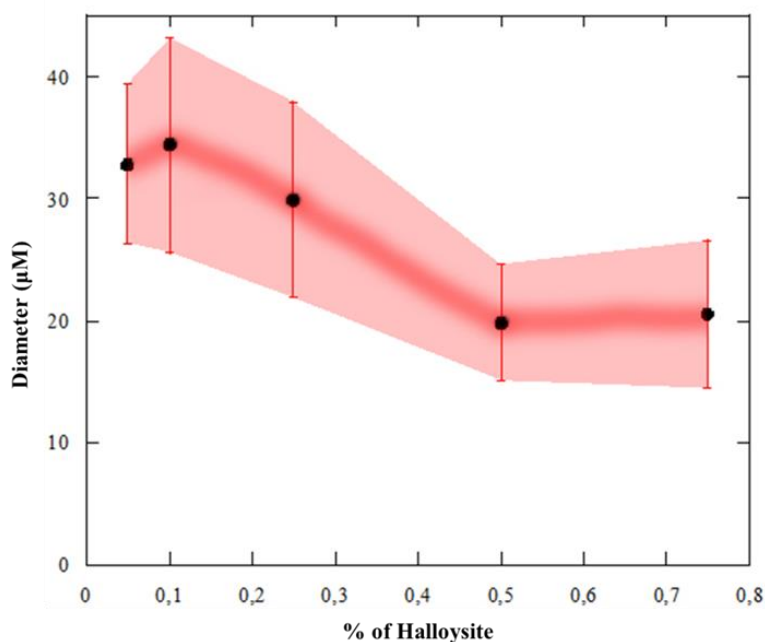


Figure 7.2.5. Average diameter as a function of halloysite content for wax/HNTs pickering emulsions. Bars refer to the standard deviation of the diameter distribution.

It is clear that the dimensions of the pickering emulsions decreased as the nanotubes content increased, reaching a maximum of ca. 35 μm for the wax/HNTs 0.05% w/w sample and then falling to ca. 20 μm for the wax/HNTs 0.5% w/w system.

Besides, we also report the statistical data for both the wax/HNTs 0.05% w/w and the wax/HNTs 0.5% w/w samples after completely analyzing all the particles in each micrograph (Figure 7.2.6).

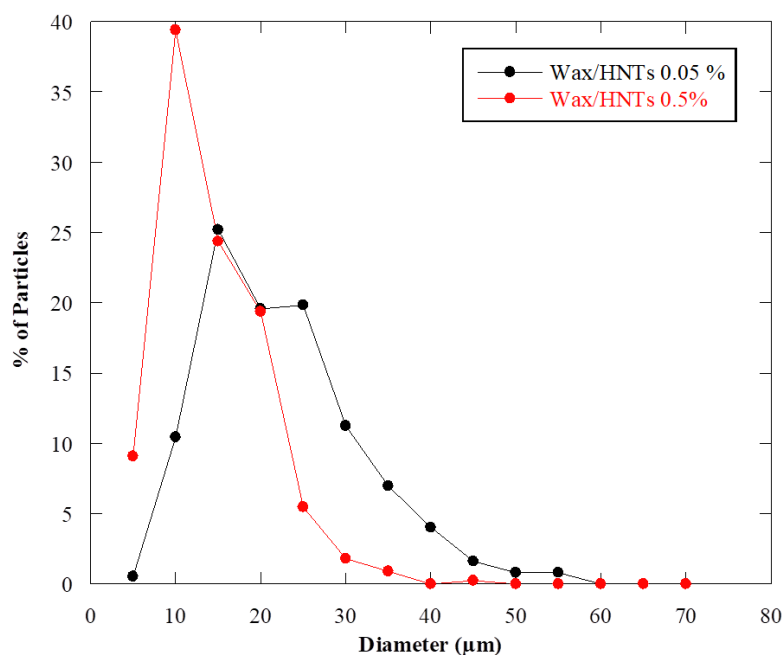


Figure 7.2.6. Dimensions of the pickering emulsions for the Wax/HNTs 0.05 and 0.5 % w/w .

It can be observed that the curve of wax/HNTs 0.05% w/w shows a peak at higher values compared to the wax/HNTs 0.5% w/w system. For the former, 25% of particles present an average diameter of 15 μm, 20% of them possess a size of 20 μm, another 20% have 25 μm as dimension and ca. 10% showing up to 30 μm in diameter and then decreasing to 5% of particles with 40 μm as average size. On the other side, the wax/HNTs 0.5% w/w sample shows a narrow distribution with ca. 90% of particles possessing an average diameter in the 5-20 μm range, having the half of this population 10 μm in size. This findings confirm that the concentration of halloysite deeply affects the dimensions of the resulting pickering emulsions, which decrease as the clay content increases, thus playing a major role in the final aspect and size distribution of such systems.

7.3 Wax/HNTs Pickering emulsions: thermal properties

The effect of halloysite on the cristallinity of the paraffin was investigating by micro-Differential Scanning Calorimetry. μ-DSC thermograms of pure wax, wax/HNTs 0.05% w/w and of wax/HNTs 0.5% w/w pickering emulsions are reported in Figure 7.3.1. It should be noted that ΔCp values were normalized to the wax weight fraction by considering the experimental composition of the investigated materials.

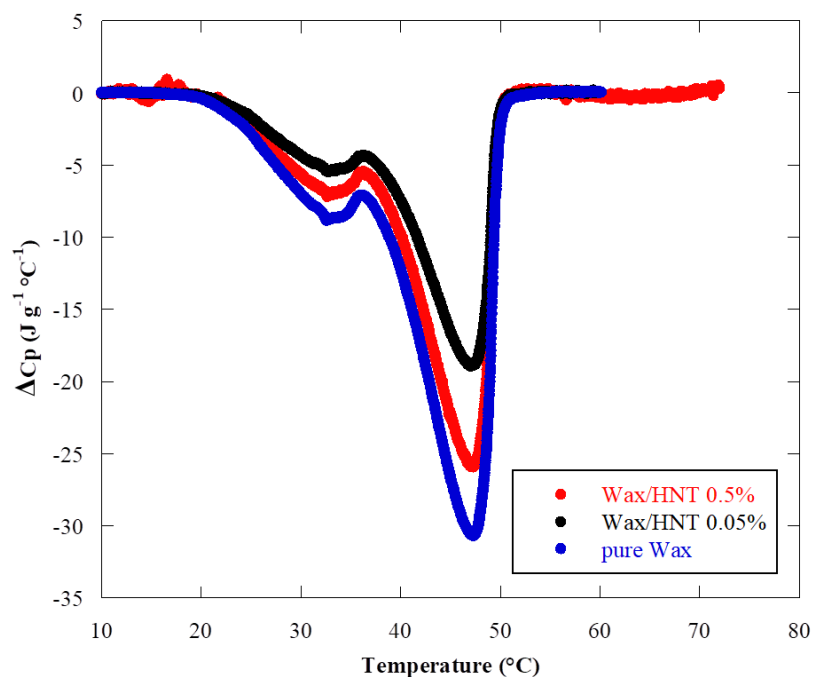


Figure 7.3.1. DSC thermograms for pure wax, wax/HNTs 0.05% w/w and wax/HNTs 0.5% w/w pickering emulsions.

As a general result, we observed an endothermic signal that can be attributed to the melting of wax. In particular, pure paraffin has two peaks related to two different phase change and due to the existence of a metastable intermediate solid phase. During melting, the first phase change peak occurs at 32.5 °C, corresponding to the solid-metastable solid phase transition of the pure paraffin. The second peak occurs at 47.5 °C, corresponding to the metastable solid-liquid phase change.¹⁴⁴ It should be noted that these transition temperatures are not altered by the addition of halloysite in the wax/HNTs pickering emulsions. Furthermore, the peaks integration provides the enthalpy (ΔH_m) of the paraffin melting process, which is expressed as Joule per gram of wax by taking into account its stoichiometric amount in the different systems. It is clear, by the observation of the curves, that the nanoclay entrapment onto the outer surface of wax induced a reduction of ΔC_p and ΔH_m , highlighting a modification of the thermodynamics of the melting phase transitions. In particular, the values of enthalpy calculated by integration of the peaks of the DSC complete thermograms, are measured to be 336.6 J g⁻¹ for the pure wax, 208.8 J g⁻¹ for the wax/HNTs 0.05% w/w and 274.6 J g⁻¹ for the wax/HNTs 0.5% w/w pickering emulsions systems. The decrease of ΔH_m after the addition of halloysite is due to the presence the nanotubes, which partially destroy the cristallinity of paraffin, as observed for both beeswax and mineral wax.¹⁴⁵

With the aim to have more precise insights into the thermodynamics of the melting process, the deconvolution of the DSC curves was carried out in order to differentiate the two distinct contributions, and namely the “solid-metastable solid” and the “metastable solid-liquid” phase

transitions. Figure 7.3.2 reports the result of data manipulation for the wax/HNTs 0.05% w/w pickering emulsions, as an example.

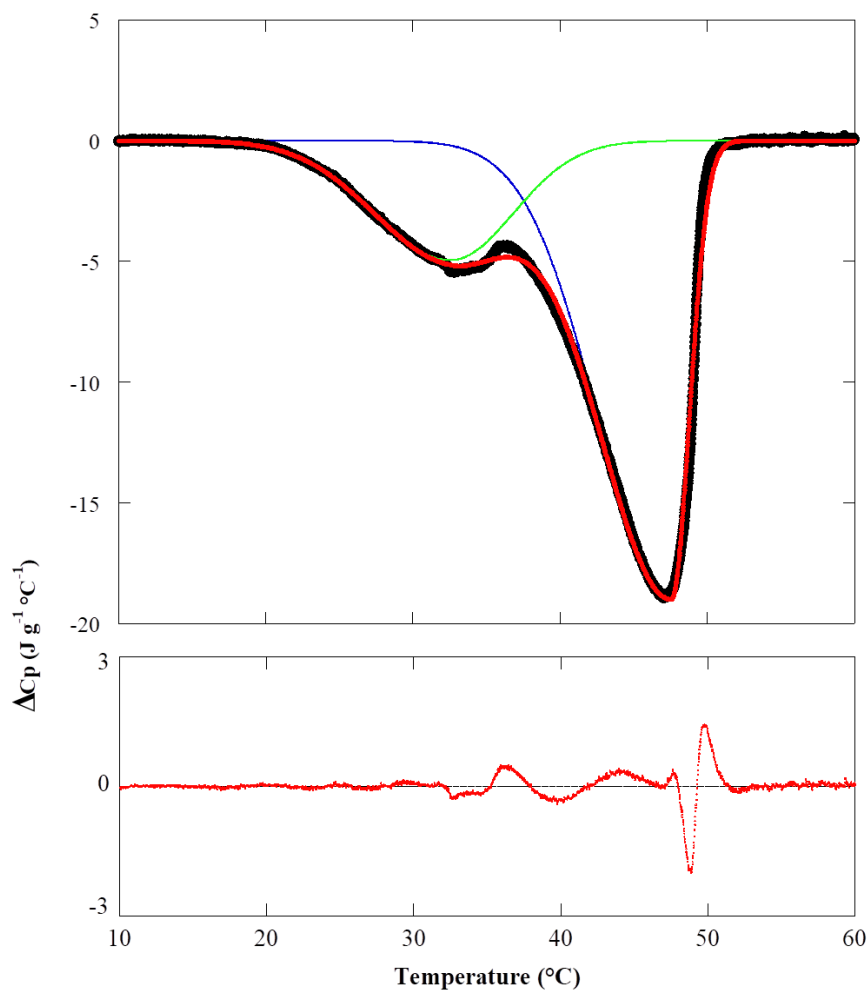


Figure 7.3.2. DSC thermogram deconvolution for the wax/HNTs 0.05% w/w pickering emulsions. The black line represents the experimental data, the blue and green lines represent the two curves for each peak and the red line represents the sum of these two contributions which better fits the experimental data. Residues are reported in the bottom figure.

By integrating the two separate curves (the blue and the green lines in figure) it is possible to estimate the enthalpies for the solid-metastable solid (ΔH_{S-M}) and for the metastable solid-liquid (ΔH_{M-L}) transitions, respectively. Table 7.3.1 reports the ratio between ΔH_{M-L} and ΔH_{S-M} for the three investigated samples.

Table 7.3.1. Ratios between the areas of the curves representing the solid-metastable solid (ΔH_{S-M}) and the metastable solid-liquid (ΔH_{M-L}) transitions in the DSC thermograms, derived from deconvolution and nonlinear fitting.

Sample	$R\Delta H_{M-L} / \Delta H_{S-M}$
pure Wax	2.41
Wax/HNTs 0.05% w/w	2.52
Wax/HNTs 0.5% w/w	2.63

It is noteworthy that the $R\Delta H_{M-L} / \Delta H_{S-M}$ values increase with the concentration of halloysite nanotubes, thus meaning that the contribution of the metastable solid-liquid transition is greater than the solid-metastable solid phase change. This is most likely due to the effect of HNTs, which promote the transition occurring at lower temperature by making easier the shift from the solid to the metastable solid phases. In other words, the paraffin wax is already in its metastable intermediate solid state because of the presence of halloysite external shell.

7.4 Treatment of archaeological woods by Wax/HNTs Pickering emulsions

Wax/HNTs Pickering emulsions were investigated as consolidants for waterlogged archaeological woods using the immersion procedure. One of the most important features of the proposed consolidation protocol is its eco-friendliness. Indeed, this method can be considered totally environmentally safe being that water was used as solvent for the wood impregnation. Moreover, it overcomes some limitations regarding the possibility to be scaled up and employed for samples with big dimensions. The consolidation efficiency was tested by performing Dynamic Mechanical experiments (DMA). In particular, the mechanical properties of the treated samples were evaluated from the stress vs. strains curves (Figure 7.4.1) to estimate Young's modulus, stress at breaking and elongation at breaking, which are summarized in Table 7.4.1. It should be noted that the untreated wood sample was not tested because of its high fragility.

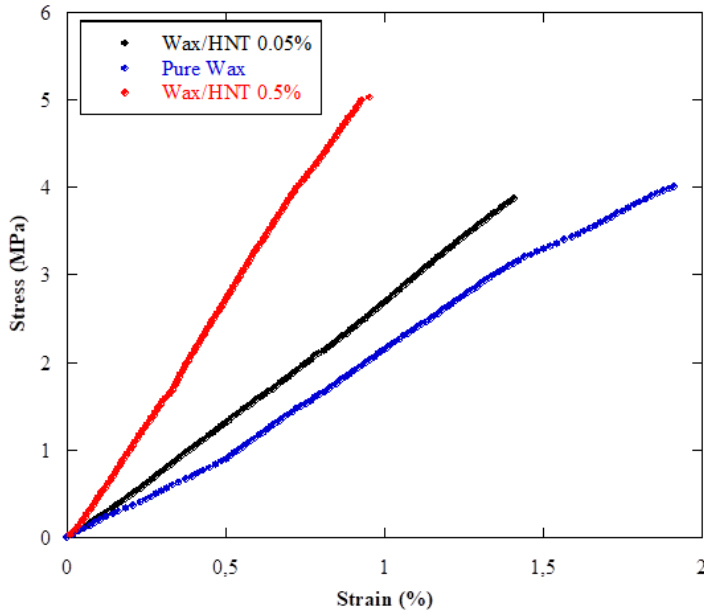


Figure 7.4.1. Stress vs strain curves for archeological wood consolidated with pure wax, wax/HNTs 0.05% w/w and wax/HNTs 0.5% w/w pickering emulsions.

Table 7.4.1. Young's modulus, stress at breaking and elongation at breaking for treated waterlogged archeological woods for all the tested consolidant materials.

	Elastic Modulus / MPa	Stress at Breaking Point/MPa	Elongation at Breaking Point/%
pure Wax	214	4.0	1.9
Wax/HNTs 0.05% w/w	282	3.9	1.4
Wax/HNTs 0.5% w/w	549	5.1	0.9

The relative error is 2%

Herein, it was observed a strong enhancement of the elastic modulus of the treated wooden samples after consolidation with the wax/HNTs pickering emulsions, reaching a maximum when the concentration of nanoclay is 0.5% w/w. These findings can be related to the increase of the consolidation efficiency and, more interestingly, to the filling of wooden pores and channels. Therefore the stiffness of the archeological wood was strongly improved. Accordingly, the stress at the breaking point showed similar trends as well, with a strong increment when the wax/HNTs 0.5% w/w pickering emulsions are employed as consolidants, thus confirming the improvement in the rigidity of the waterlogged wood samples. Contrarily to it, the elongation at breaking point showed a relevant reduction, with a loss of ca. 50% of the elongation capability for the wax/HNTs 0.5% w/w pickering emulsions. This can be attributed to the filling of the empty space with wax and halloysite. Furthermore, all the three investigated parameters show a more reliable variation in the case of Wax/HNTs 0.5% w/w. Due to the smaller dimensions of the pickering emulsions in this

system, as evidenced by SEM images and statistical analysis, the consolidants can access the wooden structure and, there, perform their role as functional biohybrid materials more easily. Figure 7.4.2 shows, by optical photograph, that the consolidated wood sample exhibited robustness and mechanical resistance from the macroscopic point of view after its treatment. Moreover, the aspect of specimen was not altered upon drying and its volume reduction was lower than 5%. Contrarily, the untreated sample is very fragile and it breaks very easily.

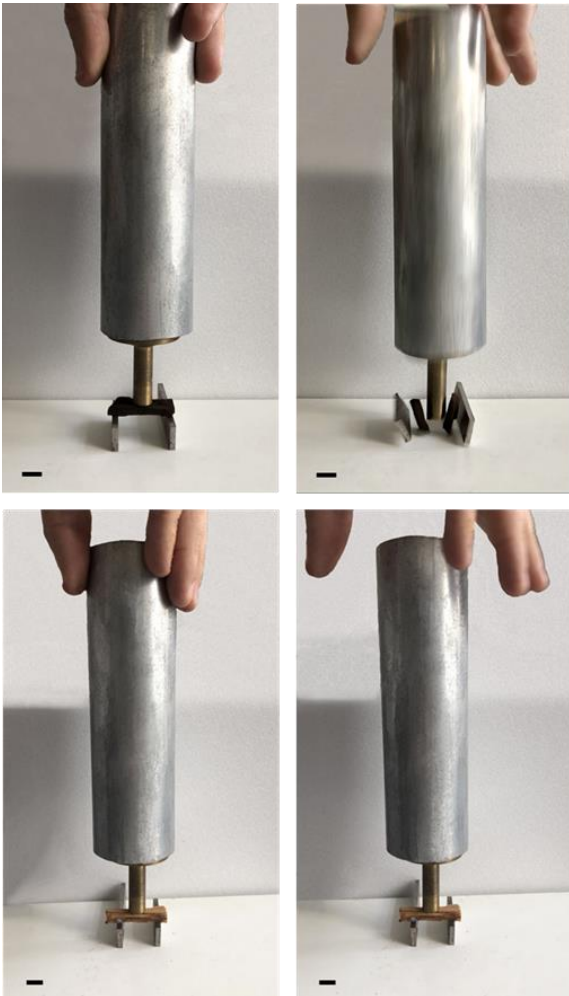


Figure 7.4.2. Optical photos of the waterlogged archeological wood before (up) and after (down) consolidation with Wax/HNTs 0.5% w/w pickering emulsions. A mass object of 0.960 kg is placed on the top of the samples. The scale bar is 1 cm.

In conclusions, this study is encouraging for designing a green protocol for the durable preservation of waterlogged archaeological woods by using biocompatible and eco-sustainable pickering emulsions based on paraffin wax and halloysite nanotubes, and by using water as the unique solvent in the whole method. Several interesting perspectives emerge, which can lead to the possibility to treat shipwrecks of big dimensions.

8. Concluding remarks

Halloysite is a natural occurring material possessing some interesting features which make this nanoclay very promising for a wide range of applications. For instance, halloysite nanotubes (HNTs) can be effectively used as nanofillers for the reinforce of polymeric matrix, as nanocontainers for the loading and smart delivery of active species after the encapsulation within their inner lumen and, also, as solid stabilizers for pickering emulsions.

The thesis allowed to provide new significant insights on the design and development of smart nanostructured eco-friendly materials. In particular, the first thermodynamic demonstration of the water confinement within the cavity of halloysite nanotubes was proposed and it represents the starting point for a proper description of the loading mechanism of HNTs from aqueous solutions of guest molecules. Due to the Gibbs-Thomson effect, the confined solvent exhibits a vapor pressure larger than the bulk water and, as a consequence, a faster evaporation rate. By using the vacuum pumping, the vapor pressure of the solvent is approached and the confined liquid evaporates so the guest molecules precipitate inside the cavity. Afterwards, the confinement effect of ethanol was also investigated with particular focus on targeting the drug site into the lumen of halloysite. The drug release kinetics was tuned by the loading conditions and by the site of drug accumulation. These findings are fundamental contributions for the development of optimized loading protocols into narrow and confined spaces in order to target the drug localization within the nanoclay and, consequently, to control the releasing kinetics of active species from the inner lumen. Thereafter, we also worked on the selective functionalization of halloysite surfaces by exploiting electrostatic interactions between the clay and different polymers. In particular, we used two temperature responsive PNIPAAms in order to create smart nanohybrids. Due to their charges, the negatively charged Poly(N-isopropylacrylamide)-co-methacrylic acid was selectively adsorbed into the halloysite lumen whereas the positively charged amino-terminal PNIPAAm was selectively interacting with the outer surface of the nanotubes. The precise adsorption site, together with the macromolecular transition from a hydrophilic (or swelled) to a hydrophobic (or shrunken) structure typical of the PNIPAAms, allowed to generate thermo-sensitive nanocarriers. Definitely, the PNIPAAms/HNTs hybrids are smart stimuli-responsive systems whose release can be controlled by varying the temperature conditions. The electrostatic interactions between two components have also been exploited for the design of hybrid nanostructures with controlled release properties towards khellin. For this purpose, halloysite nanotubes external surface was coated with chitosan. It was observed that the chitosan coating efficiency is remarkably improved in aqueous medium with higher ionic strength and that this procedure generates the hydrophobization of HNTs surface. Release kinetics of khellin from uncoated and coated nanotubes evidenced that the higher ionic strength improved the coating efficiency, with a delaying effect on the drug exit from the inner

lumen. We can hypothesize that chitosan coating layer onto HNTs is thicker in NaCl solution and, consequently, the controlling efficiency on the khellin release is more effective. We also prepared hydrogel beads based on chitosan with uniformly dispersed halloysite nanotubes and coated with an external layer of alginate. These systems were investigated for application in controlled drug release by using doxycycline, an antibiotic of the tetracycline class, as the model drug. The details of the release profiles highlighted that the halloysite incorporation within the chitosan matrix did not have any profound effect on the release rate but, contrarily to it, the presence of alginate in the alginate/chitosan/HNTs system significantly affected the kinetics by slowing down the drug release from the hybrid beads, thus acting as a highly viscous external barrier. Furthermore, in order to prepare bioplastic with improved mechanical properties, we used Mater-Bi and different nanoclays, namely sepiolite, laponite and halloysite. The analysis of the tensile properties of the nanocomposite films showed that halloysite is the most promising nanoclay in inducing the most significant improvement of the mechanical performances under traction force. Then, the effect of HNTs content was also investigated, showing that the physico-chemical performances of Mater-Bi were improved by the presence of small amounts of nanotubes, which evidenced a homogenous distribution within the polymer matrix. A part of this work was also focused on the design of functional biohybrid nano-engineered materials for health applications. For this purpose, we prepared a tablet-like material by using a composite film made of chitosan with drug loaded embedded halloysite, being the nanocomposite then sandwiched between two alginate layers. In particular, it was found that the presence of the external alginate layers slows down the drug release kinetics and this mechanism is also influenced by the different thickness of the prepared materials. In addition, a simulation of the typical conditions of the human gastro-intestinal path allowed to state that the sandwich like structure of the hybrid tablet is efficient in controlling the drug release with a dependence on the pH conditions of the physiological aqueous medium. Besides, we reported the development of an alternative strategy for the preparation of a new type of multicomponent hybrid nanopaper constituted by the co-assembling in water of cellulose nanofibers, sepiolite and halloysite nanotubes. The main advantage of this choice is represented by the different chemical surfaces that the resulting materials possess and by the homogeneous aspect, flexibility and good mechanical properties of the films. Owing to their hierarchical porosity and to the diverse surface characteristics of the HNTs-SEP-CNF hybrids, *in vitro* antibacterial assays from salicylic acid loaded nanopapers allowed to evaluate their very good antimicrobial activity against *S. aureus* at pH = 5.5, thus confirming their potential employ in controlled delivery and health applications. Finally, we designed a new protocol for the preparation of Pickering emulsions based on halloysite and wax that can be used for the treatment of waterlogged archeological woods. The prepared particles are

spherical and well-shaped and they present nanotubes at the wax/water interface. In particular, HNTs were added to the wax at different concentrations and it was highlighted that the coverage degree strictly depends on the amount of HNTs added during the preparation procedure, the coverage being higher the higher is the concentration of nanoclay. More interestingly, the dimensions of the Pickering emulsion are deeply affected by the clay amount, since they decreased as the nanotubes content increased. The presence of halloysite has also effects on the thermal properties of the paraffin. The Wax/HNTs Pickering emulsions were investigated as consolidants for waterlogged archaeological woods. One of the most important features of the proposed consolidation protocol is its eco-friendliness, being that only water was used as immersion solvent for the wood impregnation. The result of this treatment showed that the consolidation efficiency increased compared to the use of pure wax and, more interestingly, wooden pores and channels appear to be filled by the pickering emulsions. The rigidity and stiffness of the archeological wood were strongly improved. In conclusions, the proposed protocol is encouraging for the durable preservation of waterlogged archaeological woods and it overcomes some limitations regarding the possibility to be scaled up and employed for shipwrecks of big dimensions.

Overall, the sustainability is a key factor throughout this thesis. Several critical issues are addressed by materials with different architectures that can be used for various applications in a wide range of industrial relevant fields.

9. References

- 1 D. Lasrado, S. Ahankari and K. Kar, *Journal of Applied Polymer Science*, 2020, **137**, 48959.
- 2 R. A. Gross and B. Kalra, *Science*, 2002, **297**, 803–807.
- 3 C. Silvestre, D. Duraccio and S. Cimmino, *Progress in Polymer Science*, 2011, **36**, 1766–1782.
- 4 D. S. Cha and M. S. Chinnan, *Crit Rev Food Sci Nutr*, 2004, **44**, 223–237.
- 5 P. Xu, T. Erdem and E. Eiser, *Soft Matter*, 2020, **16**, 5497–5505.
- 6 G. Gorrasi, R. Pantani, M. Murariu and P. Dubois, *Macromolecular Materials and Engineering*, 2014, **299**, 104–115.
- 7 R. D. Silva, P. Pasbakhsh, K. L. Goh, S.-P. Chai and J. Chen, *Journal of Composite Materials*, 2014, **48**, 3705–3717.
- 8 Y. Kojima, A. Usuki, M. Kawasumi, A. Okada, Y. Fukushima, T. Kurauchi and O. Kamigaito, *Journal of Materials Research*, 1993, **8**, 1185–1189.
- 9 E. Ruiz-Hitzky and B. Wicklein, *Advanced Functional Materials*, 2018, **28**, 1803407.
- 10 E. Ruiz-Hitzky, P. Aranda, M. Darder and M. Ogawa, *Chem. Soc. Rev.*, 2011, **40**, 801–828.
- 11 H. Lee, J. Ryu, D. Kim, Y. Joo, S. U. Lee and D. Sohn, *Journal of Colloid and Interface Science*, 2013, **406**, 165–171.
- 12 F. Uddin, *Metallurgical and Materials Transactions A*, 2008, **39**, 2804–2814.
- 13 M. Calabi-Floody, B. Theng and M. L. Mora, *Clay Minerals - CLAY MINER*, 2009, **44**, 161–176.
- 14 S. Jayrajshin, G. Shankar, Y. K. Agrawal and L. Bakre, *Journal of Drug Delivery Science and Technology*, 2017, **39**, 200–209.
- 15 C. Aguzzi, P. Cerezo, C. Viseras and C. Caramella, *Applied Clay Science*, 2007, **36**, 22–36.
- 16 M. I. Carretero, C. S. F. Gomes and F. Tateo, in *Developments in Clay Science*, Elsevier, 2013, vol. 5, pp. 711–764.
- 17 M. Djellali, P. Aranda and E. Ruiz-Hitzky, *Applied Clay Science*, 2019, **171**, 65–73.
- 18 E. Abdullayev, K. Sakakibara, K. Okamoto, W. Wei, K. Ariga and Y. Lvov, *ACS Appl. Mater. Interfaces*, 2011, **3**, 4040–4046.
- 19 J. Tully, R. Yendluri and Y. Lvov, *Biomacromolecules*, 2016, **17**, 615–621.
- 20 E. Joussein, S. Petit, G. J. Churchman, B. Theng, D. Righi and B. Delvaux, *Clay Minerals*, 2005, **40**, 383–426.
- 21 Y. M. Lvov, D. G. Shchukin, H. Mohwald and R. R. Price, *ACS Nano*, 2008, **2**, 814–820.
- 22 M. Du, B. Guo and D. Jia, *Polym. Int.*, 2010, **59**, 574–582.
- 23 P. Sidheswaran, A. N. Bhat and P. Ganguli, *Clays Clay Miner.*, 1990, **38**, 29–32.
- 24 G. Cavallaro, L. Chiappisi, P. Pasbakhsh, M. Gradzielski and G. Lazzara, *Applied Clay Science*, 2018, **160**, 71–80.
- 25 E. Abdullayev, A. Joshi, W. Wei, Y. Zhao and Y. Lvov, *ACS Nano*, 2012, **6**, 7216–7226.
- 26 G. Cavallaro, G. Lazzara, S. Milioto, F. Parisi and V. Sanzillo, *ACS Appl. Mater. Interfaces*, 2014, **6**, 606–612.
- 27 H. Zhang, C. Cheng, H. Song, L. Bai, Y. Cheng, X. Ba and Y. Wu, *Chem. Commun.*, 2019, **55**, 1040–1043.
- 28 G. Cavallaro, I. Grillo, M. Gradzielski and G. Lazzara, *J. Phys. Chem. C*, 2016, **120**, 13492–13502.
- 29 G. I. Fakhruullina, F. S. Akhatova, Y. M. Lvov and R. F. Fakhruullin, *Environ. Sci.: Nano*, 2015, **2**, 54–59.
- 30 G. Lazzara, G. Cavallaro, A. Panchal, R. Fakhruullin, A. Stavitskaya, V. Vinokurov and Y. Lvov, *Current Opinion in Colloid & Interface Science*, 2018, **35**, 42–50.
- 31 H. Wan, H. Xiong, X. Liu, G. Chen, N. Zhang, H. Wang, R. Ma and G. Qiu, *Dalton Trans.*, 2018, **47**, 7522–7527.
- 32 Z. Su, H. Zhang, Y. Gao, L. Huo, Y. Wu and X. Ba, *Chemical Engineering Journal*, 2020, **393**, 124695.
- 33 T. G. Shutava, R. F. Fakhruullin and Y. M. Lvov, *Current Opinion in Pharmacology*, 2014, **18**, 141–148.
- 34 S. Levis and P. Deasy, *Int. J. Pharm.*, 2003, **253**, 145–157.
- 35 B. P. G. R. Price Y. Lvov, R., *Journal of Microencapsulation*, 2001, **18**, 713–722.
- 36 P. Yuan, D. Tan and F. Annabi-Bergaya, *Applied Clay Science*, 2015, **112–113**, 75–93.
- 37 C. Cheng, Y. Gao, W. Song, Q. Zhao, H. Zhang and H. Zhang, *Chemical Engineering Journal*, 2020, **380**, 122474.

- 38 M. R. Dзамukova, E. A. Naumenko, Y. M. Lvov and R. F. Fakhrullin, *Scientific Reports*, 2015, **5**, 10560.
- 39 M. T. Viseras, C. Aguzzi, P. Cerezo, C. Viseras and C. Valenzuela, *Micropor. Mesopor. Mat.*, 2008, **108**, 112–116.
- 40 C. Aguzzi, C. Viseras, P. Cerezo, I. Salcedo, R. Sánchez-Espejo and C. Valenzuela, *Colloids and Surfaces B: Biointerfaces*, 2013, **105**, 75–80.
- 41 S. Sadjadi, F. Koohestani and N. Bahri-Laleh, *Applied Clay Science*, 2020, **192**, 105645.
- 42 S. Lin, Y. Zhang, Y. You, C. Zeng, X. Xiao, T. Ma and H. Huang, *Advanced Functional Materials*, 2019, **29**, 1903825.
- 43 S. Sadjadi, P. Mohammadi and M. Heravi, *Scientific Reports*, 2020, **10**, 6535.
- 44 E. A. Naumenko, I. D. Guryanov, R. Yendluri, Y. M. Lvov and R. F. Fakhrullin, *Nanoscale*, 2016, **8**, 7257–7271.
- 45 B. Huang, M. Liu and C. Zhou, *Carbohydrate Polymers*, 2017, **175**, 689–698.
- 46 B. Huang, M. Liu and C. Zhou, *Cellulose*, 2017, **24**, 2861–2875.
- 47 Y. Zhang, L. Bai, C. Cheng, Q. Zhou, Z. Zhang, Y. Wu and H. Zhang, *Applied Clay Science*, 2019, **182**, 105259.
- 48 K. Ramadass, G. Singh, K. S. Lakhi, M. R. Benzigar, J.-H. Yang, S. Kim, A. M. Almajid, T. Belperio and A. Vinu, *Microporous and Mesoporous Materials*, 2019, **277**, 229–236.
- 49 F. Wu, K. Pickett, A. Panchal, M. Liu and Y. Lvov, *ACS Appl. Mater. Interfaces*, 2019, **11**, 25445–25456.
- 50 E. Emmanuel, L. L. Yong, V. Anggraini and P. Pasbakhsh, *Applied Clay Science*, 2020, **186**, 105441.
- 51 V. Bugatti, G. Viscusi, C. Naddeo and G. Gorrasi, *Nanomaterials*, 2017, **7**, 213.
- 52 G. Cavallaro, S. Milioto, S. Konnova, G. Fakhrullina, F. Akhatova, G. Lazzara, R. Fakhrullin and Y. Lvov, *ACS Appl. Mater. Interfaces*, 2020, **12**, 24348–24362.
- 53 K. Govindasamy, N. A. Dahlan, P. Janarthanan, K. L. Goh, S.-P. Chai and P. Pasbakhsh, *Applied Clay Science*, 2020, **190**, 105601.
- 54 M. Liu, C. Wu, Y. Jiao, S. Xiong and C. Zhou, *J. Mater. Chem. B*, 2013, **1**, 2078–2089.
- 55 V. Bertolino, G. Cavallaro, G. Lazzara, S. Milioto and F. Parisi, *New J. Chem.*, 2018, **42**, 8384–8390.
- 56 T. T. Haw, F. Hart, A. Rashidi and P. Pasbakhsh, *Applied Clay Science*, 2020, **188**, 105533.
- 57 B. Micó-Vicent, F. M. Martínez-Verdú, A. Novikov, A. Stavitskaya, V. Vinokurov, E. Rozhina, R. Fakhrullin, R. Yendluri and Y. Lvov, *Advanced Functional Materials*, 2018, **28**, 1703553.
- 58 E. Abdullayev and Y. Lvov, *J. Mater. Chem.*, 2010, **20**, 6681–6687.
- 59 I. L. Hia, W. H. Lam, S.-P. Chai, E.-S. Chan and P. Pasbakhsh, *Materials Chemistry and Physics*, 2018, **215**, 69–80.
- 60 G. Cavallaro, S. Milioto and G. Lazzara, *Langmuir*, 2020, **36**, 3677–3689.
- 61 G. Cavallaro, S. Milioto, F. Parisi and G. Lazzara, *ACS Appl Mater Interfaces*, 2018, **10**, 27355–27364.
- 62 E. Ruiz-Hitzky, *J. Mater. Chem.*, 2001, **11**, 86–91.
- 63 M. Akkari, P. Aranda, A. Mayoral, M. García-Hernández, A. B. H. Amara and E. Ruiz-Hitzky, *Journal of Hazardous Materials*, 2017, **340**, 281–290.
- 64 J. L. Ahlrichs, C. Serna and J. M. Serratosa, *Clays and Clay Minerals*, 1975, **23**, 119–124.
- 65 P. Aranda, R. Kun, M. A. Martín-Luengo, S. Letaïef, I. Dékány and E. Ruiz-Hitzky, *Chemistry of Materials*, 2008, **20**, 84–91.
- 66 Y. González-Alfaro, P. Aranda, F. M. Fernandes, B. Wicklein, M. Darder and E. Ruiz-Hitzky, *Advanced Materials*, **23**, 5224–5228.
- 67 S. Ragu, E. Dardillac, D. A. Brooks, F. A. Castro-Smirnov, P. Aranda, E. Ruiz-Hitzky and B. S. Lopez, *Applied Clay Science*, 2020, **194**, 105655.
- 68 F. M. Fernandes and E. Ruiz-Hitzky, *Carbon*, 2014, **72**, 296–303.
- 69 R.-H. Eduardo, S. M. M. C, G.-A. Almudena, N. Claudia, R.-G. Cristina, F. Paula and A. Pilar, *Advanced Functional Materials*, 2016, **26**, 7394–7405.
- 70 E. Ruiz-Hitzky, M. Darder, F. M. Fernandes, B. Wicklein, A. C. S. Alcântara and P. Aranda, *Progress in Polymer Science*, 2013, **38**, 1392–1414.
- 71 B. Wicklein, M. Darder, P. Aranda and E. Ruiz-Hitzky, *ACS Appl Mater Interfaces*, 2011, **3**, 4339–4348.
- 72 M. Darder, M. López-Blanco, P. Aranda, A. J. Aznar, J. Bravo and E. Ruiz-Hitzky, *Chem. Mater.*, 2006, **18**, 1602–1610.

- 73 R. Rebelo, M. Fernandes and R. Figueiro, *Procedia Engineering*, 2017, **200**, 236–243.
- 74 H. Zhang and G. Mittal, *Environmental Progress & Sustainable Energy*, 2010, **29**, 203–220.
- 75 R. N. Tharanathan, *Trends Food Sci. Tech.*, 2003, **14**, 71–78.
- 76 G. Mensitieri, E. Di Maio, G. G. Buonocore, I. Nedi, M. Oliviero, L. Sansone and S. Iannace, *Trends in Food Science & Technology*, 2011, **22**, 72–80.
- 77 K. L. Hamner, C. M. Alexander, K. Coopersmith, D. Reishofer, C. Provenza and M. M. Maye, *ACS Nano*, 2013, **7**, 7011–7020.
- 78 V. Bertolino, G. Cavallaro, G. Lazzara, M. Merli, S. Milioto, F. Parisi and L. Sciascia, *Ind. Eng. Chem. Res.*, 2016, **55**, 7373–7380.
- 79 P. R. Chang, Y. Xie, D. Wu and X. Ma, *Carbohydr. Polym.*, 2011, **84**, 1426–1429.
- 80 S. Sarkar, D. Das, P. Dutta, J. Kalita, S. B. Wann and P. Manna, *Carbohydrate Polymers*, 2020, **247**, 116594.
- 81 S. Islam, M. A. R. Bhuiyan and M. N. Islam, *J Polym Environ*, 2017, **25**, 854–866.
- 82 W. P. Silvestre, C. Baldasso and I. C. Tessaro, *Carbohydrate Polymers*, 2020, **247**, 116676.
- 83 N. Gull, S. M. Khan, O. M. Butt, A. Islam, A. Shah, S. Jabeen, S. U. Khan, A. Khan, R. U. Khan and M. T. Z. Butt, *International Journal of Biological Macromolecules*, 2020, **162**, 175–187.
- 84 I. A. Sogias, A. C. Williams and V. V. Khutoryanskiy, *Biomacromolecules*, 2008, **9**, 1837–1842.
- 85 R. Abdeen and N. Salahuddin, *E-Journal of Chemistry*.
- 86 K.-H. Liu, T.-Y. Liu, S.-Y. Chen and D.-M. Liu, *Acta Biomaterialia*, 2008, **4**, 1038–1045.
- 87 E. Grządka, J. Matusiak and E. Godek, *Carbohydrate Polymers*, 2020, **246**, 116634.
- 88 C.-L. Mou, Q.-Z. Deng, J.-X. Hu, L.-Y. Wang, H.-B. Deng, G. Xiao and Y. Zhan, *Journal of Colloid and Interface Science*, 2020, **569**, 307–319.
- 89 S. H. Hong, M. Shin, E. Park, J. H. Ryu, J. A. Burdick and H. Lee, *Advanced Functional Materials*, 2020, **30**, 1908497.
- 90 M. P. Batista, V. S. S. Gonçalves, F. B. Gaspar, I. D. Nogueira, A. A. Matias and P. Gurikov, *International Journal of Biological Macromolecules*, 2020, **156**, 773–782.
- 91 V. Gopinath, S. Saravanan, A. R. Al-Maleki, M. Ramesh and J. Vadivelu, *Biomedicine & Pharmacotherapy*, 2018, **107**, 96–108.
- 92 E. S. Abdel-Halim and S. S. Al-Deyab, *Carbohydrate Polymers*, 2011, **84**, 454–458.
- 93 R. J. Moon, A. Martini, J. Nairn, J. Simonsen and J. Youngblood, *Chem. Soc. Rev.*, 2011, **40**, 3941–3994.
- 94 M. Tavakolian, S. M. Jafari and T. G. M. van de Ven, *Nano-Micro Lett.*, 2020, **12**, 73.
- 95 M. Pääkkö, M. Ankerfors, H. Kosonen, A. Nykänen, S. Ahola, M. Österberg, J. Ruokolainen, J. Laine, P. T. Larsson, O. Ikkala and T. Lindström, *Biomacromolecules*, 2007, **8**, 1934–1941.
- 96 T. Saito, S. Kimura, Y. Nishiyama and A. Isogai, *Biomacromolecules*, 2007, **8**, 2485–2491.
- 97 K. Zhang and H. Liimatainen, *Small*, 2018, **14**, 1801937.
- 98 Y. Habibi, L. A. Lucia and O. J. Rojas, *Chemical Reviews*, 2010, **110**, 3479–3500.
- 99 C. Aulin, G. Salazar-Alvarez and T. Lindstrom, *Nanoscale*, 2012, **4**, 6622–6628.
- 100 J. Li, R. Cha, K. Mou, X. Zhao, K. Long, H. Luo, F. Zhou and X. Jiang, *Advanced Healthcare Materials*, 2018, **7**, 1800334.
- 101 F. Li, E. Mascheroni and L. Piergiovanni, *Packaging Technology and Science*, 2015, **28**, 475–508.
- 102 B. Wicklein, A. Kocjan, G. Salazar-Alvarez, F. Carosio, G. Camino, M. Antonietti and L. Bergström, *Nature nanotechnology*, 2015, **10**, 277–283.
- 103 H. Zhu, Z. Fang, C. Preston, Y. Li and L. Hu, *Energy Environ. Sci.*, 2014, **7**, 269–287.
- 104 H. Nainggolan, S. Gea, E. Bilotti, T. Peijs and S. D. Hutagalung, *Beilstein J. Nanotechnol.*, 2013, **4**, 325–329.
- 105 M. Aldas, E. Rayón, J. López-Martínez and M. P. Arrieta, *Polymers*, 2020, **12**, 226.
- 106 M. Aldas, J. M. Ferri, J. Lopez-Martinez, M. D. Samper and M. P. Arrieta, *Journal of Applied Polymer Science*, 2020, **137**, 48236.
- 107 C. Bastioli, V. Bellotti, L. Del Giudice and G. Gilli, *J Environ Polym Degr*, 1993, **1**, 181–191.
- 108 C. Bastioli, *Polymer Degradation and Stability*, 1998, **59**, 263–272.
- 109 K. E. Borchani, C. Carrot and M. Jaziri, *Composites Part A: Applied Science and Manufacturing*, 2015, **78**, 371–379.

- 110 Y. Fukushima and S. Inagaki, *Journal of Inclusion Phenomena*, 1987, **5**, 473–482.
- 111 G. Kwon, K. Lee, D. Kim, Y. Jeon, U.-J. Kim and J. You, *Journal of Hazardous Materials*, 2020, **398**, 123100.
- 112 K. M. Rao, A. Kumar, M. Suneetha and S. S. Han, *International Journal of Biological Macromolecules*, 2018, **112**, 119–125.
- 113 K. Varaprasad, G. M. Raghavendra, T. Jayaramudu, M. M. Yallapu and R. Sadiku, *Materials Science and Engineering: C*, 2017, **79**, 958–971.
- 114 Z. Wei, J. H. Yang, Z. Q. Liu, F. Xu, J. X. Zhou, M. Zrínyi, Y. Osada and Y. M. Chen, *Advanced Functional Materials*, 2015, **25**, 1352–1359.
- 115 Y. Wang, L. Zhu, H. Zhang, H. Huang and L. Jiang, *Carbohydrate Polymers*, 2020, **241**, 116373.
- 116 S. U. Pickering, *J. Chem. Soc., Trans.*, 1907, **91**, 2001–2021.
- 117 B. M. Kim, S. Qian and H. H. Bau, *Nano Lett.*, 2005, **5**, 873–878.
- 118 Y. Joo, J. H. Sim, Y. Jeon, S. U. Lee and D. Sohn, *Chem. Commun.*, 2013, **49**, 4519–4521.
- 119 S. Wu, M. Qiu, B. Guo, L. Zhang and Y. Lvov, *ACS Sustainable Chemistry & Engineering*, 2017, **5**, 1775–1783.
- 120 M. Massaro, G. Barone, G. Biddeci, G. Cavallaro, F. Di Blasi, G. Lazzara, G. Nicotra, C. Spinella, G. Spinelli and S. Riela, *Journal of Colloid and Interface Science*, 2019, **552**, 236–246.
- 121 D. G. Shchukin, S. V. Lamaka, K. A. Yasakau, M. L. Zheludkevich, M. G. S. Ferreira and H. Mohwald, *J. Phys. Chem. C*, 2008, **112**, 958–964.
- 122 Y. Lvov, W. Wang, L. Zhang and R. Fakhrullin, *Advanced Materials*, 2016, **28**, 1227–1250.
- 123 G. Cavallaro, G. Lazzara and S. Milioto, *J. Phys. Chem. C*, 2012, **116**, 21932–21938.
- 124 P. Clausen, M. Signorelli, A. Schreiber, E. Hughes, C. J. G. Plummer, D. Fessas, A. Schiraldi and J.-A. E. Månson, *J Therm Anal Calorim*, 2009, **98**, 833–841.
- 125 G. Fotie, R. Rampazzo, M. A. Ortenzi, S. Checchia, D. Fessas and L. Piergiovanni, *Polymers*, 2017, **9**, 415.
- 126 B. V. Derjaguin and L. D. Landau, *Acta Physicochim.*, 1941, **14**, 733–762.
- 127 G. Cavallaro, G. Lazzara, S. Milioto and F. Parisi, *Langmuir*, 2015, **31**, 7472–7478.
- 128 N. M. Correa, J. J. Silber, R. E. Riter and N. E. Levinger, *Chem. Rev.*, 2012, **112**, 4569–4602.
- 129 V. Bertolino, G. Cavallaro, G. Lazzara, S. Milioto and F. Parisi, *Langmuir*, 2017, **33**, 3317–3323.
- 130 P. L. Ritger and N. A. Peppas, *Journal of Controlled Release*, 1987, **5**, 23–36.
- 131 Y. Lvov, G. Decher and H. Moehwald, *Langmuir*, 1993, **9**, 481–486.
- 132 S. Morariu, C.-E. Brunchi and M. Bercea, *Ind. Eng. Chem. Res.*, 2012, **51**, 12959–12966.
- 133 M. Fan, Q. Hu and K. Shen, *Carbohydrate Polymers*, 2009, **78**, 66–71.
- 134 E. M. Ahmed, *Journal of Advanced Research*, 2015, **6**, 105–121.
- 135 G. Cavallaro, G. Lazzara and S. Milioto, *Polymer Degradation and Stability*, 2013, **98**, 2529–2536.
- 136 M. Du, B. Guo and D. Jia, *Eur. Polym. J.*, 2006, **42**, 1362–1369.
- 137 S. Farris, L. Introzzi, P. Biagioni, T. Holz, A. Schiraldi and L. Piergiovanni, *Langmuir*, 2011, **27**, 7563–7574.
- 138 W. Yang, Z. Zhao, K. Wu, R. Huang, T. Liu, H. Jiang, F. Chen and Q. Fu, *J. Mater. Chem. C*, 2017, **5**, 3748–3756.
- 139 G. Chantereau, M. Sharma, A. Abednejad, B. M. Neves, G. Sèbe, V. Coma, M. G. Freire, C. S. R. Freire and A. J. D. Silvestre, *ACS Sustainable Chem. Eng.*, 2019, **7**, 14126–14134.
- 140 M. Makaremi, P. Pasbakhsh, G. Cavallaro, G. Lazzara, Y. K. Aw, S. M. Lee and S. Milioto, *ACS Appl. Mater. Interfaces*, 2017, **9**, 17476–17488.
- 141 H. Jiang, Y. Sheng and T. Ngai, *Current Opinion in Colloid & Interface Science*, 2020, **49**, 1–15.
- 142 H. Sun, S. Li, S. Chen, C. Wang, D. Liu and X. Li, *International Journal of Biological Macromolecules*, 2020, **159**, 696–703.
- 143 V. Calabrese, J. C. Courtenay, K. J. Edler and J. L. Scott, *Current Opinion in Green and Sustainable Chemistry*, 2018, **12**, 83–90.
- 144 Y. Zhao, W. Kong, Z. Jin, Y. Fu, W. Wang, Y. Zhang, J. Liu and B. Zhang, *Applied Energy*, 2018, **222**, 180–188.
- 145 G. Cavallaro, G. Lazzara, S. Milioto, F. Parisi and V. Sparacino, *Polymer Degradation and Stability*, 2015, **120**, 220–225.

10. Attached papers



Contents lists available at ScienceDirect

Journal of Colloid and Interface Science

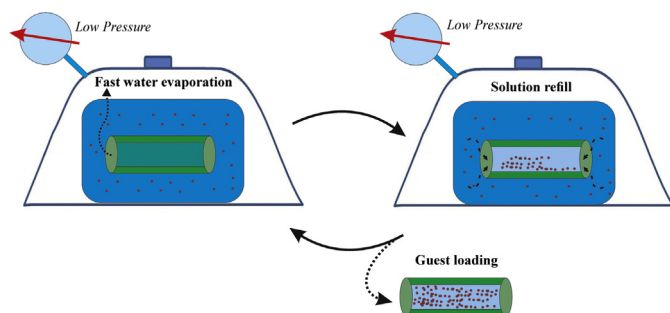
journal homepage: www.elsevier.com/locate/jcis

Regular Article

Why does vacuum drive to the loading of halloysite nanotubes? The key role of water confinement

Lorenzo Lisuzzo^a, Giuseppe Cavallaro^{a,b,*}, Pooria Pasbakhsh^c, Stefana Milioto^{a,b}, Giuseppe Lazzara^{a,b}^a Dipartimento di Fisica e Chimica, Università degli Studi di Palermo, Viale delle Scienze, pad. 17, 90128 Palermo, Italy^b Consorzio Interuniversitario Nazionale per la Scienza e Tecnologia dei Materiali, INSTM, Via G. Giusti, 9, I-50121 Firenze, Italy^c Mechanical Engineering Discipline, School of Engineering, Monash University Malaysia, 47500 Selangor, Malaysia

GRAPHICAL ABSTRACT



ARTICLE INFO

Article history:

Received 8 February 2019

Revised 28 March 2019

Accepted 3 April 2019

Available online 4 April 2019

Keywords:

Halloysite
Nanotubes
Water confinement
Clay nanoparticles
Loading mechanism
Vacuum pumping

ABSTRACT

The filling of halloysite nanotubes with active compounds solubilized in aqueous solvent was investigated theoretically and experimentally. Based on Knudsen thermogravimetric data, we demonstrated the water confinement within the cavity of halloysite. This process is crucial to properly describe the driving mechanism of halloysite loading. In addition, Knudsen thermogravimetric experiments were conducted on kaolinite nanoplates as well as on halloysite nanotubes modified with an anionic surfactant (sodium dodecanoate) in order to explore the influence of both the nanoparticle morphology and the hydrophobic/hydrophilic character of the lumen on the confinement phenomenon. The analysis of the desorption isotherms allowed us to determine the water adsorption properties of the investigated nanoclays. The pore sizes of the nanotubes' lumen was determined by combining the vapor pressure of the confined water with the nanoparticles wettability, which was studied through contact angle measurements. The thermodynamic description of the water confinement inside the lumen was correlated to the influence of the vacuum pumping in the experimental loading of halloysite. Metoprolol tartrate, salicylic acid and malonic acid were selected as anionic guest molecules for the experimental filling of the positively charged halloysite lumen. According to the filling mechanism induced by the water confinement, the vacuum operation and the reduced pressure enhanced the loading of halloysite nanotubes for all the investigated bioactive compounds.

This work represents a further and crucial step for the development of halloysite based nanocarriers being that the filling mechanism of the nanotube's cavity from aqueous dispersions was described according to the water confinement process.

© 2019 Elsevier Inc. All rights reserved.

* Corresponding author.

1. Introduction

The encapsulation of active molecules within the cavity of tubular nanoparticles represents an emerging issue because of its implications on the fundamental sciences and nanotechnologies [1–7]. Literature [2] reports that the filling of carbon nanotubes from aqueous solutions depends on the confinement of water, which exhibits an increase of its boiling temperature. Kim et al. [1] evidenced that the loading of carbon nanotubes is driven by the peculiar evaporation process occurring in the confined space.

Among the nanoparticles with tubular morphology, halloysite nanoclay has attracted a growing interest because of its biocompatibility, geometrical characteristics and peculiar surface properties [8,9]. Due to its high specific surface, halloysite was employed as efficient catalytic support for the deposition of Pd [10,11] and Ag nanoparticles and bimetallic catalysts, such as Cu-Co [12] and AgPd [13]. As concerns the biocompatibility, halloysite nanotubes (HNTs) revealed a low toxicity towards nematodes [14], mice [15] and microorganisms [16,17]. In vitro tests showed that halloysite generates a very low cytotoxicity on human cells, such as endothelial [18] and epithelial [19] cells as well as peripheral blood lymphocytes [20].

As described in a recent review [3], halloysite possess a hollow tubular structure as a consequence of the rolling of kaolinite nanosheets. According to both microscopy [21] and scattering results [22], the geological origin affects the sizes and the corresponding polydispersion degree of halloysite nanotubes. The HNTs length is about 1 μm , while the external and inner diameters are within 20–200 and 10–70 nm, respectively. Halloysite belongs to the mineralogical class of 1:1 phyllosilicates being that the component layers are formed by two sheets with different configuration (one octahedral sheet of alumina and one tetrahedral sheet of silica). As a consequence of the rolling of the sheets [23], the inner and outer surfaces of halloysite possess different chemical composition and opposite charge within a pH range between 2 and 8. Specifically, the alumina internal surface is positively charged, while the silica shell presents a negative charge [24]. Consequently, electrostatic attractive forces between ionic molecules and the charged halloysite surfaces drives to the selective functionalization of the clay nanotubes [25]. As example, the adsorption of sodium alkanoates onto the HNTs inner surfaces generated inorganic tubular micelles with excellent removal ability towards hydrocarbons (both aliphatic and aromatic) [26] as well as organic dyes [25]. It was demonstrated that the peculiar interfaces of halloysite control the self-assembling processes [27,28], the formation of liquid crystals [29] and the preparation of Pickering emulsions [30,31], which can be used for oil spill remediation.

Several studies [32–38] showed that HNTs can be employed as nanocontainers for biologically and chemically active compounds, which are filled within the confined space of the halloysite lumen. The sustained release of the entrapped molecules extends their action time, which can be exploited for specific pharmaceutical, medical and technological purposes [35]. The combination of eco-compatible polymers and loaded HNTs generated composite films with antioxidant [39,40] anticorrosive [34,41] and antimicrobial activities [3,42,43] that are useful for food packaging, protection coatings and tissue engineering.

The most common procedure for the HNTs loading consists of three steps: (1) mixing of the clay dry powder with the saturated solution of the guest molecule; (2) sonication and stirring of the HNTs/guest molecule dispersion; (3) vacuum pumping in/out operation, in which the dispersion is transferred from atmospheric pressure to a vacuum jar. The latter step was introduced with the aim to optimize the amount of active molecules loaded inside the nanotubes by keeping the system under vacuum for 1–5 h and

then cycling it back to atmospheric pressure. Generally, this operation is repeated for 3 times. The first demonstration on the usage of vacuum pumping for an enhancement of the drug loading inside the HNTs cavity is reported by Price et al. [44]. The influence of the vacuum pumping on the filling mechanism of HNTs lumen is still unclear. Macroscopically, we observe a slight fizzing of the HNTs suspension under vacuum. Firstly, this observation was related to the air removal from the HNTs inner space and the consequent promotion of the filling of the drug solution [45–47]. The most recent hypothesis report that the vacuum conditions increase the loading efficiency because of the water removal from the nanotubes occurring during the observed slight fizzing [35].

Here, we explored the loading mechanism by focusing on the unusual thermodynamics of water restrained inside a confined space. According to the Gibbs-Thomson effect [48], the curvature of the HNTs cavity increases the water vapor pressure and, consequently, the evaporation process is faster. Namely, the increase of the vapor pressure is related to the surface/volume ratio, which is enhanced for water confined within the HNTs pores. In general, the dependence of the vapor pressure $P(r)$ of a liquid on the curvature of the pores is expressed by the Kelvin equation

$$P(r) = P^\infty \exp(\gamma/r \cdot \rho \cdot k_B \cdot T) \quad (1)$$

where P^∞ is the vapour pressure of the bulk liquid, γ is the surface tension, r is the pore radius, ρ is the density, k_B is the Boltzmann constant and T is the temperature.

In our previous study [48], the filling of *n*-decane within the hydrophobically modified HNTs was proved by the significant decrease (ca. 40 °C) of the volatilization temperature for the confined hydrocarbon. This finding highlights the relevant effect of the confinement phenomenon on the liquid volatilization and, consequently, on its tendency to move from the HNTs cavity.

Based on these considerations, this work was aimed to (1) demonstrate the water confinement inside the HNTs cavity; (2) provide a clear and unequivocal description of the HNTs filling from aqueous solutions of guest molecules. Accordingly, the attained knowledge could open new routes in the preparation procedure of effective delivery systems based on clay nanotubes.

2. Experimental

2.1. Materials

Halloysite nanotubes (HNTs), kaolinite (Kao), sodium dodecanoate (NaL) and metoprolol tartrate (MT) are Sigma Aldrich products. Salicylic acid (SA) and malonic acid (MA) are from Fluka and Acros Organics, respectively. All the products were used without any purification treatment.

2.2. Hydrophobization of halloysite cavity

Halloysite nanotubes with a hydrophobic cavity were prepared by using the same procedure reported in our previous papers [25,26]. Firstly, we prepared a stable NaL aqueous solution (concentration of 1.25 wt%) by magnetically stirring for 2 h at 20 °C. Then, we added an appropriate amount of halloysite and the obtained dispersion was magnetically stirred for 48 h at 20 °C. Based on the geometrical characteristics of halloysite, the maximum surfactant loading in the cavity is ca. 10 vol%. Therefore, the selected HNT/surfactant ratio (1:1) of the suspension assures the full loading of the halloysite cavity. Afterwards, the dispersion was centrifuged allowing to recover the HNTs/NaL solid material, which was washed three times with water in order to avoid the presence of unbound surfactant. As shown by FESEM images (Fig. 1), the hydrophobization of the HNTs cavity did not alter

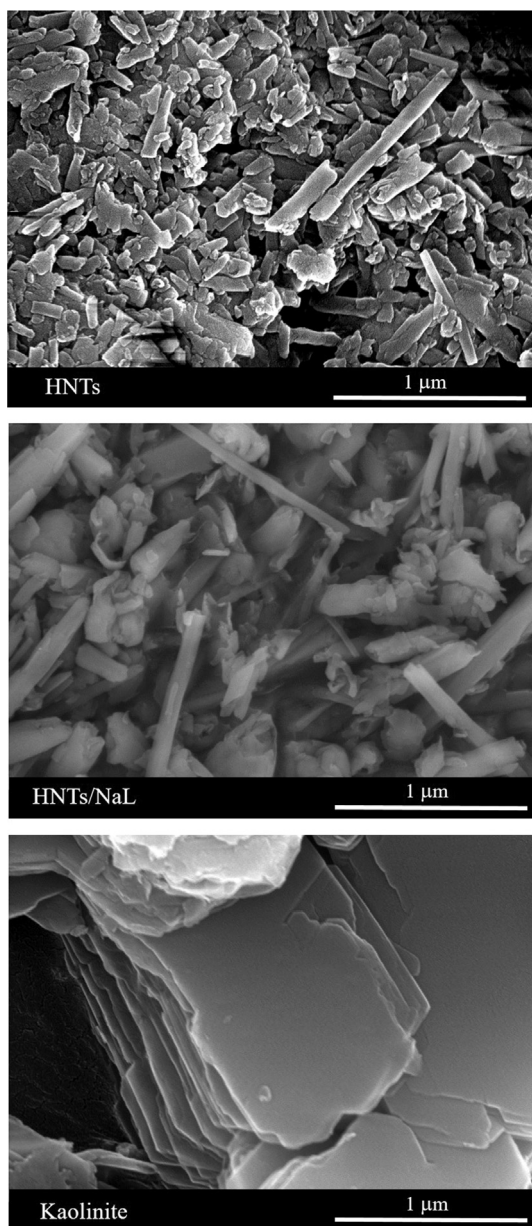


Fig. 1. FESEM images for HNTs, HNTs/NaL and kaolinite.

the hollow tubular shape of halloysite. For comparison, the platy morphology of kaolinite is displayed in FESEM microscopies (Fig. 1).

2.3. Encapsulation of active molecules within halloysite lumen

The encapsulation of the active molecules (metoprolol tartrate, salicylic acid and malonic acid) within the halloysite cavity was performed by aqueous suspensions as described elsewhere [35]. Due to their carboxylate groups, the selected guest molecules can be entrapped within the lumen as a consequence of electrostatic interactions with HNTs inner surface, which is positively charged. Firstly, we prepared saturated solutions of the active compounds in water by magnetically stirring for 2 h at 20 °C. To these solutions, we added a certain amount of halloysite in order to obtain aqueous dispersions with a HNTs/guest molecule ratio of 2:1. The HNTs/drug suspensions were subjected to ultrasonication for 5 min and transferred to a vacuum jar, which allows to reduce

the pressure conditions ($P = 0.01$ atm). The suspensions were kept under reduced pressure for 30 min and, then, the vacuum was broken. The cyclic vacuum pumping in/out procedure was repeated three times. Finally, the dispersions were centrifuged to recover the loaded nanotubes, which were washed three times with water to remove the unbound guest molecules. The obtained nanomaterials were dried and stored in a desiccator at room temperature. Besides the described preparation procedure, the loading of the nanotubes was carried out by keeping the HNTs/guest molecule suspensions at $P = 1$ atm for 90 min. The latter replaced the vacuum pumping in/out cycles. The comparison of the loadings at different pressure ($P = 0.01$ and 1 atm) allowed us to investigate the influence of the vacuum conditions on the filling process. Moreover, we conducted the loading of salicylic acid into kaolinite plates by using the same protocols employed for halloysite.

2.4. Methods

2.4.1. Thermogravimetry

Thermogravimetry (TG) measurements were performed by means of a Q5000 IR apparatus (TA Instruments) under the nitrogen flows of $25 \text{ cm}^3 \text{ min}^{-1}$ and $10 \text{ cm}^3 \text{ min}^{-1}$ for the sample and the balance, respectively. The temperature calibration of the apparatus was conducted on the basis of the Curie temperatures of standards (nickel, cobalt, and their alloys) as reported elsewhere [49]. TG experiments were conducted on HNTs/active molecules and their pure components by heating the samples (ca. 5 mg) from room temperature to 800 °C with a scanning rate of 20 °C min^{-1} . The quantitative analysis of TG data provided the loading through the rule of mixtures [33]. Details on the calculation of the loading amounts of guest molecules are presented in Supporting Information. Moreover, Knudsen thermogravimetry (KTG) tests were conducted in isothermal conditions (temperature was fixed at 30 °C) by replacing the standard open pan with the Knudsen cell, which possesses an orifice with a diameter of 20 μm. In this regards, it should be noted that KTG analysis is a proper method to investigate the interactions between water and nanoclays, as reported for smectite [50]. KTG measurements were conducted on 30 wt% aqueous dispersions of clay samples (kaolinite, HNTs and HNTs/NaL). As shown in Supporting Information, the masses of the highly concentrated suspensions (that corresponds to wet clays) decrease with the time until a constant value, which represents the mass of the dried nanomaterials indicating that the evaporation is complete.

KTG measurements allowed us to study the isothermal water evaporation from wet nanoclays. The mass loss rate (that corresponds to the evaporation velocity) can be expressed as

$$\frac{dm}{dt} = K \cdot (P_{\text{int}} - P_{\text{ext}}) \quad (1)$$

where K is a constant related to the volatile gas, P_{int} is the partial pressure of the water vapor inside the cell and P_{ext} is the external pressure. Due to the small orifice of the Knudsen cell, P_{int} is much larger (at least two order) than P_{ext} and, consequently, the evaporation velocity can be considered proportional to P_{int} . On this basis, we can estimate the evolution of the thermodynamic water activity (a_w) during the evaporation according to the following equation

$$\left(\frac{dm}{dt}\right)_n / \left(\frac{dm}{dt}\right)_w \approx (P_{\text{int}})_n / (P_{\text{int}})_w = a_w \quad (2)$$

being $(dm/dt)_n$ and $(dm/dt)_w$ the mass loss rates for the nanoclay aqueous dispersion and pure water, respectively. It should be noted that $(P_{\text{int}})_w$ represents the relative vapor pressure for pure water, while $(P_{\text{int}})_n$ is the vapor pressure of water contained in the nanoclay dispersion.

Based on the KTG data analysis, we investigated the effect of the nanoparticles morphology on the relative vapor pressure of water evaporated from wet nanoclays.

2.4.2. Water contact angle

Water contact angle tests were conducted on HNTs, HNTs/NaL and kaolinite by using an optical contact angle apparatus (OCA 20, Data Physics Instruments) equipped with a video measuring system having a high-resolution CCD camera and a high-performance digitizing adapter. Data acquisition was conducted by SCA 20 software (Data Physics Instruments). The contact angle (θ) of water in air was detected through the sessile drop method by placing a water droplet of 10 ± 0.5 mL onto the surface of nanoclay tablets. The measurements were conducted at 30.0 ± 0.1 °C. Images were collected 50 times per second, starting from the deposition of the drop to 6 s. The evolution of the water contact angle on time was fitted by an empiric approach based on the following equation [51]

$$\theta = \theta_i \cdot \exp(-k_0 \cdot t^n) \quad (3)$$

where θ_i corresponds to the initial contact angle, k_0 and n are characteristic coefficients related to the kinetics and the mechanism of the process. Specifically, n ranges between 0 and 1 on dependence of the absorption and spreading contributions to the kinetic θ evolution.

2.4.3. Field emission scanning electron microscopy (FESEM)

FESEM experiments were carried out by means of FE-SEM, Hitachi SU8010 microscope. To prevent electrostatic charging during observation, the samples were coated with a thin layer of platinum.

3. Results and discussion

3.1. Thermodynamics of water evaporation from nanoclay aqueous dispersions: Knudsen thermogravimetry

The thermodynamics of water evaporation from halloysite nanotubes and platy-like kaolinite was explored by KTG experiments in order to investigate the effect of the nanoclay morphology on the vapor pressure of the evaporating water. Based on the KTG data analysis, we determined the dependence of the water evaporation rate on the moisture content (M_w) of the nanoclays for HNTs, HNTs/NaL and kaolinite dispersions (Fig. 2). It should be noted that M_w was calculated from the mass ratio between water and dry nanoclay. The trends in Fig. 2 allows to classify the evaporating water in three categories: (1) bulk water ($(dm/dt)_n/(dm/dt)_w = 1$); (2) confined water ($(dm/dt)_n/(dm/dt)_w > 1$); (3) adsorbed water ($(dm/dt)_n/(dm/dt)_w < 1$). It should be noted that halloysite possesses two interlayer water molecules per formula unit. The evaporation of the interlayer water cannot be detected by KTG experiments being that their expulsion from halloysite structure occurs at ca. 500 °C [23].

3.1.1. Water confinement within the halloysite nanotubes cavity

As concerns both pure and surfactant modified halloysite (Fig. 2), a large content (ca. 25 wt%) of evaporating water presents $(dm/dt)_n/(dm/dt)_w > 1$, which means that its vapor pressure is greater than that of bulk water. This result can be attributed to the confinement of water within the nanotube's cavity in agreement with the Gibbs-Thomson effect [52]. Due to its higher vapor pressure, the water confined inside the nanotubes' cavity can evaporate faster than the bulk water. The difference of the water evaporation rate represents the main driving force for the filling of HNTs cavity through aqueous dispersions. Interestingly, we observed that the surfactant hydrophobization of the halloysite lumen does not alter the water confinement. On this basis, we can assert that the chemical composition of the HNTs inner surface does not influence the confinement process. Contrary to halloysite

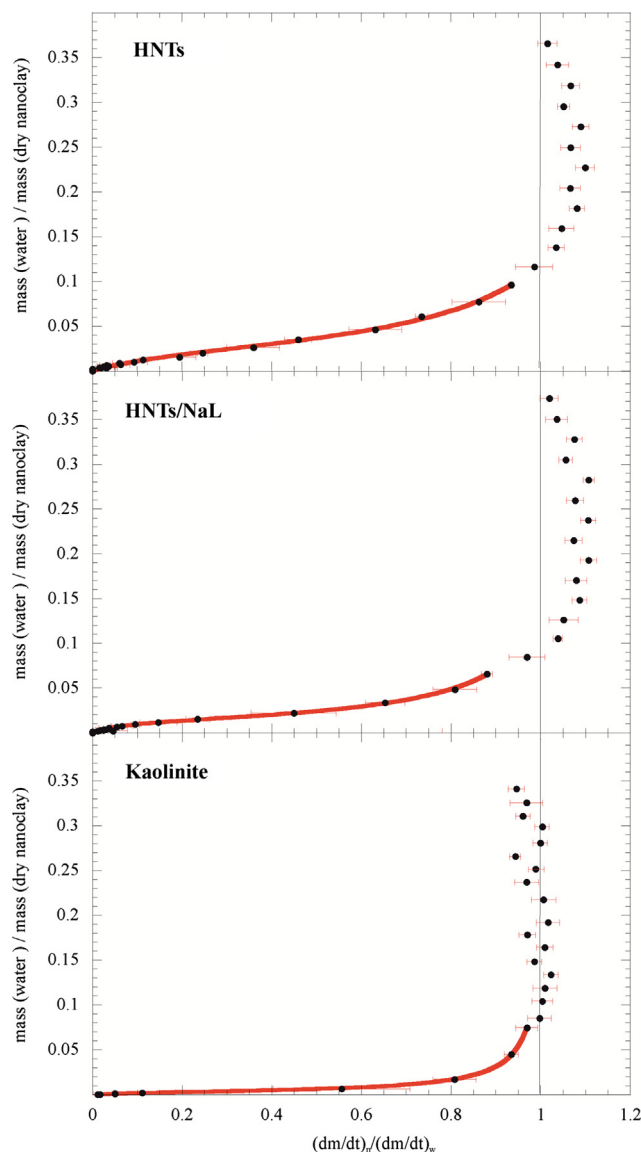


Fig. 2. Mass loss rates for the nanoclay aqueous dispersions normalized for pure water evaporation as a function of the mass ratio between water and dry nanoclay. The experimental data in water activity range between 0.05 and 0.95 were fitted according to GAB model (red solid line).

nanotubes, the water evaporated from kaolinite dispersion possesses $(dm/dt)_n/(dm/dt)_w \leq 1$ within the entire evaporation process (Fig. 2) evidencing that the platy morphology did not provide any confinement site for the aqueous solvent. As sketched in Fig. 3, we can conclude that the water confinement is totally related to the geometrical characteristics of the nanoclay particles.

3.1.2. Water adsorption onto nanoclay surfaces

Water molecules with $(dm/dt)_n/(dm/dt)_w < 1$ are related to the isothermal desorption from the nanoclays surfaces occurring during the evaporation process. As shown in Fig. 2, the desorption isotherms were successfully fitted by using the Guggenheim-Anderson-de Boer (GAB) model [53], which is expressed by the following equation

$$M_w = (M_0 \cdot C \cdot K \cdot a_w) / [(1 - K \cdot a_w) / (1 - K \cdot a_w + C \cdot K \cdot a_w)] \quad (4)$$

where M_0 is the monolayer moisture content, while C and K are adsorption constants associated to the monolayer and the upper multilayers, respectively.

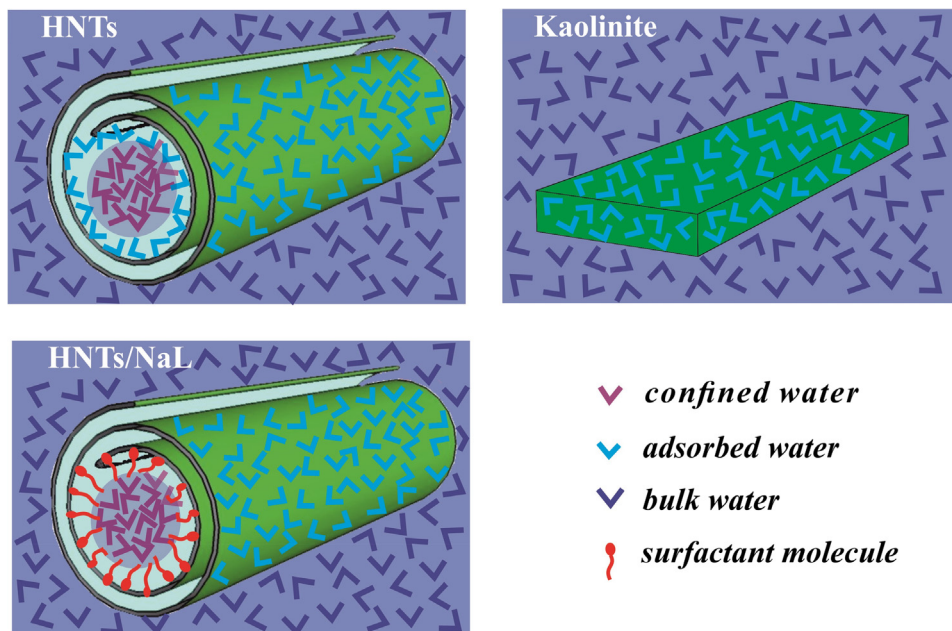


Fig. 3. Schematic representation of the water confinement process within clay nanoparticles. The comparison between halloysite nanotubes and platy kaolinite.

It should be noted that the GAB equation is valid for $0.05 \leq a_w \leq 0.95$. The suitability of GAB model for the experimental desorption isotherms was proved by the K values, which range between 0 and 1 as requested for the validation of this approach.

Table 1 collects the adsorption parameters calculated for HNTs, HNTs/NaL and kaolinite.

Regarding the monolayer moisture content, we detected that M_0 of kaolinite is much lower compared to those of both pure and modified HNTs. Based on M_0 values, the specific surface area (SSA) for water sorption can be determined as [54] (see Table 2)

$$SSA = (M_0 \cdot N_A \cdot A_w) / MM_w \quad (5)$$

being N_A the Avogadro number, whereas A_w and MM_w are the surface area and the molecular weight of water, respectively. According to the morphological characteristics, kaolinite possesses a smaller SSA respect to that of halloysite. Namely, the rolling of kaolinite plates into halloysite nanotubes generates an enhancement of the surface area because of geometrical considerations.

The surfactant modification of halloysite inner surface determined a SSA decrease that cannot be ascribed to morphological variations. As displayed by FESEM micrographs (Fig. 1), HNTs/NaL preserves the hollow tubular morphology of HNTs and the sizes of pure and modified halloysite are comparable. On the other hand, the SSA reduction can be attributed to changes on the chemical composition of halloysite inner surface. Specifically, pristine HNTs possess a hydrophilic lumen that allows for the water adsorption onto the internal surface. In contrast, water molecules cannot be adsorbed within the hydrophobically modified cavity of HNTs/NaL. HNTs exhibits two hydrophilic adsorption sites (outer and inner surfaces), while the water sorption is limited to the HNTs/NaL outer shell. As concerns the adsorption constants, we calcu-

Table 1
GAB fitting parameters for the water desorption from nanoclays.

Nanoclay	M_0	K	C
HNTs	$(2.72 \pm 0.11) \cdot 10^{-2}$	0.78 ± 0.01	7.1 ± 0.7
HNTs/NaL	$(1.46 \pm 0.03) \cdot 10^{-2}$	0.885 ± 0.007	15.1 ± 1.2
Kaolinite	$(0.37 \pm 0.09) \cdot 10^{-2}$	0.979 ± 0.001	7 ± 2

Table 2

Specific surface area of the nanoclays determined by the fitting of water desorption isotherms.

Nanoclay	SSA/m ² g ⁻¹
HNTs	96 ± 4
HNTs/NaL	51.9 ± 1.3
Kaolinite	13.4 ± 0.3

lated C values larger than K for all the nanoclays highlighting that the adsorption heat of the first water layer is higher respect to that of the multilayers [55]. This difference was enhanced by the hydrophobization of the HNTs cavity. As general result, the desorption isotherms can be classified as type III being that C is larger than 2 [53].

3.2. Wettability of nanoclays

The wettability properties of HNTs, HNTs/NaL and kaolinite were investigated by water contact angle experiments. Fig. 4a shows the images of the water droplets just after their deposition on the nanoclay surface. According to their chemical composition, kaolinite and HNTs exhibited a hydrophilic surface as demonstrated by their θ_i values (30.1 and 30.7° , respectively). Interestingly, the hydrophobization of the HNTs cavity did not alter the hydrophilic behavior of the halloysite surface in agreement with the selective adsorption of the anionic NaL inside the lumen. Similar results were detected for HNTs modified with negatively charged polymers, such as polystyrene sulfonate [27].

Additional information on the interactions between water and nanoclay surface were obtained by the analysis of the kinetic evolution of the water contact angle. As displayed in Fig. 4b for HNTs, the θ vs t trends were successfully fitted by the Eq. (1) providing the kinetic constant and the n exponential parameter, which are collected in Table 3.

The goodness of the Eq. (1) as model fitting for the θ vs t functions was proved by the n values, which range between 0 and 1 indicating that the kinetic evolution of the contact angle is affected by both the absorption and the spreading of water onto

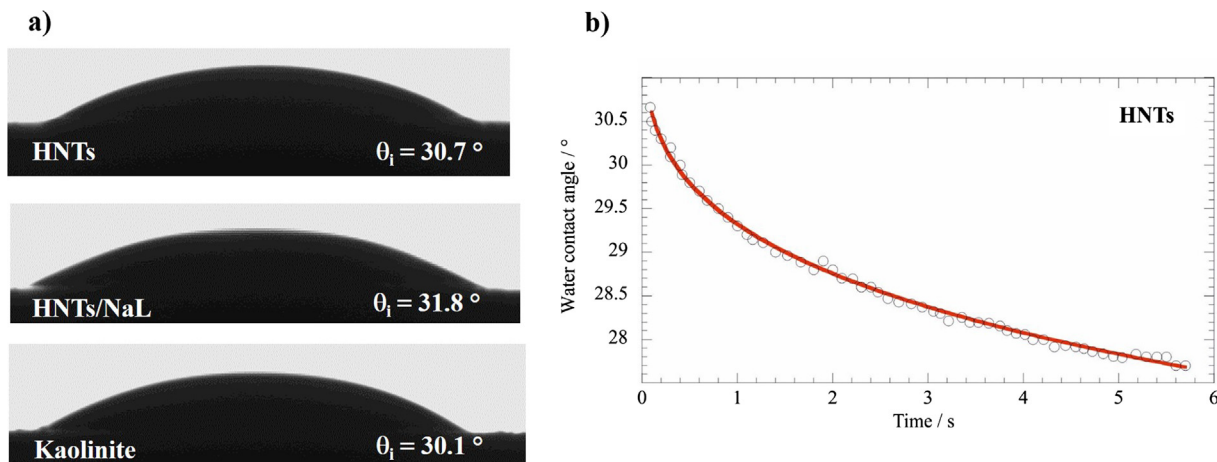


Fig. 4. (a) Images of the water droplets just after their deposition on the surface of HNTs, HNTs/NaL and kaolinite. The corresponding θ_i are reported. (b) The water contact angle as a function of time for HNTs. The solid red line represents the fitting based on the Eq. (3).

Table 3
Fitting parameters on the kinetic evolution of the water contact angle.

Nanoclay	k_0/s^{-1}	n
HNTs	0.087 ± 0.009	0.28 ± 0.02
HNTs/NaL	0.036 ± 0.003	0.65 ± 0.02
Kaolinite	0.063 ± 0.011	0.82 ± 0.06

the nanoclay surface. The presence of NaL within the HNTs lumen generated a decrease of the process rate and an enhancement of the spreading contribution, which is evidenced by the n reduction.

The combination of the water contact angle with Knudsen thermogravimetry data allowed us to estimate the cavity radius (r_c) of HNTs and HNTs/NaL. According to the La Place-Kelvin equation, r_c can be calculated by θ_i and the ratio between the vapor pressure of confined water (P) and bulk water (P°) as

$$r_c = (2 \cdot \gamma_w \cdot V_w \cdot \cos(\theta_i)) / (R \cdot T \cdot \ln(P/P^\circ)) \quad (5)$$

where γ_w and V_w are the surface tension and the molar volume of water, T is the temperature and R is the ideal gas constant.

Based on the KTG analysis (Fig. 1), the confinement process within the halloysite lumen was proved by the detection of evaporating water molecules with $(dm/dt)_n / (dm/dt)_w > 1$. Assuming that P/P° corresponds to the largest $(dm/dt)_n / (dm/dt)_w$ value, $r_c = 9.0 \pm 0.2$ and 11.7 ± 0.2 nm were calculated for HNTs and HNTs/NaL, respectively. These results are consistent with the structural investigations of halloysite nanotubes reported in literature [21,22].

3.3. The effect of the vacuum pumping on the guest molecules loading within HNTs cavity

We investigated the effect of the pressure conditions on the loading efficiency of HNTs towards several bioactive compounds including metoprolol tartrate (MT), salicylic acid (SA) and malonic acid (MA). In particular, the filling of HNTs lumen was conducted by aqueous solutions of the guest molecules exposed at ambient pressure ($P = 1$ atm) as well as under forced reduced pressure ($P = 0.01$ atm). The amount of active molecules loaded into the HNTs cavity was determined through thermogravimetry. Fig. 5a compares the thermogravimetric curves of pristine halloysite and HNTs filled with malonic acid.

As expected, the presence of the active molecules generated a decrease of the residual mass at high temperature because the organic moiety thermally decomposes in the range from 200 to

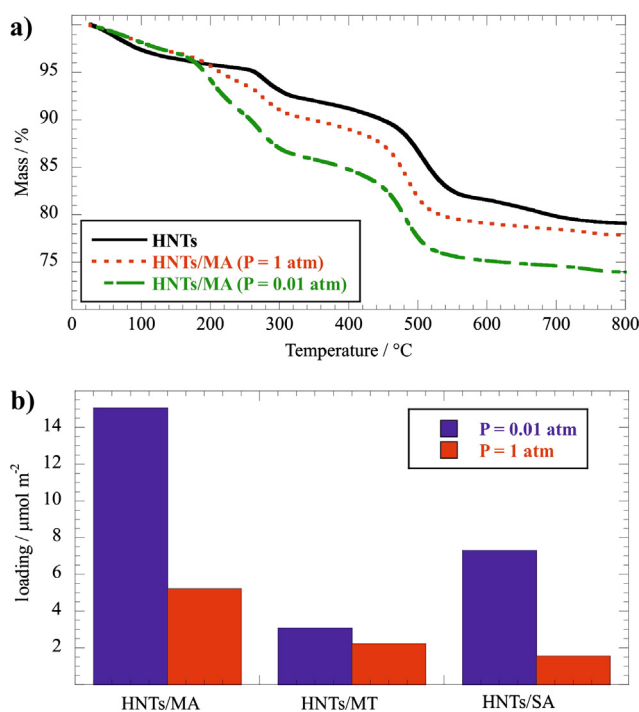


Fig. 5. (a) Thermogravimetric curves for HNTs and HNTs loaded with malonic. (b) Loadings for HNTs filled with malonic acid, metoprolol tartrate and salicylic acid.

400 °C (see Supporting Information). The nanotubes loaded under vacuum exhibited a lower residual matter with respect to that prepared at ambient pressure highlighting the better loading efficiency at reduced pressure. As reported elsewhere [33], we calculated the amount of active molecules encapsulated inside HNTs by using the rule of mixtures on the residual masses at 800 °C.

Table 4
Mass percentages of the guest molecules filled into halloysite nanotubes.

Hybrid nanomaterial	Loading/wt%	
	P = 1 atm	P = 0.01 atm
HNTs/MA	2.52 ± 0.12	7.3 ± 0.3
HNTs/MT	2.77 ± 0.13	3.84 ± 0.19
HNTs/SA	1.01 ± 0.07	4.7 ± 0.2

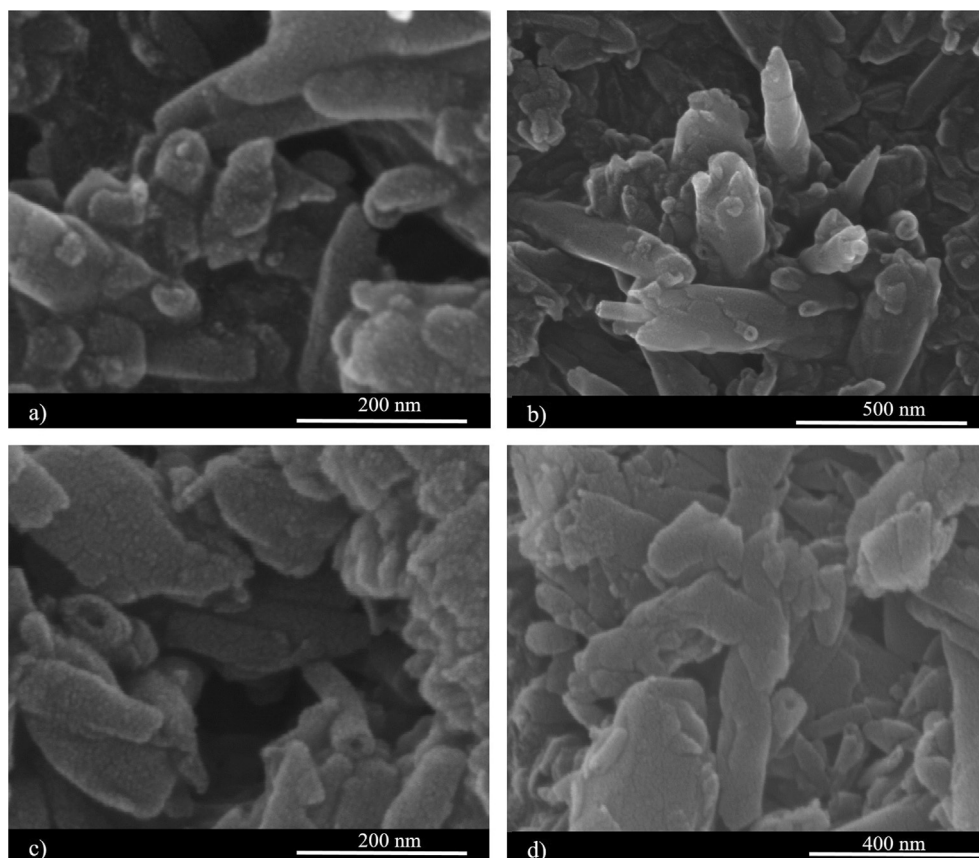
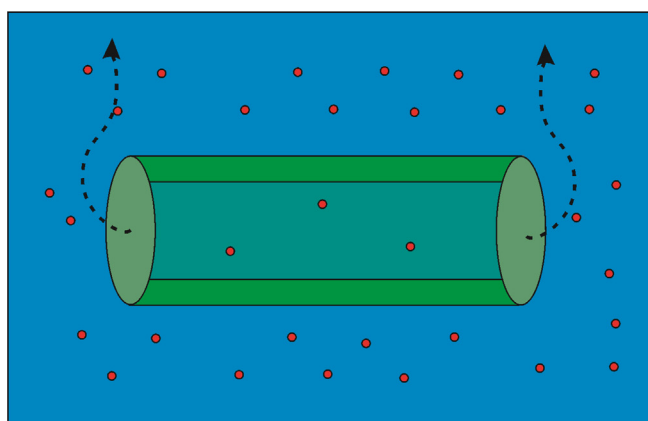


Fig. 6. FESEM images for HNTs/MA prepared at $P = 0.01$ atm (a,b) and 1 atm (c,d).

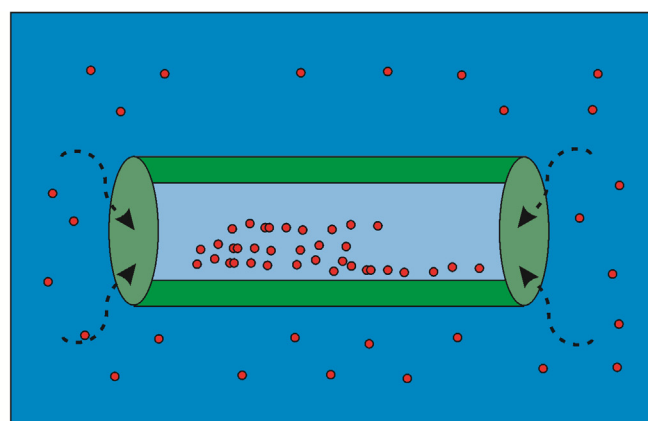
Fig. 5b presents the loading results as surface molar coverage (μmol of guest molecule per m^2 of halloysite surface), while Table 4 collects the mass percentages of the guest molecules in HNTs based hybrids. It should be noted that the active molecules possess anionic carboxylate groups in their chemical structure. Accordingly, the loading process is favored by the attractive interactions between the guest molecules and the halloysite inner surface, which is positively charged.

As a general result, an enhancement of the loading efficiency was determined by the reduction of the pressure confirming that the vacuum favors the filling of the HNTs cavity. In detail, the amount of guest molecule incorporated within the nanotubes

increased by 38, 188 and 369% for MT, MA and SA, respectively. Contrary to these results, the loading capacity of kaolinite was slightly affected by the pressure conditions in agreement with its platy morphology. As shown in Supporting Information, we detected similar thermogravimetric curves for kaolinite/SA samples prepared at different pressure. In particular, the residual matter at 800°C was not significantly altered by vacuum application and, consequently, similar SA loadings (0.45 and 0.62 wt% for the hybrids prepared at $P = 1$ and 0.01 atm, respectively) were estimated through the rule of mixtures. Morphological investigations of loaded HNTs confirmed that a lower pressure increases the filling of the halloysite lumen. In this regards, Fig. 6 shows FESEM



Water evaporation from the lumen is faster



Aqueous solution refills the lumen and guest accumulates

Fig. 7. Schematic representation on the filling process of halloysite nanotubes.

images of HNTs/MA samples prepared at different pressure conditions.

As a general result, the loading did not significantly modify the halloysite tubular morphology. Halloysite loaded at $P = 0.01$ atm (Fig. 6a,b) evidenced several nanotubes fully closed with some spherical nanoparticles at the lumen gate as a consequence of the MA filling. This peculiarity was not observed for HNTs/MA prepared at $P = 1$ atm (Fig. 6c,d). Namely, halloysite filled at ambient pressure preserved the hollow cavity indicating a lower loading efficiency.

The influence of the pressure conditions on the loading of halloysite is strictly correlated to the water confinement within HNTs cavity proved by Knudsen thermogravimetry. As sketched in Fig. 7, the filling of the HNTs cavity is due to the different volatility of confined and bulk water. The fraction of water confined into the lumen possess a larger vapor pressure compared to that of the bulk water generating a difference in the evaporation rate. Based on KTG measurements at 30°C , confined water presents a vapor pressure equals to 0.0460 ± 0.0008 atm, which is 12% larger than that of bulk water (0.0419 atm) and, consequently, a flux of water from the bulk phase to the confined part is needed to compensate the different evaporation velocity and to refill the lumen. Namely, the faster evaporation of the confined water determines a flux of the aqueous solution within the HNTs cavity and a consequent enrichment of the entrapped guest molecules. Then, the evaporation of aqueous solvent causes the precipitation of the active molecules within the HNTs lumen. The replacement of the aqueous solution inside the halloysite lumen is facilitated under low-pressure conditions because the water vapor pressure is approaching. Consequently, the solvent volatilization rate increases.

4. Conclusions

This work represents the first thermodynamic demonstration of the water confinement within the cavity of halloysite nanotubes (HNTs). The water confinement was not observed in kaolinite nanosheets, while this process occurred in HNTs/sodium dodecanoate hybrid highlighting that water molecules can be confined within halloysite nanotubes with a hydrophobically modified cavity. The thermodynamic evidence of the water confinement is the starting point for a proper description of the loading mechanism of HNTs cavity from aqueous solutions of guest molecules. Compared to the bulk water, the confined fraction exhibits a larger vapor pressure and, consequently, a faster evaporation rate that can be attributed to the Gibbs-Thomson effect. During the water evaporation, the guest molecules precipitate inside the cavity and fresh aqueous solution from bulk phase migrates to the halloysite lumen. This phenomenon is favored by vacuum pumping once that vapor pressure of the solvent is approached. The latter was experimentally proved by loading three different guest molecules with anionic carboxylate groups, which can interact with the positive HNT internal surface because of electrostatic attractions. In this regards, we observed that the vacuum pumping operation induces relevant increases on the loading efficiency of halloysite nanotubes. The amount of salicylic acid filled into the HNTs lumen was enhanced by 369% as a consequence of the cyclic vacuum pumping in/out procedure. In contrast, the loading capacity of kaolinite nanosheets was not significantly altered by vacuum application.

In conclusion, this study describes the physico-chemical aspects of halloysite filling, which is controlled by water confinement within the nanotubes' cavity. The attained knowledge represents a fundamental step for the development of loading protocols into confined spaces of tubular nanoparticles.

Acknowledgements

The work was financially supported by Progetto di ricerca e sviluppo "AGM for CuHe" (ARS01_00697) and University of Palermo.

Appendix A. Supplementary material

Supplementary data to this article can be found online at <https://doi.org/10.1016/j.jcis.2019.04.012>.

References

- [1] B.M. Kim, S. Qian, H.H. Bau, Filling carbon nanotubes with particles, *Nano Lett.* 5 (5) (2005) 873–878, <https://doi.org/10.1021/nl050278v>.
- [2] V.V. Chaban, O.V. Prezhdo, Water boiling inside carbon nanotubes: toward efficient drug release, *ACS Nano* 5 (7) (2011) 5647–5655, <https://doi.org/10.1021/nn201277a>.
- [3] G. Lazzara, G. Cavallaro, A. Panchal, R. Fakhruddin, A. Stavitskaya, V. Vinokurov, Y. Lvov, An assembly of organic-inorganic composites using halloysite clay nanotubes, *Curr. Opin. Colloid Interface Sci.* 35 (2018) 42–50, <https://doi.org/10.1016/j.cocis.2018.01.002>.
- [4] S. Wu, M. Qiu, B. Guo, L. Zhang, Y. Lvov, Nanodot-loaded clay nanotubes as green and sustained radical scavengers for elastomer, *ACS Sustain. Chem. Eng.* 5 (2) (2017) 1775–1783, <https://doi.org/10.1021/acssuschemeng.6b02523>.
- [5] Y. Joo, J.H. Sim, Y. Jeon, S.U. Lee, D. Sohn, Opening and blocking the inner-pores of halloysite, *Chem. Commun.* 49 (40) (2013) 4519–4521, <https://doi.org/10.1039/C3CC40465j>.
- [6] Z. Zhuang, W. Chen, Ultra-low loading of Pd5 nanoclusters on carbon nanotubes as bifunctional electrocatalysts for the oxygen reduction reaction and the ethanol oxidation reaction, *J. Colloid Interface Sci.* 538 (2019) 699–708, <https://doi.org/10.1016/j.jcis.2018.12.015>.
- [7] Y.-D. Yu, Y.-J. Zhu, C. Qi, Y.-Y. Jiang, H. Li, J. Wu, Hydroxyapatite nanorod-assembled porous hollow polyhedra as drug/protein carriers, *J. Colloid Interface Sci.* 496 (2017) 416–424, <https://doi.org/10.1016/j.jcis.2017.02.041>.
- [8] L. Jiang, Y. Huang, T. Liu, Enhanced visible-light photocatalytic performance of electrospun carbon-doped TiO₂/halloysite nanotube hybrid nanofibers, *J. Colloid Interface Sci.* 439 (2015) 62–68, <https://doi.org/10.1016/j.jcis.2014.10.026>.
- [9] F. Liu, L. Bai, H. Zhang, H. Song, L. Hu, Y. Wu, X. Ba, Smart H₂O₂-responsive drug delivery system made by halloysite nanotubes and carbohydrate polymers, *ACS Appl. Mater. Interfaces* 9 (37) (2017) 31626–31633, <https://doi.org/10.1021/acsmi.7b10867>.
- [10] S. Sadjadi, M.M. Heravi, M. Malmir, Pd@HNTs-CDNS-g-C₃N₄: a novel heterogeneous catalyst for promoting ligand and copper-free sonogashira and heck coupling reactions, benefits from halloysite and cyclodextrin chemistry and g-C₃N₄ contribution to suppress Pd leaching, *Carbohydr. Polym.* 186 (2018) 25–34, <https://doi.org/10.1016/j.carbpol.2018.01.023>.
- [11] S. Sadjadi, M.M. Heravi, S.S. Kazemi, Ionic liquid decorated chitosan hybridized with clay: a novel support for immobilizing Pd nanoparticles, *Carbohydr. Polym.* 200 (2018) 183–190, <https://doi.org/10.1016/j.carbpol.2018.07.093>.
- [12] Y. Liu, J. Zhang, H. Guan, Y. Zhao, J.-H. Yang, B. Zhang, Preparation of bimetallic Cu-Co nanocatalysts on poly (diallyldimethylammonium chloride) functionalized halloysite nanotubes for hydrolytic dehydrogenation of ammonia borane, *Appl. Surf. Sci.* 427 (2018) 106–113, <https://doi.org/10.1016/j.apsusc.2017.08.171>.
- [13] Y. Liu, H. Guan, J. Zhang, Y. Zhao, J.-H. Yang, B. Zhang, Polydopamine-coated halloysite nanotubes supported AgPd nanoalloy: an efficient catalyst for hydrolysis of ammonia borane, *Int. J. Hydrogen Energy* 43 (5) (2018) 2754–2762, <https://doi.org/10.1016/j.ijhydene.2017.12.105>.
- [14] G.I. Fakhruddina, F.S. Akhatova, Y.M. Lvov, R.F. Fakhruddin, Toxicity of halloysite clay nanotubes in vivo: a caenorhabditis elegans study, *Environ. Sci. Nano* 2 (1) (2015) 54–59, <https://doi.org/10.1039/C4EN00135D>.
- [15] X. Wang, J. Gong, R. Rong, Z. Gui, T. Hu, X. Xu, Halloysite nanotubes-induced AI accumulation and fibrotic response in lung of mice after 30-day repeated oral administration, *J. Agric. Food Chem.* 66 (11) (2018) 2925–2933, <https://doi.org/10.1021/acs.jafc.7b04615>.
- [16] G. Cavallaro, G. Lazzara, S. Milioto, F. Parisi, V. Evtugyn, E. Rozhina, R. Fakhruddin, Nanohydrogel formation within the halloysite lumen for triggered and sustained release, *ACS Appl. Mater. Inter.* 10 (9) (2018) 8265–8273, <https://doi.org/10.1021/acsmi.7b19361>.
- [17] M. Makaremi, P. Pasbakhsh, G. Cavallaro, G. Lazzara, Y.K. Aw, S.M. Lee, S. Milioto, Effect of morphology and size of halloysite nanotubes on functional pectin bionanocomposites for food packaging applications, *ACS Appl. Mater. Inter.* 9 (20) (2017) 17476–17488, <https://doi.org/10.1021/acsmi.7b04297>.
- [18] E. Tarasova, E. Naumenko, E. Rozhina, F. Akhatova, R. Fakhruddin, Cytocompatibility and uptake of polycations-modified halloysite clay nanotubes, *Appl. Clay Sci.* 169 (2019) 21–30, <https://doi.org/10.1016/j.clay.2018.12.016>.
- [19] F.R. Ahmed, M.H. Shoaib, M. Azhar, S.H. Um, R.I. Yousuf, S. Hashmi, A. Dar, In-vitro assessment of cytotoxicity of halloysite nanotubes against HepG2, HCT116 and human peripheral blood lymphocytes, *Colloids Surf. B*

- Biointerfaces 135 (2015) 50–55, <https://doi.org/10.1016/j.colsurfb.2015.07.021>.
- [20] V. Vergaro, E. Abdullayev, Y.M. Lvov, A. Zeitoun, R. Cingolani, R. Rinaldi, S. Leporatti, Cytocompatibility and uptake of halloysite clay nanotubes, *Biomacromolecules* 11 (3) (2010) 820–826, <https://doi.org/10.1021/bm9014446>.
- [21] P. Pasbakhsh, G.J. Churchman, J.L. Keeling, Characterisation of properties of various halloysites relevant to their use as nanotubes and microfibre fillers, *Appl. Clay Sci.* 74 (2013) 47–57, <https://doi.org/10.1016/j.clay.2012.06.014>.
- [22] G. Cavallaro, L. Chiappisi, P. Pasbakhsh, M. Gradzielski, G. Lazzara, A structural comparison of halloysite nanotubes of different origin by small-angle neutron scattering (SANS) and electric birefringence, *Appl. Clay Sci.* 160 (2018) 71–80, <https://doi.org/10.1016/j.clay.2017.12.044>.
- [23] E. Joussein, S. Petit, G.J. Churchman, B. Theng, D. Righi, B. Delvaux, Halloysite clay minerals—a review, *Clay Miner.* 40 (4) (2005) 383–426.
- [24] H. Zhang, T. Ren, Y. Ji, L. Han, Y. Wu, H. Song, L. Bai, X. Ba, Selective modification of halloysite nanotubes with 1-pyrenylboronic acid: a novel fluorescence probe with highly selective and sensitive response to hyperoxide, *ACS Appl. Mater. Interfaces* 7 (42) (2015) 23805–23811, <https://doi.org/10.1021/acsami.5b08600>.
- [25] G. Cavallaro, I. Grillo, M. Gradzielski, G. Lazzara, Structure of hybrid materials based on halloysite nanotubes filled with anionic surfactants, *J. Phys. Chem. C* 120 (25) (2016) 13492–13502, <https://doi.org/10.1021/acs.jpcc.6b01282>.
- [26] G. Cavallaro, G. Lazzara, S. Milioto, F. Parisi, V. Sanzillo, Modified halloysite nanotubes: nanoarchitectures for enhancing the capture of oils from vapor and liquid phases, *ACS Appl. Mater. Interfaces* 6 (1) (2014) 606–612, <https://doi.org/10.1021/am404693r>.
- [27] Y. Zhao, G. Cavallaro, Y. Lvov, Orientation of charged clay nanotubes in evaporating droplet meniscus, *J. Colloid Interface Sci.* 440 (2015) 68–77, <https://doi.org/10.1016/j.jcis.2014.10.050>.
- [28] M. Liu, Z. Huo, T. Liu, Y. Shen, R. He, C. Zhou, Self-assembling halloysite nanotubes into concentric ring patterns in a sphere-on-flat geometry, *Langmuir* 33 (12) (2017) 3088–3098, <https://doi.org/10.1021/acs.langmuir.6b04460>.
- [29] Z. Luo, H. Song, X. Feng, M. Run, H. Cui, L. Wu, J. Gao, Z. Wang, Liquid Crystalline phase behavior and sol-gel transition in aqueous halloysite nanotube dispersions, *Langmuir* 29 (40) (2013) 12358–12366, <https://doi.org/10.1021/la402836d>.
- [30] O. Owoseni, E. Nyankson, Y. Zhang, S.J. Adams, J. He, G.L. McPherson, A. Bose, R. B. Gupta, V.T. John, Release of surfactant cargo from interfacially-active halloysite clay nanotubes for oil spill remediation, *Langmuir* 30 (45) (2014) 13533–13541, <https://doi.org/10.1021/la503687b>.
- [31] R. von Klitzing, D. Stehl, T. Pogrzeba, R. Schomäcker, R. Minullina, A. Panchal, S. Konnova, R. Fakhruillin, J. Koetz, H. Möhwald, et al., Halloysites stabilized emulsions for hydroformylation of long chain olefins, *Adv. Mater. Interf.* (2016), <https://doi.org/10.1002/admi.201600435>. 1600435–n/a.
- [32] G. Cavallaro, S. Milioto, F. Parisi, G. Lazzara, Halloysite nanotubes loaded with calcium hydroxide: alkaline fillers for the deacidification of waterlogged archaeological woods, *ACS Appl. Mater. Interf.* 10 (32) (2018) 27355–27364, <https://doi.org/10.1021/acsami.8b09416>.
- [33] M. Massaro, G. Cavallaro, C.G. Colletti, G. D'Azzo, S. Guernelli, G. Lazzara, S. Pieraccini, S. Riela, Halloysite nanotubes for efficient loading, stabilization and controlled release of insulin, *J. Colloid Interface Sci.* 524 (2018) 156–164, <https://doi.org/10.1016/j.jcis.2018.04.025>.
- [34] E. Abdullayev, Y. Lvov, Halloysite clay nanotubes as a ceramic “Skeleton” for functional biopolymer composites with sustained drug release, *J. Mater. Chem. B* 1 (23) (2013) 2894–2903, <https://doi.org/10.1039/C3TB20059K>.
- [35] Y. Lvov, W. Wang, L. Zhang, R. Fakhruillin, Halloysite clay nanotubes for loading and sustained release of functional compounds, *Adv. Mater.* 28 (6) (2016) 1227–1250, <https://doi.org/10.1002/adma.201502341>.
- [36] J. Kurczewska, M. Ceglowski, B. Messyasz, G. Schroeder, Dendrimer-functionalized halloysite nanotubes for effective drug delivery, *Appl. Clay Sci.* 153 (2018) 134–143, <https://doi.org/10.1016/j.clay.2017.12.019>.
- [37] E. Abdullayev, K. Sakakibara, K. Okamoto, W. Wei, K. Ariga, Y. Lvov, Natural tubule clay template synthesis of silver nanorods for antibacterial composite coating, *ACS Appl. Mater. Interfaces* 3 (10) (2011) 4040–4046, <https://doi.org/10.1021/am200896d>.
- [38] J. Ouyang, B. Guo, L. Fu, H. Yang, Y. Hu, A. Tang, H. Long, Y. Jin, J. Chen, J. Jiang, Radical guided selective loading of silver nanoparticles at interior lumen and out surface of halloysite nanotubes, *Mater. Des.* 110 (2016) 169–178, <https://doi.org/10.1016/j.matdes.2016.07.127>.
- [39] B. Zhong, J. Lin, M. Liu, Z. Jia, Y. Luo, D. Jia, F. Liu, Preparation of halloysite nanotubes loaded antioxidant and its antioxidative behaviour in natural rubber, *Polym. Degrad. Stab.* 141 (2017) 19–25, <https://doi.org/10.1016/j.polymerdegradstab.2017.05.009>.
- [40] M. Du, B. Guo, D. Jia, Newly emerging applications of halloysite nanotubes: a review, *Polym. Int.* 59 (5) (2010) 574–582.
- [41] E. Abdullayev, R. Price, D. Shchukin, Y. Lvov, Halloysite tubes as nanocontainers for anticorrosion coating with benzotriazole, *ACS Appl. Mater. Interfaces* 1 (7) (2009) 1437–1443, <https://doi.org/10.1021/am9002028>.
- [42] G. Gorrasi, Dispersion of halloysite loaded with natural antimicrobials into pectins: characterization and controlled release analysis, *Carbohydr. Polym.* 127 (2015) 47–53, <https://doi.org/10.1016/j.carbpol.2015.03.050>.
- [43] M.K. Pierchala, M. Makaremi, H.L. Tan, J. Pushpamalar, S. Muniyandy, A. Solouk, S.M. Lee, P. Pasbakhsh, Nanotubes in nanofibers: antibacterial multilayered polylactic acid/halloysite/gentamicin membranes for bone regeneration application, *Appl. Clay Sci.* 160 (2018) 95–105, <https://doi.org/10.1016/j.clay.2017.12.016>.
- [44] Price, In vitro release characteristics of tetracycline HCl, Khellin and nicotinamide adenine dinucleotide from halloysite; a cylindrical mineral, *J. Microencapsul.* 18 (6) (2001) 713.
- [45] D.G. Shchukin, S.V. Lamaka, K.A. Yasakau, M.L. Zheludkevich, M.G.S. Ferreira, H. Mohwald, Active anticorrosion coatings with halloysite nanocontainers, *J. Phys. Chem. C* 112 (4) (2008) 958–964, <https://doi.org/10.1021/jp076188r>.
- [46] Y.M. Lvov, D.G. Shchukin, H. Mohwald, R.R. Price, Halloysite clay nanotubes for controlled release of protective agents, *ACS Nano* 2 (5) (2008) 814–820, <https://doi.org/10.1021/nn800259q>.
- [47] K.M. Rao, S. Nagappan, D.J. Seo, C.-S. Ha, PH sensitive halloysite-sodium hyaluronate/poly(hydroxyethyl methacrylate) nanocomposites for colon cancer drug delivery, *Appl. Clay Sci.* 97–98 (2014) 33–42, <https://doi.org/10.1016/j.clay.2014.06.002>.
- [48] G. Cavallaro, G. Lazzara, S. Milioto, Exploiting the colloidal stability and solubilization ability of clay nanotubes/ionic surfactant hybrid nanomaterials, *J. Phys. Chem. C* 116 (41) (2012) 21932–21938, <https://doi.org/10.1021/jp307961q>.
- [49] I. Blanco, L. Abate, F.A. Bottino, P. Bottino, Thermal behaviour of a series of novel aliphatic bridged polyhedral oligomeric silsesquioxanes (POSSs)/ polystyrene (PS) nanocomposites: the influence of the bridge length on the resistance to thermal degradation, *Polym. Degrad. Stab.* 102 (2014) 132–137, <https://doi.org/10.1016/j.polymerdegradstab.2014.01.029>.
- [50] P. Clausen, M. Signorelli, A. Schreiber, E. Hughes, C.J.G. Plummer, D. Fessas, A. Schiraldi, J.-A.E. Manson, Equilibrium desorption isotherms of water, ethanol, ethyl acetate, and toluene on a sodium smectite clay, *J. Therm. Anal. Calorim.* 98 (3) (2009) 833–841, <https://doi.org/10.1007/s10973-009-0003-x>.
- [51] S. Farris, L. Introzzi, P. Biagioni, T. Holz, A. Schiraldi, L. Piergiorganni, Wetting of biopolymer coatings: contact angle kinetics and image analysis investigation, *Langmuir* 27 (12) (2011) 7563–7574, <https://doi.org/10.1021/la2017006>.
- [52] J.C. Johnston, V. Molinero, Crystallization, melting, and structure of water nanoparticles at atmospherically relevant temperatures, *J. Am. Chem. Soc.* 134 (15) (2012) 6650–6659, <https://doi.org/10.1021/ja210878c>.
- [53] G. Fotie, R. Rampazzo, A.M. Ortenzi, S. Checchia, D. Fessas, L. Piergiorganni, The effect of moisture on cellulose nanocrystals intended as a high gas barrier coating on flexible packaging materials, *Polymers* 9 (9) (2017), <https://doi.org/10.3390/polym9090415>.
- [54] N. Arslan, H. Togrul, The fitting of various models to water sorption isotherms of tea stored in a chamber under controlled temperature and humidity, *J. Stored Prod. Res.* 42 (2) (2006) 112–135, <https://doi.org/10.1016/j.jspr.2005.01.001>.
- [55] P. Yogendrarajah, S. Samapundo, F. Devlieghere, S. De Saeger, B. De Meulenaer, Moisture sorption isotherms and thermodynamic properties of whole black peppercorns (*Piper Nigrum* L.), *Food Sci. Technol. Int.* 64 (1) (2015) 177–188, <https://doi.org/10.1016/j.lwt.2015.05.045>.

Selective adsorption of oppositely charged PNIPAAm on halloysite surfaces: a route to thermo-responsive nanocarriers

Giuseppe Cavallaro, Giuseppe Lazzara , Lorenzo Lisuzzo, Stefana Milioto and Filippo Parisi

Dipartimento di Fisica e Chimica, Università degli Studi di Palermo, Viale delle Scienze pad 17, I-90128 Palermo, Italy

E-mail: giuseppe.lazzara@unipa.it

Received 27 February 2018, revised 14 May 2018

Accepted for publication 17 May 2018

Published 5 June 2018



CrossMark

Abstract

Halloysite nanotubes were functionalized with stimuli-responsive macromolecules to generate smart nanohybrids. Poly(N-isopropylacrylamide)-co-methacrylic acid (PNIPAAm-co-MA) was selectively adsorbed into halloysite lumen by exploiting electrostatic interactions. Amine-terminated PNIPAAm polymer was also investigated that selectively interacts with the outer surface of the nanotubes. The adsorption site has a profound effect on the thermodynamic behavior and therefore temperature responsive features of the hybrid material. The drug release kinetics was investigated by using diclofenac as a non-steroidal anti-inflammatory drug model. The release kinetics depends on the nanoarchitecture of the PNIPAAm/halloysite based material. In particular, diclofenac release was slowed down above the LCST for PNIPAAm-co-MA/halloysite. Opposite trends occurred for halloysite functionalized with PNIPAAm at the outer surface. This work represents a further step toward the opportunity to extend and control the delivery conditions of active species, which represent a key point in technological applications.

Supplementary material for this article is available [online](#)

Keywords: halloysite, nanotube, thermo-responsive material, controlled release

(Some figures may appear in colour only in the online journal)

1. Introduction

Nanotechnology deals with the manipulation of matter at the nanometric scale in order to fabricate new materials with some requested features. Among nanomaterials, hybrid systems prepared by the combination of inorganic nanoparticles and biomolecules are promising for several applications within materials science and biotechnology [1–5]. Clay nanoparticles are promising solid supports because of their sustainability and low cost [6]. Halloysite is an emerging hollow tubular clay, which is naturally available worldwide and cheap compared to synthetic nanoparticles with similar morphology [7, 8]. From the mineralogical viewpoint, halloysite is a 1:1 aluminosilicate ($\text{Al}_2\text{Si}_2\text{O}_5(\text{OH})_4 \cdot 2\text{H}_2\text{O}$) that possesses two water molecules in the interlayer wall with a

spacing of 10 Å [7–9]. Similarly to kaolinite, dehydrated halloysite presents a shorter interlayer wall periodicity (7.2 Å) due to the loss of the water molecules. Typically, halloysite nanotubes (HNTs) are quite polydisperse in nature depending on the geological deposit [10]. Their length ranges between 50 and 1500 nm, while the intervals for external and internal diameters are 20–150 and 10–15 nm, respectively [10]. Due to the hydrophilicity of HNTs and their small dimensions, raw HNTs can be readily dispersed in water easily by mechanical stirring or ultrasonic treatment [11].

The HNT tubular morphology is caused by the packing disorder induced by the interlayer water molecules. Namely, the rolling up of overlapped silica tetrahedral and alumina octahedral sheets generates the hollow tubular shape of halloysite [8]. Furthermore, the HNT surfaces possess a different

chemical composition: the lumen is formed by alumina, while the shell consists of silica. According to the specific acidic-base equilibria, the inner and external surfaces are positively and negatively charged, respectively, in a wide pH range (2–8). Therefore, the HNT cavity represents an efficient container for negative macromolecules, such as polymers and surfactants [7, 12]. Targeted chemical functionalization can be achieved by covalent interactions at the inner/outer surfaces [13–15].

The different surface chemistry [16] combined to the biocompatibility (evidenced by biological tests on cells and microorganisms [17–19]) explains the suitability of HNT as nanocontainers and delivery systems (proteins, gas, drugs, antimicrobials, corrosion inhibitors) [7, 19–27]. Halloysite oral administration limit was established in a recent paper as 20–30 mg kg⁻¹ of body weight. Firstly, Price *et al* demonstrated halloysite is a viable and inexpensive nanoscale container for the encapsulation of oxytetracycline, khellin and nicotinamide adenine dinucleotide (NAD) [28]. A further control on molecule incorporation and release from HNTs are obtained by end-capping [22, 29, 30], or hydrogel microgel lumen filling [31] strategies. HNTs are suitable supports for catalytic applications [32–34].

Polymers are largely used to generate hybrid organic/inorganic nanostructures to produce a wide group of new materials. Poly-N-isopropylacrylamide (PNIPAAm) [35, 36], poly(ethylene oxide) and poly(propylene oxide) based copolymers [37, 38] are examples of thermo-sensitive moieties. As concerns PNIPAAm, its macromolecular transition from a hydrophilic (or swelled) to a hydrophobic (or shrunken) structure occurs rather abruptly at the lower critical solution temperature (LCST), which is at ca. 32 °C but can vary in a wide range on dependence of the microstructure of the macromolecule [39–41]. Copolymerization of two or more monomers with different functional groups leads to stimuli-responsive polymers. Effective nanocarriers with controlled release capacity can be obtained by using polymers sensitive to multiple external stimuli, such as temperature and pH [42]. PNIPAAm based polymers were used as pH- and temperature sensitive drug delivery systems. Some examples may include the intestinal release of human calcitonin, insulin, and ibuprofen [43, 44]. As an example, PNIPAAm polymers are successful in the targeted release of drugs (calcitonin, insulin, and ibuprofen) within the human intestine [43, 44]. Protein adsorption can be tuned on PNIPAAm coatings [45]. PNIPAAm beads can be employed for the immobilization of drugs in the stomach because of their resistance to acidic pH. On the contrary, the disintegration of PNIPAAm beads at basic pH allows the release of the drugs in the intestine [46].

The grafting of PNIPAAm onto the halloysite external surface was proposed to obtain a novel thermo-responsive drug carrier for curcumin delivery [47]. PNIPAAm/HNT hybrid exhibited thermo-sensitive properties that are not detected in the pristine nanotubes. Below LCST, modified HNT showed a significant enhancement of the colloidal stability in water with respect to that of pure halloysite [48].

This work was aimed to develop a new drug delivery system composed by halloysite and charged PNIPAAm-co-methacrylic

acid, which selectively interacts with the HNT surface. Amine-terminated PNIPAAm was also investigated for comparison. The influence of the adsorption site on the structural and thermodynamic behavior of the hybrids was investigated. Finally, the functionalized nanotubes were studied as carriers for diclofenac, which is used as a non-steroidal anti-inflammatory drug model. The release kinetics of the drug was studied at variable temperatures in order to evaluate the efficiency of the hybrids as thermo-responsive nanocarriers. On this basis, the opportunity to extend and control the delivery conditions represents a key point in pharmaceutical and biomedical applications.

2. Experimental section

2.1. Materials

HNTs are from Imerys Ceramics. Pyrene ($\geq 99.0\%$), diclofenac sodium salt (molecular weight = 318.13 g mol⁻¹), poly(N-isopropylacrylamide)-amine-terminated (PNIPAAm-NH₂, average molecular weight = 5500 g mol⁻¹) and poly(N-isopropylacrylamide-co-methacrylic acid) (PNIPAAm-co-MA, average molecular weight = 10 000 g mol⁻¹, 10 mol% methacrylic acid) are from Sigma Aldrich.

2.2. Preparation of PNIPAAm/HNTs dispersions in water

Aqueous PNIPAAm solutions were prepared by dissolving 0.1 g of polymer in 10 g of water. Then, a proper amount of halloysite was added in order to obtain PNIPAAm/HNT dispersions with a weight ratio of 1:10. Stable dispersions were achieved by magnetically stirring for 24 h.

2.3. Loading of diclofenac into PNIPAAm/HNT hybrids

Firstly, 0.5 g of HNT was added to a saturated solution of diclofenac sodium salt and the mixture was stirred for 24 h to obtain a stable dispersion. Then, 0.05 g of PNIPAAm was added and kept stirred overnight allowing the polymer adsorption on the HNT surfaces. Finally, the dispersions were centrifuged to separate the solid material, which represents the PNIPAAm/HNT containing diclofenac. The material was washed with water five times and dried at 25 °C.

2.4. Methods

Micro differential scanning calorimetry (micro-DSC) analysis was performed by using a Setaram DSC III apparatus. Measurements were conducted under constant nitrogen flow in the range from 10 °C to 55 °C with a scan rate of 1 °C min⁻¹. The stainless steel (1 cm³) sample cell was filled with ca. 500 mg of the aqueous dispersion and the reference cell with the corresponding amount of water. The calibration was performed by using naphthalene. The enthalpy of the process was calculated from the signal integral area and normalized per moles of PNIPAAm. Dynamic light scattering (DLS) experiments were carried out by means of a Zetasizer NANO-ZS (Malvern Instruments) within a temperature range

between 10 °C and 50 °C. The field-time autocorrelation functions were well described by a single decay, which provides the decay rate (C) of the diffusive mode. For the translational motion, the collective diffusion coefficient at a given concentration is $D_t = \Gamma/q^2$ where q is the scattering vector given by $4\pi n \lambda^{-1} \sin(\theta/2)$ being n the water refractive index, λ the wavelength (632.8 nm) and θ the scattering angle (173°). The apparent hydrodynamic radius (R_h) of the equivalent (with equivalent translational diffusion coefficients) spherical particle was calculated by using the Stokes–Einstein equation as $R_h = k_b T / (6\pi\eta)$, k_b being the Boltzmann constant, T the absolute temperature, and η the water viscosity.

Fluorescence spectra of saturated aqueous solutions of pyrene were recorded using Fluoromax 4 (Jobin-Yvon) spectrofluorometer (90° angle geometry, 1 cm × 1 cm quartz cell). The excitation wavelength was fixed at 333 nm, while the emission spectra were registered from 350 to 500 nm. The analyses were conducted from 10 °C to 50 °C with a temperature step of 10 °C. The temperature was controlled by using a thermostat (± 0.1 °C).

The functionalized nanotubes were imaged by using a microscope ESEM FEI QUANTA 200F. Before each experiment, the sample was coated with gold in argon by means of an Edwards Sputter Coater S150A to avoid charging under the electron beam.

UV–vis spectrophotometry analyses were performed by means of a UV–vis spectrophotometer (Analytic Jena Specord S 600 BU). In order to measure the release of diclofenac sodium salt, a calibration curve was firstly recorded at $\lambda = 276$ nm. The molar extinction coefficient was $102701 \text{ mol}^{-1} \text{ cm}^{-1}$. Release kinetics were measured by immersing 10 mg of solid sample (PNIPAAm/HNT hybrid containing diclofenac) into a dialysis bag (12 kDa cut off) filled with 50 ml of water. The release kinetics of diclofenac from PNIPAAm/HNT nanocarriers was followed by UV–vis. For comparison, release experiments were conducted on HNT loaded with diclofenac. These tests were performed at 25 °C and 50 °C.

3. Results and discussion

PNIPAAm/HNT aqueous dispersions were characterized in order to investigate their colloidal stability, thermodynamics, and structural properties. In particular, we explored the effect of the site adsorption on the thermo-responsive behavior of the PNIPAAm/HNT hybrids. On this basis, PNIPAAms with opposite charge (positive PNIPAAm-NH₂ and negative PNIPAAm-co-MA) were selected because of their targeted adsorption is driven by electrostatic interactions with HNT surfaces.

3.1. Thermo-responsive characteristics of PNIPAAm/HNT hybrids: the effect of the adsorption site

Figure 1 shows the hydrodynamic radius versus temperature trends for pure PNIPAAms and PNIPAAm/HNT hybrids.

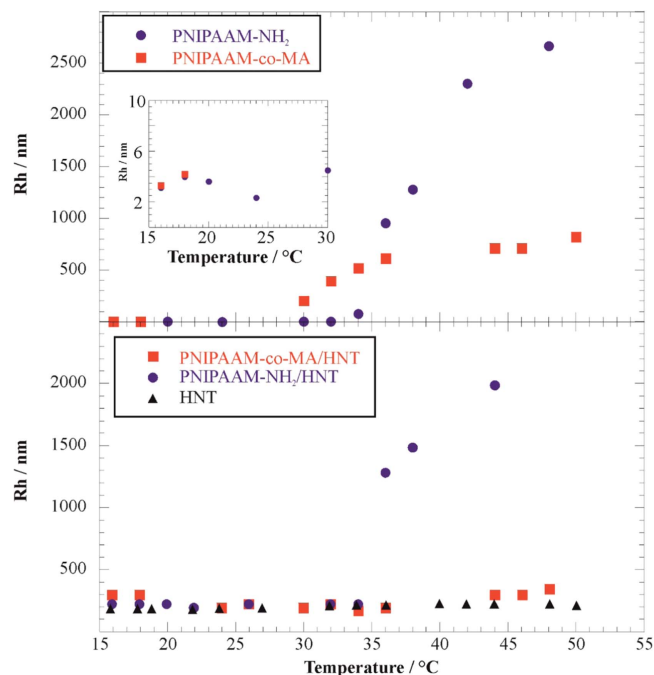


Figure 1. Hydrodynamic radius as a function of temperature.

Below LCST, R_h values are ca. 3 and 4 nm for PNIPAAm-NH₂ and PNIPAAm-co-MA, respectively (see inset in figure 1). These data can be correlated to the gyration radius (R_g) of both PNIPAAms estimated by the random coil model, which can be expressed as

$$R_g = \sqrt{\frac{C_\infty \cdot N \cdot l^2}{6}}, \quad (1)$$

where l is the PNIPAAm monomer length (0.34 nm) [49], C_∞ is the characteristic ratio in the limit of long chains (0.70 for PNIPAAm) [49], and N is the number of monomer units. We calculated that the R_g of PNIPAAm-NH₂ and PNIPAAm-co-MA are 8 and 11 nm, respectively. The R_g values are ca. two times larger than the R_h ones indicating that the chain is nearly in a Gaussian conformation. For temperature $>$ LCST, the R_h value significantly increased (ca. 2000 nm and 800 nm for PNIPAAm-NH₂ and PNIPAAm-co-MA, respectively) as a consequence of the polymer aggregation, which promotes the coalescence and phase separation of the polymer (figure 2). Above the LCST, the PNIPAAm-co-MA shows an R_h value smaller than that of PNIPAAm-NH₂. This effect is probably due to the presence of large negative charge related to the methacrylic functionalities that are responsible for electrostatic repulsions between particles hindering further aggregation. Regarding the hybrids systems, we observed that the temperature increase does not affect the R_h of PNIPAAm-co-MA/HNT, which is constantly at ca. 200–300 nm reflecting the diffusion behavior of pristine halloysite (figure 1). Namely, the LCST of PNIPAAm-co-MA was not detected by DLS measurements demonstrating that the negatively charged copolymer is incorporated into the HNT positively charged lumen. ζ -potential measurements were carried out as a function of temperature on pristine polymers and hybrid systems to highlight this aspect (figure 2).

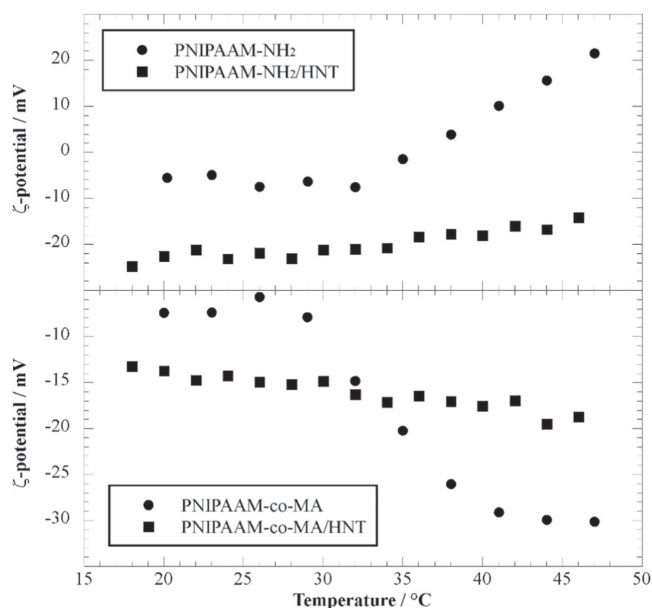


Figure 2. Hydrodynamic radius as a function of temperature for PNIPAAms aqueous solutions and PNIPAAms/HNT aqueous dispersions.

PNIPAAm based polymers presented a nearly negligible charge below the LCST. At temperature larger than LCST, a large negative potential is observed for PNIPAAm-co-MA while PNIPAAm-NH₂ turns to slightly positive potentials. These trends are consistent with the formation of polymers agglomerates above LCST with an opposite charge for the two polymer systems. The large negative ζ -potential values for PNIPAAm-co-MA at high temperature is due to the ionization effect of the methacrylic acid functionalities in the copolymer chain. The combination of PNIPAAm-co-MA and PNIPAAm-NH₂ with HNTs clearly reduces the temperature effect on ζ -potential values preserving the general increasing/decreasing trend observed for each polymer.

Moreover, PNIPAAm-co-MA encapsulation within HNT cavity rules out the formation of aggregates because the polymer dehydration process takes place only within the nanotubes. In contrast, the PNIPAAm-NH₂/HNT composite showed a strong R_h enhancement (from ca. 200 to 2000 nm) at ca. 35 °C due to the collapsing of the polymer chains and the formation of aggregates driven by the hydrophobic interactions between the nanotubes, which present PNIPAAm-NH₂ on their external surface (figure 2) [48]. Similarly, HNT modified with cationic surfactants (selectively adsorbed on the outer surface) evidenced the clustering of nanotubes due to the hydrophobic interactions between the alkyl chains [12, 50]. The peculiar effect of the temperature increase on the nanostructure of PNIPAAm/HNT composites is sketched in figure 3.

The specific correlation between the PNIPAAm/HNT site adsorption and the thermo-sensitive characteristics of the hybrids was confirmed by DSC experiments, which are used to investigate the hydration/dehydration processes induced by temperature for polymers dispersed in water [48, 51, 52].

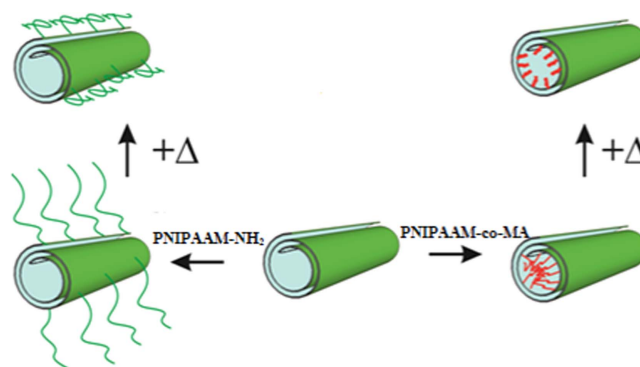


Figure 3. Schematic representation of PNIPAAm-NH₂ and PNIPAAm-co-MA interaction with HNT surfaces and the effect of temperature increase on the nanostructures of PNIPAAm/HNT hybrids.

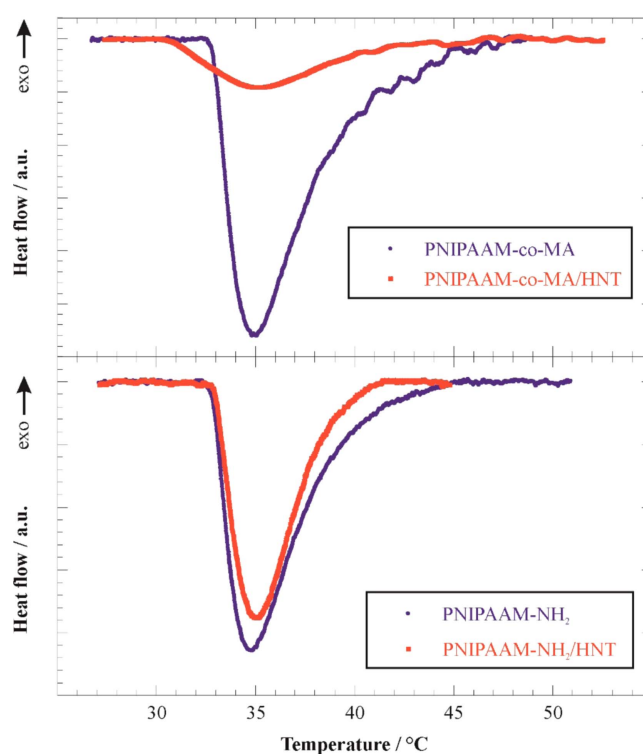


Figure 4. DSC thermograms for pure PNIPAAms and PNIPAAms/HNT hybrid systems.

DSC thermograms of pristine PNIPAAms and PNIPAAm/HNTs mixtures are presented in figure 4.

As a general result, we observed an endothermic signal that can be attributed to the polymer dehydration. Its integration provides the enthalpy (ΔH) of the PNIPAAm dehydration, while the peak temperature corresponds to the LCST value. Table 1 collects ΔH and LCST data for the investigated systems.

It should be noted that ΔH is expressed as kJ per mole of PNIPAAm by taking into account the stoichiometric polymer amount in solution. According to table 1, the presence of halloysite not altered the LCST neither for PNIPAAm-NH₂ nor for PNIPAAm-co-MA. As concerns ΔH , the polymer adsorption onto the HNT surfaces induced a reduction

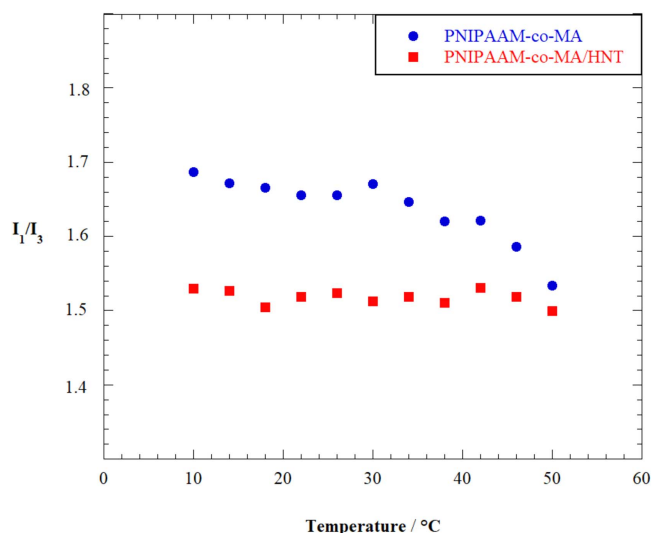


Figure 5. The dependence of I_1/I_3 ratio on the temperature for saturated aqueous solutions of pyrene in presence of pure PNIPAAM-co-MA and PNIPAAM-co-MA/HNT hybrid.

Table 1. Enthalpy of PNIPAAM dehydration and LCST from micro-DSC data.

	LCST/°C	$\Delta H/\text{kJ mol}^{-1}$
PNIPAAM-NH ₂	34.4	95.8
PNIPAAM-NH ₂ /HNTs	34.6	70.2
PNIPAAM-co-MA	34.4	145.8
PNIPAAM-co-MA/HNTs	34.4	30.9

(table 1) highlighting a modification of the thermodynamics of hydration/dehydration process of PNIPAAMs molecules. This effect is likely related to lateral interactions between the molecules adsorbed onto HNTs surfaces that provide a partial dehydration of PNIPAAM moieties already below LCST, thus confirming data already existing in literature for PNIPAAM grafted silica particles [53]. The larger ΔH decrease detected for PNIPAAM-co-MA/HNT hybrid shows that the negative copolymer undergoes a stronger dehydration effect upon adsorption compared to that of positive PNIPAAM-NH₂. These results agree with the different site adsorption. The selective interaction of PNIPAAM-co-MA with the positive HNT surface generates both curvature and confining effects, which promote the lateral interactions between the polymer molecules and, consequently, the dehydration process before LCST. On the other hand, the adsorption of PNIPAAM-NH₂ on the negative external surface of halloysite determined a smaller effect in favoring the lateral interactions between the polymer chains.

A further evidence of the PNIPAAM dehydration induced by temperature can be provided by proving the presence of hydrophobic microenvironments in the hybrid systems. To this purpose, pyrene can be used as a fluorescent probe sensitive to the nature/polarity of the microenvironment [54]. The emission spectrum of pyrene consists of five bands. The ratio between the intensity of the first (373 nm)

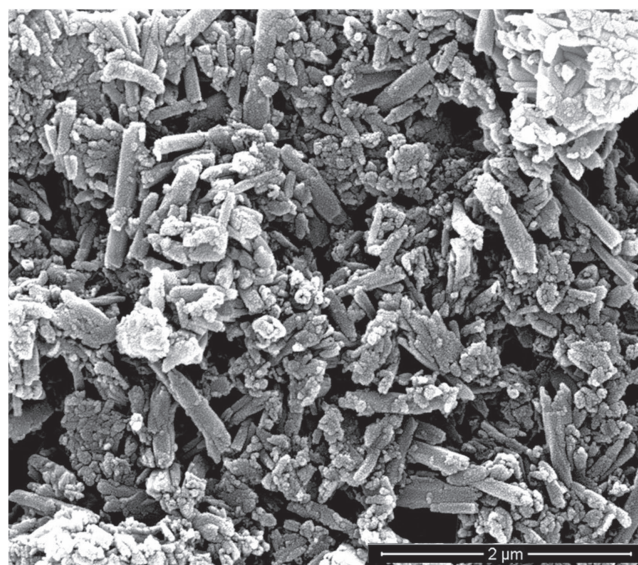


Figure 6. SEM micrograph of PNIPAAM/HNT.

and the third (384 nm) vibration bands (I_1/I_3) depends on the polarity of the medium being ca. 1.8 in aqueous solvents and ca. 0.8 in hydrophobic solvents. Figure 5 displays the I_1/I_3 versus temperature trends for saturated aqueous solutions of pyrene in presence of PNIPAAM-co-MA and PNIPAAM-co-MA/HNT composite.

The pyrene/PNIPAAM-co-MA solution evidenced a reduction of the I_1/I_3 ratio (from ca. 1.7 to ca. 1.53) at ca. 35 °C because of the formation of hydrophobic microdomains that promote the polymer dehydration process. In contrast, we observed that I_1/I_3 ratio constantly equals to ca. 1.52 in all the investigated temperature range for the pyrene solution in presence of PNIPAAM-co-MA/HNT hybrid. This trend highlights that PNIPAAM-co-MA encapsulated within the HNT lumen possesses a partially dehydrated state even below the LCST confirming the calorimetric results.

3.2. Release kinetics of diclofenac from PNIPAAM/HNT nanocarriers

Before recording release profiles, PNIPAAM/HNT hybrids have been imaged by SEM. Micrograph reported in figure 6 shows HNTs randomly distributed, being the material processed like powder. Moreover, it is interesting to observe that tubular shape of halloysite and its characteristic lengths in the hybrid nanomaterial were preserved.

The release kinetics of diclofenac loaded into PNIPAAM/HNT hybrids were studied at 25 °C and 50 °C (see supporting information is available online at stacks.iop.org/NANO/29/325702/mmedia), which are below and above the LCST value, respectively. On this basis, we estimated the suitability of the functionalized HNTs as thermo-sensitive drug delivery systems. Release experiments allowed to determine the total amount of diclofenac adsorbed by the PNIPAAM/HNT composites. We estimated that the drug loadings are 4.7 and 5.3 mg g⁻¹ for PNIPAAM-co-MA/HNT and PNIPAAM-NH₂/HNT, respectively.

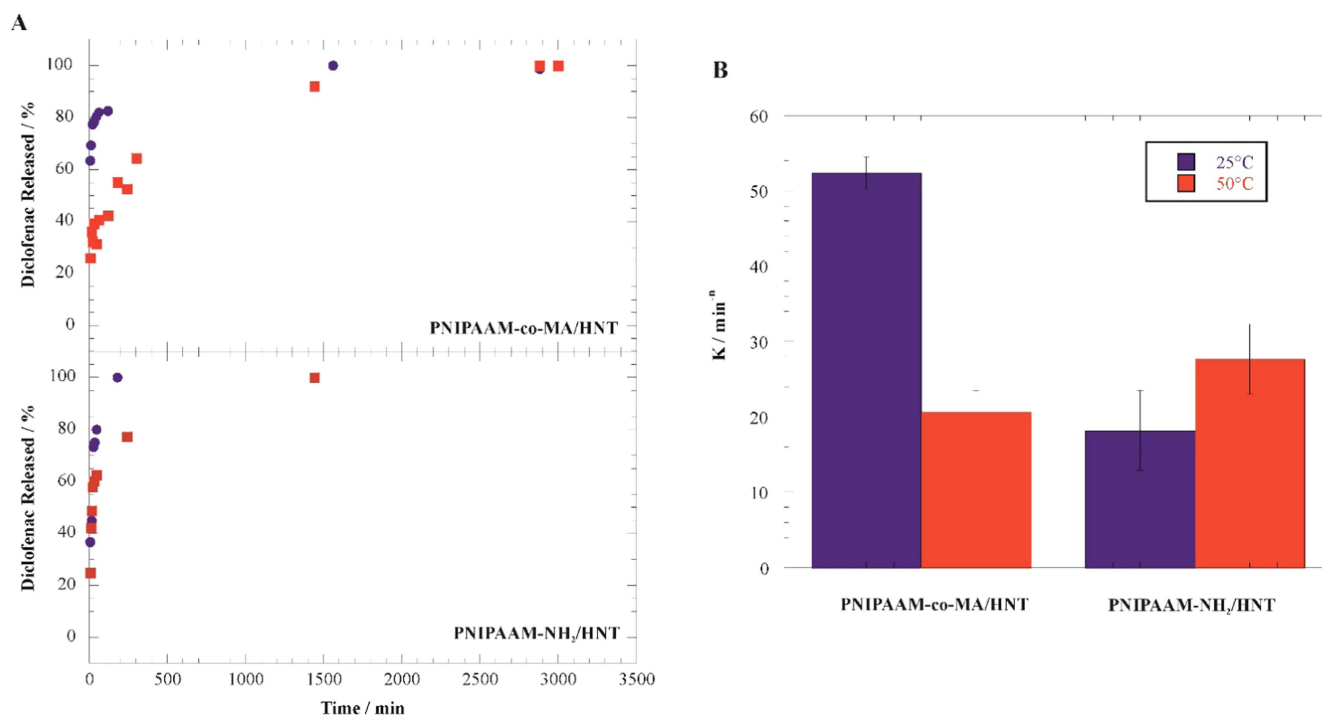


Figure 7. (A) Release profiles of diclofenac from hybrid systems at 25 °C (blue) and 50 °C (red). (B) Kinetics constants of diclofenac released from PNIPAAM-co-MA/HNT and PNIPAAM-NH₂/HNT.

The release profiles (figure 7) were fitted according to the Korsmeyer–Peppas equation [55]

$$R\%(t) = kt^n, \quad (2)$$

where $R\%(t)$ is the percent of diclofenac released at time t , while k and n are the kinetics constant and the release exponent, respectively. The fitting parameters are presented in supporting information. The n value depends on the release mechanism as well as on the specific geometry of the matrix. We observed that n values are lower than 0.45 for all the investigated systems indicating a quasi fickian diffusion for both PNIPAAM-co-MA/HNT and PNIPAAM-NH₂/HNT at 25 °C and 50 °C.

Concerning the kinetics, we found that the specific site adsorption of the charged PNIPAAMs influences the release properties of the hybrids. Below LCST, k value is larger for PNIPAAM-co-MA/HNT with respect to that of PNIPAAM-NH₂/HNT composite (figure 7).

PNIPAAM-NH₂/HNT carrier exhibited a faster release kinetics at higher temperature (figure 7). Oppositely, the diclofenac release from PNIPAAM-co-MA/HNT hybrid was strongly slowed down by the temperature increase (figure 7) in agreement with the confinement of the polymer within the halloysite cavity. Namely, the hydrated PNIPAAM-co-MA at 25 °C allows for a fast release of the drug from the lumen, while at temperature > LCST, the polymer shrinking and dehydration slow down the drug release determining a reduction of the k value. This effect cannot be observed in the composite nanocarrier based on HNT and PNIPAAM-NH₂ as a consequence of the selective adsorption of the polymer on the halloysite outer surface. Based on these results, we can conclude that the release of diclofenac from PNIPAAMs/

HNT nanocarriers depends on their specific nanoarchitecture. In particular, the drug release can be easily controlled by the temperature using nanotubes modified with oppositely charged PNIPAAMs.

4. Conclusions

Thermo-sensitive nanocarriers were prepared by selective modification of halloysite (HNT) surfaces with oppositely charged poly(N-isopropylacrylamide) (PNIPAAM) polymers. Specifically, amine-terminated PNIPAAM (PNIPAAM-NH₂) and copolymer based on PNIPAAM and methacrylic acid ((PNIPAAM-co-MA) were selected. DLS and differential scanning calorimetry highlighted that the specific PNIPAAM/HNT site interaction influences the structure and the thermodynamics of the hybrid systems. The incorporation of PNIPAAM-co-MA within the positive halloysite promoted the lateral interactions between the polymer molecules favoring the dehydration process, while the adsorption of PNIPAAM-NH₂ on the HNT outer surface favored the formation of aggregates as a consequence of hydrophobic interactions. Fluorescence experiments confirmed the encapsulation of negatively charged PNIPAAM-co-MA inside the halloysite lumen, which assumes a hydrophobic nature. PNIPAAM/HNT hybrids were investigated as thermo-responsive delivery systems for diclofenac. The drug release kinetics was slowed down by temperature increase for PNIPAAM-co-MA/HNT composite because of the shrinking of the polymer adsorbed inside the halloysite cavity. This effect was not detected for the hybrid based on halloysite and PNIPAAM-NH₂ according to the polymer adsorption on the

HNT outer surface. Based on these results, we can conclude that the specific site adsorption of PNIPAAms/HNT hybrids influences their thermo-responsive behavior in terms of structural/thermodynamic properties. It should be noted that the drug loading does not depend on the architecture while the release kinetics and its temperature dependence is influenced by the polymers. Definitely, the selective modification of HNT with oppositely charged PNIPAAm polymers represents a reliable strategy to obtain advanced nanocarriers with thermo-sensitive characteristics, which allow controlling the effect of the temperature on the release kinetics of drugs.

Acknowledgments

The authors acknowledge University of Palermo for financial support.

ORCID iDs

Giuseppe Lazzara  <https://orcid.org/0000-0003-1953-5817>

References

- [1] Ma W, Yah W O, Otsuka H and Takahara A 2012 *J. Mater. Chem.* **22** 11887–92
- [2] Lvov Y and Abdullayev E 2013 *Prog. Polym. Sci.* **38** 1690–719
- [3] Ruiz-Hitzky E, Aranda P, Darder M and Rytwo G 2010 *J. Mater. Chem.* **20** 9306–21
- [4] Ruiz-Hitzky E, Aranda P, Darder M and Ogawa M 2011 *Chem. Soc. Rev.* **40** 801–28
- [5] Gorrasi G, Pantani R, Murariu M and Dubois P 2014 *Macromol. Mater. Eng.* **299** 104–15
- [6] Ma W, Higaki Y and Takahara A 2016 *Dev. Clay Sci.* **7** 628–71
- [7] Lvov Y M, Shchukin D G, Mohwald H and Price R R 2008 *ACS Nano* **2** 814–20
- [8] Joussein E, Petit S, Churchman G J, Theng B, Righi D and Delvaux B 2005 *Clay Miner.* **40** 383–426
- [9] Lvov Y M, DeVilliers M M and Fakhrullin R F 2016 *Expert Opin. Drug Deliv.* **13** 977–86
- [10] Pasbakhsh P, Churchman G J and Keeling J L 2013 *Appl. Clay Sci.* **74** 47–57
- [11] Liu M, Zhang Y, Wu C, Xiong S and Zhou C 2012 *Int. J. Biol. Macromol.* **51** 566–75
- [12] Cavallaro G, Lazzara G and Milioto S 2012 *J. Phys. Chem. C* **116** 21932–8
- [13] Yah W O, Takahara A and Lvov Y M 2011 *J. Am. Chem. Soc.* **134** 1853–9
- [14] Massaro M, Riela S, Lo Meo P, Noto R, Cavallaro G, Milioto S and Lazzara G 2014 *J. Mater. Chem. B* **2** 7732–8
- [15] Lazzara G, Cavallaro G, Panchal A, Fakhrullin R, Stavitskaya A, Vinokurov V and Lvov Y 2018 *Curr. Opin. Colloid Interface Sci.* **35** 42–50
- [16] Bertolino V, Cavallaro G, Lazzara G, Milioto S and Parisi F 2017 *Langmuir* **33** 3317–23
- [17] Fakhrullina G I, Akhatova F S, Lvov Y M and Fakhrullin R F 2015 *Environ. Sci. Nano* **2** 54–9
- [18] Shutava T G, Fakhrullin R F and Lvov Y M 2014 *Curr. Opin. Pharmacol.* **18** 141–8
- [19] Hu Y, Chen J, Li X, Sun Y, Huang S, Li Y, Liu H, Xu J and Zhong S 2017 *Nanotechnology* **28** 375101
- [20] Gorrasi G 2015 *Carbohydr. Polym.* **127** 47–53
- [21] Du M, Guo B and Jia D 2010 *Polym. Int.* **59** 574–82
- [22] Abdullayev E, Price R, Shchukin D and Lvov Y 2009 *ACS Appl. Mater. Interfaces* **1** 1437–43
- [23] Tully J, Yendluri R and Lvov Y 2016 *Biomacromolecules* **17** 615–21
- [24] Owoseni O, Nyankson E, Zhang Y, Adams S J, He J, McPherson G L, Bose A, Gupta R B and John V T 2014 *Langmuir* **30** 13533–41
- [25] Joshi A, Abdullayev E, Vasiliev A, Volkova O and Lvov Y 2013 *Langmuir* **29** 7439–48
- [26] Duce C, Porta V D, Bramanti E, Campanella B, Spepi A and Tiné M R 2017 *Nanotechnology* **28** 055706
- [27] Wang X, Gong J, Gui Z, Hu T and Xu X 2018 *Environ. Toxicol.* **33** 623–30
- [28] Price B P G R R and Lvov Y 2001 *J. Microencapsul.* **18** 713–22
- [29] Cavallaro G, Danilushkina A A, Evtugyn V G, Lazzara G, Milioto S, Parisi F, Rozhina E V and Fakhrullin R F 2017 *Nanomaterials* **7** 199
- [30] Dzamukova M R, Naumenko E A, Lvov Y M and Fakhrullin R F 2015 *Sci. Rep.* **5** 10560
- [31] Cavallaro G, Lazzara G, Milioto S, Parisi F, Evtugyn V, Rozhina E and Fakhrullin R 2018 *ACS Appl. Mater. Interfaces.* **10** 8265–73
- [32] Sadjadi S and Atai M 2018 *Appl. Clay Sci.* **153** 78–89
- [33] Wang Q, Wang Y, Zhao Y, Zhang B, Niu Y, Xiang X and Chen R 2015 *Cryst. Eng. Comm.* **17** 3110–6
- [34] Vinokurov V A, Stavitskaya A V, Chudakov Y A, Ivanov E V, Shrestha L K, Ariga K, Darrat Y A and Lvov Y M 2017 *Sci. Technol. Adv. Mater.* **18** 147–51
- [35] Schild H G 1992 *Prog. Polym. Sci.* **17** 163–249
- [36] Lazzara G, Olofsson G, Alfredsson V, Zhu K, Nystrom B and Schillen K 2012 *Soft Matter* **8** 5043–54
- [37] Gonzalez-Lopez J, Alvarez-Lorenzo C, Taboada P, Sosnik A, Sandez-Macho I and Concheiro A 2008 *Langmuir* **24** 10688–97
- [38] Taboada P, Barbosa S and Mosquera V 2004 *Langmuir* **20** 8903–8
- [39] Chung J E, Yokoyama M, Yamato M, Aoyagi T, Sakurai Y and Okano T 1999 *J. Control. Release* **62** 115–27
- [40] Yan H and Tsujii K 2005 *Colloids Surf. B* **46** 142–6
- [41] Antunes F, Gentile L, Tavano L and Oliviero C 2009 *Appl. Rheol.* **19** 42064–9
- [42] Rwei S-P, Way T-F, Chang S-M, Chiang W-Y and Lien Y-Y 2015 *J. Appl. Polym. Sci.* **132** 42367–74
- [43] Zhou Z, Zhu S and Zhang D 2007 *J. Mater. Chem.* **17** 2428–33
- [44] Schmaljohann D 2006 *Adv. Drug. Deliv. Rev.* **58** 1655–70
- [45] Stetsyshyn Y et al 2012 *Colloid Interface Sci* **387** 95–105
- [46] Okano T, Bae Y H, Jacobs H and Kim S W 1990 *J. Control. Release* **11** 255–65
- [47] Cavallaro G, Lazzara G, Massaro M, Milioto S, Noto R, Parisi F and Riela S 2015 *J. Phys. Chem. C* **119** 8944–51
- [48] Cavallaro G, Lazzara G, Milioto S and Parisi F 2016 *J. Colloid Interface Sci.* **461** 346–51
- [49] Zhang W, Zou S, Wang C and Zhang X 2000 *J. Phys. Chem. B* **104** 10258–64
- [50] Cavallaro G, Lazzara G, Milioto S and Parisi F 2015 *Langmuir* **31** 7472–8
- [51] Cavallaro G, Lazzara G and Milioto S 2012 *Soft Matter* **8** 3627–33
- [52] Cavallaro G, Lazzara G, Milioto S and Parisi F 2015 *Colloids Surf. A* **474** 85–91
- [53] Park J-H, Lee Y-H and Oh S-G 2007 *Macromol. Chem. Phys.* **208** 2419–27
- [54] Kalyanasundaram K and Thomas J K 1977 *J. Am. Chem. Soc.* **99** 2039–44
- [55] Ritger P L and Peppas N A 1987 *J. Control. Release* **5** 23–36

Article

Halloysite Nanotubes Coated by Chitosan for the Controlled Release of Khellin

Lorenzo Lisuzzo ¹, Giuseppe Cavallaro ^{1,2,*}, Stefana Milioto ^{1,2} and Giuseppe Lazzara ^{1,2}

¹ Dipartimento di Fisica e Chimica, Università degli Studi di Palermo, Viale delle Scienze, pad. 17, 90128 Palermo, Italy; lorenzo.lisuzzo@unipa.it (L.L.); stefana.milioto@unipa.it (S.M.); giuseppe.lazzara@unipa.it (G.L.)

² Consorzio Interuniversitario Nazionale per la Scienza e Tecnologia dei Materiali, INSTM, Via G. Giusti, 9, I-50121 Firenze, Italy

* Correspondence: giuseppe.cavallaro@unipa.it; Tel.: +39-091-2389-7962

Received: 9 July 2020; Accepted: 5 August 2020; Published: 7 August 2020



Abstract: In this work, we have developed a novel strategy to prepare hybrid nanostructures with controlled release properties towards khellin by exploiting the electrostatic interactions between chitosan and halloysite nanotubes (HNT). Firstly, khellin was loaded into the HNT lumen by the vacuum-assisted procedure. The drug confinement within the halloysite cavity has been proved by water contact angle experiments on the HNT/khellin tablets. Therefore, the loaded nanotubes were coated with chitosan as a consequence of the attractions between the cationic biopolymer and the halloysite outer surface, which is negatively charged in a wide pH range. The effect of the ionic strength of the aqueous medium on the coating efficiency of the clay nanotubes was investigated. The surface charge properties of HNT/khellin and chitosan/HNT/khellin nanomaterials were determined by ζ potential experiments, while their morphology was explored through Scanning Electron Microscopy (SEM). Water contact angle experiments were conducted to explore the influence of the chitosan coating on the hydrophilic/hydrophobic character of halloysite external surface. Thermogravimetry (TG) experiments were conducted to study the thermal behavior of the composite nanomaterials. The amounts of loaded khellin and coated chitosan in the hybrid nanostructures were estimated by a quantitative analysis of the TG curves. The release kinetics of khellin were studied in aqueous solvents at different pH conditions (acidic, neutral and basic) and the obtained data were analyzed by the Korsmeyer–Peppas model. The release properties were interpreted on the basis of the TG and ζ potential results. In conclusion, this study demonstrates that halloysite nanotubes wrapped by chitosan layers can be effective as drug delivery systems.

Keywords: chitosan; halloysite nanotubes; khellin; release properties; thermogravimetry

1. Introduction

In recent years, hybrid nanomaterials composed by biopolymers and inorganic nanoparticles have attracted growing interest within several fields, including biomedicine [1–5], pharmaceuticals [6–10], food packaging [11–15], remediation [16,17] and cultural heritage [18–20]. As evidenced in a recent review [21], both ionic and non-ionic polysaccharides can be suitable polymers for the development of functional nanocomposites, with excellent performances in terms of thermal stability, barrier properties and mechanical behavior. Among the polysaccharides, chitosan was largely employed because of its chemical properties (such as hydrophobicity and pH sensitive features) as well as its antibacterial capacity [22]. It should be noted that the properties and the consequent applications of chitosan depend on both its molecular weight and the deacetylation degree [23]. Smart bionanocomposites were obtained by filling the chitosan matrix with both synthetic and natural nanoparticles. Among

synthetic fillers, metal nanoparticles (Cu, Ag and Au) were deposited on chitosan supports [24]. The microwave heating technique was employed to fabricate chitosan/ZnO nanoparticle hybrids with excellent removal capacity towards methylene blue [16], while the casting method was used to prepare chitosan/CuO nanoparticles' composite films as H₂S gas sensor membranes [25]. Multiwalled carbon nanotubes (MWCNT) were added to chitosan hydrogel in order to obtain composite scaffolds for sensing nitrofurantoin [2]. Concerning the natural fillers, nanoclays represent a green option to generate hybrids based on chitosan. Composite films with antibacterial properties were obtained by filling the chitosan/glycerol blend with several clay nanoparticles (bentonite, sepiolite and montmorillonite), which possess different morphological characteristics [26]. Variable contents of nano-hydroxyapatite were incorporated within the chitosan matrix to fabricate composite scaffolds with enhanced elasticity and flexibility [27]. An injectable viscous mucus was achieved by adding rectorite clay nanoparticles into chitosan [28]. Antibacterial and antioxidative films were prepared by mixing chitosan and kaolinite nanosheets [29]. Moreover, the chitosan/kaolinite nanocomposites exhibited better mechanical performances (in terms of tensile strength) with respect to those of the pristine biopolymer [29]. Recently, halloysite was largely investigated as a filler of chitosan in different phases, including aqueous suspensions [21,30], hydrogels [6,17] and solid films [1,31]. Composite scaffolds for tissue engineering purposes were obtained by filling chitosan with halloysite through the solution-mixing and freeze-drying methods [31]. The prepared chitosan/halloysite composite exhibited improved thermo-mechanical performances compared to those of pure chitosan [31]. Gel beads formed by chitosan and halloysite were revealed to be efficient removal agents towards dyes [17] and proper drug delivery systems for doxycycline [6]. Halloysite presents a hollow tubular shape with sizes dependent on its geological source [14]. Halloysite nanotubes (HNTs) possess an average length of 1 µm, while the inner and outer diameters range between 5–70 and 20–150 nm, respectively [14]. Interestingly, the pore volume of halloysite can be increased by acid treatment of its inner surface [32,33]. Due to their morphological characteristics, halloysite nanotubes are efficient as catalytic supports [34–37], adsorbents of pollutants [38,39] and nanocarriers for functional molecules with biological [40–45] and chemical activities [46–49]. In this regards, it should be highlighted that halloysite is suitable for biomedical and pharmaceutical applications because of its biocompatibility and low toxicity, which was observed to both unicellular and multicellular organisms [50–54]. Interestingly, the inside/outside surfaces of halloysite are oppositely charged within the pH interval between 2 and 8 [55]. This peculiarity was exploited for the targeted functionalization of halloysite nanotubes through ionic molecules, such as polyelectrolytes [30,56], proteins [57,58] and surfactants [43,59]. Structural investigations by electric birefringence and fluorescence correlation spectroscopy evidenced that the cationic chitosan wraps the clay nanotubes as a consequence of its selective adsorption onto the negative external surface of halloysite [56]. Here, we prepared a novel nanocarrier for khellin by exploiting the electrostatic attractions of chitosan with the halloysite outer surface. The chitosan coating of the nanoclay was designed to control the khellin release under variable pH conditions, which simulate pharmaceutical applications. The release properties of the chitosan-coated nanotubes were correlated to their morphology, surface charge characteristics and thermal behavior.

2. Materials and Methods

2.1. Materials

Halloysite nanotubes (HNT), chitosan (Mw = 50–190 kg mol⁻¹, deacetylation degree 75–85%), khellin (Mw = 260.24 g mol⁻¹), acetone, glacial acetic acid, sodium sodium hydroxide and hydrochloric acid (37% v/v) are Sigma Aldrich products (St. Louis, MO, USA). All products were used without any further purification.

2.2. Khellin Loading within Halloysite Cavity

Halloysite cavity was filled with khellin by using the procedure reported elsewhere for HNT/drug composites [6]. Firstly, we prepared a khellin saturated solution in acetone. Then, we added halloysite powder to the khellin solution in order to obtain a dispersion with HNT/khellin mass ratio equals to 1:1. The dispersion was ultrasonicated for 10 min and, subsequently, it was magnetically stirred for 24 h. Afterwards, the HNT/khellin suspension was kept under vacuum ($p = 0.01$ atm for 1 h) to favour the encapsulation of the drug within the halloysite cavity as a consequence of the Gibbs–Thomson effect [60]. The latter step was repeated three times in order to enhance the amount of khellin loaded into halloysite nanotubes. According to the literature [61], the dispersion was magnetically stirred for 10 min between two consecutive vacuum steps. Finally, the HNT/khellin composite was separated by centrifugation, which was conducted for 10 min at 7000 rpm. The solid material was rinsed with water three times to remove the unbound khellin, and then dried under vacuum. All steps were carried out at room temperature.

2.3. Chitosan Coating of Halloysite/Khellin Composite

The HNT/khellin composite was coated by chitosan, exploiting the electrostatic interactions occurring between the cationic biopolymer and the halloysite outer surface, which possesses a negative charge within a large pH interval (2–8) [55]. Firstly, chitosan was solubilized in 0.5 wt % acetic acid solution by magnetically stirring for 2 h. The chitosan concentration was set at 1 wt %. The chitosan solution was mixed with HNT aqueous dispersion (concentration equals 1 wt %). It should be noted that the HNT dispersion was prepared in two different media (water and 0.5 mol L⁻¹ NaCl aqueous solution) in order to explore the effect of the ionic strength on the chitosan-coating efficiency. The obtained mixtures were ultrasonicated for 2 min and, subsequently, stirred for 30 min. Finally, the chitosan/HNT/khellin composites were separated by the aqueous solution through centrifugation (10 min at 7000 rpm). Similarly to the khellin loading into HNT cavity, all steps were performed at room temperature.

2.4. Khellin Release Experiments

The kinetics of khellin release from HNT and chitosan-coated HNT nanocarriers were investigated by UV-VIS spectroscopy (Analytik, Jena, Germany) using the approach reported elsewhere [61]. Specifically, 100 mg of the composite (HNT/khellin or chitosan/HNT/khellin samples) was immersed in 30 mL of water (pH = 6), which represents the release medium. After a fixed time interval, 2 mL of aqueous medium was taken and investigated by UV-Vis spectroscopy to determine the khellin concentration. Meanwhile, 2 mL of fresh solution (water at pH = 6) was added to the release medium in order to maintain its volume at a constant. The release experiments were conducted up to 5 h. As V and V_0 were equal to 2 and 30 mL, respectively, the corrected khellin concentrations in the release medium at different times were calculated as follows [61]

$$C'_n = C_n + (V/V_0) \cdot \sum_{i=0}^{n-1} C_i \quad (1)$$

where C'_n and C_n represent the corrected and the measured khellin concentrations, respectively. The khellin release data were determined by considering the C'_n values.

2.5. Methods

2.5.1. ζ Potential

ζ -potential measurements were conducted by Zetasizer Nano-ZS (Malvern Instruments, London, UK) using disposable folded capillary cells. The experiments were conducted on 0.005 wt % aqueous dispersions of the investigated nanomaterials in isothermal conditions ($T = 25$ °C). Prior to

the measurements, the suspensions were ultrasonicated for 5 min to avoid the aggregation of the nanoparticles.

2.5.2. Scanning Electron Microscopy (SEM)

SEM analyses in high vacuum ($<6 \times 10^{-4}$ Pa) were carried out through the ESEM FEI QUANTA 200F microscope (Hillsboro, OR, USA). The energy of the beam was set at 25 kV, while the working distance was fixed at 10 mm.

2.5.3. Thermogravimetry

Thermogravimetric experiments were performed by using a Q5000 IR apparatus (TA Instruments, New Castle, DE, USA). The measurements were conducted under inert atmosphere using nitrogen flows for the sample and the balance (25 and $10 \text{ cm}^3 \text{ min}^{-1}$, respectively). The samples were heated (scanning rate of $20 \text{ }^\circ\text{C min}^{-1}$) from 25 to $800 \text{ }^\circ\text{C}$. According to the literature [62,63], the temperature calibration was carried out by exploiting the Curie temperatures of specific standards (nickel, cobalt, and their alloys). Thermogravimetric measurements were repeated three times for all the investigated samples. The average values with the corresponding standard deviations for the thermogravimetric parameters are presented.

2.5.4. UV-VIS Spectroscopy

UV-VIS spectra were registered by using the Specord S600 (Analytik, Jena, Germany) spectrophotometer within the wavelength range between 200 and 400 nm . To this purpose, quartz cuvettes were used. The khellin absorption peak at 250 nm was analyzed for the investigation of the release kinetics.

2.5.5. Water Contact Angle

Water contact angle experiments were conducted by using an optical contact angle apparatus (OCA 20, Data Physics Instruments, Filderstadt, Germany) equipped, with a video measuring system with a high-resolution CCD camera and a high-performance digitizing adapter. Data acquisition was conducted by SCA 20 software (Data Physics Instruments, Filderstadt, Germany). The initial contact angle (θ_i) of water in air was detected through the sessile drop method by placing a water droplet of $10 \pm 0.5 \text{ mL}$ onto the surface of the sample tablets. The tests were performed at $25.0 \pm 0.1 \text{ }^\circ\text{C}$. Each sample was analyzed three times. The average values with the corresponding standard deviation for the initial water contact angle are reported.

3. Results

3.1. Surface Charge and Morphological Characteristics

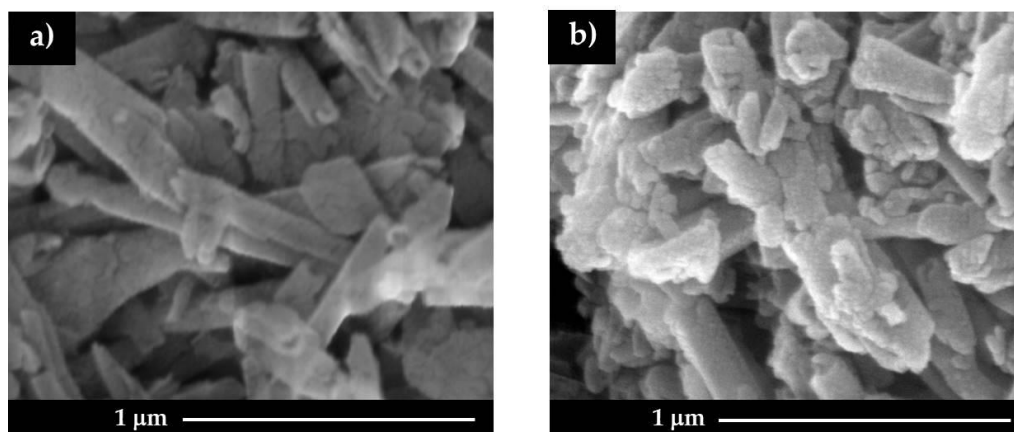
The surface charge of HNT/khellin and chitosan/HNT/khellin composite materials was investigated by ζ potential measurements. As shown in Table 1, the khellin loading into the HNT cavity did not significantly alter the ζ potential of halloysite, avoiding any electrostatic interactions between the drug and the internal surface of the clay nanotubes. This finding agrees with the hydrophobic character of khellin, which is encapsulated within the HNT cavity as a consequence of the solvent confinement [60]. The khellin confinement into the halloysite cavity was confirmed by water contact angle experiments, which evidenced that the θ_i values for HNT and HNT/khellin tablets are $30.5 \pm 1.1^\circ$ and $30.9 \pm 1.2^\circ$, respectively. These results indicate that the khellin loading did not alter the hydrophilic character of the HNT outer surface, demonstrating that the hydrophobic drug is mostly confined to the halloysite cavity.

Table 1. ζ potential for halloysite nanotubes (HNT), HNT/khellin and chitosan/HNT/khellin composite materials.

Material	ζ Potential/mV
HNT	-20.0 ± 0.6
HNT/khellin	-21.5 ± 0.3
Chitosan/HNT/khellin (NaCl)	$+23.5 \pm 0.8$
Chitosan/HNT/khellin	-18.5 ± 0.4

As concerns the chitosan/HNT/khellin composites, we observed that the presence of NaCl strongly affects the ζ potential of the polymer coated nanotubes. In particular, an inversion of ζ potential (from negative to positive) was detected after the chitosan coating was conducted in NaCl aqueous solution. On this basis, we can assert that electrostatic attractions between cationic chitosan and the HNT outer surface (negatively charged) take place. As reported for alkyltrimethylammonium bromides/HNT hybrids [43], the effective adsorption of cationic molecules neutralizes the negative charges of the HNT shell, causing an inversion in the ζ potential. In contrast, the coating procedure in water generated a slight decrease in the HNT surface charge. These results highlighted that the chitosan coating efficiency is remarkably improved in aqueous medium with higher ionic strength. The chitosan coating generated the hydrophobization of the HNT outer surface, as evidenced by the significant enhancements of the θ_i values ($75 \pm 2^\circ$ and $80 \pm 3^\circ$ in water and NaCl solution, respectively) compared to that of the HNT/khellin composite ($30.9 \pm 1.2^\circ$). In this regard, Lvov et al. [64] evidenced that the addition of small amounts of electrolyte is used in the layer by layer technique because of the “rod-to-coil” transition of polyelectrolytes in solution. Additionally, it is reported that the increase in the ionic strength enhances the chitosan flexibility [65].

SEM images (Figure 1) show that the hollow tubular morphology of halloysite was preserved in both HNT/khellin and chitosan/HNT/khellin hybrid prepared in NaCl solution. We observed that the nanotubes are glued to each other after their coating with chitosan.

**Figure 1.** SEM images for HNT/khellin (a) and HNT/khellin coated with chitosan in NaCl solution (b).

3.2. Thermal Properties

3.2.1. HNT/Khellin

Figure 2 compares the thermogravimetric (TG) curve of HNT/khellin hybrid with those of the pristine components (HNT and khellin).

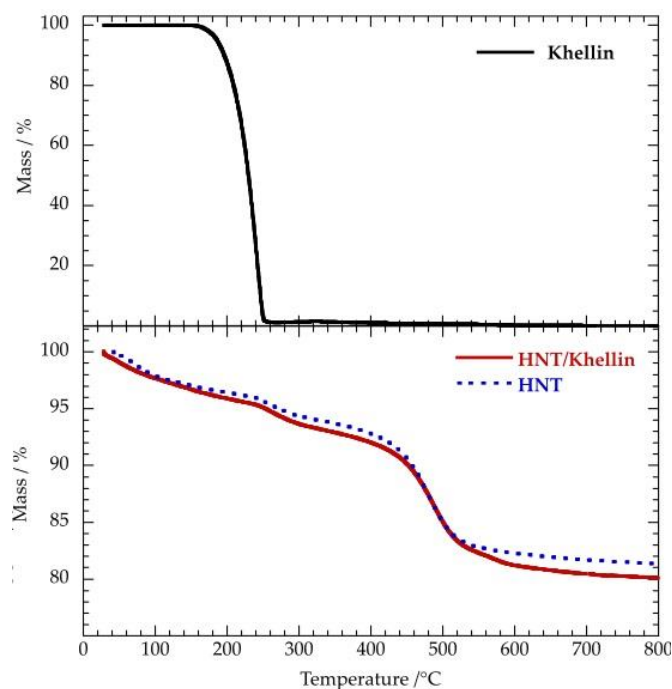


Figure 2. Thermogravimetric curves for Khellin, HNT and HNT/Khellin.

We observed that khellin totally decomposes in one single step occurring in the temperature range between 200 and 300 °C, while both HNT and HNT/khellin exhibit three different mass losses at 25–150, 200–300 and 450–550 °C. As reported elsewhere [66], the mass reduction from room temperature to 150 °C reflects the loss of the physically adsorbed water molecules. On the other hand, the mass change at 450–550 °C can be attributed to the expulsion of the interlayer water molecules that are present in the structure of halloysite mineral [66]. The mass change at 200–300 °C was enhanced in the loaded nanotubes, highlighting the successful khellin loading into the HNT cavity. According to the literature [60], we calculated the loading efficiency by considering the mass losses at 25–150 °C (ML_{150}) and the residual masses at 800 °C (MR_{800}) for the pure components and the composite material. Table 2 collects the ML_{150} and MR_{800} values of khellin, HNT and HNT/khellin samples.

Table 2. Thermogravimetric parameters of Khellin, HNT and HNT/Khellin composite.

Material	$ML_{150}/wt\%$	$MR_{800}/wt\%$	$MD_{800}/wt\%$
Khellin	0	0	100
HNT	2.93 ± 0.04	81.4 ± 1.2	15.7 ± 0.2
HNT/khellin	3.27 ± 0.04	80.2 ± 1.1	16.5 ± 0.2

The degraded matters at 800 °C (MD_{800}) for each sample was determined as

$$MD_{800} = 100 - (MR_{800} + ML_{150}) \tag{2}$$

Based on the rule of mixture [60], the MD_{800} of HNT/khellin composite (MD_{800-KH}) can be expressed as

$$MD_{800-HK} = (C_H \cdot MD_{800-H} + C_K \cdot MD_{800-K})/100 \tag{3}$$

where MD_{800-K} and MD_{800-H} are the degraded matters at 800 °C for khellin and HNT, respectively, whereas C_K and C_H represent the mass percentages of halloysite and khellin, respectively.

The combination of Equations (2) and (3) allowed us to estimate the khellin loading (1.03 ± 0.02 wt %) in the composite material on the basis of the thermogravimetric parameters presented in Table 2.

3.2.2. Chitosan/HNT/Khellin

The thermal effects of the chitosan coating on the khellin loaded nanotubes were investigated by thermogravimetry. Within this, Figure 3 shows the TG curves for chitosan and chitosan/HNT/khellin composites.

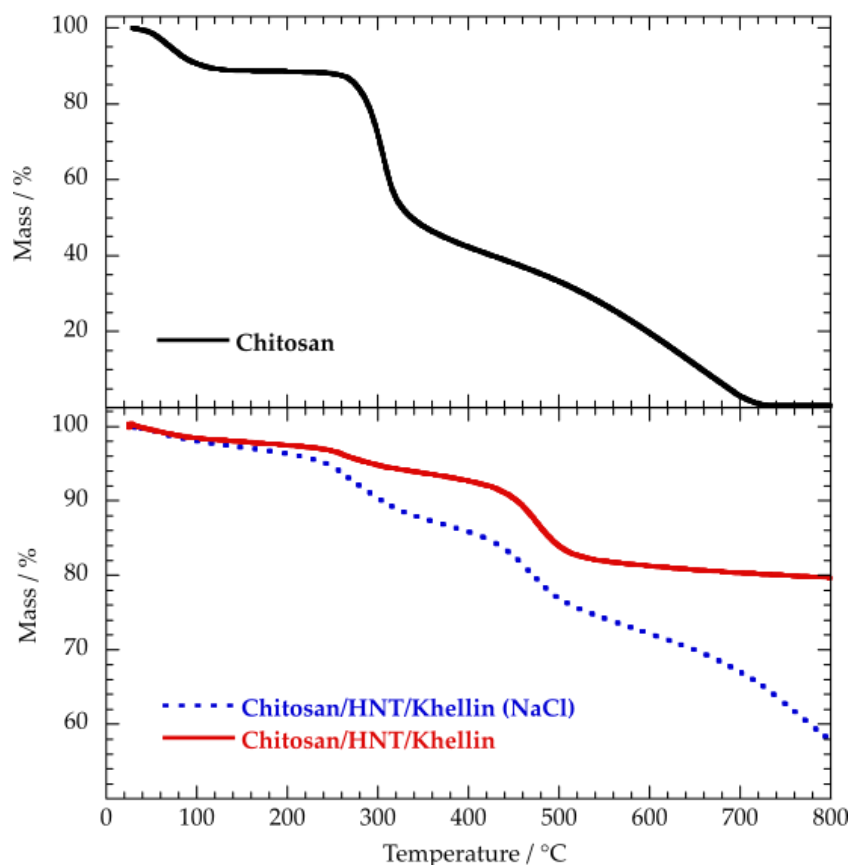


Figure 3. Thermogravimetric curves for chitosan and chitosan/HNT/khellin samples.

The TG curve of chitosan evidenced three mass losses that can be related to different processes. As reported in the previous paragraph, the mass reduction up to 150 °C reflects the moisture content of the material. The mass loss at 250–400 °C is due to the depolymerisation/decomposition of chitosan chains as a consequence of the deacetylation and cleavage of glycosidic bonds [67]. The last degradation step is caused by the decomposition of pyranose ring and residual carbon [68]. The corresponding mass loss was detected in the temperature interval between 400 and 700 °C. The thermogravimetric curves of the chitosan/HNT/khellin composites (Figure 3) evidenced that the presence of NaCl strongly affects the thermal behavior of the polymer coated nanotubes. As shown in Table 3, the MR_{800} value is much larger for the composite prepared with the electrolyte, highlighting its larger thermal stability.

Table 3. Thermogravimetric parameters of Chitosan and Chitosan/HNT/Khellin samples.

Material	$ML_{150}/wt\%$	$MR_{800}/wt\%$	$MD_{800}/wt\%$
Chitosan	11.3 ± 0.2	0	88.7 ± 1.5
Chitosan/HNT/Khellin (NaCl)	2.88 ± 0.03	57.9 ± 0.6	33.2 ± 0.3
Chitosan/HNT/Khellin	2.11 ± 0.03	79.6 ± 0.9	18.2 ± 0.3

Interestingly, the last degradation step of chitosan was clearly detected only for the composite prepared in the NaCl aqueous solution. This result could be quantitatively explained on the basis of ζ potential experiments, which highlighted that the chitosan-coating efficiency can be enhanced by increasing the ionic strength of the aqueous medium. In addition, we observed that the thermal decomposition of the pyranose ring and residual carbon is shifted to a larger temperature range, indicating that chitosan was thermally stabilized by its electrostatic interactions with the halloysite external surface. We calculated the chitosan coating efficiencies by using the rule of mixtures on the degraded masses at 800 °C, using the same approach employed for the determination of the khellin loading. Accordingly, the MD₈₀₀ of chitosan/HNT/khellin (MD_{800-CHK}) can be expressed by the following equation:

$$MD_{800-CHK} = (C_{HK} \cdot MD_{800-HK} + C_C \cdot MD_{800-C})/100 \quad (4)$$

MD_{800-C} represents the degraded mass at 800 °C of chitosan, while C_C represents its mass percent in the coated nanotubes.

Based on Equations (2) and (4) and taking into account the thermogravimetric parameters (Table 3), we estimated that the biopolymer amount in the chitosan/HNT/khellin prepared in water is 2.38 ± 0.03 wt %. The coating efficiency was significantly improved by dispersing chitosan in NaCl aqueous solution and water, as evidenced by the biopolymer content (31.4 ± 0.3 wt %) of the coated nanotubes. These results could be related to the effect of the electrolyte on the chitosan chains' flexibility.

3.3. Khellin Release Experiments

The effect of the chitosan coating on the khellin release from halloysite nanotubes was investigated at variable pH conditions. Figure 4 shows the khellin release kinetics under neutral conditions for HNT and HNT coated with chitosan. As a general result, the adsorption of chitosan onto the HNT outer surface slowed down the khellin release from the halloysite cavity. In this regard, the amount of khellin released after 6 h was 78% for uncoated nanotubes. This percentage was reduced in the chitosan/HNT nanocarriers (62 and 28% for the composites prepared in water and NaCl solution, respectively). These results are consistent with the ζ potential and TGA experiments, which evidenced that the presence of electrolyte improved the chitosan-coating efficiency of the nanotubes. Namely, the nanotubes coated in the NaCl solution are more effective in controlling the khellin release because of the larger amount of chitosan on the HNT shell. The khellin release profiles were analyzed using the Korsmeyer–Peppas model, which is expressed by the following equation

$$R\% = k \cdot t^n \quad (5)$$

where R% is the drug percentage release at a certain time (t), while k and n are the kinetic constant and the release exponent, respectively. It should be noted that this equation is valid for R% ≤ 80%, as evidenced for drug release from polymer/HNT hybrids [43]. The obtained fitting parameters are presented in Table 4. Compared to the HNT-based carrier, the kinetic contact was reduced in the coated nanotubes, confirming the chitosan-retarding effect on the drug release. As expected, this effect is stronger for the coated nanotubes obtained in the NaCl aqueous solution. In general, the release data reflect a Fickian diffusion mechanism being that the n values are lower than 0.43 for all the nanocarriers [43].

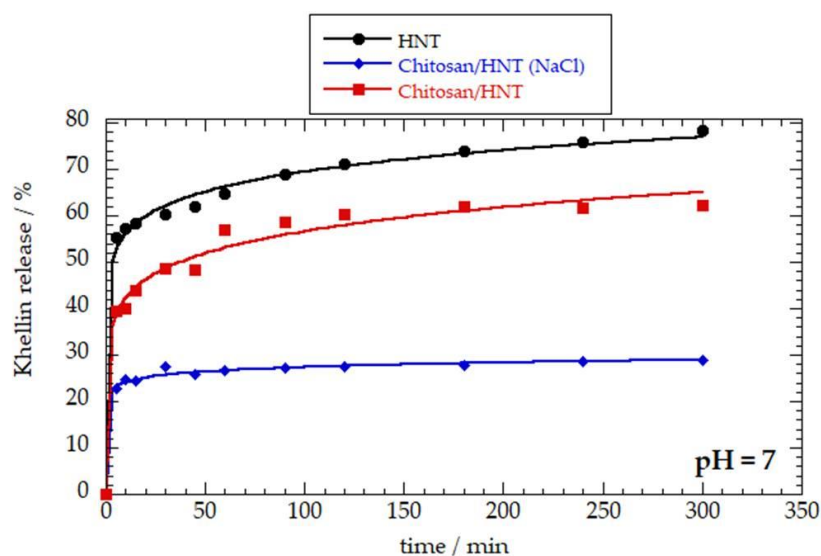


Figure 4. Khellin release as a function of time in water under neutral conditions (pH = 7). Solid lines represent the fitting according to the Korsmeyer–Peppas model (Equation (5)).

Table 4. Fitting Parameters for khellin release at pH = 7.

Nanocarrier	k/min^{-n}	n
HNT	45.46 ± 1.14	0.092 ± 0.006
Chitosan/HNT (NaCl)	21.6 ± 0.5	0.052 ± 0.006
Chitosan/HNT	31.7 ± 1.6	0.12 ± 0.01

We explored the influence of pH on the khellin release from chitosan/HNT hybrid carriers (Figure 5). As previously shown in Figure 4, the release data were fitted by using Equation (5). Table 5 shows that the chitosan retarding effect was reduced under acidic conditions, as evidenced by the lower k values with respect to those obtained at pH = 9. These results can be attributed to the enhanced chitosan solubility in water at $\text{pH} \leq 4$ [69]. As observed at pH = 7, the khellin release is slower for the nanotubes coated in NaCl solution. This finding is valid for both basic and acidic conditions. Finally, the n values (<0.43) highlight that the release mechanism for all the investigated systems can be ascribed to the Fickian diffusion.

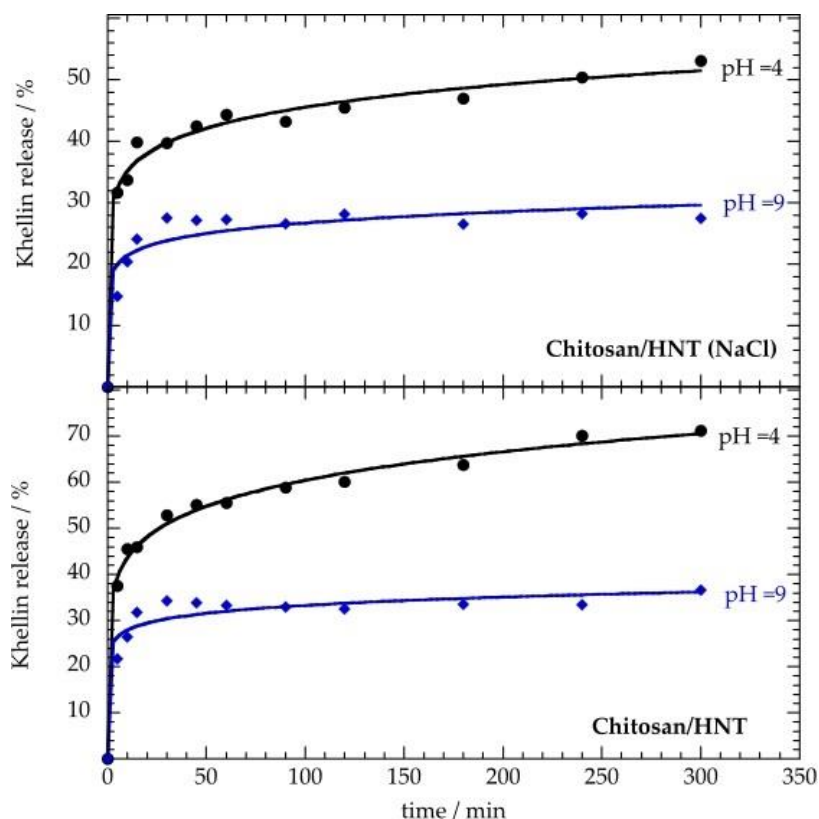


Figure 5. Khellin release as a function of time in water under acidic (pH = 4) and basic (pH = 9) conditions. Solid lines represent the fitting according to the Korsmeyer–Peppas model (Equation (5)).

Table 5. Fitting parameters for khellin release under acidic (pH = 4) and basic (pH = 9) conditions.

Nanocarrier	pH	k/min^{-n}	n
Chitosan/HNT (NaCl)	4	27.2 ± 1.1	0.112 ± 0.009
Chitosan/HNT (NaCl)	9	17.2 ± 1.9	0.09 ± 0.02
Chitosan/HNT	4	31.6 ± 1.1	0.141 ± 0.007
Chitosan/HNT	9	23 ± 2	0.08 ± 0.02

4. Discussion

The application value of chitosan/HNT hybrid as nanocarrier for khellin was highlighted by the release experiments conducted at variable pH simulating the typical conditions along the human gastro-intestinal path, which moves from acidic (stomach) to basic (colon) conditions. Within this, it should be pointed out that khellin is largely used by oral administration. As a general result, the release kinetics were successfully analyzed by the Korsmeyer–Peppas model. The release mechanism (Fickian diffusion) was not affected by either pH or chitosan coating, with the release exponent (n) being ≤ 0.43 for all the kinetics (Tables 4 and 5). We observed that the chitosan coated onto the nanotubes in NaCl solution is more effective in controlling the khellin release compared to those without NaCl. This observation is valid at pH = 7 (Figure 4) as well under acidic/basic conditions (Figure 5). These results could be related to the larger amount of coated chitosan onto the nanotubes in NaCl solution with respect to that in water as a consequence of the influence of the electrolyte on the flexibility of the polymeric chains. Specifically, the increase in the solvent ionic strength makes chitosan more flexible in agreement with the reduction in the repulsive interactions between the polymeric chains [65]. We can hypothesize that the chitosan coating layer onto HNT is thicker in NaCl solution and, consequently, the controlling efficiency on the khellin release is more effective. As shown in Figures 4 and 5, the final drug release is lower than 100% for all the investigated systems in

acidic, neutral and basic conditions. Similar observations were detected for the aspirin release from pristine and APTES modified halloysite, which exhibited final drug releases of 89 and 68%, respectively, at pH = 6.8 [70]. The final curcumin releases from thiahelicene-grafted HNT were ca. 10 and 3% at pH = 5 and 6.8, respectively [71]. Recent reviews [40,72] evidenced that halloysite nanotubes (both pristine and functionalized ones) are considered promising drug delivery systems, although the 100% release is not achieved.

5. Conclusions

We demonstrated that the specific electrostatic attractions between halloysite outer surface and the cationic chitosan are effective to obtain composite tubular nanocarriers with controlled release properties towards khellin. The preparation of the chitosan/halloysite/khellin hybrid was conducted in aqueous medium on the basis of the following steps: (1) loading of khellin into the halloysite cavity; (2) chitosan coating of halloysite shell. The latter was carried out both in water and in NaCl aqueous medium to explore the effect of the ionic strength on the polymer coating efficiency. Scanning Electron Microscopy evidenced that the hollow tubular shape of halloysite was not altered by the khellin loading or the chitosan coating. The ζ potential of halloysite was not significantly affected by the encapsulated khellin (1.03 wt %), avoiding the presence of electrostatic interactions between the drug molecule and the nanotubes. In contrast, the surface charge of halloysite was influenced by the chitosan coating. Remarkably, an inversion in the halloysite ζ potential was detected by the chitosan wrapping conducted in NaCl solution, highlighting that the biopolymer/nanoclay interactions are favored by the electrolyte addition. According to these results, the coating efficiency was improved by ca. 10% in NaCl solution compared to that in water. Water contact angle experiments evidenced that the hydrophilic character of halloysite is not affected by khellin loading, confirming the drug's confinement into the HNT cavity. On the other hand, the chitosan coating generated a significant hydrophobization of HNT/khellin composite as a consequence of the biopolymer adsorption onto the HNT shell. The presence of chitosan onto halloysite outer surface slowed down the khellin release. This effect is stronger for chitosan-coated nanotubes prepared in NaCl solution, as expected by ζ potential and thermogravimetric data. Release kinetics at variable pH evidenced that the chitosan retarding effect decreases under acidic conditions. Based on these considerations, we can conclude that the chitosan coating of halloysite nanotubes driven by electrostatic interactions can be considered a suitable strategy to obtain drug delivery systems with tunable properties.

Author Contributions: Conceptualization, G.L. and S.M.; methodology, G.C.; software, G.C.; validation, G.C., G.L. and S.M.; formal analysis, G.C.; investigation, L.L.; resources, S.M.; data curation, G.C.; writing—original draft preparation, L.L.; writing—review and editing, G.C.; visualization, G.C.; supervision, G.L.; project administration, S.M.; funding acquisition, S.M. All authors have read and agreed to the published version of the manuscript.

Funding: The work was financially supported by University of Palermo and Progetto di ricerca e sviluppo “AGM for CuHe” (ARS01_00697).

Conflicts of Interest: The authors declare no conflict of interest.

References

1. Xie, M.; Huang, K.; Yang, F.; Wang, R.; Han, L.; Yu, H.; Ye, Z.; Wu, F. Chitosan nanocomposite films based on halloysite nanotubes modification for potential biomedical applications. *Int. J. Biol. Macromol.* **2020**, *151*, 1116–1125. [[CrossRef](#)] [[PubMed](#)]
2. Velmurugan, S.; Palanisamy, S.; Yang, T.C.; Gochoo, M.; Chen, S.-W. Ultrasonic assisted functionalization of MWCNT and synergistic electrocatalytic effect of nano-hydroxyapatite incorporated MWCNT-chitosan scaffolds for sensing of nitrofurantoin. *Ultrason. Sonochem.* **2020**, *62*, 104863. [[CrossRef](#)] [[PubMed](#)]
3. Radwan-Pragłowska, J.; Janus, Ł.; Piątkowski, M.; Bogdał, D.; Matýsek, D. Hybrid Bilayer PLA/Chitosan Nanofibrous Scaffolds Doped with ZnO, Fe₃O₄, and Au Nanoparticles with Bioactive Properties for Skin Tissue Engineering. *Polymers* **2020**, *12*, 159. [[CrossRef](#)] [[PubMed](#)]

4. Nastyshyn, S.; Raczowska, J.; Stetsyshyn, Y.; Orzechowska, B.; Bernasik, A.; Shymborska, Y.; Brzychczy-Włoch, M.; Gosiewski, T.; Lishchynskiy, O.; Ohar, H.; et al. Non-cytotoxic, temperature-responsive and antibacterial POEGMA based nanocomposite coatings with silver nanoparticles. *RSC Adv.* **2020**, *10*, 10155–10166. [[CrossRef](#)]
5. Govindasamy, K.; Dahlan, N.A.; Janarthanan, P.; Goh, K.L.; Chai, S.-P.; Pasbakhsh, P. Electrospun chitosan/polyethylene-oxide (PEO)/halloysites (HAL) membranes for bone regeneration applications. *Appl. Clay Sci.* **2020**, *190*, 105601. [[CrossRef](#)]
6. Lisuzzo, L.; Cavallaro, G.; Parisi, F.; Milioto, S.; Fakhrullin, R.; Lazzara, G. Core/Shell Gel Beads with Embedded Halloysite Nanotubes for Controlled Drug Release. *Coatings* **2019**, *9*, 70. [[CrossRef](#)]
7. Koosha, M.; Hamed, S. Intelligent Chitosan/PVA nanocomposite films containing black carrot anthocyanin and bentonite nanoclays with improved mechanical, thermal and antibacterial properties. *Prog. Org. Coat.* **2019**, *127*, 338–347. [[CrossRef](#)]
8. Wu, Y.; Rashidpour, A.; Almajano, M.-P.; Metón, I. Chitosan-Based Drug Delivery System: Applications in Fish Biotechnology. *Polymers* **2020**, *12*, 1177. [[CrossRef](#)]
9. Rebitski, E.P.; Souza, G.P.; Santana, S.A.A.; Pergher, S.B.C.; Alcântara, A.C.S. Bionanocomposites based on cationic and anionic layered clays as controlled release devices of amoxicillin. *Appl. Clay Sci.* **2019**, *173*, 35–45. [[CrossRef](#)]
10. Rebitski, E.P.; Alcântara, A.C.S.; Darder, M.; Cansian, R.L.; Gómez-Hortigüela, L.; Pergher, S.B.C. Functional Carboxymethylcellulose/Zein Bionanocomposite Films Based on Neomycin Supported on Sepiolite or Montmorillonite Clays. *ACS Omega* **2018**, *3*, 13538–13550. [[CrossRef](#)]
11. García-Quiles, L.; Valdés, A.; Cuello, Á.F.; Jiménez, A.; Garrigós, M.C.; Castell, P. Reducing off-Flavour in Commercially Available Polyhydroxyalkanoate Materials by Autooxidation through Compounding with Organoclays. *Polymers* **2019**, *11*, 945. [[CrossRef](#)] [[PubMed](#)]
12. Gorrasi, G. Dispersion of halloysite loaded with natural antimicrobials into pectins: Characterization and controlled release analysis. *Carbohydr. Polym.* **2015**, *127*, 47–53. [[CrossRef](#)] [[PubMed](#)]
13. Gorrasi, G.; Pantani, R.; Murariu, M.; Dubois, P. PLA/Halloysite Nanocomposite Films: Water Vapor Barrier Properties and Specific Key Characteristics. *Macromol. Mater. Eng.* **2014**, *299*, 104–115. [[CrossRef](#)]
14. Cavallaro, G.; Chiappisi, L.; Pasbakhsh, P.; Gradzielski, M.; Lazzara, G. A structural comparison of halloysite nanotubes of different origin by Small-Angle Neutron Scattering (SANS) and Electric Birefringence. *Appl. Clay Sci.* **2018**, *160*, 71–80. [[CrossRef](#)]
15. Makaremi, M.; De Silva, R.T.; Pasbakhsh, P. Electrospun Nanofibrous Membranes of Polyacrylonitrile/Halloysite with Superior Water Filtration Ability. *J. Phys. Chem. C* **2015**, *119*, 7949–7958. [[CrossRef](#)]
16. Mostafa, M.H.; ElSawy, M.A.; Darwish, M.S.A.; Hussein, L.I.; Abdaleem, A.H. Microwave-Assisted preparation of Chitosan/ZnO nanocomposite and its application in dye removal. *Mater. Chem. Phys.* **2020**, *248*, 122914. [[CrossRef](#)]
17. Peng, Q.; Liu, M.; Zheng, J.; Zhou, C. Adsorption of dyes in aqueous solutions by chitosan–halloysite nanotubes composite hydrogel beads. *Microporous Mesoporous Mater.* **2015**, *201*, 190–201. [[CrossRef](#)]
18. Cavallaro, G.; Milioto, S.; Nigamatzyanova, L.; Akhatova, F.; Fakhrullin, R.; Lazzara, G. Pickering Emulsion Gels Based on Halloysite Nanotubes and Ionic Biopolymers: Properties and Cleaning Action on Marble Surface. *ACS Appl. Nano Mater.* **2019**, *2*, 3169–3176. [[CrossRef](#)]
19. Cavallaro, G.; Milioto, S.; Lazzara, G. Halloysite Nanotubes: Interfacial Properties and Applications in Cultural Heritage. *Langmuir* **2020**, *36*, 3677–3689. [[CrossRef](#)]
20. Cavallaro, G.; Lazzara, G.; Milioto, S.; Parisi, F.; Ruisi, F. Nanocomposites based on esterified colophony and halloysite clay nanotubes as consolidants for waterlogged archaeological woods. *Cellulose* **2017**, *24*, 3367–3376. [[CrossRef](#)]
21. Bertolino, V.; Cavallaro, G.; Milioto, S.; Lazzara, G. Polysaccharides/Halloysite nanotubes for smart bionanocomposite materials. *Carbohydr. Polym.* **2020**, *245*, 116502. [[CrossRef](#)] [[PubMed](#)]
22. Li, J.; Wu, Y.; Zhao, L. Antibacterial activity and mechanism of chitosan with ultra high molecular weight. *Carbohydr. Polym.* **2016**, *148*, 200–205. [[CrossRef](#)] [[PubMed](#)]
23. Rinaudo, M. Chitin and chitosan: Properties and applications. *Prog. Polym. Sci.* **2006**, *31*, 603–632. [[CrossRef](#)]
24. Rubina, M.; Shulenina, A.; Svetogorov, R.; Vasilkov, A. Metal-Chitosan Nanocomposites: A Perspective Way to Preparation, Morphology, and Structural Studies. *Macromol. Symp.* **2020**, *389*, 1900067. [[CrossRef](#)]

25. Ali, F.I.; Mahmoud, S.T.; Awwad, F.; Greish, Y.E.; Abu-Hani, A.F. Low power consumption and fast response H₂S gas sensor based on a chitosan-CuO hybrid nanocomposite thin film. *Carbohydr. Polym.* **2020**, *236*, 116064. [[CrossRef](#)] [[PubMed](#)]
26. Benucci, I.; Liburdi, K.; Cacciotti, I.; Lombardelli, C.; Zappino, M.; Nanni, F.; Esti, M. Chitosan/clay nanocomposite films as supports for enzyme immobilization: An innovative green approach for winemaking applications. *Food Hydrocoll.* **2018**, *74*, 124–131. [[CrossRef](#)]
27. Ying, R.; Wang, H.; Sun, R.; Chen, K. Preparation and properties of a highly dispersed nano-hydroxyapatite colloid used as a reinforcing filler for chitosan. *Mater. Sci. Eng. C* **2020**, *110*, 110689. [[CrossRef](#)]
28. Li, X.; Li, Y.-C.; Chen, M.; Shi, Q.; Sun, R.; Wang, X. Chitosan/rectorite nanocomposite with injectable functionality for skin hemostasis. *J. Mater. Chem. B* **2018**, *6*, 6544–6549. [[CrossRef](#)]
29. Neji, A.B.; Jridi, M.; Kchaou, H.; Nasri, M.; Sahnoun, R.D. Preparation, characterization, mechanical and barrier properties investigation of chitosan-kaolinite nanocomposite. *Polym. Test.* **2020**, *84*, 106380. [[CrossRef](#)]
30. Bertolino, V.; Cavallaro, G.; Lazzara, G.; Milioto, S.; Parisi, F. Biopolymer-Targeted Adsorption onto Halloysite Nanotubes in Aqueous Media. *Langmuir* **2017**, *33*, 3317–3323. [[CrossRef](#)]
31. Liu, M.; Wu, C.; Jiao, Y.; Xiong, S.; Zhou, C. Chitosan-halloysite nanotubes nanocomposite scaffolds for tissue engineering. *J. Mater. Chem. B* **2013**, *1*, 2078–2089. [[CrossRef](#)]
32. Lim, S.; Park, S.; Sohn, D. Modification of halloysite nanotubes for enhancement of gas-adsorption capacity. *Clays Clay Miner.* **2020**. [[CrossRef](#)]
33. Joo, Y.; Sim, J.H.; Jeon, Y.; Lee, S.U.; Sohn, D. Opening and blocking the inner-pores of halloysite. *Chem. Commun.* **2013**, *49*, 4519–4521. [[CrossRef](#)]
34. Sadjadi, S.; Heravi, M.M.; Kazemi, S.S. Ionic liquid decorated chitosan hybridized with clay: A novel support for immobilizing Pd nanoparticles. *Carbohydr. Polym.* **2018**, *200*, 183–190. [[CrossRef](#)] [[PubMed](#)]
35. Liu, Y.; Guan, H.; Zhang, J.; Zhao, Y.; Yang, J.; Zhang, B. Polydopamine-coated halloysite nanotubes supported AgPd nanoalloy: An efficient catalyst for hydrolysis of ammonia borane. *Int. J. Hydrogen Energy* **2018**, *43*, 2754–2762. [[CrossRef](#)]
36. Liu, Y.; Zhang, J.; Guan, H.; Zhao, Y.; Yang, J.-H.; Zhang, B. Preparation of bimetallic Cu-Co nanocatalysts on poly (diallyldimethylammonium chloride) functionalized halloysite nanotubes for hydrolytic dehydrogenation of ammonia borane. *Appl. Surf. Sci.* **2018**, *427*, 106–113. [[CrossRef](#)]
37. Feng, Y.; Zhou, X.; Yang, J.-H.; Gao, X.; Yin, L.; Zhao, Y.; Zhang, B. Encapsulation of Ammonia Borane in Pd/Halloysite Nanotubes for Efficient Thermal Dehydrogenation. *ACS Sustain. Chem. Eng.* **2020**, *8*, 2122–2129. [[CrossRef](#)]
38. Deng, L.; Yuan, P.; Liu, D.; Du, P.; Zhou, J.; Wei, Y.; Song, Y.; Liu, Y. Effects of calcination and acid treatment on improving benzene adsorption performance of halloysite. *Appl. Clay Sci.* **2019**, *181*, 105240. [[CrossRef](#)]
39. Song, Y.; Yuan, P.; Du, P.; Deng, L.; Wei, Y.; Liu, D.; Zhong, X.; Zhou, J. A novel halloysite-CeO_x nanohybrid for efficient arsenic removal. *Appl. Clay Sci.* **2020**, *186*, 105450. [[CrossRef](#)]
40. Lvov, Y.; Wang, W.; Zhang, L.; Fakhrullin, R. Halloysite Clay Nanotubes for Loading and Sustained Release of Functional Compounds. *Adv. Mater.* **2015**, *28*, 1227–1250. [[CrossRef](#)]
41. Dзамukova, M.R.; Naumenko, E.A.; Lvov, Y.M.; Fakhrullin, R. Enzyme-activated intracellular drug delivery with tubule clay nanoformulation. *Sci. Rep.* **2015**, *5*, 10560. [[CrossRef](#)] [[PubMed](#)]
42. Vergaro, V.; Lvov, Y.M.; Leporatti, S. Halloysite Clay Nanotubes for Resveratrol Delivery to Cancer Cells. *Macromol. Biosci.* **2012**, *12*, 1265–1271. [[CrossRef](#)] [[PubMed](#)]
43. Cavallaro, G.; Lazzara, G.; Milioto, S.; Parisi, F.; Evtugyn, V.; Rozhina, E.; Fakhrullin, R. Nanohydrogel Formation within the Halloysite Lumen for Triggered and Sustained Release. *ACS Appl. Mater. Interfaces* **2018**, *10*, 8265–8273. [[CrossRef](#)] [[PubMed](#)]
44. Fizir, M.; Dramou, P.; Dahiru, N.S.; Ruya, W.; Huang, T.; He, H. Halloysite nanotubes in analytical sciences and in drug delivery: A review. *Microchim. Acta* **2018**, *185*, 389. [[CrossRef](#)] [[PubMed](#)]
45. Dramou, P.; Fizir, M.; Taleb, A.; Itatahine, A.; Dahiru, N.S.; Mehdi, Y.A.; Wei, L.; Zhang, J.; He, H. Folic acid-conjugated chitosan oligosaccharide-magnetic halloysite nanotubes as a delivery system for camptothecin. *Carbohydr. Polym.* **2018**, *197*, 117–127. [[CrossRef](#)]
46. Liu, F.; Bai, L.; Zhang, H.; Song, H.; Hu, L.; Wu, Y.; Ba, X. Smart H₂O₂-Responsive Drug Delivery System Made by Halloysite Nanotubes and Carbohydrate Polymers. *ACS Appl. Mater. Interfaces* **2017**, *9*, 31626–31633. [[CrossRef](#)]

47. Cheng, C.; Gao, Y.; Song, W.; Zhao, Q.; Zhang, H.; Zhang, H. Halloysite nanotube-based H₂O₂-responsive drug delivery system with a turn on effect on fluorescence for real-time monitoring. *Chem. Eng. J.* **2020**, *380*, 122474. [[CrossRef](#)]
48. Cavallaro, G.; Milioto, S.; Parisi, F.; Lazzara, G. Halloysite Nanotubes Loaded with Calcium Hydroxide: Alkaline Fillers for the Deacidification of Waterlogged Archeological Woods. *ACS Appl. Mater. Interfaces* **2018**, *10*, 27355–27364. [[CrossRef](#)]
49. Joshi, A.; Abdullayev, E.; Vasiliev, A.; Volkova, O.; Lvov, Y. Interfacial Modification of Clay Nanotubes for the Sustained Release of Corrosion Inhibitors. *Langmuir* **2013**, *29*, 7439–7448. [[CrossRef](#)]
50. Zhao, X.; Wan, Q.; Fu, X.; Meng, X.; Ou, X.; Zhong, R.; Zhou, Q.; Liu, M. Toxicity Evaluation of One-Dimensional Nanoparticles Using *Caenorhabditis elegans*: A Comparative Study of Halloysite Nanotubes and Chitin Nanocrystals. *ACS Sustain. Chem. Eng.* **2019**, *7*, 18965–18975. [[CrossRef](#)]
51. Fakhrullina, G.I.; Akhatova, F.S.; Lvov, Y.M.; Fakhrullin, R. Toxicity of halloysite clay nanotubes in vivo: A *Caenorhabditis elegans* study. *Environ. Sci. Nano* **2015**, *2*, 54–59. [[CrossRef](#)]
52. Kryuchkova, M.; Danilushkina, A.; Lvov, Y.; Fakhrullin, R. Evaluation of toxicity of nanoclays and graphene oxide in vivo: A *Paramecium caudatum* study. *Environ. Sci. Nano* **2016**, *3*, 442–452. [[CrossRef](#)]
53. Long, Z.; Wu, Y.-P.; Gao, H.-Y.; Zhang, J.; Ou, X.; He, R.-R.; Liu, M. In vitro and in vivo toxicity evaluation of halloysite nanotubes. *J. Mater. Chem. B* **2018**, *6*, 7204–7216. [[CrossRef](#)] [[PubMed](#)]
54. Wang, X.; Gong, J.; Rong, R.; Gui, Z.; Hu, T.; Xu, X. Halloysite Nanotubes-Induced Al Accumulation and Fibrotic Response in Lung of Mice after 30-Day Repeated Oral Administration. *J. Agric. Food Chem.* **2018**, *66*, 2925–2933. [[CrossRef](#)] [[PubMed](#)]
55. Vergaro, V.; Abdullayev, E.; Lvov, Y.M.; Zeitoun, A.; Cingolani, R.; Rinaldi, R.; Leporatti, S.; Rinaldi, R. Cytocompatibility and Uptake of Halloysite Clay Nanotubes. *Biomacromolecules* **2010**, *11*, 820–826. [[CrossRef](#)]
56. Cavallaro, G.; Chiappisi, L.; Gradzielski, M.; Lazzara, G. Effect of the supramolecular interactions on the nanostructure of halloysite/biopolymer hybrids: A comprehensive study by SANS, fluorescence correlation spectroscopy and electric birefringence. *Phys. Chem. Chem. Phys.* **2020**, *22*, 8193–8202. [[CrossRef](#)]
57. Tully, J.; Yendluri, R.; Lvov, Y. Halloysite Clay Nanotubes for Enzyme Immobilization. *Biomacromolecules* **2016**, *17*, 615–621. [[CrossRef](#)]
58. Cavallaro, G.; Milioto, S.; Konnova, S.; Fakhrullina, G.; Akhatova, F.; Lazzara, G.; Fakhrullin, R.; Lvov, Y. Halloysite/Keratin Nanocomposite for Human Hair Photoprotection Coating. *ACS Appl. Mater. Interfaces* **2020**, *12*, 24348–24362. [[CrossRef](#)]
59. Cavallaro, G.; Grillo, I.; Gradzielski, M.; Lazzara, G. Structure of Hybrid Materials Based on Halloysite Nanotubes Filled with Anionic Surfactants. *J. Phys. Chem. C* **2016**, *120*, 13492–13502. [[CrossRef](#)]
60. Lisuzzo, L.; Cavallaro, G.; Pasbakhsh, P.; Milioto, S.; Lazzara, G. Why does vacuum drive to the loading of halloysite nanotubes? The key role of water confinement. *J. Colloid Interface Sci.* **2019**, *547*, 361–369. [[CrossRef](#)]
61. Lisuzzo, L.; Cavallaro, G.; Milioto, S.; Lazzara, G. Layered composite based on halloysite and natural polymers: A carrier for the pH controlled release of drugs. *New J. Chem.* **2019**, *43*, 10887–10893. [[CrossRef](#)]
62. Blanco, I.; Abate, L.; Bottino, F.A.; Bottino, P. Thermal behaviour of a series of novel aliphatic bridged polyhedral oligomeric silsesquioxanes (POSSs)/polystyrene (PS) nanocomposites: The influence of the bridge length on the resistance to thermal degradation. *Polym. Degrad. Stab.* **2014**, *102*, 132–137. [[CrossRef](#)]
63. Abate, L.; Bottino, F.A.; Cicala, G.; Chiacchio, M.A.; Ognibene, G.; Blanco, I. Polystyrene Nanocomposites Reinforced with Novel Dumbbell-Shaped Phenyl-POSSs: Synthesis and Thermal Characterization. *Polymer* **2019**, *11*, 1475. [[CrossRef](#)] [[PubMed](#)]
64. Lvov, Y.; Decher, G.; Moehwald, H. Assembly, structural characterization, and thermal behavior of layer-by-layer deposited ultrathin films of poly (vinyl sulfate) and poly (allylamine). *Langmuir* **1993**, *9*, 481–486. [[CrossRef](#)]
65. Morariu, S.; Brunchi, C.-E.; Bercea, M. The Behavior of Chitosan in Solvents with Different Ionic Strengths. *Ind. Eng. Chem. Res.* **2012**, *51*, 12959–12966. [[CrossRef](#)]
66. Duce, C.; Cipriotti, S.V.; Ghezzi, L.; Ierardi, V.; Tiné, M.R. Thermal behavior study of pristine and modified halloysite nanotubes. *J. Therm. Anal. Calorim.* **2015**, *121*, 1011–1019. [[CrossRef](#)]
67. Ziegler-Borowska, M.; Chelminiak, D.; Kaczmarek, H. Thermal stability of magnetic nanoparticles coated by blends of modified chitosan and poly(quaternary ammonium) salt. *J. Therm. Anal. Calorim.* **2015**, *119*, 499–506. [[CrossRef](#)]

68. Corazzari, I.; Nisticò, R.; Turci, F.; Faga, M.G.; Franzoso, F.; Tabasso, S.; Magnacca, G. Advanced physico-chemical characterization of chitosan by means of TGA coupled on-line with FTIR and GCMS: Thermal degradation and water adsorption capacity. *Polym. Degrad. Stab.* **2015**, *112*, 1–9. [[CrossRef](#)]
69. Fan, M.; Hu, Q.; Shen, K. Preparation and structure of chitosan soluble in wide pH range. *Carbohydr. Polym.* **2009**, *78*, 66–71. [[CrossRef](#)]
70. Lun, H.; Ouyang, J.; Yang, H. Natural halloysite nanotubes modified as an aspirin carrier. *RSC Adv.* **2014**, *4*, 44197–44202. [[CrossRef](#)]
71. Taroni, T.; Cauteruccio, S.; Vago, R.; Franchi, S.; Barbero, N.; Licandro, E.; Ardizzone, S.; Meroni, D. Thiahelicene-grafted halloysite nanotubes: Characterization, biological studies and pH triggered release. *Appl. Surf. Sci.* **2020**, *520*, 146351. [[CrossRef](#)]
72. Leporatti, S. Halloysite clay nanotubes as nano-bazookas for drug delivery. *Polym. Int.* **2017**, *66*, 1111–1118. [[CrossRef](#)]



© 2020 by the authors. Licensee MDPI, Basel, Switzerland. This article is an open access article distributed under the terms and conditions of the Creative Commons Attribution (CC BY) license (<http://creativecommons.org/licenses/by/4.0/>).

Communication

Core/Shell Gel Beads with Embedded Halloysite Nanotubes for Controlled Drug Release

Lorenzo Lisuzzo ¹, Giuseppe Cavallaro ², Filippo Parisi ¹, Stefana Milioto ²,
Rawil Fakhruллин ³ and Giuseppe Lazzara ^{2,*}

¹ Dipartimento di Fisica e Chimica, Università degli Studi di Palermo, Viale delle Scienze, pad. 17, 90128 Palermo, Italy; lorenzo.lisuzzo@unipa.it (L.L.); giuseppe.cavallaro@unipa.it (G.C.); filippo.parisi@unipa.it (F.P.)

² Dipartimento di Fisica e Chimica, Università degli Studi di Palermo, Viale delle Scienze, pad. 17, 90128 Palermo, Italy and Consorzio Interuniversitario Nazionale per la Scienza e Tecnologia dei Materiali, INSTM, Via G. Giusti 9, I-50121 Firenze, Italy; stefana.milioto@unipa.it

³ Institute of Fundamental Medicine and Biology, Kazan Federal University, Kremlyuramı 18, Kazan, Republic of Tatarstan 420008, Russia; kazanbio@gmail.com

* Correspondence: giuseppe.lazzara@unipa.it; Tel.: +39-091-2389-7962

Received: 15 November 2018; Accepted: 22 January 2019; Published: 24 January 2019



Abstract: The use of nanocomposites based on biopolymers and nanoparticles for controlled drug release is an attractive notion. We used halloysite nanotubes that were promising candidates for the loading and release of active molecules due to their hollow cavity. Gel beads based on chitosan with uniformly dispersed halloysite nanotubes were obtained by a dropping method. Alginate was used to generate a coating layer over the hybrid gel beads. This proposed procedure succeeded in controlling the morphology at the mesoscale and it had a relevant effect on the release profile of the model drug from the nanotube cavity.

Keywords: halloysite; alginate; chitosan; gel beads; drug release

1. Introduction

Researchers have defined hydrogels in many different ways, but nowadays the most accepted definition is the existence of a three-dimensional network, formed by the cross-linking of polymeric chains, that possesses the capability to swell thanks to the presence of hydrophilic groups and to maintain a very high amount of water in its structure [1,2]. Since their discovery, hydrogels have received attention from the scientific community due to the wide range of applications they can be used for: Environmental issues like water remediation, drug delivery systems and tissue engineering, cosmetic and food packaging industry, and oil spill recovery [3–8]. Furthermore, with the evolution of nanotechnology, the challenge to design and prepare hydrogels with specific and requested features at the nano-scale led to the development of nanohydrogels. Among the different polymeric species that can be used to achieve this aim, polysaccharides cover a marked importance, especially in the preparation of the so-called “polysaccharide-based natural hydrogels”, for some of their most peculiar properties such as water solubility and swelling capacity, biocompatibility and biodegradability, self-healing and pH sensitivity that are crucial for their use [9,10]. Moreover, the possibility to modify the structure of the polysaccharides and the adaptability of their networks allows for the development of eco-friendly smart materials [11,12]. To date, the most widely used raw materials include natural biopolymers such as chitosan, alginate, pectin and cellulose. One of the major factors limiting the use of nanohydrogels is their structural instability, thus making necessary the use, among others, of inorganic nanoparticles to overcome them [13–16].

Among clays, halloysite nanotubes (HNTs) have great importance thanks to their own main characteristics [17]. HNTs are a naturally occurring aluminosilicate whose structural formula is $\text{Al}_2\text{Si}_2\text{O}_5(\text{OH})_4 \cdot n\text{H}_2\text{O}$, where Al is disposed in an gibbsite-like octahedral organization of Al–OH groups whereas Si–O groups form a tetrahedral sheet [18,19]. Both aluminols and siloxanes layers are overlapped in a kaolinite typical sheet that rolls up due to some structural defects and to the presence of water molecules, thus giving halloysite its peculiar narrow nanotubular structure [20–22].

HNTs dimensions depend on the natural deposit the clay is extracted from. In particular, the internal and external diameters are approximately 10–15 and 50–80 nm respectively, while the nanotubes length can range from 100 nm to 2 μm . [19] Interestingly, it is possible to classify halloysite by considering the distance between interlayers. For instance, it can be 7 or 10 Å depending on the number of water molecules present between the layers, which is namely 0 or 2, respectively [23,24]. Moreover, one of halloysite's most fascinating and important features is the different charge, in the pH interval from 3 to 8, between the outer surface that is mainly composed of Si–O groups and negatively charged, and the inner surface that is mainly composed of Al–OH and positively charged [25,26]. This different charge, due to the chemical composition, allows for selective functionalization, exploiting both the covalent and electrostatic interactions of each surface with other oppositely charged species: Drug molecules, polysaccharides, proteins, lipids, surfactants and so on [27–29]. All these features, and also considering that they are low cost, eco- and biocompatible materials [30], make HNTs suitable for designing hybrid materials for waste water remediation [31–35], cultural heritage treatment [36,37], biotechnological applications [38–44], and packaging [45–50].

Notably, halloysite is commonly used as a component in drug delivery systems through exploiting its characteristics in combination with other organic moieties, for example the temperature responsive polymers such as poly(N-isopropylacrylamide) (PNIPAAms) that can selectively interact with the inner/outer surfaces thus influencing the release kinetics by changing their adsorption site [51], or natural occurring biopolymers for the preparation of end capped nanotubes with smart gates, or reverse inorganic micelles for the formation of nanohydrogels inside the HNTs lumen for a triggered absorption or release [52,53].

As evidenced in a recent review [17], the combination of polymer hydrogels and hollow inorganic nanotubes represents a perspective strategy for the fabrication of functional carriers in an advanced application.

In this work, we prepared hydrogel beads based on chitosan containing halloysite nanotubes. An alginate layer was introduced by diffusion and immersion of the beads in a sodium alginate solution. The dispersion of nanotubes into the hybrid gel and the localization of the alginate was investigated by SEM and fluorescence microscopy. Doxycycline, an antibiotic of the tetracycline class, was used as the model drug and it was loaded into the halloysite cavity by using a literature protocol [54]. This work represents a promising step for a valid alternative to generate hybrid hydrogels with oppositely charged polysaccharides and nanoclay with specific morphology for controlled drug release.

2. Results and Discussion

2.1. Morphology of the Hybrid Gel Beads

Figure 1 shows the optical image of the prepared chitosan/HNTs gel beads covered with a calcium alginate layer. They had an average diameter of 3.5 mm that shrank to 0.8 mm when dried. To highlight the halloysite nanotubes distribution in the beads, SEM images were taken and they showed the presence of halloysite nanotubes in a random orientation within the polymer matrix (Figure 1). Similar findings have been reported by us for alginate/halloysite gel beads [55]. The dispersibility of the nanoparticles could be explained by the affinity between the polymer and halloysite and the colloidal stability of the nanoclay in polymer solution [56]. It should be noted that the halloysite cavity did not interact with the chitosan polycation as the inner surface of the nanotubes was positively charged [26]. Therefore, the HNTs lumen was preserved for drug loading.

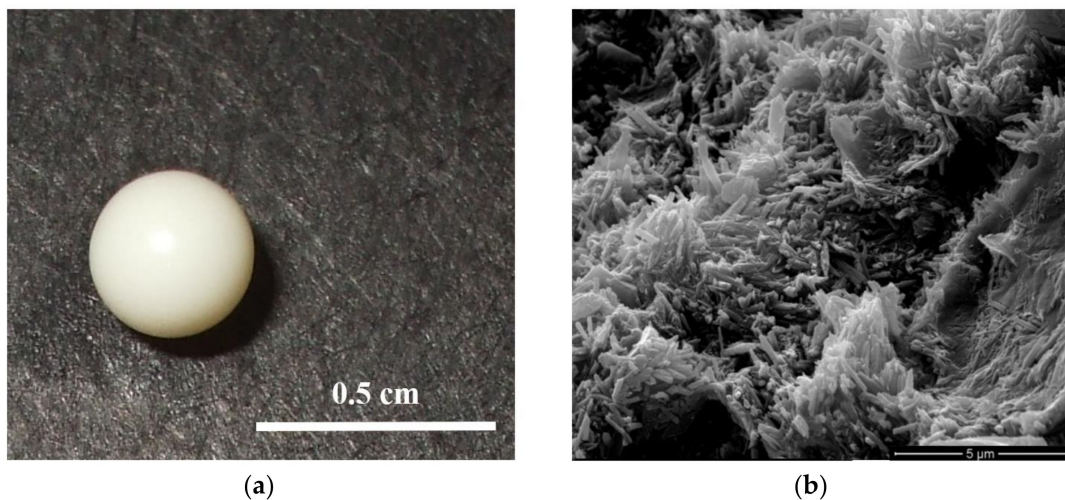


Figure 1. (a) Optical image of wet alginate/chitosan/halloysite nanotubes (HNTs) gel beads and (b) SEM image of the inner part of the dried gel beads.

Neither optical nor SEM imaging were able to identify the alginate location in the beads. We therefore thought to label the alginate polymer with a fluorescent probe 5-(4,6-dichlorotriazinyl) aminofluorescein (DTAF) that showed fluorescent emission when excited at 490 nm. Firstly, a blank experiment on chitosan/halloysite gel beads was carried out and negligible fluorescence was observed. The laser scanning confocal microscopy images on chitosan/HNTs gel beads covered with a calcium alginate layer clearly showed a fluorescent layer with an average thickness of approximately 130 μm , revealing that the diffusion of alginate into the chitosan/halloysite gel beads occurred up to a certain extent and the core of the beads was alginate free (Figure 2). On this basis, one could conclude that the simple preparation protocol allowed us to prepare a controlled complex architecture in mesoscopic scale that might be suitable for sustained release of active substances.

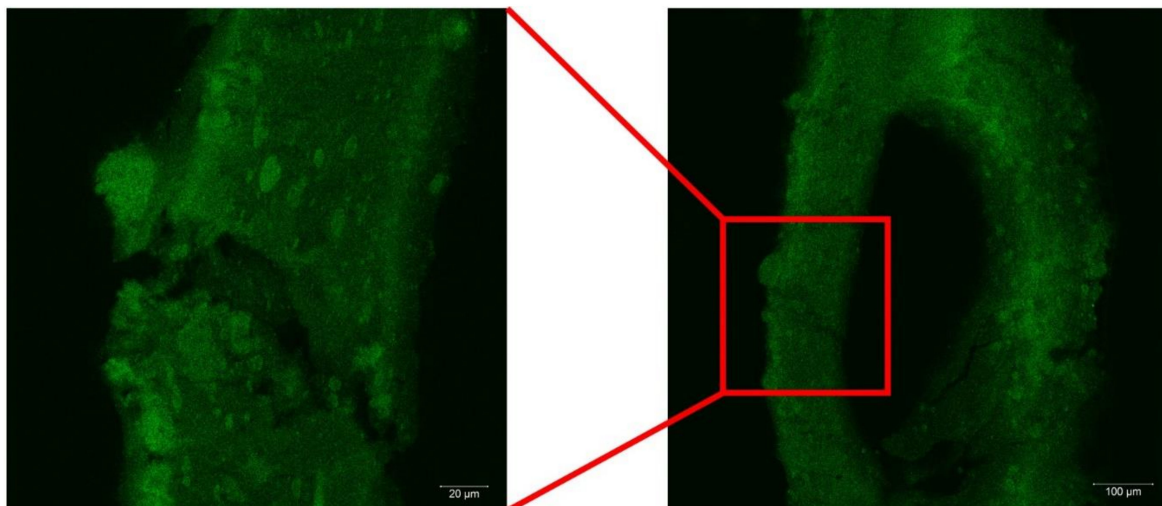


Figure 2. Laser scanning confocal microscopy images of alginate/chitosan/HNTs gel beads. Note that Alginate was labelled with 5-(4,6-dichlorotriazinyl) aminofluorescein (DTAF).

2.2. Drug Release Experiments

Release experiments were carried out by using doxycycline chlorohydrate as a model drug that could be loaded into the halloysite nanotubes [54]. The pK value for the drug was approximately 3 and the solubility dropped down as soon as the non-ionic form was obtained at $\text{pH} > \text{pK}$. Therefore, under our experimental conditions the drug was always neutral. The release profiles in water are

provided in Figure 3 for doxycycline from halloysite nanotubes, chitosan/HNTs dried beads and alginate/chitosan/HNTs dried beads. It was clearly observed that halloysite incorporation into chitosan gel beds only slightly slowed down the drug release from being fully available in the solvent media in 20 min. The sustained release was due to the slow release of the drug from the nanotube cavity and the subsequent drug diffusion through the polymer matrix to the solvent. The presence of an alginate coating significantly slowed down the doxycycline release from the hybrid beads. In particular after 20 min only 50% of the drug was released into the solvent media while a full release occurs in more than 80 min. These results could be interpreted by considering that the alginate shell in combination with the oppositely charged chitosan could generate a highly viscous layer that further delayed the drug diffusion from the beads to the solvent.

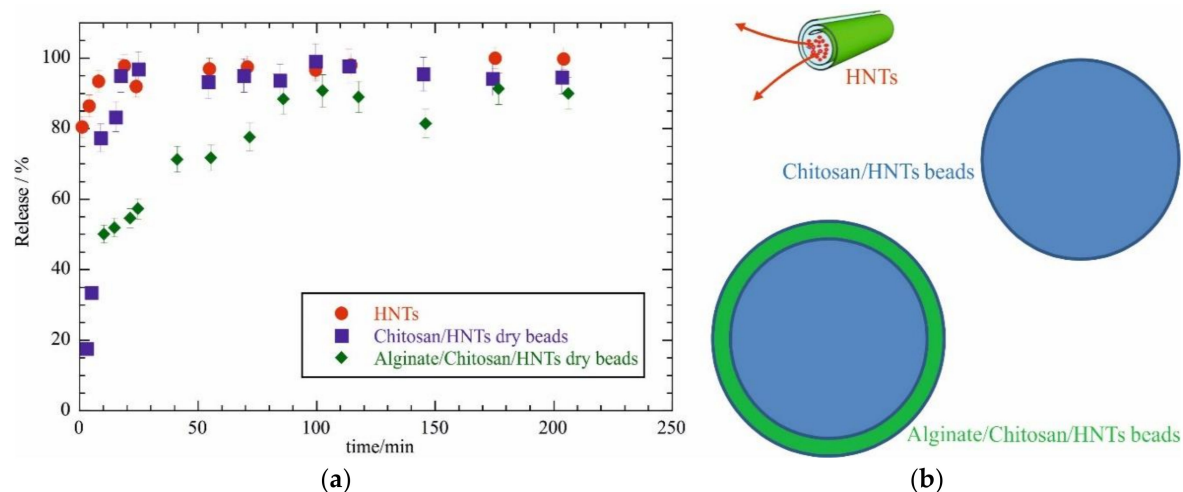


Figure 3. (a) Doxycycline chlorohydrate release as a function of time for different carriers. (b) Sketch view of the different release systems.

3. Materials and Methods

3.1. Materials

Halloysite, acetic acid, sodium hydroxide, ethylenediaminetetraacetic acid and DTAF, sodium alginate ($M_w = 70\text{--}100 \text{ kg mol}^{-1}$), and chitosan ($M_w = 50\text{--}190 \text{ kg mol}^{-1}$) were Sigma products. Doxycycline chlorohydrate ($\text{C}_{22}\text{H}_{24}\text{N}_2\text{O}_8 \bullet \text{HCl}$, $M_w = 480.90 \text{ kg mol}^{-1}$) was from Alfa Aesar. Halloysite characterization was reported in our recent publication [19].

3.2. HNTs Loading with Doxycycline Chlorohydrate

The drug loading into HNTs cavity was carried out by using a procedure well established in literature [54]. Briefly, 0.5 g of doxycycline chlorohydrate was mixed with 2 g of HNTs in 20 cm^3 of water. The dispersion was kept under vacuum for 30 min. This procedure was repeated three times before centrifugation at 8000 rpm for 20 min to separate the loaded HNTs from the supernatant. The loaded HNTs were rinsed with water and the drug loading of 4.2 wt % was determined by thermogravimetry. The experimental thermogravimetric curves are provided in Supplementary Material. The method used for drug loading calculation was detailed elsewhere [57].

3.3. Preparation of Gel Beds

The chitosan based gel beads were prepared by using the dropping technique [58]. Chitosan (2 wt %) was dissolved in water containing 0.5 wt % of acetic acid. A peristaltic pump was used to drop the chitosan solution into an aqueous solution of NaOH 1.5 M. The needle diameter was 0.4 mm and the distance from the needle to the liquid surface was 2 cm. The obtained gel beads stood in the NaOH solution overnight, and afterwards they were rinsed with water three times. The preparation

of the hybrid HNTs/Chitosan gel beads was carried out by using the same methodology. In this case, HNTs loaded with doxycycline chlorohydrate were dispersed into the chitosan solution with a polymer: HNTs weight ratio of 1:1. Some of the beads were in contact with a sodium alginate solution (2 wt %) for 10 mins and then with CaCl_2 0.1 M to cross-link the alginate polymer. Beads were dried out at 40 °C overnight.

3.4. Doxycycline Chlorohydrate Release Experiments

The release profiles in water were determined by measuring UV-VIS spectra in a quartz cuvettes without stirring. In particular, one dried bead or the equivalent amount of loaded HNTs was weighted and directly placed into a cuvette. An amount of 2 cm³ of distilled water was added and the spectra was recorded for 200 min.

3.5. Synthesis of DTAF Labeled Sodium Alginate

Alginate fluorescent labelling was carried out following the literature [59]. Sodium alginate (10 mg cm⁻³) was solubilized in sodium bicarbonate (50 mM) and 1.0 M NaOH was used to adjust the pH to 9. DTAF (concentration of 10 mg mL⁻¹ in dimethyl sulfoxide) was added at room temperature with an alginate: DTAF solutions volume ratio of 1:0.4. After one night of stirring, the mixture was dialysed in a 10 kDa cut-off dialysis tubing against phosphate-buffered saline (PBS) until the DTAF was not detected in the dialysate by UV at 490 nm.

3.6. Experimental Methods

UV-VIS spectra of doxycycline chlorohydrate were recorded by a Specord S600 (Analytik, Jena, Germany). Doxycycline chlorohydrate in water had a peak at 362 nm with an extinction coefficient of $23.6 \pm 0.3 \text{ cm}^3 \text{ mg}^{-1}$. SEM images were obtained by using a microscope ESEM FEI QUANTA 200F (FEI, Hillsboro, OR, USA) in high vacuum mode ($<6 \times 10^{-4}$ Pa). Before each SEM experiment, the surface of the sample was coated with gold in argon by means of an Edwards Sputter Coater S150A (Edwards Lifesciences, Milan, Italy) to avoid charging under an electron beam. Laser scanning confocal microscopy images were obtained using a LSM 780 instrument (Carl Zeiss, Jena, Germany) equipped with apochromatic 20× and 40× objectives and argon laser (488 nm). Images were processed using ZEN Black software (Carl Zeiss MicroImaging GmbH, Göttingen, Germany). Thermogravimetry (TG) measurements were performed by means of a Q5000 IR apparatus (TA Instruments, Milan, Italy) under nitrogen flows of 25 and 10 cm³ min⁻¹ for the sample and the balance, respectively. The sample (approximately 3 mg) was heated from room temperature to 700 °C at 10 °C min⁻¹. Calibration was carried out by following the procedure reported in literature [60].

4. Conclusions

In summary, we prepared hybrid gel beads with a chitosan rich core and an alginate rich shell containing halloysite nanotubes. The clay nanoparticles were loaded with a model drug and showed a good dispersion within the beads. The kinetics of the drug release was controlled by a core/shell structure. This work opens new perspectives into the preparation of hybrid biopolymer/nanoclay structures for drug delivery applications, and proposes a new strategy for obtaining tuned drug release.

Supplementary Materials: The following are available online at <http://www.mdpi.com/2079-6412/9/2/70/s1>, Figure S1: Thermogravimetric curves for HNTs loaded with Doxycycline chlorohydrate and their pure components (HNTs and Doxycycline chlorohydrate).

Author Contributions: Conceptualization, G.L. and R.F.; Methodology, G.C.; Validation, G.C., G.L. and R.F.; Formal Analysis, G.L.; Investigation, L.L. and F.P.; Data Curation, L.L.; Writing-Original Draft Preparation, L.L.; Writing-Review & Editing, G.L.; Supervision, G.L.; Project Administration, S.M.; Funding Acquisition, S.M. and R.F.

Acknowledgments: The work was financially supported by Progetto di ricerca e sviluppo "AGM for CuHe" (No. ARS01_00697) and the CORI 2018 project by the University of Palermo. The work was performed according

to the Russian Government Program of Competitive Growth of the Kazan Federal University. This work was funded by the subsidy allocated to the Kazan Federal University for the state assignment in the sphere of scientific activities (No. 16.2822.2017/4.6) and by RFBR (No. 18-29-11031).

Conflicts of Interest: The authors declare no conflict of interest.

References

1. Ahmed, E.M. Hydrogel: Preparation, characterization, and applications: A review. *J. Adv. Res.* **2015**, *6*, 105–121. [[CrossRef](#)]
2. Akhtar, M.F.; Hanif, M.; Ranjha, N.M. Methods of synthesis of hydrogels: A review. *Saudi Pharm. J.* **2016**, *24*, 554–559. [[CrossRef](#)] [[PubMed](#)]
3. Ullah, F.; Othman, M.B.H.; Javed, F.; Ahmad, Z.; Akil, H.M. Classification, processing and application of hydrogels: A review. *Mater. Sci. Eng. C* **2015**, *57*, 414–433. [[CrossRef](#)] [[PubMed](#)]
4. Li, Y.; Huang, G.; Zhang, X.; Li, B.; Chen, Y.; Lu, T.; Lu, T.J.; Xu, F. Magnetic Hydrogels and Their Potential Biomedical Applications. *Adv. Funct. Mater.* **2012**, *23*, 660–672. [[CrossRef](#)]
5. Cao, J.; Tan, Y.; Che, Y.; Xin, H. Novel complex gel beads composed of hydrolyzed polyacrylamide and chitosan: An effective adsorbent for the removal of heavy metal from aqueous solution. *Bioresour. Technol.* **2010**, *101*, 2558–2561. [[CrossRef](#)] [[PubMed](#)]
6. Zheng, Y.; Wang, A. Enhanced Adsorption of Ammonium Using Hydrogel Composites Based on Chitosan and Halloysite. *J. Macromol. Sci. Part A* **2009**, *47*, 33–38. [[CrossRef](#)]
7. Li, J.; Li, X.; Zhou, Z.; Ni, X.; Leong, K.W. Formation of Supramolecular Hydrogels Induced by Inclusion Complexation between Pluronics and α -Cyclodextrin. *Macromolecules* **2001**, *34*, 7236–7237. [[CrossRef](#)]
8. Dadsetan, M.; Taylor, K.E.; Yong, C.; Bajzer, Z.; Lu, L.; Yaszemski, M.J. Controlled release of doxorubicin from pH-responsive microgels. *Acta Biomater.* **2013**, *9*, 5438–5446. [[CrossRef](#)]
9. Varaprasad, K.; Raghavendra, G.M.; Jayaramudu, T.; Yallapu, M.M.; Sadiku, R. A mini review on hydrogels classification and recent developments in miscellaneous applications. *Mater. Sci. Eng. C* **2017**, *79*, 958–971. [[CrossRef](#)]
10. Ganguly, K.; Chaturvedi, K.; More, U.A.; Nadagouda, M.N.; Aminabhavi, T.M. Polysaccharide-based micro/nanohydrogels for delivering macromolecular therapeutics. *Drug Deliv. Res. Asia Pac. Reg.* **2014**, *193*, 162–173. [[CrossRef](#)]
11. Wei, Z.; Yang, J.H.; Liu, Z.Q.; Xu, F.; Zhou, J.X.; Zrínyi, M.; Osada, Y.; Chen, Y.M. Novel biocompatible polysaccharide-based self-healing hydrogel. *Adv. Funct. Mater.* **2015**, *25*, 1352–1359. [[CrossRef](#)]
12. Sahiner, N.; Godbey, W.T.; McPherson, G.L.; John, V.T. Microgel, nanogel and hydrogel–hydrogel semi-IPN composites for biomedical applications: Synthesis and characterization. *Colloid Polym. Sci.* **2006**, *284*, 1121–1129. [[CrossRef](#)]
13. Liu, K.-H.; Liu, T.-Y.; Chen, S.-Y.; Liu, D.-M. Drug release behavior of chitosan–montmorillonite nanocomposite hydrogels following electrostimulation. *Acta Biomater.* **2008**, *4*, 1038–1045. [[CrossRef](#)]
14. Yang, H.; Hua, S.; Wang, W.; Wang, A. Composite Hydrogel Beads Based on Chitosan and Laponite: Preparation, Swelling, and Drug Release Behaviour. *Iran. Polym. J.* **2011**, *20*, 479–490.
15. Bonifacio, M.A.; Gentile, P.; Ferreira, A.M.; Cometa, S.; De Giglio, E. Insight into halloysite nanotubes-loaded gellan gum hydrogels for soft tissue engineering applications. *Carbohydr. Polym.* **2017**, *163*, 280–291. [[CrossRef](#)] [[PubMed](#)]
16. Lee, H.; Ryu, J.; Kim, D.; Joo, Y.; Lee, S.U.; Sohn, D. Preparation of an imogolite/poly(acrylic acid) hybrid gel. *J. Colloid Interface Sci.* **2013**, *406*, 165–171. [[CrossRef](#)] [[PubMed](#)]
17. Lazzara, G.; Cavallaro, G.; Panchal, A.; Fakhrullin, R.; Stavitskaya, A.; Vinokurov, V.; Lvov, Y. An assembly of organic-inorganic composites using halloysite clay nanotubes. *Curr. Opin. Colloid Interface Sci.* **2018**, *35*, 42–50. [[CrossRef](#)]
18. Lisuzzo, L.; Cavallaro, G.; Parisi, F.; Milioto, S.; Lazzara, G. Colloidal stability of halloysite clay nanotubes. *Ceram. Int.* **2018**. [[CrossRef](#)]
19. Cavallaro, G.; Chiappisi, L.; Pasbakhsh, P.; Gradzielski, M.; Lazzara, G. A structural comparison of halloysite nanotubes of different origin by Small-Angle Neutron Scattering (SANS) and Electric Birefringence. *Appl. Clay Sci.* **2018**, *160*, 71–80. [[CrossRef](#)]

20. Lvov, Y.M.; Shchukin, D.G.; Mohwald, H.; Price, R.R. Halloysite Clay Nanotubes for Controlled Release of Protective Agents. *ACS Nano* **2008**, *2*, 814–820. [[CrossRef](#)]
21. Luo, Z.; Song, H.; Feng, X.; Run, M.; Cui, H.; Wu, L.; Gao, J.; Wang, Z. Liquid Crystalline Phase Behavior and Sol–Gel Transition in Aqueous Halloysite Nanotube Dispersions. *Langmuir* **2013**, *29*, 12358–12366. [[CrossRef](#)] [[PubMed](#)]
22. Viseras, C.; Cerezo, P.; Sanchez, R.; Salcedo, I.; Aguzzi, C. Current challenges in clay minerals for drug delivery. *Appl. Clay Sci.* **2010**, *48*, 291–295. [[CrossRef](#)]
23. Joussein, E.; Petit, S.; Churchman, G.J.; Theng, B.; Righi, D.; Delvaux, B. Halloysite clay minerals—A review. *Clay Miner.* **2005**, *40*, 383–426. [[CrossRef](#)]
24. Pasbakhsh, P.; Churchman, G.J.; Keeling, J.L. Characterisation of properties of various halloysites relevant to their use as nanotubes and microfibre fillers. *Appl. Clay Sci.* **2013**, *74*, 47–57. [[CrossRef](#)]
25. Cavallaro, G.; Lazzara, G.; Milioto, S. Exploiting the Colloidal Stability and Solubilization Ability of Clay Nanotubes/Ionic Surfactant Hybrid Nanomaterials. *J. Phys. Chem. C* **2012**, *116*, 21932–21938. [[CrossRef](#)]
26. Bertolino, V.; Cavallaro, G.; Lazzara, G.; Milioto, S.; Parisi, F. Biopolymer-Targeted Adsorption onto Halloysite Nanotubes in Aqueous Media. *Langmuir* **2017**, *33*, 3317–3323. [[CrossRef](#)]
27. Abdullayev, E.; Price, R.; Shchukin, D.; Lvov, Y. Halloysite Tubes as Nanocontainers for Anticorrosion Coating with Benzotriazole. *ACS Appl. Mater. Interfaces* **2009**, *1*, 1437–1443. [[CrossRef](#)]
28. Cavallaro, G.; Lazzara, G.; Milioto, S.; Palmisano, G.; Parisi, F. Halloysite nanotube with fluorinated lumen: Non-foaming nanocontainer for storage and controlled release of oxygen in aqueous media. *J. Colloid Interface Sci.* **2014**, *417*, 66–71. [[CrossRef](#)]
29. Aguzzi, C.; Viseras, C.; Cerezo, P.; Salcedo, I.; Sánchez-Espejo, R.; Valenzuela, C. Release kinetics of 5-aminosalicylic acid from halloysite. *Colloids Surf. B Biointerfaces* **2013**, *105*, 75–80. [[CrossRef](#)]
30. Fakhrullina, G.I.; Akhatova, F.S.; Lvov, Y.M.; Fakhrullin, R.F. Toxicity of halloysite clay nanotubes in vivo: A *Caenorhabditis elegans* study. *Environ. Sci. Nano* **2015**, *2*, 54–59. [[CrossRef](#)]
31. Zhao, Y.; Abdullayev, E.; Vasiliev, A.; Lvov, Y. Halloysite nanotubule clay for efficient water purification. *J. Colloid Interface Sci.* **2013**, *406*, 121–129. [[CrossRef](#)] [[PubMed](#)]
32. Cavallaro, G.; Lazzara, G.; Milioto, S.; Parisi, F.; Sanzillo, V. Modified Halloysite Nanotubes: Nanoarchitectures for Enhancing the Capture of Oils from Vapor and Liquid Phases. *ACS Appl. Mater. Interfaces* **2014**, *6*, 606–612. [[CrossRef](#)]
33. Luo, P.; Zhang, J.; Zhang, B.; Wang, J.; Zhao, Y.; Liu, J. Preparation and Characterization of Silane Coupling Agent Modified Halloysite for Cr(VI) Removal. *Ind. Eng. Chem. Res.* **2011**, *50*, 10246–10252. [[CrossRef](#)]
34. Zhao, M.; Liu, P. Adsorption behavior of methylene blue on halloysite nanotubes. *Microporous Mesoporous Mater.* **2008**, *112*, 419–424. [[CrossRef](#)]
35. Hermawan, A.A.; Chang, J.W.; Pasbakhsh, P.; Hart, F.; Talei, A. Halloysite nanotubes as a fine grained material for heavy metal ions removal in tropical biofiltration systems. *Appl. Clay Sci.* **2018**, *160*, 106–115. [[CrossRef](#)]
36. Cavallaro, G.; Milioto, S.; Parisi, F.; Lazzara, G. Halloysite Nanotubes Loaded with Calcium Hydroxide: Alkaline Fillers for the Deacidification of Waterlogged Archeological Woods. *ACS Appl. Mater. Interfaces* **2018**, *10*, 27355–27364. [[CrossRef](#)] [[PubMed](#)]
37. Cavallaro, G.; Lazzara, G.; Milioto, S.; Parisi, F. Halloysite Nanotubes for Cleaning, Consolidation and Protection. *Chem. Rec.* **2018**, *18*, 940–949. [[CrossRef](#)]
38. Lvov, Y.; Abdullayev, E. Functional polymer–clay nanotube composites with sustained release of chemical agents. *Prog. Polym. Sci.* **2013**, *38*, 1690–1719. [[CrossRef](#)]
39. Abdullayev, E.; Sakakibara, K.; Okamoto, K.; Wei, W.; Ariga, K.; Lvov, Y. Natural Tubule Clay Template Synthesis of Silver Nanorods for Antibacterial Composite Coating. *ACS Appl. Mater. Interfaces* **2011**, *3*, 4040–4046. [[CrossRef](#)]
40. Liu, M.; Wu, C.; Jiao, Y.; Xiong, S.; Zhou, C. Chitosan-halloysite nanotubes nanocomposite scaffolds for tissue engineering. *J. Mater. Chem. B* **2013**, *1*, 2078–2089. [[CrossRef](#)]
41. Zhang, H.; Cheng, C.; Song, H.; Bai, L.; Cheng, Y.; Ba, X.; Wu, Y. A facile one-step grafting of polyphosphonium onto halloysite nanotubes initiated by Ce(IV). *Chem. Commun.* **2019**. [[CrossRef](#)] [[PubMed](#)]
42. Liu, F.; Bai, L.; Zhang, H.; Song, H.; Hu, L.; Wu, Y.; Ba, X. Smart H₂O₂-Responsive Drug Delivery System Made by Halloysite Nanotubes and Carbohydrate Polymers. *ACS Appl. Mater. Interfaces* **2017**, *9*, 31626–31633. [[CrossRef](#)] [[PubMed](#)]

43. Wei, W.; Minullina, R.; Abdullayev, E.; Fakhrullin, R.; Mills, D.; Lvov, Y. Enhanced efficiency of antiseptics with sustained release from clay nanotubes. *RSC Adv.* **2014**, *4*, 488–494. [[CrossRef](#)]
44. Kurczewska, J.; Ceglowski, M.; Messyasz, B.; Schroeder, G. Dendrimer-functionalized halloysite nanotubes for effective drug delivery. *Appl. Clay Sci.* **2018**, *153*, 134–143. [[CrossRef](#)]
45. Gorrasi, G.; Pantani, R.; Murariu, M.; Dubois, P. PLA/Halloysite Nanocomposite Films: Water Vapor Barrier Properties and Specific Key Characteristics. *Macromol. Mater. Eng.* **2014**, *299*, 104–115. [[CrossRef](#)]
46. De Silva, R.T.; Pasbakhsh, P.; Goh, K.L.; Chai, S.-P.; Ismail, H. Physico-chemical characterisation of chitosan/halloysite composite membranes. *Polym. Test.* **2013**, *32*, 265–271. [[CrossRef](#)]
47. He, Y.; Kong, W.; Wang, W.; Liu, T.; Liu, Y.; Gong, Q.; Gao, J. Modified natural halloysite/potato starch composite films. *Carbohydr. Polym.* **2012**, *87*, 2706–2711. [[CrossRef](#)]
48. Biddeci, G.; Cavallaro, G.; Di Blasi, F.; Lazzara, G.; Massaro, M.; Milioto, S.; Parisi, F.; Riela, S.; Spinelli, G. Halloysite nanotubes loaded with peppermint essential oil as filler for functional biopolymer film. *Carbohydr. Polym.* **2016**, *152*, 548–557. [[CrossRef](#)]
49. Sun, P.; Liu, G.; Lv, D.; Dong, X.; Wu, J.; Wang, D. Simultaneous improvement in strength, toughness, and thermal stability of epoxy/halloysite nanotubes composites by interfacial modification. *J. Appl. Polym. Sci.* **2016**, *133*. [[CrossRef](#)]
50. Kim, M.; Kim, S.; Kim, T.; Lee, D.K.; Seo, B.; Lim, C.-S. Mechanical and Thermal Properties of Epoxy Composites Containing Zirconium Oxide Impregnated Halloysite Nanotubes. *Coatings* **2017**, *7*, 231. [[CrossRef](#)]
51. Cavallaro, G.; Lazzara, G.; Lisuzzo, L.; Milioto, S.; Parisi, F. Selective adsorption of oppositely charged PNIPAAm on halloysite surfaces: A route to thermo-responsive nanocarriers. *Nanotechnology* **2018**, *29*, 325702. [[CrossRef](#)]
52. Cavallaro, G.; Danilushkina, A.A.; Evtugyn, V.G.; Lazzara, G.; Milioto, S.; Parisi, F.; Rozhina, E.V.; Fakhrullin, R.F. Halloysite Nanotubes: Controlled Access and Release by Smart Gates. *Nanomaterials* **2017**, *7*, 199. [[CrossRef](#)] [[PubMed](#)]
53. Cavallaro, G.; Lazzara, G.; Milioto, S.; Parisi, F.; Evtugyn, V.; Rozhina, E.; Fakhrullin, R. Nanohydrogel Formation within the Halloysite Lumen for Triggered and Sustained Release. *ACS Appl. Mater. Interfaces* **2018**, *10*, 8265–8273. [[CrossRef](#)] [[PubMed](#)]
54. Lvov, Y.M.; DeVilliers, M.M.; Fakhrullin, R.F. The application of halloysite tubule nanoclay in drug delivery. *Expert Opin. Drug Deliv.* **2016**, *13*, 977–986. [[CrossRef](#)]
55. Cavallaro, G.; Gianguzza, A.; Lazzara, G.; Milioto, S.; Piazzese, D. Alginate gel beads filled with halloysite nanotubes. *Appl. Clay Sci.* **2013**, *72*, 132–137. [[CrossRef](#)]
56. Lisuzzo, L.; Cavallaro, G.; Lazzara, G.; Milioto, S.; Parisi, F.; Stetsyshyn, Y. Stability of Halloysite, Imogolite, and Boron Nitride Nanotubes in Solvent Media. *Appl. Sci.* **2018**, *8*, 1068. [[CrossRef](#)]
57. Cavallaro, G.; Lazzara, G.; Milioto, S.; Parisi, F.; Ruisi, F. Nanocomposites based on esterified colophony and halloysite clay nanotubes as consolidants for waterlogged archaeological woods. *Cellulose* **2017**, *24*, 3367–3376. [[CrossRef](#)]
58. Kofuji, K.; Shibata, K.; Murata, Y.; Miyamoto, E.; Kawashima, S. Preparation and Drug Retention of Biodegradable Chitosan Gel Beads. *Chem. Pharm. Bull. (Tokyo)* **1999**, *47*, 1494–1496. [[CrossRef](#)]
59. Mackie, A.; Bajka, B.; Rigby, N. Roles for dietary fibre in the upper GI tract: The importance of viscosity. *Food Res. Int.* **2016**, *88*, 234–238. [[CrossRef](#)]
60. Blanco, I.; Abate, L.; Bottino, F.A.; Bottino, P. Thermal degradation of hepta cyclopentyl, mono phenyl-polyhedral oligomeric silsesquioxane (hcp-POSS)/polystyrene (PS) nanocomposites. *Polym. Degrad. Stabil.* **2012**, *97*, 849–855. [[CrossRef](#)]



Communication

Filling of Mater-Bi with Nanoclays to Enhance the Biofilm Rigidity

Giuseppe Cavallaro *, Giuseppe Lazzara, Lorenzo Lisuzzo, Stefana Milioto and Filippo Parisi

Dipartimento di Fisica e Chimica, Università degli Studi di Palermo, Viale delle Scienze, pad. 17, 90128 Palermo, Italy; giuseppe.lazzara@unipa.it (G.L.); lorenzo.lisuzzo@unipa.it (L.L.); stefana.milioto@unipa.it (S.M.); filippo.parisi@unipa.it (F.P.)

* Correspondence: giuseppe.cavallaro@unipa.it

Received: 26 September 2018; Accepted: 18 October 2018; Published: 21 October 2018



Abstract: We investigated the efficacy of several nanoclays (halloysite, sepiolite and laponite) as nanofillers for Mater-Bi, which is a commercial bioplastic extensively used within food packaging applications. The preparation of Mater-Bi/nanoclay nanocomposite films was easily achieved by means of the solvent casting method from dichloroethane. The prepared bio-nanocomposites were characterized by dynamic mechanical analysis (DMA) in order to explore the effect of the addition of the nanoclays on the mechanical behavior of the Mater-Bi-based films. Tensile tests found that filling Mater-Bi with halloysite induced the most significant improvement of the mechanical performances under traction force, while DMA measurements under the oscillatory regime showed that the polymer glass transition was not affected by the addition of the nanoclay. The tensile properties of the Mater-Bi/halloysite nanotube (HNT) films were competitive compared to those of traditional petroleum plastics in terms of the elastic modulus and stress at the breaking point. Both the mechanical response to the temperature and the tensile properties make the bio-nanocomposites appropriate for food packaging and smart coating purposes. Here, we report a preliminary study of the development of sustainable hybrid materials that could be employed in numerous industrial and technological applications within materials science and pharmaceuticals.

Keywords: halloysite; sepiolite; laponite; nanoclays; Mater-Bi; bio-nanocomposites; mechanical performance

1. Introduction

Recently, eco-compatible polymers have been extensively investigated as potential alternatives to traditional plastics for several purposes within the packaging [1,2], biotechnology [3–5] and engineering [6–8] fields. The industrial use of biopolymers can be limited by their low barrier properties [9], thermal instability [10] and moderate mechanical behavior [11]. The addition of inorganic fillers to the biopolymer matrix represents an efficient strategy to fabricate composite materials with improved performance, which are suitable for numerous technological applications [11]. Ruiz-Hitzky et al. [12] highlighted that the filling of the polymeric matrix with clay nanoparticles enhanced the thermal and mechanical characteristics of pure polymers. Generally, the polymer/filler interactions can be favored by the high surface/volume ratio of the nanoclays, promoting an improvement of the mesoscopic properties of the nanocomposites [13]. The filling of polymers can be carried out using nanoclays with a variable shape, such sepiolite nanofibers [14], laponite nanodisks [15,16] and halloysite nanotubes [17,18]. The barrier properties of polylactic acid (PLA)-based films were improved by the addition of halloysite nanotubes (HNTs), allowing us to obtain hybrid materials useful for packaging [9]. The performance of the films was strongly

dependent on the mesoscopic structure of the nanocomposites [18,19]. As a general consideration, the uniform distribution of the nanoparticles within the matrix determined the thermal stabilization of the polymers, because the filler acted as a barrier towards the volatile products generated by the polymer degradation [18,20]. Additionally, nanocomposites with a homogeneous morphology possess an improved mechanical resistance to tensile stress as a consequence of the adhesion of the polymers to the filler surface [21]. The literature [22,23] reports that composite films with a multilayer structure present peculiar characteristics. Flame retardant action was detected in multilayer nanocomposites formed by a middle clay layer sandwiched between the polymer [22]. As an example, a middle layer of montmorillonite between the alginate allowed the fabrication of multilayer bio-nanocomposite films with fire-shielding properties [16]. Recently, we proposed a sequential casting procedure to prepare flame-retardant films obtained by the confinement of HNTs between chitosan layers [22]. Among the nanoclays, halloysite represents an emerging filler with excellent properties in terms of the morphology and surface properties [24,25]. The peculiar tubular shape of halloysite is due to the rolling of flat kaolinite sheets [26,27]. The length of the HNTs ranged from 50 to 1500 nm, while the external and internal diameters ranged from 20–150 and 10–15 nm, respectively [27]. It should be noted that the polydispersity of the HNT sizes is affected by their geological deposit, as evidenced by microscopies [28] and neutron scattering [29] investigations. Interestingly, the halloysite surfaces exhibited opposite charges in a wide pH range (between 2 and 8) that can be attributed to their different chemistry, being that the shell and the lumen are composed of SiO_2 and Al_2O_3 groups, respectively [30]. As proved by both *in vitro* and *in vivo* tests [31–34], HNTs can be considered to be biocompatible nanomaterials with a low toxicity effect. Accordingly, halloysite is suitable for biomedical and pharmaceutical applications as a nanocarrier for the controlled delivery of drugs [35–37]. HNTs have been successfully used as reinforcing nanofillers for several biopolymers, such as chitosan [22,38,39], cellulose ethers [18], pectin [17,21,40] and alginate [18]. The different HNT surface charge influences the properties of the bio-nanocomposites due to the specific electrostatic interactions occurring between ionic biopolymers and halloysite interfaces [18]. Anionic biopolymers are thermally stabilized due to their encapsulation within the HNT cavity as has been observed for nanocomposites based on alginate [18] and pectin [21]. Contrary to these results, the thermal stabilization effect was not observed for chitosan/HNT hybrid films where the biopolymer was adsorbed onto the halloysite external surface [18]. Sepiolite ($\text{Si}_{12}\text{Mg}_8\text{O}_{30}(\text{OH})_4(\text{OH}_2)_4 \cdot 8\text{H}_2\text{O}$) presents a nanofiber morphology with an average length between 1 and 2 μm and a diameter in the nanometric range (20–30 nm) [14]. Sepiolite nanofibers were used as nanofillers for poly (methyl methacrylate), improving both the thermal stability and the mechanical performance of the polymer [41]. Laponite ($\text{Si}_8(\text{Mg}_{5.45}\text{Li}_{0.4})\text{O}_{20}(\text{OH})_4\text{Na}_{0.7}$) possesses a disk-like shape with a diameter of ca. 25 nm and a thickness of 1 nm. Laponite nanodisks were filled with pectins, generating biofilms with moderate tensile properties [16]. Recently, nanocomposites based on poly (ethylene glycol) (PEG) silane and laponite were investigated as transparent non-fouling surfaces [42]. In this communication, we report the preparation and mechanical characterization of Mater Bi/nanoclay nanocomposite films with variable filler contents. Sepiolite nanofibers, laponite nanodisks and halloysite nanotubes were selected as the inorganic nanofillers. Dynamic mechanical analysis (DMA) provided the tensile properties as well as the thermo-mechanical behavior of the prepared films. The experimental data showed that filling Mater-Bi with halloysite allowed the fabrication of biocomposite films with promising mechanical performance for food packaging applications.

2. Results and Discussion

2.1. Tensile Properties of Mater-Bi/Nanoclay Composite Film

Figure 1 shows the stress–strain curves of pure Mater-Bi and the bio-nanocomposites with a nanoclay content of 30 wt %.

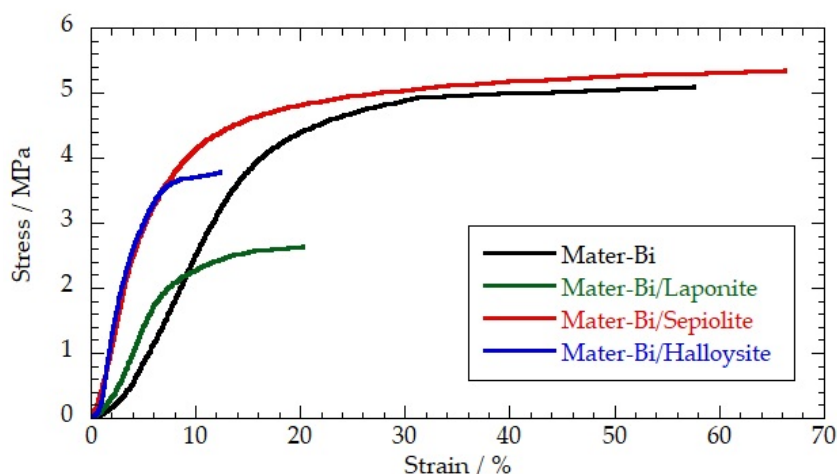


Figure 1. Stress–strain curves of Mater-Bi, Mater-Bi/ halloysite nanotubes (HNTs), Mater-Bi/sepiolite and Mater-Bi/laponite. The nanoclay content for the bio-nanocomposites was fixed at 30 wt %.

The analysis of the stress–strain profiles allowed us to determine a complete description of the tensile behavior of the prepared biofilms in terms of the elastic modulus, yielding and breaking points. The tensile data were collected in Table 1.

Table 1. Tensile properties of Mater-Bi and Mater-Bi/nanoclay films.

Film	Elastic Modulus/MPa	Stress at Yielding Point/MPa	Elongation at Yielding Point/%	Stress at Breaking Point/MPa	Elongation at Breaking Point/%
Mater-Bi	32 ± 3	3.8 ± 0.5	15.4 ± 1.8	5.0 ± 0.6	57 ± 6
Mater-Bi/HNTs	109 ± 8	2.8 ± 0.4	4.6 ± 0.5	3.8 ± 0.5	12 ± 2
Mater-Bi/Sepiolite	79 ± 7	3.4 ± 0.4	6.3 ± 0.6	5.3 ± 0.6	63 ± 6
Mater-Bi/Laponite	38 ± 4	1.98 ± 0.19	7.1 ± 0.6	2.6 ± 0.4	20 ± 2

According to the literature results for the pectin/nanoclay nanocomposites [16], we observed that the nanofiller morphology affected the tensile characteristics of the hybrid biofilms. As a general result, the nanoclay addition generated an improvement in the film rigidity, as evidenced by the variations of the elastic modulus. This effect was significant for the Mater-Bi/HNT and Mater-Bi/sepiolite films, which showed relevant increases in the elastic modulus compared to that of the pure polymer (240% and 146%, respectively). On the other hand, the influence of the laponite nanodisks was negligible. With regard to the yielding point, the addition of the nanoclays reduced both the stress and elongation. The presence of the HNTs and laponite caused a decrease in the ultimate tensile strength as well as the maximum elongation. The latter can be attributed to the adsorption of Mater-Bi onto the nanoclay surface that avoids the sliding of the polymeric chains against each other [15,19]. Contrary to these results, the presence of sepiolite nanofibers did not alter the breaking point of Mater-Bi.

2.2. Thermo-Mechanical Behaviour of Mater-Bi/Nanoclay Bio-Nanocomposites

The mechanical response to temperature of the Mater-Bi based films was investigated by DMA test in the oscillatory regime. The obtained data allowed us to determine the effect of the temperature on the storage (G') and loss (G'') moduli, which describe the viscoelastic characteristics of the materials. Figure 2 compares the dependence of $\tan \delta$ (G''/G' ratio) on the temperature of the Mater-Bi and Mater-Bi/sepiolite nanocomposite. We observed that $\tan \delta$ exhibited a peak at ca. 85 °C due to the glass transition of the polymer. Similarly to sepiolite, the addition of HNTs and laponite did not change the glass transition temperature of Mater-Bi. Based on these results, we concluded that filling with nanoclays of variable shape does not alter the thermo-mechanical behaviour of the Mater-Bi biofilm.

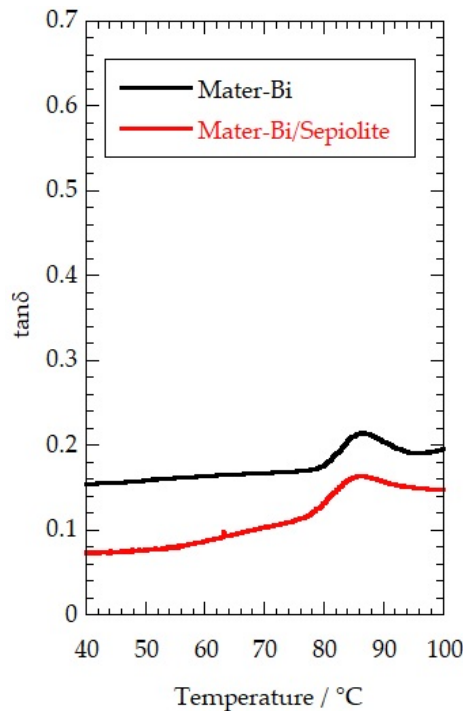


Figure 2. Dependence of $\tan\delta$ on the temperature of Mater-Bi and Mater-Bi/sepiolite. The nanoclay content of the bio-nanocomposite was fixed at 30 wt %.

3. Materials and Methods

3.1. Materials

The halloysite and 1,2-Dichloroethane were from Sigma-Aldrich (St. Louis, MO, USA). The sepiolite and laponite were from TOLSA S.A (Madrid, Spain) and BASF AG (Ludwigshafen, Germany), respectively. The Mater-Bi was a Novamont product (Novara, Italy).

3.2. Preparation of Mater-Bi/Nanoclay Nanocomposites

The solvent casting method for 1,2-Dichloroethane was employed for the preparation of the nanocomposites. Firstly, we prepared a 2 wt % Mater-Bi solution in 1,2-Dichloroethane by magnetically stirring for 2 h at 25 °C. Then, we added appropriate amounts of the nanoclay and the obtained dispersions were stirred overnight at 25 °C. The Mater-Bi/nanoclay mixtures were poured into glass Petri dishes at 25 °C to evaporate the 1,2-Dichloroethane. The obtained films were removed from the supports and stored in a desiccator at 25 °C. We selected 30 wt % as the filler concentration, which corresponds to the grams of nanoclay per 100 g of nanocomposite.

3.3. Methods

Dynamic Mechanical Analysis

DMA Q800 apparatus (TA Instruments, New Castle, DE, USA) was used to perform the dynamic mechanical analyses (DMA) of the Mater-Bi/nanoclay composite films. The DMA tests were conducted on rectangular films ($10.00 \times 6.00 \times 0.060 \text{ mm}^3$). Tensile investigations were carried out with a stress ramp of 1 MPa min^{-1} at $25.0 \pm 0.5 \text{ °C}$. The mechanical response to the temperature was conducted in the oscillatory regime (with a frequency of 1.0 Hz and a strain amplitude of 0.5%) by heating the films from 40 to 100 °C at a heating rate of 5 °C min^{-1} .

4. Conclusions

In summary, we prepared bio-nanocomposite films by filling Mater-Bi with several nanoclays using the solvent casting process. We observed that the presence of halloysite nanotubes and sepiolite nanofibers strongly increased the rigidity of the Mater-Bi-based films, extending the potential applications in the packaging fields. As evidenced by the variations of the elastic modulus, sepiolite and halloysite induced an increase of the Mater-Bi rigidity of 146% and 240%, respectively. The mechanical performance (regarding the yielding and breaking points) was still competitive with that of traditional plastics. The addition of the nanoclays did not affect the viscoelastic properties of the Mater-Bi and the polymer response to the temperature variations. In particular, the glass transition temperatures of the bio-nanocomposites were similar to that of the pure polymer.

Author Contributions: Conceptualization, G.C, G.L. and S.M.; Methodology, F.P.; Validation, G.C. and G.L.; Formal Analysis, G.C.; Investigation, L.L.; Writing-Original Draft Preparation, G.C.; Writing-Review & Editing, G.C.; Supervision, G.L.; Funding Acquisition, S.M.

Funding: This research received no external funding.

Acknowledgments: The work was financially supported by the University of Palermo. The authors acknowledge the Progetto di ricerca e sviluppo “AGM for CuHe”.

Conflicts of Interest: The authors declare no conflict of interest.

References

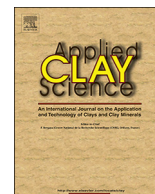
1. Tharanathan, R.N. Biodegradable films and composite coatings: Past, present and future. *Trends Food Sci. Technol.* **2003**, *14*, 71–78. [[CrossRef](#)]
2. Sapalidis, A.A.; Katsaros, F.K.; Romanos, G.E.; Kakizis, N.K.; Kanellopoulos, N.K. Preparation and characterization of novel poly-(vinyl alcohol)–Zostera flakes composites for packaging applications. *Compos. Part B Eng.* **2007**, *38*, 398–404. [[CrossRef](#)]
3. Stetsyshyn, Y.; Zemla, J.; Zolobko, O.; Fornal, K.; Budkowski, A.; Kostruba, A.; Donchak, V.; Harhay, K.; Awsiuk, K.; Rysz, J.; et al. Temperature and pH dual-responsive coatings of oligoperoxide-graft-poly(N-isopropylacrylamide): Wettability, morphology, and protein adsorption. *J. Colloid Interface Sci.* **2012**, *387*, 95–105. [[CrossRef](#)] [[PubMed](#)]
4. Gunbas, I.D.; Aydemir Sezer, U.; Gülce İz, S.; Deliloğlu Gürhan, İ.; Hasirci, N. Semi-IPN Chitosan/PEG Microspheres and films for biomedical applications: Characterization and sustained release optimization. *Ind. Eng. Chem. Res.* **2012**, *51*, 11946–11954. [[CrossRef](#)]
5. Moneghini, M.; De Zordi, N.; Solinas, D.; Macchiavelli, S.; Princivale, F. Characterization of solid dispersions of itraconazole and vitamin E TPGS prepared by microwave technology. *Future Med. Chem.* **2010**, *2*, 237–246. [[CrossRef](#)] [[PubMed](#)]
6. Naumenko, E.A.; Guryanov, I.D.; Yendluri, R.; Lvov, Y.M.; Fakhrullin, R.F. Clay nanotube-biopolymer composite scaffolds for tissue engineering. *Nanoscale* **2016**, *8*, 7257–7271. [[CrossRef](#)] [[PubMed](#)]
7. Wei, H.; Rodriguez, K.; Renneckar, S.; Vikesland, P.J. Environmental science and engineering applications of nanocellulose-based nanocomposites. *Environ. Sci. Nano* **2014**, *1*, 302–316. [[CrossRef](#)]
8. Cicala, G.; Tosto, C.; Latteri, A.; La Rosa, A.D.; Blanco, I.; Elsabbagh, A.; Russo, P.; Ziegmann, G. Green composites based on blends of polypropylene with liquid wood reinforced with hemp fibers: Thermomechanical properties and the effect of recycling cycles. *Materials* **2017**, *10*, 998. [[CrossRef](#)] [[PubMed](#)]
9. Gorrasi, G.; Pantani, R.; Murariu, M.; Dubois, P. PLA/Halloysite nanocomposite films: Water vapor barrier properties and specific key characteristics. *Macromol. Mater. Eng.* **2014**, *299*, 104–115. [[CrossRef](#)]
10. Espitia, P.J.P.; Du, W.-X.; de Jesús Avena-Bustillos, R.; Soares, N.D.F.F.; McHugh, T.H. Edible films from pectin: Physical-mechanical and antimicrobial properties—A review. *Food Hydrocoll.* **2014**, *35*, 287–296. [[CrossRef](#)]
11. Lvov, Y.; Abdullayev, E. Functional polymer–clay nanotube composites with sustained release of chemical agents. *Prog. Polym. Sci.* **2013**, *38*, 1690–1719. [[CrossRef](#)]
12. Ruiz-Hitzky, E.; Aranda, P.; Darder, M.; Rytwo, G. Hybrid materials based on clays for environmental and biomedical applications. *J Mater. Chem.* **2010**, *20*, 9306–9321. [[CrossRef](#)]

13. Ozkoc, G.; Kemaloglu, S. Morphology, biodegradability, mechanical, and thermal properties of nanocomposite films based on PLA and plasticized PLA. *J. Appl. Polym. Sci.* **2009**, *114*, 2481–2487. [[CrossRef](#)]
14. Darder, M.; López-Blanco, M.; Aranda, P.; Aznar, A.J.; Bravo, J.; Ruiz-Hitzky, E. Microfibrillar chitosan—sepiolite nanocomposites. *Chem. Mater.* **2006**, *18*, 1602–1610. [[CrossRef](#)]
15. Tang, X.; Alavi, S. Structure and physical properties of starch/poly vinyl alcohol/laponite RD nanocomposite films. *J. Agric. Food Chem.* **2012**, *60*, 1954–1962. [[CrossRef](#)] [[PubMed](#)]
16. Cavallaro, G.; Lazzara, G.; Milioto, S. Dispersions of nanoclays of different shapes into aqueous and solid biopolymeric matrices. Extended physicochemical study. *Langmuir* **2011**, *27*, 1158–1167. [[CrossRef](#)] [[PubMed](#)]
17. Biddeci, G.; Cavallaro, G.; Di Blasi, F.; Lazzara, G.; Massaro, M.; Milioto, S.; Parisi, F.; Riela, S.; Spinelli, G. Halloysite nanotubes loaded with peppermint essential oil as filler for functional biopolymer film. *Carbohydr. Polym.* **2016**, *152*, 548–557. [[CrossRef](#)] [[PubMed](#)]
18. Bertolino, V.; Cavallaro, G.; Lazzara, G.; Merli, M.; Milioto, S.; Parisi, F.; Sciascia, L. Effect of the biopolymer charge and the nanoclay morphology on nanocomposite materials. *Ind. Eng. Chem. Res.* **2016**, *55*, 7373–7380. [[CrossRef](#)]
19. Cavallaro, G.; Lazzara, G.; Milioto, S. Sustainable nanocomposites based on halloysite nanotubes and pectin/polyethylene glycol blend. *Polym. Degrad. Stab.* **2013**, *98*, 2529–2536. [[CrossRef](#)]
20. Du, M.; Guo, B.; Jia, D. Thermal stability and flame retardant effects of halloysite nanotubes on poly(propylene). *Eur. Polym. J.* **2006**, *42*, 1362–1369. [[CrossRef](#)]
21. Makaremi, M.; Pasbakhsh, P.; Cavallaro, G.; Lazzara, G.; Aw, Y.K.; Lee, S.M.; Milioto, S. Effect of morphology and size of halloysite nanotubes on functional pectin bionanocomposites for food packaging applications. *ACS Appl. Mater. Interfaces* **2017**, *9*, 17476–17488. [[CrossRef](#)] [[PubMed](#)]
22. Bertolino, V.; Cavallaro, G.; Lazzara, G.; Milioto, S.; Parisi, F. Halloysite nanotubes sandwiched between chitosan layers: Novel bionanocomposites with multilayer structures. *New J. Chem.* **2018**, *42*, 8384–8390. [[CrossRef](#)]
23. Pierchala, M.K.; Makaremi, M.; Tan, H.L.; Pushpamalar, J.; Muniyandy, S.; Solouk, A.; Lee, S.M.; Pasbakhsh, P. Nanotubes in nanofibers: Antibacterial multilayered polylactic acid/halloysite/gentamicin membranes for bone regeneration application. *Appl. Clay Sci.* **2017**. [[CrossRef](#)]
24. Du, M.; Guo, B.; Jia, D. Newly emerging applications of halloysite nanotubes: A review. *Polym. Int.* **2010**, *59*, 574–582. [[CrossRef](#)]
25. Sadjadi, S.; Hosseinnajad, T.; Malmir, M.; Heravi, M.M. Cu@furfural imine-decorated halloysite as an efficient heterogeneous catalyst for promoting ultrasonic-assisted A³ and KA² coupling reactions: A combination of experimental and computational study. *New J. Chem.* **2017**, *41*, 13935–13951. [[CrossRef](#)]
26. Churchman, G.J.; Pasbakhsh, P.; Hillier, S. The rise and rise of halloysite. *Clay Miner.* **2016**, *51*, 303–308. [[CrossRef](#)]
27. Joussein, E.; Petit, S.; Churchman, G.J.; Theng, B.; Righi, D.; Delvaux, B. Halloysite clay minerals—A review. *Clay Miner.* **2005**, *40*, 383–426. [[CrossRef](#)]
28. Pasbakhsh, P.; Churchman, G.J.; Keeling, J.L. Characterisation of properties of various halloysites relevant to their use as nanotubes and microfibre fillers. *Appl. Clay Sci.* **2013**, *74*, 47–57. [[CrossRef](#)]
29. Cavallaro, G.; Chiappisi, L.; Pasbakhsh, P.; Gradzielski, M.; Lazzara, G. A structural comparison of halloysite nanotubes of different origin by Small-Angle Neutron Scattering (SANS) and electric birefringence. *Appl. Clay Sci.* **2018**, *160*, 71–80. [[CrossRef](#)]
30. Lazzara, G.; Cavallaro, G.; Panchal, A.; Fakhrullin, R.; Stavitskaya, A.; Vinokurov, V.; Lvov, Y. An assembly of organic-inorganic composites using halloysite clay nanotubes. *Curr. Opin. Colloid Interface Sci.* **2018**, *35*, 42–50. [[CrossRef](#)]
31. Kryuchkova, M.; Danilushkina, A.; Lvov, Y.; Fakhrullin, R. Evaluation of toxicity of nanoclays and graphene oxide in vivo: A paramecium caudatum study. *Environ. Sci. Nano* **2016**, *3*, 442–452. [[CrossRef](#)]
32. Tan, D.; Yuan, P.; Annabi-Bergaya, F.; Liu, D.; Wang, L.; Liu, H.; He, H. Loading and in vitro release of ibuprofen in tubular halloysite. *Appl. Clay Sci.* **2014**, *96*, 50–55. [[CrossRef](#)]
33. Wang, X.; Gong, J.; Rong, R.; Gui, Z.; Hu, T.; Xu, X. Halloysite nanotubes-induced Al accumulation and fibrotic response in lung of mice after 30-day repeated oral administration. *J. Agric. Food Chem.* **2018**, *66*, 2925–2933. [[CrossRef](#)] [[PubMed](#)]

34. Cavallaro, G.; Lazzara, G.; Milioto, S.; Parisi, F.; Evtugyn, V.; Rozhina, E.; Fakhrullin, R. Nanohydrogel Formation within the halloysite lumen for triggered and sustained release. *ACS Appl. Mater. Interfaces* **2018**, *10*, 8265–8273. [[CrossRef](#)] [[PubMed](#)]
35. Aguzzi, C.; Viseras, C.; Cerezo, P.; Salcedo, I.; Sánchez-Espejo, R.; Valenzuela, C. Release kinetics of 5-aminosalicylic acid from halloysite. *Colloids Surf. B Biointerfaces* **2013**, *105*, 75–80. [[CrossRef](#)] [[PubMed](#)]
36. Massaro, M.; Amorati, R.; Cavallaro, G.; Guernelli, S.; Lazzara, G.; Milioto, S.; Noto, R.; Poma, P.; Riela, S. Direct chemical grafted curcumin on halloysite nanotubes as dual-responsive prodrug for pharmacological applications. *Colloids Surf. B Biointerfaces* **2016**, *140*, 505–513. [[CrossRef](#)] [[PubMed](#)]
37. Lvov, Y.M.; DeVilliers, M.M.; Fakhrullin, R.F. The application of halloysite tubule nanoclay in drug delivery. *Expert Opin. Drug Deliv.* **2016**, *13*, 977–986. [[CrossRef](#)] [[PubMed](#)]
38. Liu, M.; Wu, C.; Jiao, Y.; Xiong, S.; Zhou, C. Chitosan-halloysite nanotubes nanocomposite scaffolds for tissue engineering. *J. Mater. Chem. B* **2013**, *1*, 2078–2089. [[CrossRef](#)]
39. Arcudi, F.; Cavallaro, G.; Lazzara, G.; Massaro, M.; Milioto, S.; Noto, R.; Riela, S. Selective functionalization of halloysite cavity by click reaction: Structured filler for enhancing mechanical properties of bionanocomposite films. *J. Phys. Chem. C* **2014**, *118*, 15095–15101. [[CrossRef](#)]
40. Gorrasi, G. Dispersion of halloysite loaded with natural antimicrobials into pectins: Characterization and controlled release analysis. *Carbohydr. Polym.* **2015**, *127*, 47–53. [[CrossRef](#)] [[PubMed](#)]
41. Bernardo, V.; Martín-de León, J.; Laguna-Gutiérrez, E.; Rodríguez-Pérez, M.Á. PMMA-sepiolite nanocomposites as new promising materials for the production of nanocellular polymers. *Eur. Polym. J.* **2017**, *96*, 10–26. [[CrossRef](#)]
42. Wassel, E.; Es-Souni, M.; Berger, N.; Schopf, D.; Dietze, M.; Solterbeck, C.-H.; Es-Souni, M. Nanocomposite films of laponite/PEG-grafted polymers and polymer brushes with nonfouling properties. *Langmuir* **2017**, *33*, 6739–6750. [[CrossRef](#)] [[PubMed](#)]



© 2018 by the authors. Licensee MDPI, Basel, Switzerland. This article is an open access article distributed under the terms and conditions of the Creative Commons Attribution (CC BY) license (<http://creativecommons.org/licenses/by/4.0/>).



Research paper

Effects of halloysite content on the thermo-mechanical performances of composite bioplastics

Lorenzo Lisuzzo^a, Giuseppe Cavallaro^{a,b,*}, Stefana Milioto^{a,b}, Giuseppe Lazzara^{a,b}^a Dipartimento di Fisica e Chimica, Università degli Studi di Palermo, Viale delle Scienze, pad. 17, 90128 Palermo, Italy^b Consorzio Interuniversitario Nazionale per la Scienza e Tecnologia dei Materiali, INSTM, Via G. Giusti, 9, I-50121 Firenze, Italy

ARTICLE INFO

Keywords:

Halloysite
Bioplastics
Biopolymer
Nanocomposites
DMA
TGA

ABSTRACT

The aim of this study is the design and preparation of Mater-Bi/halloysite nanocomposite materials that could be employed as bioplastics alternative to the petroleum derived products. The biocomposite materials at variable halloysite content (from 0 to 30 wt%) were prepared by using the solvent casting method. We investigated the mechanical behaviour and the thermal properties of the prepared nanocomposites in order to estimate their suitability as biocompatible packaging materials. The thermo-mechanical characteristics were correlated to the nanocomposites' morphologies, which were studied by Scanning Electron Microscopy (SEM). As a general result, the physico-chemical performances of Mater-Bi were improved by the presence of small amounts of nanotubes, which evidenced a homogenous distribution in the polymer matrix. The strongest enhancements of the thermal stability and tensile properties were achieved for Mater-Bi/halloysite 10 wt%. A further addition of nanotubes determined the worsening of both thermal stability and mechanical behaviour.

The attained knowledge represents the starting step for the development of packaging films composed by Mater-Bi and halloysite nanotubes.

1. Introduction

Environmental issues, e.g. pollution and climate change, are the most urgent challenges that science must tackle in the medium period. The need to exploit and strengthen all the possibilities that green chemistry offers is compelling. Therefore, scientists and researchers are making great efforts with the aim to provide new green tools to the society, thus ensuring a more respectful development model. Herein, the use of petroleum derived materials must be restricted due to their harmful impact on the ecosystem and their non-biocompatibility. In the most recent years, new bio-derived materials have been designed and studied with the purpose to replace traditional plastics. Hence, the term "bioplastics" derived from the need to develop novel eco-sustainable systems without waiving some important physico-chemical properties.

Biopolymers represent a profitable alternative for the design of new eco-friendly functional materials being completely green, eco-sustainable and non-toxic (Liu et al., 2012; Gorrasi, 2015; Biddeci et al., 2016; Rebitski et al., 2018). They can display some different features in relation with the natural source where the raw matter is extracted and used during the preparation procedure (Tharanathan, 2003; Mensitieri et al., 2011). The biopolymers charge is one of the most important feature that affect their suitability in numerous applications (Bertolino

et al., 2016). Among the sustainable polymers, chitosan is positively charged, alginate and pectin are negatively charged, starch and cellulose are neutral. It is also important to consider the different hydrophilic/hydrophobic behaviours of such species that, in light of these reasons, offer a wide range of choice to material scientists and engineers.

Nevertheless, some limitations to the use of pure biopolymers still exist and they are related to the mechanical, thermal or gas barrier properties (Gorrasi et al., 2014; Lvov et al., 2016; Sharma et al., 2018). In order to overcome these constraints, the most promising bioplastics are prepared through the combination of both organic moieties and some inorganic fillers, such as clay nanoparticles (Dziadkowiec et al., 2017; Almeida et al., 2019; Rebitski et al., 2019). Nanoclays are attracting the attention of the scientific community due to their peculiar features in terms of chemistry, morphology, aspect ratio and charge (Peyne et al., 2017; Djellali et al., 2019; Lisuzzo et al., 2019b). Among the clay nanoparticles, halloysite (Hal) is a 1:1 aluminosilicate that can be found in nature, whose main property is its distinctive hollow tubular shape combined with its eco-compatibility, no-toxicity and low cost (Joo et al., 2013; Zhang, 2017). Each halloysite nanotube is composed by a layer of tetrahedral siloxanes and a layer of octahedral aluminols forming a sheet that rolls up, thus creating two chemically

* Corresponding author at: Dipartimento di Fisica e Chimica, Università degli Studi di Palermo, Viale delle Scienze, pad. 17, 90128 Palermo, Italy.

E-mail addresses: giuseppe.cavallaro@unipa.it (L. Lisuzzo), giuseppe.cavallaro@unipa.it (G. Cavallaro).

different surfaces (Joussein et al., 2005). The outer surface (composed by Si-O-Si groups) is negatively charged and the inner one (composed by Al-OH groups) is positively charged in the 2–8 pH range (Lazzara et al., 2018). Moreover, halloysite nanotubes show a high aspect ratio, since the inner diameter is about 10–20 nm, the outer diameter is 50–70 nm and the length is 1–2 μm . Within this, it should be noted that the polydispersion degree in sizes is strongly affected by the specific geological source of halloysite (Cavallaro et al., 2018a). Recently, halloysite nanotube-based functional materials have received increasing attention as evidenced by research articles (Tan et al., 2014; Zeng et al., 2019) and reviews (Yuan et al., 2015; Papoulis, 2019). Halloysite is a promising nanoclay in numerous applications, including drug delivery (Viseras et al., 2008; Aguzzi et al., 2013; Dзамukova et al., 2015), catalysis (Liu et al., 2018; Sadjadi et al., 2018) and remediation (Berthonneau et al., 2015; Nyankson et al., 2015; Panchal et al., 2018; Deng et al., 2019; Wei et al., 2019). There are many examples proving the importance of halloysite in addition to eco-compatible polymers as starting building blocks for the preparation of novel green materials with specific biomedical and technological functionalities (Silva et al., 2014; Naumenko et al., 2016; Qin et al., 2016; Liu et al., 2017; Zhou et al., 2017; Ali and Ahmed, 2018; Zhao et al., 2018; Suner et al., 2019). For instance, biocomposites with a multilayered morphology based on a layer of halloysite sandwiched between two layers of chitosan were designed for medical or fire retardancy applications (Bertolino et al., 2018). Literature reports the formation of a chitosan film with embedded clay nanotubes used for the preparation of alginate covered tablets, which exhibited pH controlled drug delivery capacity (Blanco et al., 2017; Lisuzzo et al., 2019a; Silva et al., 2014; Viseras et al., 2008). Bioplastics were prepared by filling halloysite into the pectin matrix for food packaging applications (Makaremi et al., 2017) and by combining lysozyme loaded nanotubes and poly (ϵ -caprolactone) (PCL) for the preparation of antimicrobial packaging membrane (Bugatti et al., 2017). Moreover, bionanocomposites based were obtained by the halloysite addition into cellulose and chitosan for the delivery of curcumin or tissue engineering applications, respectively (Liu et al., 2013; Huang et al., 2017).

In our previous work Cavallaro et al., 2018b, we investigated the effect of different nanoclays (sepiolite, halloysite, laponite and kaolinite) in the mechanical properties of Mater-Bi polymer based nanocomposites with a fixed polymer/nanofiller ratio. The results showed that halloysite is the most promising nanoclay for the preparation of bioplastics that present Mater-Bi as polymeric matrix. Here, we studied the influence of the halloysite content on both the mechanical and thermal features of the bionanocomposites in order to determine an effective protocol for the development of Mater-Bi/halloysite hybrid films with proper characteristics for packaging purposes.

2. Materials and methods

2.1. Materials

Halloysite (Hal) was supplied as a “processed product” by Imerys from their Matauri Bay operation. Mater-Bi is a Novamont product (Novara, Italy) and 1,2-Dichloroethane was purchased by Sigma-Aldrich.

2.2. Preparation of the nanocomposites

The nanocomposites based on halloysite nanotubes and Mater-Bi were prepared by solvent casting method. Firstly, the biopolymer (2 wt %) was solubilized in 1,2-Dichloroethane and Hal was added as dry powder to the solution at different concentrations, from 0 to 30% w/w. Thereafter, each mixture was magnetically stirred overnight at 25 °C and poured down into glass Petri dishes in order to evaporate the solvent, thus obtaining different nanocomposite films, which were stored in a desiccator at 25 °C.

2.3. Methods

2.3.1. Dynamic mechanical analysis

A DMA Q800 instrument (TA Instruments) was used in order to study the tensile properties of the Mater-Bi/Hal nanocomposites. In particular, the films were cut into rectangular shaped portions (10.00 \times 5.00 \times 0.20 mm³) and the measurements were performed with a stress ramp of 1 MPa min⁻¹.

at 25.0 \pm 0.5 °C. The analysis of the stress vs strain curves allowed us to determine the Young modulus (Y_m), the tensile strength (σ_r) and the percentage of elongation at break ($\epsilon_{\%}$). The integration of each curve provided the stored energy (E) for each film due to the mechanical stress until the breaking point.

2.3.2. Thermogravimetry

Thermogravimetric analysis (TGA) was performed using a Q5000 IR apparatus (TA Instruments) under the nitrogen flow of 25 cm³ min⁻¹ for the sample and 10 cm³ min⁻¹ for the balance. The calibration was carried out by means of Curie temperature of standards (nickel, cobalt and their alloys) as reported in literature (Blanco et al., 2014, 2017). Each sample, whose mass was ca. 5 mg, was heated from room temperature to 750 °C with a rate of 20 °C min⁻¹. TGA allowed to study the thermal degradation of Mater-Bi/Hal nanocomposites and to investigate any effects on the thermal stability of these materials.

2.3.3. Scanning electron microscopy

The morphological features of the nanocomposites were studied by scanning electron microscopy, which was conducted using a ESEM FEI QUANTA 200F microscope. In order to avoid any charging under electron beam, each sample was coated with gold in argon by means of an Edwards Sputter Coater S150A before the analysis. The measurements were carried out in high-vacuum mode ($< 6 \times 10^{-4}$ Pa) for simultaneous secondary electrons. The energy of the beam was 20 kV, while the working distance was set at 10 mm.

2.3.4. Fourier transform infrared (FTIR) spectroscopy

Fourier transform infrared (FTIR) measurements were performed at room temperature through a Frontier FTIR spectrometer (PerkinElmer). The spectra were recorded using 64 scans in the range between 4000 and 450 cm⁻¹, while the spectral resolution was set at 2 cm⁻¹. The experiments were conducted on KBr pellets with a low content (< 2 wt %) of milled sample.

3. Results and discussion

3.1. Mechanical properties of Mater-Bi/Halloysite composite films

Some examples of stress vs. strain curves for Mater-Bi and Mater-Bi/halloysite films are presented in Fig. 1.

The stress vs. strain curves (Fig. 1) showed that all the prepared samples are elastic at first, since the strain increases linearly with the stress, and they convert into plastic materials when the yielding point is reached, thus the deformation becomes irreversible. Moreover, it was observed that the strain at break is much higher for the Mater-Bi/Hal 10 wt% nanocomposite in comparison with the other samples. The dependence of the elongation at break on the nanofiller content is shown in Fig. 2.

It is clearly observed that the concentration of inorganic nanotubes deeply influences the ultimate elongation of Mater-Bi based films (Fig. 2). In particular, we detected that the percentage of ultimate elongation is 30 and 100% for the pure Mater-Bi film and Mater-Bi/Hal 10 wt%, respectively. The further addition of nanotubes decreased the elongation at break up to ca. 10% for the composite material with the largest Hal content (30 wt%). According to the literature (Tang and Alavi, 2012; Cavallaro et al., 2013), the reduction of the maximum elongation can be explained by considering the nanotubes/Mater-Bi

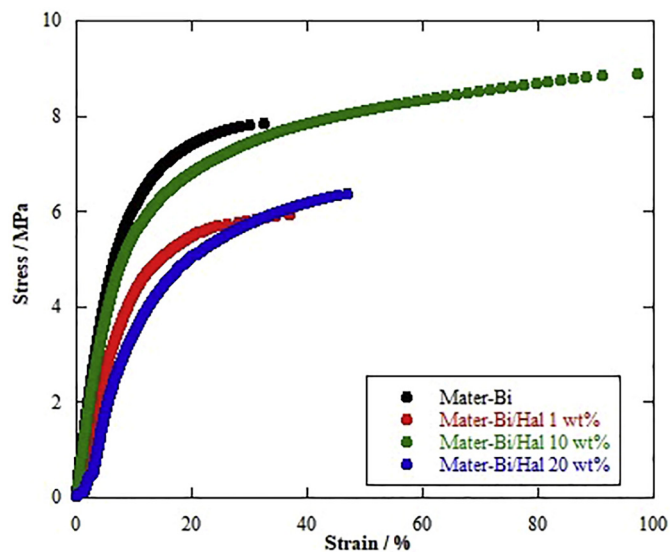


Fig. 1. Stress vs. strain curves for pure Mater-Bi and Mater-Bi/Halloysite films as a function of the nanoclay content.

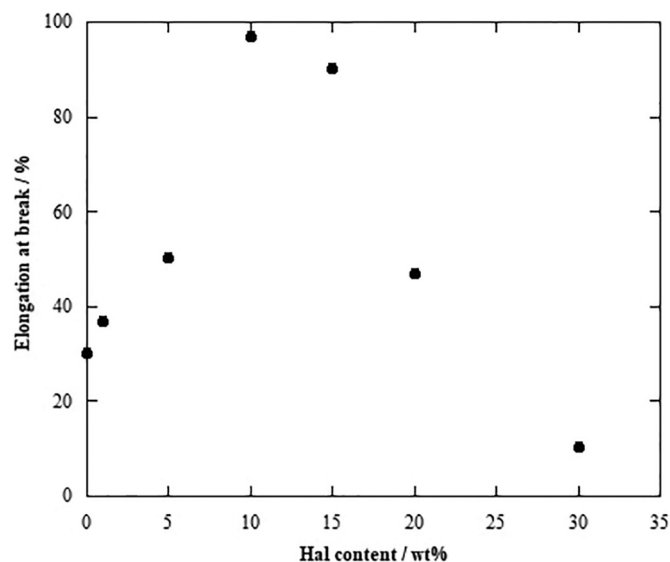


Fig. 2. Elongation at break for Mater-Bi/Halloysite composite films as a function of the nanoclay content. The relative error is 2%.

interactions, which avoid the sliding of the polymer chains. Similar effects were observed for the stored energy of the films during the tensile experiments (Fig. 3).

Specifically, we determined that the film based on pristine Mater-Bi possess a stored energy of 1718 kJ m^{-3} . This value was significantly enhanced in the composite with Hal concentration of 10 wt% (ca. 7300 kJ m^{-3}), while the Mater-Bi/Hal 30 wt% exhibited a much lower stored energy (254 kJ m^{-3}). These observations are in good agreement with the data of both stress at break and Young modulus (see Supporting Information).

3.2. Thermal properties and structure

Thermogravimetric analysis was aimed to study the thermal stability and the degradation properties of the Mater-Bi/Hal nanocomposite film. As examples, Fig. 4 reports the thermogravimetric curves for both pure Mater-Bi and Mater-Bi/Hal₁₀ wt% materials.

Compared to pristine Mater-Bi, the nanocomposite presents a larger

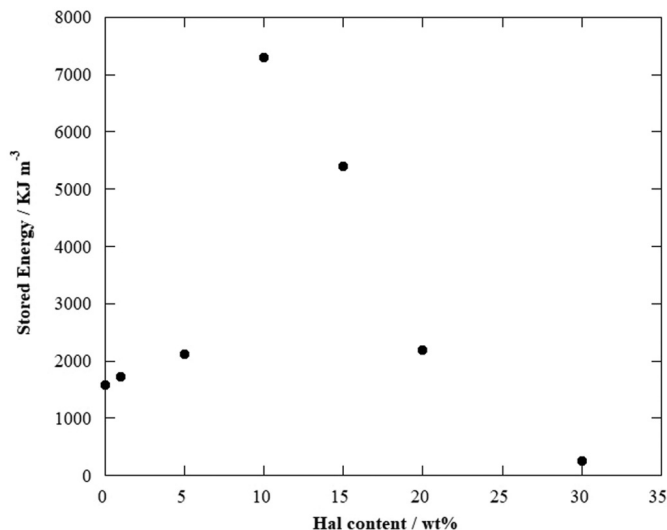


Fig. 3. Stored energy up to breaking for Mater-Bi/Halloysite composite films as a function of the nanoclay content. The relative error is 2%.

residual mass at high temperature as a consequence of the presence of the inorganic nanotubes (Fig. 4). In this regards, the residual masses at $700 \text{ }^\circ\text{C}$ for all the investigated materials are presented in Supporting Information. These results evidenced that the nanocomposites with higher Hal contents possess larger residual masses at $700 \text{ }^\circ\text{C}$. All the investigated materials showed a mass loss in the temperature range between 25 and $150 \text{ }^\circ\text{C}$ that can be attributed to the moisture content of the bioplastics. Both Mater-Bi and Mater-Bi/Hal 10 wt% nanocomposite exhibited two different degradation steps in the $300\text{--}400 \text{ }^\circ\text{C}$ range as highlighted by the corresponding differential thermogravimetric curves (Fig. 4). In order to explore the effect of halloysite on the thermal stability of Mater-Bi, we determined the onset temperatures from the analysis of the thermogravimetric curves. The onset temperature refers to the initial decomposition of Mater-Bi. Namely, it represents the temperature where the polymer starts to decompose. The onset temperature is obtained by the intersection of a line tangent to the baseline with a line tangent to the inflection point of the thermogravimetric curve.

Similarly to the tensile properties, the presence of small amounts of halloysite generated a slight improvement of the Mater-Bi thermal stability (Fig. 5). In particular, the nanocomposite with Hal content of 10 wt% showed an enhancement of ca. $4 \text{ }^\circ\text{C}$ for the onset temperature with respect to that of pristine Mater-Bi. The slight thermal stabilization effect induced by the presence of small amounts of halloysite can be observed by the comparison of the thermogravimetric curves for Mater-Bi and Mater-Bi/Hal 10 wt% within the temperature range between 200 and $340 \text{ }^\circ\text{C}$ (see inset in Fig. 4). Larger filler contents ($> 10 \text{ wt}\%$) induced a worsening of the polymer thermal stability as evidenced by the decrease of the onset temperature (Fig. 5). Similar trends are reported for the degradation temperatures estimated by the maxima of the DTG peaks (see Supporting Information). These effects might be related to the peculiar morphological characteristics of the nanocomposites that can be influenced by their specific composition. Based on thermogravimetric results, the nanotubes should be uniformly dispersed in the polymeric matrix for the composite materials with $\text{Hal} \leq 10 \text{ wt}\%$. This hypothesis was supported by SEM images (Fig. 6), which showed that Mater-Bi/Hal 10 wt% presents the nanotubes randomly dispersed in its surface.

As reported in literature (Du et al., 2006, 2010; Makaremi et al., 2017), the homogenous distribution of inorganic fillers within polymer can cause an enhancement of the thermal stability as a consequence of the barrier effect towards the volatile products of the polymer degradation. Furthermore, the encapsulation process within the Hal

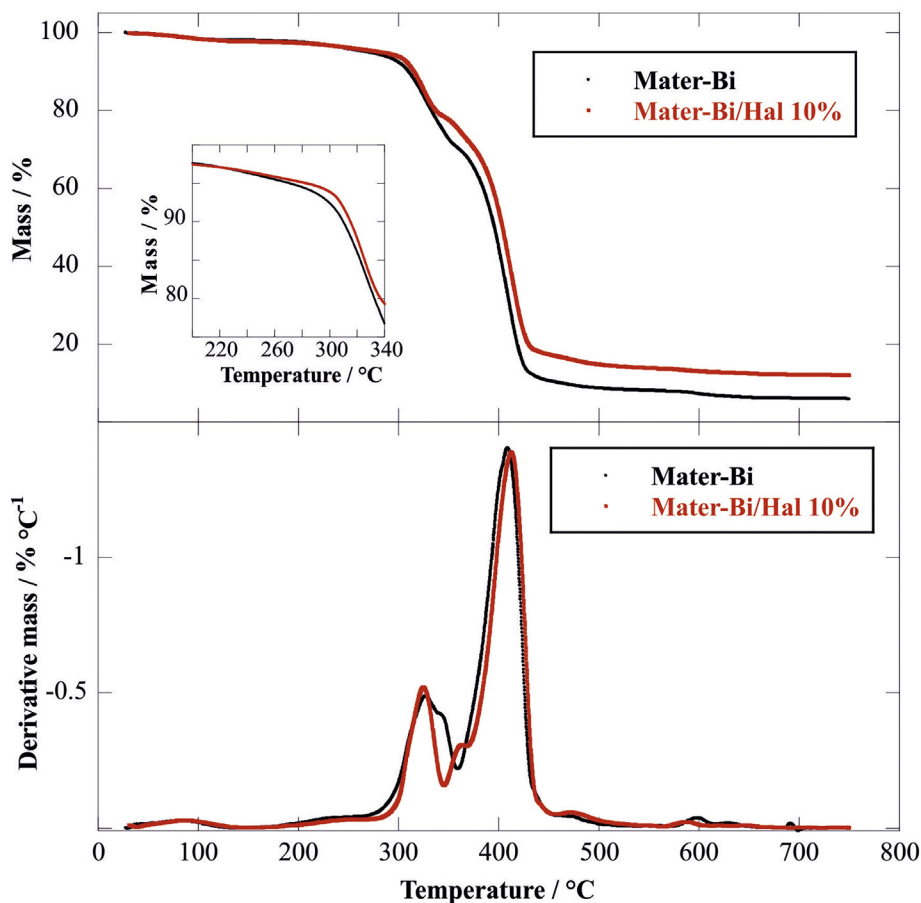


Fig. 4. Thermogravimetric (up) and differential thermogravimetric (bottom) curves for Mater-Bi and Mater-Bi/Hal 10 wt% materials. The inset shows the thermogravimetric curves for Mater-Bi and Mater-Bi/Hal 10 wt% within the temperature range between 200 and 340 °C.

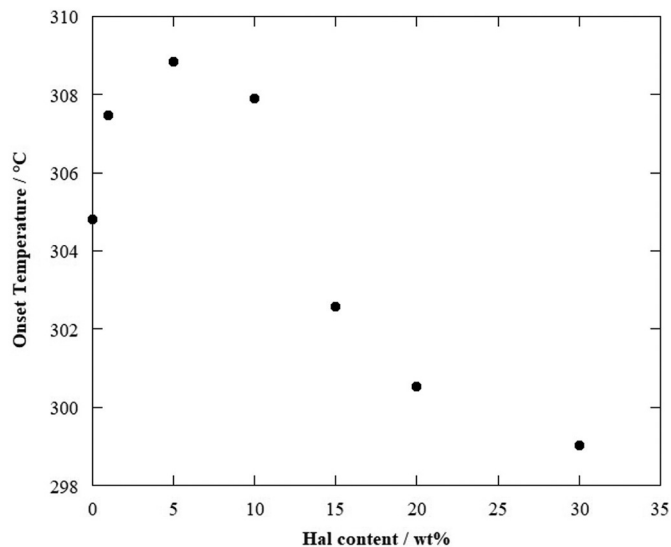


Fig. 5. Onset temperature values for pure Mater-Bi and Mater-Bi/Halloysite composite films as a function of the nanoclay content. The relative error is 2%.

cavity can contribute to the improvement of the Mater-Bi resistance to the thermal degradation. On the other hand, the decrease of the onset temperature at larger Hal contents could be an indication of the phase separation between polymer and nanotubes, which are not more able to create a barrier towards the volatile products of the Mater-Bi degradation. In this regards, it is reported that nanocomposites with a

large Hal content exhibit a lower thermal stability compared to the corresponding pure polymers because of their layered structure (Cavallaro et al., 2011) and/or formation of nanotubes aggregates within the matrix (Cavallaro et al., 2013). As evidenced in Fig. 6, Mater-Bi/Hal 30 wt% presents a rough surface with several clusters and holes indicating that the nanotubes are not homogeneously dispersed in the polymeric matrix. Accordingly, both the thermal and mechanical properties of Mater-Bi were worsened by the addition of a large amounts of halloysite nanotubes. The nature of interactions between Mater-Bi and halloysite nanotubes in the nanocomposites was investigated by FTIR spectroscopy. Fig. 7 shows the FTIR spectra for Mater-Bi and Mater-Bi with variable Hal content (10 and 30 wt%).

We observed that the characteristic FTIR signals of Mater-Bi are not influenced by the presence of halloysite. In particular, we focused on the peaks centered at 2951 and 1730 cm^{-1} , which are related to C–H aliphatic stretching and C=O stretching vibration of polyester, respectively (Cataldi et al., 2015). Both signals did not show neither shifting nor splitting phenomena in the Mater-Bi/Hal nanocomposites highlighting that the polymer structure was not altered by the addition of the nanotubes. Based on FTIR spectra, we can state that Mater-Bi is physically adsorbed onto halloysite surfaces ruling out the presence of covalent bonds between matrix and filler.

4. Conclusions

We successfully prepared a novel biohybrid material based on Mater-Bi and halloysite nanotubes by using the casting method from 1,2-Dichloroethane. The effect of the halloysite content on the tensile and thermal properties of the nanocomposites was extensively investigated by Dynamic Mechanical Analysis (DMA) and

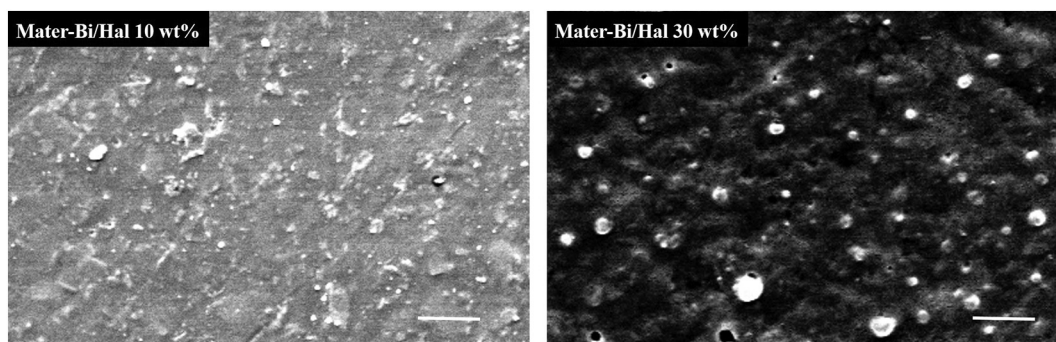


Fig. 6. Scanning Electron Microscopy image of the Mater-Bi/Hal nanocomposites at variable composition. The scale bar is 10 μm .

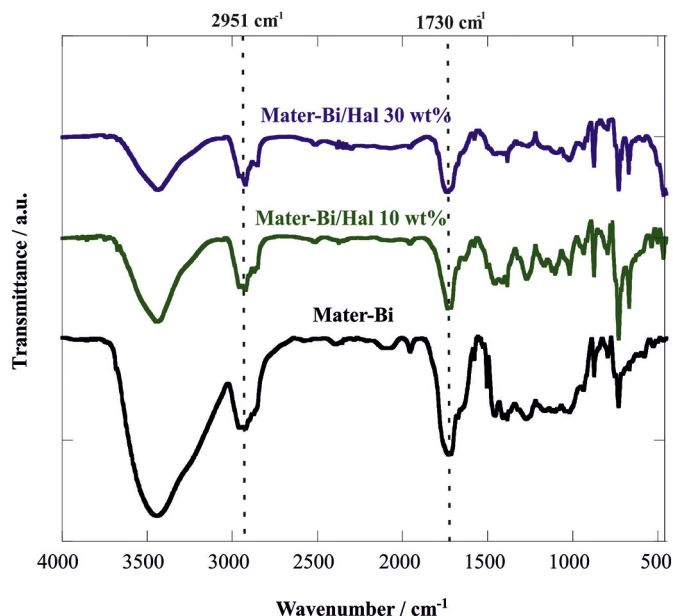


Fig. 7. Fourier Transform Infrared spectra for Mater-Bi, Mater-Bi/Hal 10 wt% and Mater-Bi/Hal 30 wt% materials.

Thermogravimetry (TGA), respectively.

As a general result, we detected that the presence of small amounts (≤ 10 wt%) of nanotubes confers improved thermo-mechanical performances with respect to those of Mater-Bi. Compared to the pure biopolymer, Mater-Bi/Hal 10 wt% composite exhibited improvements of ca. 320 and 230% for the ultimate elongation and the stored energy at the breaking point, respectively. Opposite results were detected for nanocomposites with Hal concentrations larger than 10 wt%. As example, the stored energy at break evidenced a decrease of ca. 85% in the nanocomposite with halloysite content of 30 wt%. Similar effects were observed for the elastic modulus and the stress at breaking point. As concerns the thermal behavior, we observed that the thermal stability of Mater-Bi/halloysite nanocomposites slightly depends on their specific filler content. The addition of nanotubes generated enhancements (up to 4 $^{\circ}\text{C}$) of the polymer degradation temperature for halloysite contents lower than 10 wt%. Oppositely, a thermal destabilization of Mater-Bi was detected for nanocomposites with halloysite concentrations larger than 10 wt%. In particular, Mater-Bi/halloysite 30 wt% evidenced a slight decrease (ca. 5 $^{\circ}\text{C}$) of the polymer degradation temperature with respect to that of pure Mater-Bi that can be attributed to the formation of halloysite clusters within the matrix. According to both TGA and DMA data, we can conclude that the most promising performances were achieved for Mater-Bi/halloysite 10 wt% composite film, which might be considered as a suitable biomaterial for packaging applications.

Declaration of Competing Interest

None.

Acknowledgments

The work was financially supported by Progetto di ricerca e sviluppo “AGM for CuHe” (ARS01_00697) and University of Palermo. The authors have no conflicts of interest to declare.

Appendix A. Supplementary data

Supplementary data to this article can be found online at <https://doi.org/10.1016/j.clay.2019.105416>.

References

- Aguzzi, C., Viseras, C., Cerezo, P., Salcedo, I., Sánchez-Espejo, R., Valenzuela, C., 2013. Release kinetics of 5-aminosalicylic acid from halloysite. *Colloids Surf. B: Biointerfaces* 105, 75–80. <https://doi.org/10.1016/j.colsurfb.2012.12.041>.
- Ali, A., Ahmed, S., 2018. A review on chitosan and its nanocomposites in drug delivery. *Int. J. Biol. Macromol.* 109, 273–286. <https://doi.org/10.1016/j.ijbiomac.2017.12.078>.
- Almeida, J.A., Oliveira, A.S., Rigoti, E., Neto, J.C.D., de Alcântara, A.C.S., Pergher, S.B.C., 2019. Design of solid foams for flame retardant based on bionanocomposites systems. *Appl. Clay Sci.* 180, 105173. <https://doi.org/10.1016/j.clay.2019.105173>.
- Berthonneau, J., Grauby, O., Jeannin, C., Chaudanson, D., Joussein, E., Baronnet, A., 2015. Native Morphology of Hydrated Spheroidal Halloysite Observed by Environmental Transmission Electron Microscopy. *Clay Clay Miner.* 63, 368–377. <https://doi.org/10.1346/CCMN.2015.0630503>.
- Bertolino, V., Cavallaro, G., Lazzara, G., Merli, M., Milioto, S., Parisi, F., Sciascia, L., 2016. Effect of the biopolymer charge and the nanoclay morphology on nanocomposite materials. *Ind. Eng. Chem. Res.* 55, 7373–7380. <https://doi.org/10.1021/acs.iecr.6b01816>.
- Bertolino, V., Cavallaro, G., Lazzara, G., Milioto, S., Parisi, F., 2018. Halloysite nanotubes sandwiched between chitosan layers: novel bionanocomposites with multilayer structures. *New J. Chem.* 42, 8384–8390. <https://doi.org/10.1039/C8NJ01161C>.
- Biddeci, G., Cavallaro, G., Di Blasi, F., Lazzara, G., Massaro, M., Milioto, S., Parisi, F., Riela, S., Spinelli, G., 2016. Halloysite nanotubes loaded with peppermint essential oil as filler for functional biopolymer film. *Carbohydr. Polym.* 152, 548–557. <https://doi.org/10.1016/j.carbpol.2016.07.041>.
- Blanco, I., Abate, L., Bottino, F.A., Bottino, P., 2014. Thermal behaviour of a series of novel aliphatic bridged polyhedral oligomeric silsesquioxanes (POSSs)/polystyrene (PS) nanocomposites: the influence of the bridge length on the resistance to thermal degradation. *Polym. Degrad. Stab.* 102, 132–137. <https://doi.org/10.1016/j.polydegradstab.2014.01.029>.
- Blanco, I., Cicala, G., Latteri, A., Saccullo, G., El-Sabbagh, A.M.M., Ziegmann, G., 2017. Thermal characterization of a series of lignin-based polypropylene blends. *J. Therm. Anal. Calorim.* 127, 147–153. <https://doi.org/10.1007/s10973-016-5596-2>.
- Bugatti, V., Viscusi, G., Naddeo, C., Gorrasi, G., 2017. Nanocomposites based on PCL and halloysite nanotubes filled with lysozyme: effect of draw ratio on the physical properties and release analysis. *Nanomaterials* 7. <https://doi.org/10.3390/nano7080213>.
- Cataldi, P., Bayer, I.S., Bonaccorso, F., Pellegrini, V., Athanassiou, A., Cingolani, R., 2015. Foldable conductive cellulose fiber networks modified by graphene nanoplatelet-bio-based composites. *Adv. Electron Mater.* 1, 1500224. <https://doi.org/10.1002/aeml.201500224>.
- Cavallaro, G., Donato, D.I., Lazzara, G., Milioto, S., 2011. Films of halloysite nanotubes sandwiched between two layers of biopolymer: from the morphology to the dielectric, thermal, transparency, and wettability properties. *J. Phys. Chem. C* 115, 20491–20498. <https://doi.org/10.1021/jp207261r>.

- Cavallaro, G., Lazzara, G., Milioto, S., 2013. Sustainable nanocomposites based on halloysite nanotubes and pectin/polyethylene glycol blend. *Polym. Degrad. Stab.* 98, 2529–2536. <https://doi.org/10.1016/j.polydegradstab.2013.09.012>.
- Cavallaro, G., Chiappisi, L., Pasbakhsh, P., Gradzielski, M., Lazzara, G., 2018a. A structural comparison of halloysite nanotubes of different origin by Small-Angle Neutron Scattering (SANS) and Electric Birefringence. *Appl. Clay Sci.* 160, 71–80. <https://doi.org/10.1016/j.clay.2017.12.044>.
- Cavallaro, G., Lazzara, G., Lisuzzo, L., Milioto, S., Parisi, F., 2018b. Filling of Mater-Bi with nanoclays to enhance the biofilm rigidity. *J. Funct. Biomater.* 9. <https://doi.org/10.3390/jfb9040060>.
- Deng, L., Yuan, P., Liu, D., Du, P., Zhou, J., Wei, Y., Song, Y., Liu, Y., 2019. Effects of calcination and acid treatment on improving benzene adsorption performance of halloysite. *Appl. Clay Sci.* 181, 105240. <https://doi.org/10.1016/j.clay.2019.105240>.
- Djellali, M., Aranda, P., Ruiz-Hitzky, E., 2019. Silica-layered double hydroxide nanoarchitected materials. *Appl. Clay Sci.* 171, 65–73. <https://doi.org/10.1016/j.clay.2019.02.004>.
- Du, M., Guo, B., Jia, D., 2006. Thermal stability and flame retardant effects of halloysite nanotubes on poly(propylene). *Eur. Polym. J.* 42, 1362–1369. <https://doi.org/10.1016/j.eurpolymj.2005.12.006>.
- Du, M., Guo, B., Jia, D., 2010. Newly emerging applications of halloysite nanotubes: a review. *Polym. Int.* 59, 574–582.
- Dzamikova, M.R., Naumenko, E.A., Lvov, Y.M., Fakhruddin, R.F., 2015. Enzyme-activated intracellular drug delivery with tubule clay nanof ormulation. *Sci. Rep.* 5, 10560.
- Dziadkiewicz, J., Mansa, R., Quintela, A., Rocha, F., Detellier, C., 2017. Preparation, characterization and application in controlled release of Ibuprofen-loaded Guar Gum/Montmorillonite Bionanocomposites. *Appl. Clay Sci.* 135, 52–63. <https://doi.org/10.1016/j.clay.2016.09.003>.
- Gorrasí, G., 2015. Dispersion of halloysite loaded with natural antimicrobials into pectins: Characterization and controlled release analysis. *Carbohydr. Polym.* 127, 47–53. <https://doi.org/10.1016/j.carbpol.2015.03.050>.
- Gorrasí, G., Pantani, R., Murariu, M., Dubois, P., 2014. PLA/Halloysite nanocomposite films: water vapor barrier properties and specific key characteristics. *Macromol. Mater. Eng.* 299, 104–115. <https://doi.org/10.1002/mame.201200424>.
- Huang, B., Liu, M., Zhou, C., 2017. Cellulose–halloysite nanotube composite hydrogels for curcumin delivery. *Cellulose* 24, 2861–2875. <https://doi.org/10.1007/s10570-017-1316-8>.
- Joo, Y., Sim, J.H., Jeon, Y., Lee, S.U., Sohn, D., 2013. Opening and blocking the inner-pores of halloysite. *Chem. Commun.* 49, 4519–4521. <https://doi.org/10.1039/C3CC40465J>.
- Joussein, E., Petit, S., Churchman, G.J., Theng, B., Righi, D., Delvaux, B., 2005. Halloysite clay minerals — a review. *Clay Miner.* 40, 383–426.
- Lazzara, G., Cavallaro, G., Panchal, A., Fakhruddin, R., Stavitskaya, A., Vinokurov, V., Lvov, Y., 2018. An assembly of organic-inorganic composites using halloysite clay nanotubes. *Curr. Opin. Colloid Interface Sci.* 35, 42–50. <https://doi.org/10.1016/j.cocis.2018.01.002>.
- Lisuzzo, L., Cavallaro, G., Milioto, S., Lazzara, G., 2019a. Layered composite based on halloysite and natural polymers: a carrier for the pH controlled release of drugs. *New J. Chem.* 43, 10887–10893. <https://doi.org/10.1039/C9NJ02565K>.
- Lisuzzo, L., Cavallaro, G., Pasbakhsh, P., Milioto, S., Lazzara, G., 2019b. Why does vacuum drive to the loading of halloysite nanotubes? The key role of water confinement. *J. Colloid Interface Sci.* 547, 361–369. <https://doi.org/10.1016/j.jcis.2019.04.012>.
- Liu, M., Zhang, Y., Wu, C., Xiong, S., Zhou, C., 2012. Chitosan/halloysite nanotubes bionanocomposites: structure, mechanical properties and biocompatibility. *Int. J. Biol. Macromol.* 51, 566–575. <https://doi.org/10.1016/j.ijbiomac.2012.06.022>.
- Liu, M., Wu, C., Jiao, Y., Xiong, S., Zhou, C., 2013. Chitosan-halloysite nanotubes nanocomposite scaffolds for tissue engineering. *J. Mater. Chem. B* 1, 2078–2089. <https://doi.org/10.1039/C3TB20084A>.
- Liu, F., Bai, L., Zhang, H., Song, H., Hu, L., Wu, Y., Ba, X., 2017. Smart H₂O₂-responsive drug delivery system made by halloysite nanotubes and carbohydrate polymers. *ACS Appl. Mater. Interfaces* 9, 31626–31633. <https://doi.org/10.1021/acsami.7b10867>.
- Liu, Y., Guan, H., Zhang, J., Zhao, Y., Yang, J.-H., Zhang, B., 2018. Polydopamine-coated halloysite nanotubes supported AgPd nanoalloy: an efficient catalyst for hydrolysis of ammonia borane. *Int. J. Hydrogen Energ.* 43, 2754–2762. <https://doi.org/10.1016/j.ijhydene.2017.12.105>.
- Lvov, Y., Wang, W., Zhang, L., Fakhruddin, R., 2016. Halloysite clay nanotubes for loading and sustained release of functional compounds. *Adv. Mater.* 28, 1227–1250. <https://doi.org/10.1002/adma.201502341>.
- Makaremi, M., Pasbakhsh, P., Cavallaro, G., Lazzara, G., Aw, Y.K., Lee, S.M., Milioto, S., 2017. Effect of morphology and size of halloysite nanotubes on functional pectin bionanocomposites for food packaging applications. *ACS Appl. Mater. Interfaces* 9, 17476–17488. <https://doi.org/10.1021/acsami.7b04297>.
- Mensitieri, G., Di Maio, E., Buonocore, G.G., Nedi, I., Oliviero, M., Sansone, L., Iannace, S., 2011. Processing and shelf life issues of selected food packaging materials and structures from renewable resources. *Trends Food Sci. Technol.* 22, 72–80. <https://doi.org/10.1016/j.tifs.2010.10.001>.
- Naumenko, E.A., Guryanov, I.D., Yendluri, R., Lvov, Y.M., Fakhruddin, R.F., 2016. Clay nanotube–biopolymer composite scaffolds for tissue engineering. *Nanoscale* 8, 7257–7271. <https://doi.org/10.1039/C6NR00641H>.
- Nyankson, E., Olasehinde, O., John, V.T., Gupta, R.B., 2015. Surfactant-Loaded Halloysite clay nanotube dispersants for crude oil spill remediation. *Ind. Eng. Chem. Res.* 54, 9328–9341. <https://doi.org/10.1021/acs.iecr.5b02032>.
- Panchal, A., Swientoniewski, L.T., Omarova, M., Yu, T., Zhang, D., Blake, D.A., John, V., Lvov, Y.M., 2018. Bacterial proliferation on clay nanotube Pickering emulsions for oil spill bioremediation. *Colloids Surf. B: Biointerfaces* 164, 27–33. <https://doi.org/10.1016/j.colsurfb.2018.01.021>.
- Papoulis, D., 2019. Halloysite based nanocomposites and photocatalysis: a review. *Appl. Clay Sci.* 168, 164–174. <https://doi.org/10.1016/j.clay.2018.11.009>.
- Peyne, J., Gautron, J., Doudeau, J., Joussein, E., Rossignol, S., 2017. Influence of silicate solution preparation on geomaterials based on brick clay materials. *J. Non-Cryst. Solids* 471, 110–119. <https://doi.org/10.1016/j.jnoncrysol.2017.05.017>.
- Qin, L., Zhao, Y., Liu, J., Hou, J., Zhang, Y., Wang, J., Zhu, J., Zhang, B., Lvov, Y., Van der Bruggen, B., 2016. Oriented clay nanotube membrane assembled on microporous polymeric substrates. *ACS Appl. Mater. Interfaces* 8, 34914–34923. <https://doi.org/10.1021/acsami.6b12858>.
- Rebitski, E.P., Alcántara, A.C.S., Darder, M., Cansian, R.L., Gómez-Hortigüela, L., Pergher, S.B.C., 2018. Functional carboxymethylcellulose/Zein bionanocomposite films based on neomycin supported on sepiolite or montmorillonite clays. *ACS Omega* 3, 13538–13550. <https://doi.org/10.1021/acsomega.8b01026>.
- Rebitski, E.P., Souza, G.P., Santana, S.A.A., Pergher, S.B.C., Alcántara, A.C.S., 2019. Bionanocomposites based on cationic and anionic layered clays as controlled release devices of amoxicillin. *Appl. Clay Sci.* 173, 35–45. <https://doi.org/10.1016/j.clay.2019.02.024>.
- Sadjadi, S., Heravi, M.M., Malmir, M., 2018. Pd@HNTs-CDNs-g-C₃N₄: a novel heterogeneous catalyst for promoting ligand and copper-free Sonogashira and Heck coupling reactions, benefits from halloysite and cyclodextrin chemistry and g-C₃N₄ contribution to suppress Pd leaching. *Carbohydr. Polym.* 186, 25–34. <https://doi.org/10.1016/j.carbpol.2018.01.023>.
- Sharma, B., Malik, P., Jain, P., 2018. Biopolymer reinforced nanocomposites: a comprehensive review. *Mater Today Commun.* 16, 353–363. <https://doi.org/10.1016/j.mtcomm.2018.07.004>.
- Silva, R.D., Pasbakhsh, P., Goh, K.L., Chai, S.-P., Chen, J., 2014. Synthesis and characterisation of poly (lactic acid)/halloysite bionanocomposite films. *J. Compos. Mater.* 48, 3705–3717.
- Suner, S.S., Demirci, S., Yetiskin, B., Fakhruddin, R., Naumenko, E., Okay, O., Ayyala, R.S., Sahiner, N., 2019. Cryogel composites based on hyaluronic acid and halloysite nanotubes as scaffold for tissue engineering. *Int. J. Biol. Macromol.* 130, 627–635. <https://doi.org/10.1016/j.ijbiomac.2019.03.025>.
- Tan, D., Yuan, P., Annabi-Bergaya, F., Liu, D., Wang, L., Liu, H., He, H., 2014. Loading and in vitro release of ibuprofen in tubular halloysite. *Appl. Clay Sci.* 96, 50–55. <https://doi.org/10.1016/j.clay.2014.01.018>.
- Tang, X., Alavi, S., 2012. Structure and Physical Properties of Starch/Poly Vinyl Alcohol/Laponite RD Nanocomposite Films. *J. Agric. Food Chem.* 60, 1954–1962. <https://doi.org/10.1021/jf2024962>.
- Tharanathan, R.N., 2003. Biodegradable films and composite coatings: past, present and future. *Trends Food Sci. Technol.* 14, 71–78. [https://doi.org/10.1016/S0924-2244\(02\)00280-7](https://doi.org/10.1016/S0924-2244(02)00280-7).
- Viseras, M.T., Aguzzi, C., Cerezo, P., Viseras, C., Valenzuela, C., 2008. Equilibrium and kinetics of 5-aminosalicylic acid adsorption by halloysite. *Microporous Mesoporous Mater.* 108, 112–116. <https://doi.org/10.1016/j.micromeso.2007.03.033>.
- Wei, Y., Yuan, P., Liu, D., Losic, D., Tan, D., Chen, F., Liu, H., Zhou, J., Du, P., Song, Y., 2019. Activation of natural halloysite nanotubes by introducing lanthanum oxycarbonate nanoparticles via co-calcination for outstanding phosphate removal. *Chem. Commun.* 55, 2110–2113. <https://doi.org/10.1039/C8CC10314C>.
- Yuan, P., Tan, D., Annabi-Bergaya, F., 2015. Properties and applications of halloysite nanotubes: recent research advances and future prospects. *Appl. Clay Sci.* 112–113, 75–93. <https://doi.org/10.1016/j.clay.2015.05.001>.
- Zeng, X., Zhong, B., Jia, Z., Zhang, Q., Chen, Y., Jia, D., 2019. Halloysite nanotubes as nanocarriers for plant herbicide and its controlled release in biodegradable polymers composite film. *Appl. Clay Sci.* 171, 20–28. <https://doi.org/10.1016/j.clay.2019.01.021>.
- Zhang, H., 2017. Selective modification of inner surface of halloysite nanotubes: a review. *Nanotechnol. Rev.* 6, 573. <https://doi.org/10.1515/ntrev-2017-0163>.
- Zhao, Y., Kong, W., Jin, Z., Fu, Y., Wang, W., Zhang, Y., Liu, J., Zhang, B., 2018. Storing solar energy within Ag-Paraffin/Halloysite microspheres as a novel self-heating catalyst. *Appl. Energy* 222, 180–188. <https://doi.org/10.1016/j.apenergy.2018.04.013>.
- Zhou, X., Zhang, Q., Wang, R., Guo, B., Lvov, Y., Hu, G.-H., Zhang, L., 2017. Preparation and performance of bio-based carboxylic elastomer/halloysite nanotubes nanocomposites with strong interfacial interaction. *Compos. Part A-Appl. S.* 102, 253–262. <https://doi.org/10.1016/j.compositesa.2017.08.013>.



Cite this: *New J. Chem.*, 2019, 43, 10887

Layered composite based on halloysite and natural polymers: a carrier for the pH controlled release of drugs†

Lorenzo Lisuzzo,^{id}^a Giuseppe Cavallaro,^{id}^{ab} Stefana Milioto^{ab} and Giuseppe Lazzara^{id}^{*ab}

We have prepared new biohybrid materials based on halloysite nanotubes and natural polymers (alginate and chitosan) for the controlled and sustained release of bioactive species. A functional nanoarchitecture has been designed allowing us to generate a layered tablet with a chitosan/halloysite nanocomposite film sandwiched between two alginate layers. The assembly of the raw components and the final structure of the hybrid tablet have been highlighted by the morphological and wettability properties of the prepared materials. Since the biohybrid has been designed as a smart carrier, halloysite nanotubes have been first loaded with a model drug (sodium diclofenac). The effect of the tablet thickness on the drug release kinetics has been investigated, confirming that the delivery capacity can be controlled by modifying the alginate amounts of the external layers. A simulation of the typical pH conditions along the human gastro-intestinal path has been carried out. Strong acidic conditions (pH = 3, typical in the stomach) prevent the drug release. In contrast, the drug was released at pH = 5.7 and 7.8, which simulate the duodenum/ileum and colon paths, respectively. These results demonstrate that the proposed nanoarchitecture is suitable as a functional material with tunable delivery capacity.

Received 17th May 2019,
Accepted 14th June 2019

DOI: 10.1039/c9nj02565k

rsc.li/njc

1. Introduction

Recently, the need to conciliate technological progress with a growing environmental focus has become very compelling.¹ Hence, the design of new smart materials with sustainable characteristics has been exploited for a wide range of applications.^{2,3} Since the use of petrochemical-based plastic has to be restricted, bio-derived polymers represent a valid alternative for the preparation of new eco-friendly architectures.^{4,5} Mostly, organic raw materials are derived from agricultural or marine sources and can be functionalized in order to tune their main features such as the hydrophilic character, the thermal stability and the solubilization capability towards other compounds.^{6–8} The biopolymers' charge is considered as a crucial point for their classification since they can be cationic (*e.g.* chitosan), anionic (*e.g.* pectin, alginate) or neutral species (*e.g.* amylose, starch and cellulose derivatives such as hydroxypropylcellulose) with consequent differences in their interaction behaviour and self assembly with other building blocks.^{9–11} Biohybrid materials with variable structures and morphologies were

successfully prepared by the assembly of natural polymers and inorganic particles.^{12–14} Nowadays, these systems are attracting the attention of material scientists and engineers due to their wide applications including in biomedical technology, catalysis, remediation, cultural heritage treatment and food packaging.^{15–24} Recently, great efforts have been made in the design of biohybrid materials composed of organic moieties and inorganic clay minerals, which can present different features in terms of chemistry, aspect ratio, morphology and charge.^{25,26} Among them, halloysite nanotubes (HNTs) are naturally occurring aluminosilicates composed of a layer of Si–O–Si tetrahedrons overlapping Al–OH octahedrons that create a kaolinite-like sheet, which further rolls up forming hollow tubular nanoparticles.^{27,28} Halloysite dimensions strongly depend on its natural deposit. The HNTs' external diameter is 50–200 nm, while the internal diameter and the length are 15–50 nm and 1–2 μm, respectively.^{29,30} Besides their eco-sustainability and non-toxicity, their peculiar surface characteristics (different charge between the inner and outer surfaces due to their different Si/Al composition) make HNTs very interesting for charged guest molecules, which can be selectively adsorbed onto the nanotubes through electrostatic and van der Waals interactions.^{31–34} Moreover, the tubular shape represents an appealing characteristic providing an encapsulation site for active molecules inside the lumen of the nanotubes, which can act as nanocarriers and delivery systems.^{35–38} For this purpose, several smart materials have been prepared and exploited for the release of

^a Dipartimento di Fisica e Chimica, Università degli Studi di Palermo, Viale delle Scienze, pad. 17, 90128 Palermo, Italy. E-mail: giuseppe.lazzara@unipa.it

^b Consorzio Interuniversitario Nazionale per la Scienza e Tecnologia dei Materiali, INSTM, Via G. Giusti, 9, I-50121 Firenze, Italy

† Electronic supplementary information (ESI) available. See DOI: 10.1039/c9nj02565k

corrosion inhibitors, antacid molecules, antioxidants and other species of biological interest such as antimicrobial agents and nonsteroidal anti-inflammatory drugs (NSAIDs).^{39–47} In this regard, the selective functionalization of HNTs with stimuli responsive polymers (PNIPAAms) allowed the creation of a new nano-architecture suitable for drug release triggered by temperature.^{48,49} Moreover, biohybrid gel beads composed of a chitosan embedded halloysite core in an outer alginate shell were prepared with the aim to enhance the control of the drug delivery.⁵⁰

This paper contributes to the design of new smart biohybrid materials that can be used for health applications. For this, halloysite nanotubes have been employed as both drug molecule nanocontainers and fillers for the chitosan biopolymeric matrix. The coating of the nanocomposite film with alginate layers had significant effects on the release kinetics as a function of the thickness of the layered tablets. More interestingly, the hybrid material was subjected to a simulation of the human gastrointestinal path, evidencing that strong acidic conditions (typical in the stomach) prevented drug release, which occurs at pH = 5.7 and 7.8 (simulating duodenum/ileum and colon, respectively). Therefore, the prepared hybrid tablet can be considered as an efficient system for a sustained and controlled drug delivery.

2. Results and discussion

2.1 Morphology and wettability of ALG/CHI-HNTs/ALG tablets

Table 1 lists the prepared layered tablets with variable alginate/chitosan–HNT mass ratios ($R_{\text{Alg/Film}}$). The corresponding thicknesses of the interlayer film and the tablet are presented. It should be noted that both thicknesses were measured using a micrometer.

The optical photographs of the tablet and details of cross sections of all the prepared samples are shown in Fig. 1.

It is worth noting the organization of the components in the ALG/CHI-HNTs/ALG hybrid materials (Fig. 1a–c). In particular, their structure is layered and the CHI-HNT film is always visible within the cross section. The two alginate layers, covering the composite film on both its sides, present a homogeneous morphology and their dimensions strictly depend on the amount of biopolymer employed during the preparation phase. As expected, an increase in $R_{\text{Alg/Film}}$ determined an enhancement of the tablet thickness (Table 1). All the three tablets have a sandwich-like structure, contrary to the pure alginate tablet, which is reported for comparison in Fig. 1d. As shown in Fig. 1e, the nanotubes containing diclofenac are homogeneously dispersed within the chitosan matrix. This observation is promising for drug delivery purposes.

Contact angle measurements in water were carried out in order to study the wettability of the prepared materials. As an

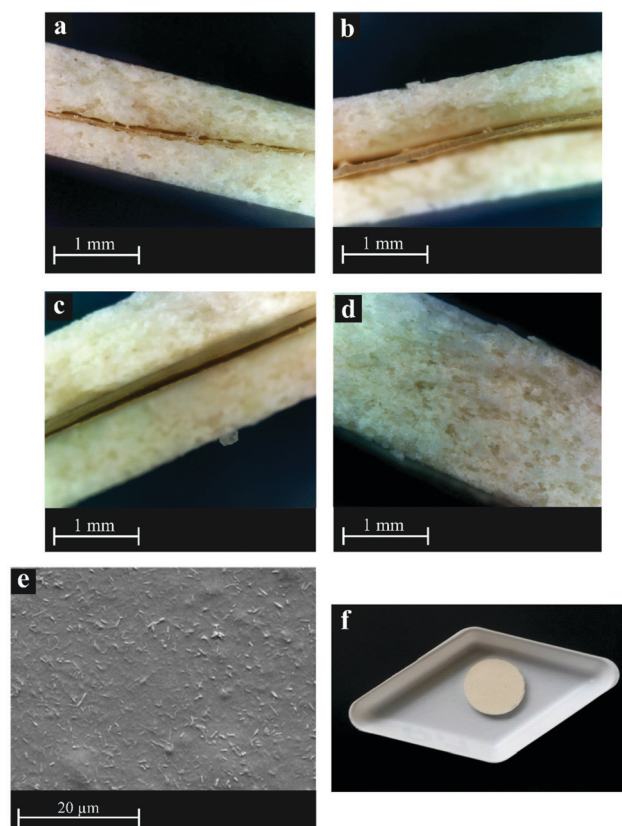


Fig. 1 Cross section optical photographs of (a) $R_{\text{Alg/Film}} = 20$, (b) $R_{\text{Alg/Film}} = 25$, (c) $R_{\text{Alg/Film}} = 30$ and (d) pure alginate prepared tablets; (e) SEM image of the nanocomposite film based on chitosan and HNTs loaded with diclofenac; (f) optical photograph of the tablet with $R_{\text{Alg/Film}} = 20$.

example, the θ vs. t trend for the tablet with $R_{\text{Alg/Film}} = 30$ has been reported in Fig. 2. The inset in Fig. 2 displays the image of the water droplet just after its deposition onto the tablet surface.

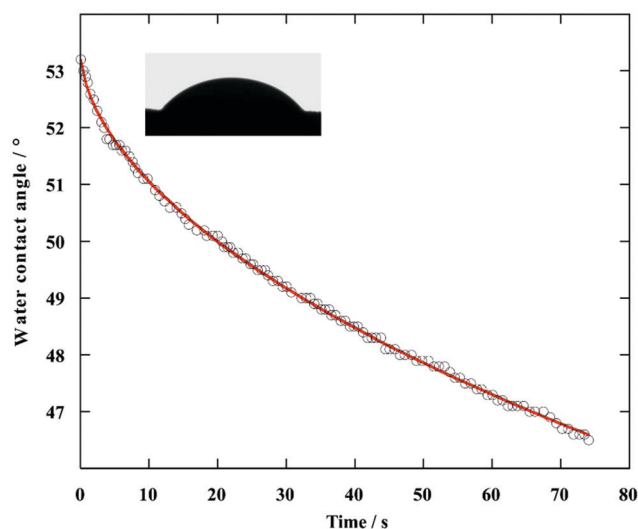


Fig. 2 Water contact angle measurement as a function of time for $R_{\text{Alg/Film}} = 30$ tablet. The inset displays the image of the water droplet just after surface deposition. The solid red line represents the fitting based on eqn (2).

Table 1 Composition and thicknesses of the layered hybrid tablets

$R_{\text{Alg/Film}}$ (wt%)	CHI-HNT thickness (μm)	Tablet thickness (mm)
20	58 ± 1	1.114 ± 0.001
25	44 ± 1	1.423 ± 0.001
30	60 ± 1	1.710 ± 0.001

Table 2 Wettability properties obtained by fitting the θ vs. t curves for tablets with variable composition

Sample	θ_i ($^\circ$)	k_θ	n
Alginate	59	0.0366	0.31
$R_{\text{Alg}/\text{Film}} = 20$	64	0.1242	0.16
$R_{\text{Alg}/\text{Film}} = 25$	58	0.0242	0.51
$R_{\text{Alg}/\text{Film}} = 30$	53	0.0115	0.57

Errors: 1% for θ_i and k_θ , 3% for n .

Table 2 reports the parameters resulting from fitting the curves with eqn (2).

It was observed that all the tablets showed a hydrophilic character, since the θ_i values are always lower than 90° . By comparing the results of the biohybrid materials with that of the pure alginate tablet, it is noticeable that the specific sandwich-like structure and the thickness variation of the layers did not deeply alter the wettability degree. Moreover, the initial contact angle is always lower than that of the chitosan/HNT nanocomposite film, which was experimentally measured to be 79° , in agreement with the literature.⁵¹ As concerns k_θ , the hybrid tablets showed lower values compared to that of pristine alginate. Accordingly, we can state that the kinetics of the contact angle evolution was slowed down by the peculiar sandwich like structure of the hybrid tablets. Hence, n depends on both spreading and adsorption mechanisms. The n values ranged from 0.16 to 0.57 for $R_{\text{Alg}/\text{Film}} = 20$ and $R_{\text{Alg}/\text{Film}} = 30$, respectively. As a general result, we observed that the increase of the alginate amount in the hybrid systems determined an enhancement of the absorption contribution.

2.2 Release studies

The release kinetics of diclofenac from loaded HNTs, chitosan/HNT nanocomposite films and ALG/CHI-HNTs/ALG tablets were investigated.

Preliminarily, we determined the amount of diclofenac encapsulated within the halloysite lumen *via* thermogravimetry. Fig. 3 reports the thermograms for the pristine halloysite nanotubes, pure diclofenac and the drug loaded HNTs. According to the rule of mixtures (see the ESI[†]),⁵² we estimated a drug loading of 10.1 wt% by comparing the mass losses at 150°C and the residual masses at 700°C . This result is in good agreement with the literature.⁵³

2.2.1 Release of diclofenac from loaded HNTs, chitosan/HNT nanocomposites and layered tablets. Fig. 4 compares the diclofenac release profiles for the loaded HNTs and CHIT-HNT nanocomposite films.

It was observed that 48% of drug was released by the loaded clay nanotubes after just 5 minutes, while a saturation of release (70%) was reached after 45 minutes. Compared to HNTs/Diclofenac, the release kinetics is slower for the drug loaded in the CHI-HNT film. In particular, we estimated that 9% and 52% of diclofenac are released after 5 min and 5 hours, respectively. This is most likely due to the barrier effect of the polymeric matrix, which can delay the drug release from the HNT inner lumen. Fig. 5 reports the release kinetics for the biohybrid tablets with variable composition.

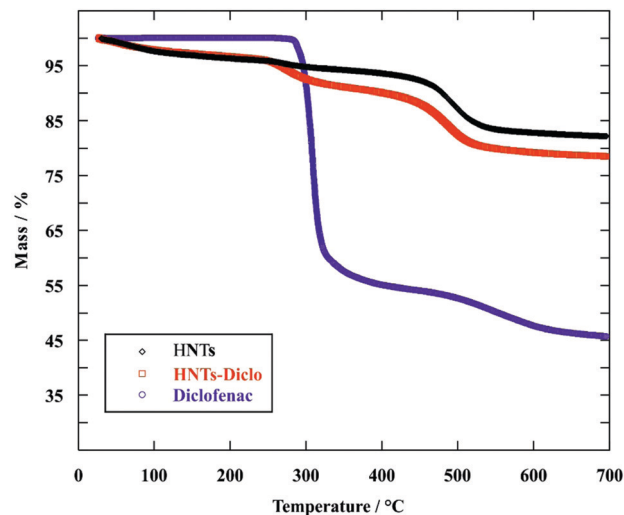


Fig. 3 Thermogravimetric curves for HNTs, HNTs-Diclo and pure diclofenac.

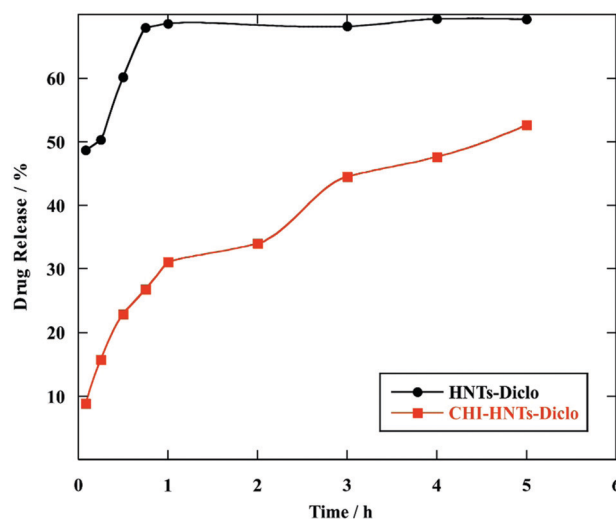


Fig. 4 Release profiles for HNT-Diclo powder and CHI-HNT-Diclo nanocomposite films as a function of time.

As a general result, we observed that the presence of external alginate layers slows down the drug release kinetics. As concerns the hybrid with $R_{\text{Alg}/\text{Film}} = 20$, we estimated that 3 and 40% of diclofenac are released after 5 minutes and 2 hours, respectively. Interestingly, an interruption in the diclofenac release was observed after 2 hours, which corresponded to the starting time of the alginate dissolution in aqueous solvent. Once the alginate dissolution was complete (after *ca.* 5 hours), the drug release restarted. Regarding the tablet with $R_{\text{Alg}/\text{Film}} = 25$, an induction time of *ca.* 5 hours was observed for the diclofenac release process. The retardant effect on the drug release can be attributed to the protection of the external alginate layers of the hybrid tablet. Once the dissolved alginate concentration was constant (*ca.* 45%), the drug release exhibited an exponential increase reaching 50 and 70% after 10 and 24 hours, respectively.

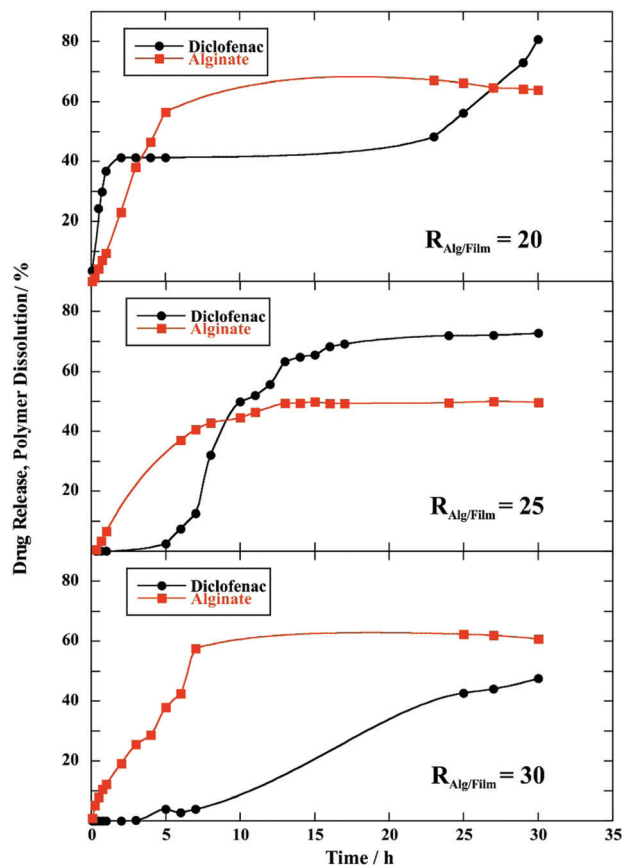


Fig. 5 Release profiles for the three prepared tablets as a function of time.

A similar behaviour was observed for the tablet with $R_{\text{Alg/Film}} = 30$, which showed a longer induction time (*ca.* 7 hours) for the diclofenac release. Only *ca.* 3% of drug was released during the polymer dissolution. Once the alginate concentration in the release medium was constant (*ca.* 57%), the drug was exponentially delivered reaching 42 and 47% after 24 and 30 hours, respectively.

In light of these observations, we can state that the alginate layers played a relevant role in controlling the kinetics due to their swelling. We can hypothesize that the outer layers of alginate can absorb water from the medium causing the formation of a gel phase that delays the drug delivery. Once the biopolymer dissolution is complete, the diclofenac release from the hybrid is allowed. Remarkably, the different thickness of the ALG/CHI-HNT/ALG tablets induced significant effects on the diclofenac release kinetics. In particular, the tablet with the thinnest alginate layers ($R_{\text{Alg/Film}} = 20$) did not evidence a clear induction time for the drug release. In contrast, this effect was highlighted for tablets with a larger amount of alginate. Moreover, the total amount of diclofenac that could be released from the tablets was affected by the specific composition. In this regard, we estimated that the diclofenac release amounts after 30 hours are *ca.* 80, 65 and 45% for tablets with $R_{\text{Alg/Film}} = 20, 25$ and 30, respectively.

2.2.2 Release of diclofenac from the hybrid tablet under human gastro-intestinal conditions. Release studies using the hybrid tablet with $R_{\text{Alg/Film}} = 25$ were carried out under different

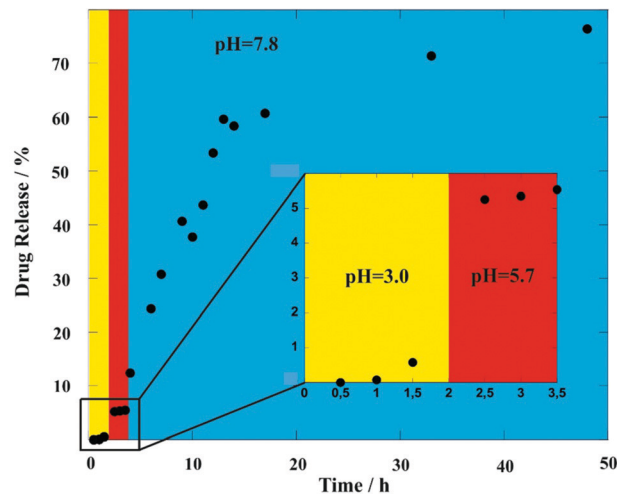


Fig. 6 Release profile for the $R_{\text{Alg/Film}} = 25$ tablet measured by simulating the human body gastrointestinal path's most typical pH conditions, as a function of time.

pH conditions simulating the human gastro-intestinal path. In particular, the drug release kinetics were studied at pH = 3.0, 5.7 and 7.8, which simulate stomach, duodenum/ileum and colon paths. These tests were conducted at 37 °C in agreement with human physiological conditions. First, the tablet was kept in aqueous solvent at pH = 3 for 2 hours. As shown in Fig. 6, we observed a negligible drug release amount (<1%). Afterwards, the tablet was kept at pH = 5.7 for 1.5 hours. Here, we detected a jump in diclofenac release up to *ca.* 5% (Fig. 6). Lastly, the release medium was changed to pH = 7.8. We observed that the alkaline conditions favour the diclofenac release, which follows an exponential increasing trend (Fig. 6). In particular, we estimated that the drug release is 12 and 75% after 4 and 50 hours, respectively. According to these results, we can conclude that the sandwich like structure of the hybrid tablet is efficient in controlling the drug release with a dependence on the pH conditions of the physiological aqueous medium.

3. Experimental section

3.1 Materials

Halloysite nanotubes (HNTs) were a gift from Imerys Ceramics. Chitosan ($M_w = 50\text{--}190 \text{ kg mol}^{-1}$), sodium alginate ($M_w = 70\text{--}100 \text{ kg mol}^{-1}$), diclofenac sodium salt ($M_w = 318.13 \text{ g mol}^{-1}$), acetic acid ($\geq 99.5\%$), hydrochloric acid (37% v/v) and sodium hydroxide are Sigma Aldrich products.

3.2 Diclofenac loading of halloysite nanotubes

Accordingly to the literature,⁴⁸ a diclofenac sodium salt saturated aqueous solution was prepared and HNT powder was added in a 1 : 1 mass ratio. The dispersion was magnetically stirred for 24 h. Then, it was subjected to three vacuum cycles ($P = 0.01 \text{ atm}$ for 1 h) in order to optimize the loading efficiency.⁵² It should be noted that the dispersion was stirred for 10 minutes between two consecutive vacuum cycles. Hence, the drug encapsulated

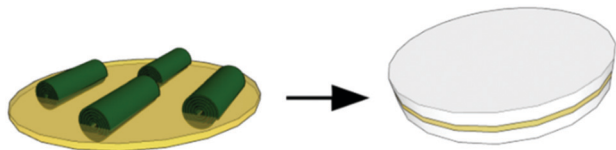


Fig. 7 Schematic representation of the biohybrid tablet.

nanoclay was separated by centrifugation (5 minutes at 8000 rpm) and it was washed with water and dried overnight in an oven.

3.3 Preparation of HNT–chitosan–alginate tablets

First, a 2% w/w chitosan (CHI) solution in H₂O/acetic acid was prepared and halloysite loaded with diclofenac was added at 0.6% w/w concentration. The dispersion was stirred for 24 h and it was poured into a Petri dish in order to obtain CHI–HNT nanocomposite films by the solvent casting method. Afterwards, the film was cut into several portions with a circular shape (diameter *ca.* 1 cm). The film was covered on both (top and bottom) sides with alginate (ALG) layers, which were compressed at 10 ton for 10 minutes allowing us to generate a compact tablet (Fig. 7). The amount of alginate was systematically changed to prepare tablets with variable thickness.

3.4 Diclofenac release kinetics

Release kinetics were studied *via* UV-VIS spectrophotometry. Hence, 10 mg of diclofenac loaded HNTs, 10 mg of the CHI–HNT film and the hybrid tablet with different thickness were placed into the release medium. At certain time intervals, 2 mL of liquid was taken from each sample, used for UV-VIS analysis and replaced with fresh solution. Release data were corrected using the following equation:⁵⁴

$$Cn' = Cn + \frac{V}{V_0} \cdot \sum_{i=0}^{n-1} C_i \quad (1)$$

where Cn' is the corrected concentration, Cn represents the n th concentration, V is the sample volume taken for each analysis (2 mL), and V_0 represents the total volume.

In particular, kinetics were studied at pH = 7.8 for all the prepared systems. In addition, a simulation of the conditions of different parts of the human body was carried out at variable pH (3, 5.7, and 7.8 that correspond to stomach, duodenum/ileum and colon, respectively).⁵⁵ Hence, since diclofenac and alginate have their main adsorption bands at $\lambda \approx 276$ nm, calibration curves were recorded for both the drug and the biopolymer in quartz cuvettes under the same acidic conditions.

3.5 Methods

Optical images were produced by using a DIGITUS[®] (DA-70351) microscope and processed by using the Digital Viewer software.

Water contact angle measurements were carried out by using an optical apparatus (OCA 20, Data Physics Instruments) equipped with a high-resolution CCD camera and a high-performance digitizing adapter. The water droplet was 10 ± 0.5 mL whereas the gas phase was air and temperature was maintained at

25.0 ± 0.1 °C. Data were acquired by using the SCA 20 software (Data Physics Instruments). Contact angle values over time were fitted by the following equation:⁵⁶

$$\theta = \theta_i \cdot \exp(-k_\theta \cdot t^n) \quad (2)$$

where θ_i represents the initial value, and k_θ and n are characteristic coefficients related to the process rate and mechanism. In particular, n ranges between 0 and 1 depending on the absorption and spreading contributions to the kinetics, being 0 for the former and 1 for the latter, respectively.

Thermogravimetric analysis (TGA) was performed by using a Q5000 IR apparatus (TA Instruments) under nitrogen flows of $25 \text{ cm}^3 \text{ min}^{-1}$ for the sample and $10 \text{ cm}^3 \text{ min}^{-1}$ for the balance, respectively. Thermal analysis was conducted on pure diclofenac, HNTs and diclofenac loaded halloysite by increasing the temperature to 700 °C with a scanning rate of 20 °C min^{-1} . The loading efficiency was provided using the rule of mixtures.⁵⁷

A UV-VIS spectrophotometer was used in order to study the release kinetics obtained from the prepared materials. For this purpose, the employed equipment was a Specord S600 (Analytik, Jena, Germany). An ESEM FEI QUANTA 200F microscope was used to image the halloysite nanotubes embedded into the chitosan polymeric matrix. To achieve this aim, the film was coated with gold in argon by means of an Edwards Sputter Coater S150A to avoid charging under the electron beam. The measurements were conducted in a high vacuum ($< 6 \times 10^{-4}$ Pa), while the energy of the beam and the working distance were set at 25 kV and 10 mm, respectively.

4. Conclusions

We prepared layered composite tablets based on biopolymers (alginate and chitosan) and halloysite nanotubes. The tablet fabrication consists of three steps: (1) loading of the halloysite lumen with diclofenac as a model drug; (2) preparation of the nanocomposite film formed by chitosan and halloysite nanotubes containing diclofenac; (3) high pressure packing of the nanocomposite film between two alginate layers. Thermogravimetric experiments evidenced the successful encapsulation (*ca.* 10.1 wt%) of the drug within the halloysite lumen, while Scanning Electron Microscopy showed that the loaded nanotubes were uniformly dispersed into the chitosan matrix. Optical observations of the hybrid tablets highlighted their peculiar layered structure with tunable thickness. The wettability properties of the tablets confirmed the sandwich like structure of the hybrids. The presence of the alginate layers slowed down the diclofenac release with respect to that from the nanocomposite film. In addition, we observed that the external biopolymer layers generated an induction time on the diclofenac release as a function of the tablet thickness. Similarly, the amount of drug released after a long time (30 hours) was affected by the composition of the hybrid tablet. These effects can be attributed to the protection of the alginate layers on the drug release. Interestingly, the sandwich like structure of the hybrid tablets allows control of the diclofenac release under variable physiological pH conditions. At pH = 3

(typical in the stomach), the diclofenac release was negligible (<1%), while an increase in the drug delivery was detected at pH = 5.7 (duodenum/ileum) wherein the released amount was ca. 5%. Alkaline conditions (pH = 7.8, typical in colon) determined an exponential increase of the diclofenac release, which reached 70% after 30 hours. Based on these results, we can conclude that the alginate/chitosan/HNT hybrid is an effective and tunable delivery system that can be used for specific physiological purposes.

Conflicts of interest

There are no conflicts to declare.

Acknowledgements

The work was financially supported by Progetto di ricerca e sviluppo "AGM for CuHe" (ARS01_00697) and the University of Palermo.

References

- 1 E. Forgacs, T. Cserháti and G. Oros, *Environ. Int.*, 2004, **30**, 953–971.
- 2 Y. Stetsyshyn, J. Zemla, O. Zolobko, K. Fornal, A. Budkowski, A. Kostruba, V. Donchak, K. Harhay, K. Awsiuk, J. Rysz, A. Bernasik and S. Voronov, *J. Colloid Interface Sci.*, 2012, **387**, 95–105.
- 3 T. Hueckel and S. Sacanna, *ACS Nano*, 2018, **12**, 3533–3540.
- 4 A. Takahara and Y. Higaki, *RSC Smart Mater.*, 2017, 131–156.
- 5 V. Bertolino, G. Cavallaro, G. Lazzara, S. Milioto and F. Parisi, *New J. Chem.*, 2018, **42**, 8384–8390.
- 6 A. C. S. Alcántara, P. Aranda, M. Darder and E. Ruiz-Hitzky, *J. Mater. Chem.*, 2010, **20**, 9495–9504.
- 7 K. L. Hamner, C. M. Alexander, K. Coopersmith, D. Reishofer, C. Provenza and M. M. Maye, *ACS Nano*, 2013, **7**, 7011–7020.
- 8 F. Liu, L. Bai, H. Zhang, H. Song, L. Hu, Y. Wu and X. Ba, *ACS Appl. Mater. Interfaces*, 2017, **9**, 31626–31633.
- 9 V. Bertolino, G. Cavallaro, G. Lazzara, S. Milioto and F. Parisi, *Langmuir*, 2017, **33**, 3317–3323.
- 10 P. R. Chang, Y. Xie, D. Wu and X. Ma, *Carbohydr. Polym.*, 2011, **84**, 1426–1429.
- 11 E. A. Naumenko, I. D. Guryanov, R. Yendluri, Y. M. Lvov and R. F. Fakhrullin, *Nanoscale*, 2016, **8**, 7257–7271.
- 12 E. Ruiz-Hitzky, M. Darder, F. M. Fernandes, B. Wicklein, A. C. S. Alcántara and P. Aranda, *Prog. Polym. Sci.*, 2013, **38**, 1392–1414.
- 13 M. H. Shamsi and D. V. Geckeler, *Nanotechnology*, 2008, **19**, 075604.
- 14 M. Liu, R. Fakhrullin, A. Novikov, A. Panchal and Y. Lvov, *Macromol. Biosci.*, 2019, **19**, 1800419.
- 15 S. Sadjadi, T. Hosseinnejad, M. Malmir and M. M. Heravi, *New J. Chem.*, 2017, **41**, 13935–13951.
- 16 Y. Lvov and E. Abdullayev, *Prog. Polym. Sci.*, 2013, **38**, 1690–1719.
- 17 R. F. Fakhrullin and Y. M. Lvov, *Nanomedicine*, 2016, **11**, 2243–2246.
- 18 Y. Liu, H. Guan, J. Zhang, Y. Zhao, J.-H. Yang and B. Zhang, *Int. J. Hydrogen Energy*, 2018, **43**, 2754–2762.
- 19 C. Chao, H. Guan, J. Zhang, Y. Liu, Y. Zhao and B. Zhang, *Water Sci. Technol.*, 2018, **77**, 809–818.
- 20 G. Cavallaro, S. Milioto, F. Parisi and G. Lazzara, *ACS Appl. Mater. Interfaces*, 2018, **10**, 27355–27364.
- 21 G. Gorrasi, R. Pantani, M. Murariu and P. Dubois, *Macromol. Mater. Eng.*, 2014, **299**, 104–115.
- 22 C. Aguzzi, C. Viseras, P. Cerezo, I. Salcedo, R. Sánchez-Espejo and C. Valenzuela, *Colloids Surf., B*, 2013, **105**, 75–80.
- 23 O. Owoseni, E. Nyankson, Y. Zhang, S. J. Adams, J. He, G. L. McPherson, A. Bose, R. B. Gupta and V. T. John, *Langmuir*, 2014, **30**, 13533–13541.
- 24 S. Sadjadi, M. Akbari, E. Monflier, M. M. Heravi and B. Leger, *New J. Chem.*, 2018, **42**, 15733–15742.
- 25 E. Abdullayev and Y. Lvov, *J. Mater. Chem. B*, 2013, **1**, 2894–2903.
- 26 C. Aulin, G. Salazar-Alvarez and T. Lindstrom, *Nanoscale*, 2012, **4**, 6622–6628.
- 27 Y. M. Lvov, D. G. Shchukin, H. Mohwald and R. R. Price, *ACS Nano*, 2008, **2**, 814–820.
- 28 Y. Joo, J. H. Sim, Y. Jeon, S. U. Lee and D. Sohn, *Chem. Commun.*, 2013, **49**, 4519–4521.
- 29 L. Lisuzzo, G. Cavallaro, F. Parisi, S. Milioto and G. Lazzara, *Ceram. Int.*, 2019, **45**, 2858–2865.
- 30 G. Cavallaro, L. Chiappisi, P. Pasbakhsh, M. Gradzielski and G. Lazzara, *Appl. Clay Sci.*, 2018, **160**, 71–80.
- 31 P. Pasbakhsh, G. J. Churchman and J. L. Keeling, *Appl. Clay Sci.*, 2013, **74**, 47–57.
- 32 Y. Zhang, Q. Liu, J. Xiang and R. L. Frost, *Appl. Clay Sci.*, 2014, **95**, 159–166.
- 33 V. Vinokurov, A. Stavitskaya, A. Glotov, A. Ostudin, M. Sosna, P. Gushchin, Y. Darrat and Y. Lvov, *J. Solid State Chem.*, 2018, **268**, 182–189.
- 34 B. Huang, M. Liu and C. Zhou, *Carbohydr. Polym.*, 2017, **175**, 689–698.
- 35 C. Aguzzi, P. Cerezo, C. Viseras and C. Caramella, *Appl. Clay Sci.*, 2007, **36**, 22–36.
- 36 T. G. Shutava, R. F. Fakhrullin and Y. M. Lvov, *Curr. Opin. Pharmacol.*, 2014, **18**, 141–148.
- 37 S. Levis and P. Deasy, *Int. J. Pharm.*, 2003, **253**, 145–157.
- 38 M. Du, B. Guo and D. Jia, *Polym. Int.*, 2010, **59**, 574–582.
- 39 G. Cavallaro, G. Lazzara, S. Milioto, F. Parisi, V. Evtugyn, E. Rozhina and R. Fakhrullin, *ACS Appl. Mater. Interfaces*, 2018, **10**, 8265–8273.
- 40 G. Gorrasi, *Carbohydr. Polym.*, 2015, **127**, 47–53.
- 41 E. Abdullayev and Y. Lvov, *J. Mater. Chem.*, 2010, **20**, 6681–6687.
- 42 M. R. Dзамukova, E. A. Naumenko, Y. M. Lvov and R. F. Fakhrullin, *Sci. Rep.*, 2015, **5**, 10560.
- 43 A. Joshi, E. Abdullayev, A. Vasiliev, O. Volkova and Y. Lvov, *Langmuir*, 2013, **29**, 7439–7448.
- 44 H. Li, X. Zhu, H. Zhou and S. Zhong, *Colloids Surf., A*, 2015, **487**, 154–161.
- 45 H. Zhang, C. Cheng, H. Song, L. Bai, Y. Cheng, X. Ba and Y. Wu, *Chem. Commun.*, 2019, **55**, 1040–1043.

- 46 J. Yang, Y. Wu, Y. Shen, C. Zhou, Y.-F. Li, R.-R. He and M. Liu, *ACS Appl. Mater. Interfaces*, 2016, **8**, 26578–26590.
- 47 K. Wang, Y. Zhang, J. Zhao, C. Yan, Y. Wei, M. Meng, X. Dai, C. Li and Y. Yan, *New J. Chem.*, 2018, **42**, 18084–18095.
- 48 G. Cavallaro, G. Lazzara, L. Lisuzzo, S. Milioto and F. Parisi, *Nanotechnology*, 2018, **29**, 325702.
- 49 D. N. Elumalai, J. Tully, Y. Lvov and P. A. Derosa, *J. Appl. Phys.*, 2016, **120**, 134311.
- 50 L. Lisuzzo, G. Cavallaro, F. Parisi, S. Milioto, R. Fakhrullin and G. Lazzara, *Coatings*, 2019, **9**, 70.
- 51 V. Bertolino, G. Cavallaro, G. Lazzara, M. Merli, S. Milioto, F. Parisi and L. Sciascia, *Ind. Eng. Chem. Res.*, 2016, **55**, 7373–7380.
- 52 L. Lisuzzo, G. Cavallaro, P. Pasbakhsh, S. Milioto and G. Lazzara, *J. Colloid Interface Sci.*, 2019, **547**, 361–369.
- 53 M. Makaremi, P. Pasbakhsh, G. Cavallaro, G. Lazzara, Y. K. Aw, S. M. Lee and S. Milioto, *ACS Appl. Mater. Interfaces*, 2017, **9**, 17476–17488.
- 54 D. Yu, J. Wang, W. Hu and R. Guo, *Mater. Des.*, 2017, **129**, 103–110.
- 55 J. M. DeSesso and C. F. Jacobson, *Food Chem. Toxicol. Int. J. Publ. Br. Ind. Biol. Res. Assoc.*, 2001, **39**, 209–228.
- 56 S. Farris, L. Introzzi, P. Biagioni, T. Holz, A. Schiraldi and L. Piergiovanni, *Langmuir*, 2011, **27**, 7563–7574.
- 57 M. Massaro, G. Cavallaro, C. G. Colletti, G. D'Azzo, S. Guernelli, G. Lazzara, S. Pieraccini and S. Riela, *J. Colloid Interface Sci.*, 2018, **524**, 156–164.



Cite this: DOI: 10.1039/c9dt03804c

Functional biohybrid materials based on halloysite, sepiolite and cellulose nanofibers for health applications†

Lorenzo Lisuzzo,^{a,b} Bernd Wicklein,^b Giulia Lo Dico,^a Giuseppe Lazzara,^a Gustavo del Real,^c Pilar Aranda^b and Eduardo Ruiz-Hitzky^{*b}

Biohybrid materials were prepared by co-assembling the three following components: nanotubular halloysite, microfibrillar sepiolite, and cellulose nanofibers dispersed in water, in order to exploit the most salient features of each individual component and to render homogeneous, flexible, yet strong films. Indeed, the incorporation of halloysite improves the mechanical performance of the resulting hybrid nanopapers and the assembly of the three components modifies the surface features concerning wetting properties compared to pristine materials, so that the main characteristics of the resulting materials become tunable with regard to certain properties. Owing to their hierarchical porosity together with their diverse surface characteristics, these hybrids can be used in diverse biomedical/pharmaceutical applications. Herein, for instance, loading with two model drugs, salicylic acid and ibuprofen, allows controlled and sustained release as deduced from antimicrobial assays, opening a versatile path for developing other related organic–inorganic materials of potential interest in diverse application fields.

Received 25th September 2019,
Accepted 28th November 2019

DOI: 10.1039/c9dt03804c

rsc.li/dalton

1. Introduction

Biohybrid materials attract the interest of both scientific and engineering communities due to their extensive use in a wide range of application fields from environmental remediation to biomedical uses and represent an alternative approach to conventional technologies for combining organic and inorganic moieties by adding particles for which at least one dimension is in the nanometer range.^{1–6} Of particular relevance are those systems in which the inorganic component is a silicate belonging to the family of clay minerals, giving rise to nanocomposite materials involving porous and layered silicates.^{7–12} The resulting materials may exhibit markedly improved mechanical, thermal, optical, and physicochemical properties compared to those of the pure polymer or conventional (microscale) composites,¹³ as first demonstrated by Fukushima and co-workers for nylon–clay nanocomposites.¹⁴ In recent years, nanocellulose

based materials have been the focus of active research with the aim of developing a wide variety of hybrid materials for applications in adaptive and responsive materials, energy storage and conversion, water treatment, biomedicine, packaging, fire retardancy, as a support for metal and metal oxide nanoparticles in catalysts, and electronics.^{15–20} In this context, the concept of “nanopaper” refers to the use of cellulose nanofibers (CNFs) for making paper instead of employing conventional, micronized cellulose pulp. The term “nanocellulose” refers to a family of cellulose nanomaterials (fibers and crystals) obtained from different chemical and mechanical methodologies that provoke a defibrillation process in raw cellulosic materials.^{21,22} Cellulose nanofibers show a high aspect ratio (up to 1 μm in length and 2–5 nm in thickness), a chemically modifiable surface, and a high elastic modulus resulting from their high crystallinity,²³ and are prepared by relatively low-expensive production methods, all of which endow CNFs with great potential for the fabrication of numerous functional structures.^{24,25} Recent studies on CNFs have been dealing with their assembly to other nanobuilding blocks of an inorganic nature, for instance, the combination of CNFs with layered silicates, such as vermiculite to produce biohybrids used as packaging material,²⁶ montmorillonite to develop materials showing high mechanical performance,²⁷ or the preparation of functional, heterofibrillar hybrid materials by an integrative approach from the dispersions of nanofibrillated cellulose and defibrillated sepiolite.^{28,29} Sepiolite is a microcrystalline

^aDepartment of Physics and Chemistry, University of Palermo, Viale delle Scienze, pad. 17, Palermo 90128, Italy

^bInstituto de Ciencia de Materiales de Madrid (ICMM), Consejo Superior de Investigaciones Científicas (CSIC), c/Sor Juana Inés de la Cruz 3, 28049 Madrid, Spain. E-mail: eduardo@icmm.csic.es

^cInstituto Nacional de Investigación y Tecnología Agraria y Alimentaria (INIA), Ctra. de la Coruña km 7.5, 28040 Madrid, Spain

†Electronic supplementary information (ESI) available. See DOI: 10.1039/C9DT03804C



hydrated magnesium silicate with $\text{Si}_{12}\text{O}_{30}\text{Mg}_8(\text{OH},\text{F})_4(\text{H}_2\text{O})_4 \cdot 8\text{H}_2\text{O}$ as the theoretical unit cell formula.³⁰ Indeed, sepiolite shows a microfibrillar morphology with a particle size typically in the 0.5–2 μm length range.³¹ Structurally, it is formed by the alternation of blocks and cavities (tunnels) that grow in the fiber direction (*c*-axis). Each structural block is composed of two tetrahedral silica sheets sandwiching a central sheet of magnesium oxide-hydroxide. Owing to the discontinuity of the silica sheets, the channels and silanol groups (Si–OH) are present on the external surface of the silicate particles.³² These groups are located at the edges of the channels (*i.e.* those tunnels acceding to the external surface of the silicate) and are directly accessible to different species, thus representing the only sites available for functionalization. Moreover, one of the most interesting features of sepiolite is its very high colloidal stability in aqueous media that has been exploited for stabilizing, among others, carbon nanotubes and graphene nanoplatelet suspensions.^{33,34} In light of these properties and features, it is clear that sepiolite represents a very interesting starting building block for designing a wide class of smart materials.³⁵ Nevertheless, one limitation of sepiolite is its restriction only to its external surface during the interaction with other active and bulky species due to the reduced accessibility of the Mg–OH groups located inside the micro-porous tunnels.³⁰

Hence, the use of further components to overcome this limitation and to fully exploit the features of sepiolite and to develop potential synergistic effects is pursued here through the co-assembly of clay nanotubes.

Halloysite (HNT) is structurally a 1 : 1 layered aluminosilicate clay showing a tubular morphology with an external diameter of 50–80 nm, an internal diameter of 10–15 nm, and a length of *ca.* 1000 nm.^{36–38} Interestingly, it displays a positively charged lumen and a negatively charged outer surface in the pH range between 2 and 8.^{39,40} This characteristic is due to the different chemical compositions: the external surface is composed of Si–O–Si groups while the inner surface consists of a gibbsite-like array of Al–OH groups.⁴¹ This peculiar surface chemistry makes possible, in contrast to sepiolite, a selective targeted modification driven by electrostatic interactions.^{42–44} These groups allow the clay to participate in electrostatic or hydrogen bonding in polar solvents and to interact favorably with the functional groups of a wide range of chemical species.^{45–48} Due to various characteristics such as a nanoscale lumen, high aspect ratio, relatively low hydroxyl group density on the surface, *etc.*, numerous advanced applications have been discovered for this unique, cheap, and abundant clay.^{49–55} Moreover, HNTs are biocompatible as shown in several *in vitro* and *in vivo* studies.⁵⁶ Beyond these aspects, one of the limitations to the use of pristine halloysite is its low colloidal stability in aqueous suspensions, which hampers its use and applicability except for adequately modified HNTs.⁵⁷ In this way, we have recently reported a protocol to produce multicomponent conductive bionanocomposite materials where the use of sepiolite is fundamental to achieve the stabilization of HNT dispersions

in which the other components can be homogeneously incorporated.⁵⁸

In this context, the main objective of this work is to develop an alternative strategy for the preparation of a new type of multi-component hybrid nanopaper constituted by cellulose nanofibers, sepiolite, and halloysite. Our purpose is to investigate the possibility to exploit the most important features of each component and to overcome their individual limitations in order to design a material with different chemical surfaces. Here, a hybrid material was prepared for drug delivery applications exemplified by using two cationic model drugs. Ibuprofen is a hydrophobic,⁵⁹ non-steroidal, anti-inflammatory drug (NSAID) that is administered for the relief of moderate pain and inflammation.⁶⁰ On the other hand, salicylic acid was tested for its bactericidal and antiseptic properties, and is used in a wide range of pharmaceutical formulations and as an additive for food and cosmetics.⁶¹ In light of the above, the possibilities of developing a multicomponent hybrid nanopaper possessing different types of chemical surfaces that can selectively interact with active species and can sustain, control and optimize their release on time represent a crucial point.

2. Experimental details

2.1. Materials

Sepiolite was obtained from Vicálvaro-Vallecas deposits, Madrid (Spain), with >95% purity. Commercialized as Pangel S9, sepiolite of rheological grade was supplied by Tolsa S.A. (Spain) and was used as supplied. Halloysite (New Zealand China Clays) was supplied by Imerys (France). Ibuprofen sodium salt (IBU) and sodium salicylate (SS) were purchased from Sigma Aldrich. The solubility of IBU (100 mg ml⁻¹) and SA (100 mg ml⁻¹) in water was tested according to Sigma Aldrich specification sheets. Deionized water (18.2 M Ω cm) was obtained using a Maxima Ultra Pure Water system from Elga. Sodium phosphate tribasic dodecahydrate ($\geq 98\%$) and sodium hydroxide ($\geq 98\%$) were supplied by Sigma Aldrich and phosphoric acid (85%) by Carlo Erba.

The preparation of CNFs used in this work was carried out through the TEMPO-mediated oxidation of eucalyptus pulp following the procedure described by Fillat *et al.*⁶² The resulting cellulose nanofibers were stored at 4 °C.

2.2. Halloysite nanotube drug loading

The loading of IBU and SA into the HNT lumen was achieved by following the procedure described elsewhere for similar systems.⁶³ Pristine HNTs were added to a saturated aqueous solution of the drugs and then magnetically stirred for *ca.* 1 h. In particular, to prepare the SA loaded HNTs, 1 g of halloysite powder was added to a concentrated solution of sodium–SA in water. The pH was adjusted to 8 by adding 0.1 M NaOH in order to optimize the loading efficiency of SA through maximizing the negative charge of salicylate. Ibuprofen was loaded into halloysite powder from a saturated solution of IBU sodium salt at a 2 : 1 wt ratio. The obtained dispersions were



transferred to a vacuum vessel and evacuated with a vacuum pump (P-Selecta Vacuo-TEM). The HNT-IBU suspensions were subjected to three vacuum cycles to ensure the infiltration of the HNT lumen.⁶⁴ The HNT-SA suspension, instead, was kept under vacuum for 3 hours, and the step was repeated three times.

Afterwards, the loaded HNTs were separated from the solution by centrifugation, washed with water and dried overnight.

2.3. Preparation of HNT-SEP-CNF hybrid nanopapers

The ratio (w/w) of HNT, SEP, and CNF was fixed at 1 : 1 : 1 even though many compositions were tested. Typically, SEP (10 mg) was dispersed in 20 mL of water and mixed with 1 g of a CNF gel prepared at 1 wt% in water using an Ultra-Turrax (IKA® T25) homogenizer. Then, 10 mg of pristine HNT were added and the HNT-SEP-CNF mixture was tip-sonicated (Vibra Cell VC 750, 13 mm titanium sonication probe) until a total energy of 1 kJ or 5 kJ was achieved. The films were prepared by casting the mixture in polystyrene Petri dishes followed by drying in a Climacell EVO 111 L climate chamber for 72 h at 30 °C and 60% relative humidity (RH) to obtain hybrid nanopapers with a thickness around 20 μm. The samples were labeled as HNT-SEP-CNF.

HNT-SEP (1 : 1 w/w), HNT-CNF (1 : 1 w/w), SEP-CNF (1 : 1 w/w) and pure CNF films were also prepared by following the same procedure.

2.4. Preparation of drug loaded HNT-SEP-CNF hybrid nanopapers

When drug loaded HNTs were used instead of neat HNTs, halloysite was added after the sonication process to prevent any degradation of drug molecules that could be produced because of the high energy applied to the system. Moreover, to achieve a higher HNT dispersion, the system was sonicated using a simple ultrasound bath (J.P. Selecta) for a few minutes. The same solvent casting procedure was followed.

2.5. Characterization

SEM analysis was performed on Cr metallized samples by using a Philips XL 30 S-FEG field emission scanning electron microscope (FE-SEM). Nanopaper cross-sections were obtained by cutting the films after immersion in liquid N₂. An energy-dispersive X-ray (EDX) spectroscope coupled to an (FEI NOVA Nano SEM 230) FE-SEM was used for elemental mapping. The EDX maps were recorded with a Type SDD Apollo 10 EDAX detector and the data acquisition conditions were kept constant at a working distance of 6.5 mm with a spot size of 50 μm and an energy of 12 kV, for 4200 counts. Atomic force microscopy (AFM) was performed in dynamic mode and under environmental conditions, and this operation provides topographical images of the surface. A Cervantes instrument from Nanotec Electrónica S.L. equipped with a PPP-FMR (a strength constant of 1.5 N m⁻¹) and with a resonance constant of 70 kHz was used. The XRD patterns of HNT and SEP powder and the CNF and HNT-SEP-CNF nanopapers were obtained using a BRUKER D8-ADVANCE diffractometer with copper Kα radi-

ation. The voltage and current sources were set at 40 kV and 30 mA, respectively. Diffraction patterns were recorded with a goniometer speed of 0.5 s per step between 4° and 70° (2θ). FTIR spectra were obtained using a Bruker iFS 66VS spectrophotometer with 2 cm⁻¹ resolution. The Young's modulus of the hybrid nanopapers was measured with a DMA Q800 apparatus (TA Instruments). The test specimen was cut in a rectangular shape (10 × 6 mm²) and the tensile tests were carried out with a stress ramp of 1 MPa min⁻¹ at 26.0 ± 0.5 °C. At least three measurements were carried out for each material.

Water sorption isotherms were measured with an Aquadyne DVS from Quantachrome Instrument. Mass changes due to water adsorption or desorption were recorded at 25 °C in the range of relative humidity from 0% to 95%. Halloysite and sepiolite were analyzed as powder, whereas CNF and HNT-SEP-CNF hybrid nanopapers were analyzed as films.

Contact angle experiments were performed by using an optical contact angle apparatus (OCA 20, Data Physics Instruments) equipped with a video measuring system having a high-resolution CCD camera and a high-performance digitizing adapter. The SCA 20 software (Data Physics Instruments) was used for data acquisition. The contact angle of water in air was measured by the sessile drop method. The water droplet volume was 10.0 ± 0.5 μL. The temperature was set at 25.0 ± 0.1 °C for the support and the injecting syringe as well. From the data analysis the contact angle and the volume of the drop were calculated.

Chemical analysis (CHN) was performed using an elemental analyzer (PerkinElmer, 2400 Series II).

The study of the specific surface area and the pore size distribution of samples was carried out through recording nitrogen adsorption/desorption isotherms with a Micromeritics ASAP 2010 equipment. The samples were degassed at 100 °C prior to the measurements. From the adsorption isotherm, the value of the specific surface was deduced using the BET method. The pore area and volume were analyzed from the adsorption isotherm using the Barret-Joyner-Hallenda (BJH) method.

2.6. Release kinetics

The release kinetics of the drug loaded pristine HNT was investigated in phosphate buffer 0.1 mol L⁻¹ at pH = 5 (which better simulates the skin's natural pH value). The suspension of the drug loaded HNT was placed in a shaking incubator (Julabo SW23) at 37 °C and 150 rpm to establish the equilibrium conditions. At certain predetermined time intervals, 2 ml of the solution was taken out from each sample, and 2 ml of fresh PBS was replaced. The samples for analysis were separated by centrifugation to eliminate light scattering from the halloysite. The collected supernatant was analyzed by carrying out UV-vis measurements (Shimadzu UV-1201) at 264 nm for IBU and at 296 nm for SA.

The following formula:⁶⁵

$$C'_n = C_n + \frac{V}{V_0} \sum_{i=0}^{n-1} C_i \quad (1)$$



corrects the concentration of release, where C'_n is the corrected concentration, C_n represents the n th concentration, V is the sample volume (2 mL), and V_0 is the total volume.

The release kinetics of the drug loaded HNT–SEP–CNF hybrid nanopapers was investigated under the same conditions, but a portion of the film was put into phosphate buffer (pH = 5) and the samples for analysis were taken from the solution and then separated by centrifugation and analyzed.

Before recording the release kinetics of SA and IBU from the loaded HNTs and from the HNT–SEP–CNF hybrid nanopapers, two calibration curves of the drugs in phosphate buffer at pH = 5 were determined. Their measured slopes are 21.63 ± 0.07 mL mg⁻¹ for SA and 1.482 ± 0.004 mL mg⁻¹ for IBU, respectively.

2.7. Antimicrobial activity

The antimicrobial activity of the SA loaded hybrid nanopapers was investigated against Gram-negative bacteria *Escherichia coli* WDCM 00012 and Gram-positive bacteria *Staphylococcus aureus* WDCM 00034 by the disk diffusion method. The strains were cultured in nutrient broth (Merck, Germany) overnight at 37 °C. Each bacterial culture was swabbed uniformly across nutrient agar plates (Merck, Germany) and allowed to be absorbed for 15 min. The discs (6 mm in diameter) of the hybrid nanopapers were placed aseptically on the surface of the agar plate and the plates were placed in a 37 °C incubator for 24 h. The antibacterial activity of the tested samples was determined by measuring the diameter of the inhibition area around the discs. Studies of the SA loaded nanopapers were conducted at pH = 7.0 and pH = 5.5. The discs were loaded with 10 μL of salicylate solutions in water at various concentrations (20 μg μL⁻¹, 2 μg μL⁻¹, 1 μg μL⁻¹, 0.1 μg μL⁻¹, 0.02 μg μL⁻¹, and 0.004 μg μL⁻¹) (Fig. S6†). The negative controls were the HNT–SEP–CNF discs without the drug.

3. Results and discussion

3.1. Preparation and characterization of the hybrid nanopapers

The microscopic features of the fibrous (SEP) and tubular (HNT) nanoclays and the morphology of the resulting hybrid nanopapers were first studied by electron microscopy. Fig. 2a shows that halloysite consists of fine nanotubes with 50–200 nm external diameter. The length of the tubes largely varies between 100 and 3000 nm. It can also be observed that these HNT samples contain some kaolinite particles (arrows in Fig. 2a). It is well known that both alumino-phyllsilicates (HNT and kaolinite) show a similar structural silica/alumina arrangement and composition but different morphological characteristics (tubular vs. hexagonal). Moreover, the microfibrillar morphology of sepiolite with a fiber length of 0.5–2 μm and a thickness of ca. 30–50 nm is shown in Fig. 2b. The typical fibrous morphology of the CNFs was clearly observed by atomic force microscopy (Fig. 2c). The CNFs consist of

2–4 nm thick fibers of 300–600 nm in length and the characteristic semi-flexibility is revealed by the fiber kinks between the crystalline domains (arrows in Fig. 2c).²⁵

The microstructure of the HNT–SEP–CNF (1:1:1 w/w) hybrid nanopaper was examined from the surface and cross sectional images of the films. The FE-SEM images show the presence of all three components though HNTs are more clearly distinguished due to their larger size (Fig. 3a). It is noteworthy that the two fibrous components (sepiolite and CNFs) cannot be easily distinguished at this magnification due to their morphological similarity and the small width of the CNF fibers as already reported by González del Campo *et al.*²⁸ The homogeneous distribution of all three components in the hybrid nanopaper was confirmed by EDX mapping (Fig. S1†). The surface images reveal a certain nematic arrangement of the nanofibers (Fig. 3a) which is also visible within the film (Fig. 3b). In fact, the fracture surface morphology of the film resembles the stratified layer structure typical of solvent cast assemblies of nanofibers or nanosheets.⁶⁶ These observations are also in agreement with the recently reported tendency of the CNFs for nematic ordering during film drying from pure CNF suspensions resulting in a plywood-like nanostructure of the evaporation-condensed films as a result of the averaging of the polydomain nematic arrangement of the CNF layers.⁶⁷ It is remarkable that the nematic arrangement also prevails in the multi-component HNT–SEP–CNF hybrid nanopaper and not only in pure CNF films. The CNFs are characterized by a squared cross-section⁶⁸ and the presence of carboxylate and hydroxyl groups that can partake in hydrogen bond formation in different directions. In addition, as the density of the carboxylate groups varies between the crystalline and disordered regions along the CNF fiber length,⁶⁹ the nanofiber assembly leads to a lower degree of lateral alignment. The non-uniform distribution of the –OH and –COO⁻ groups along the CNF length, combined with the nanofiber flexibility provided by the disordered regions, allows for hydrogen bond formation not only with the –OH groups on the side facets of other CNFs but, more importantly, also with the Si–OH groups present at the edges of the sepiolite fibers. This explanation is in good agreement with what has already been observed elsewhere on nematic ordering in a multicomponent system composed of CNFs and V₂O₅ nanofibers.²⁵ Eventually, this behavior can open up possibilities to tailor the texture and microstructure of complex composite materials with implications of their mechanical, optical and transport properties.

We studied the film formation by considering the components in pairs (*cf.* Fig. 4b–d) and also by changing the ratio between all three components in the HNT–SEP–CNF hybrid nanopaper. It was observed that the 1:1:1 (w/w) ratio gave better results than the other compositions considering the macroscopic aspect, film consistency and homogeneity. This is most likely due to the association between the various building blocks processed as shown in the scheme in Fig. 1. Hence, the multicomponent HNT–SEP–CNF hybrid nanopaper was prepared at a ratio of 1:1:1 (w/w), which displayed the best film forming behaviour (Fig. 4a). Interestingly, not only the compo-



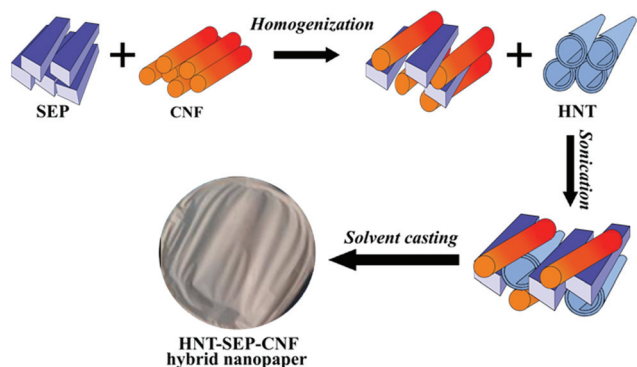


Fig. 1 Scheme of the procedures followed for the integration of HNT, SEP and CNF components leading to HNT-SEP-CNF hybrid nanopapers.

sition but also the combination of the components had a large influence on the film forming ability and therefore on their inherent properties. For instance, the HNT-SEP 1 : 1 (w/w) did not form a coherent film but rather an inconsistent, powdery material (Fig. 4b). Combining CNF with HNT rendered a self-supported film but with considerable defects (Fig. 4c). In contrast, the combination of SEP and CNF at a 1 : 1 ratio produced homogeneous films (Fig. 4d) in accordance with previous studies on CNF-sepiolite nanocomposites.²⁸ From these observations it can be concluded that the macroscopic aspect of the films largely depends on the CNF that plays a major role in providing consistency and mechanical integration to the nanopapers, while the presence of SEP produced an improved dispersion of the components as evident from Fig. 4a (HNT-SEP-CNF) and Fig. 4c (CNF-HNT). As indicated above, the increased sepiolite content (for instance 1 : 2 : 1, not shown) also results in non-uniform films undermining the film formation capacity of the CNF.

The microstructure of the films was further analyzed by X-ray diffraction (XRD) to corroborate possible intercalation within HNT silicate layers and preferential in-plane orientation of the fibers. The XRD pattern of the HNT-SEP-CNF hybrid nanopaper shows that the (001) reflection of halloysite at $12.0^\circ 2\theta$ is not displaced. This finding confirms that no intercalation occurred during the film formation (see Fig. S2† for the indexed pattern of pristine materials and the HNT-SEP-CNF hybrid nanopaper). The most prominent reflections of halloysite and sepiolite are present, whereas the low intensity reflections of the CNF are absent, which can be attributed to the relatively low crystallinity of the CNF. The intensity ratio of the $7.4^\circ 2\theta$ and $13.4^\circ 2\theta$ reflections in the patterns of sepiolite and of the HNT-SEP-CNF hybrid nanopaper (see Fig. S2†) changed from 15.9 to 2.4. It is well-known that a change in the relative intensity of peaks in a X-ray diffractogram of a given system is related to the precise orientation of the crystals and, in particular, in the present case the interactions between the CNF and sepiolite can lead to preferential orientations of the fibers.²⁸ Hence, this significant variation in the relative intensity of the (110) and (003) reflections suggests that the sepiolite fibers

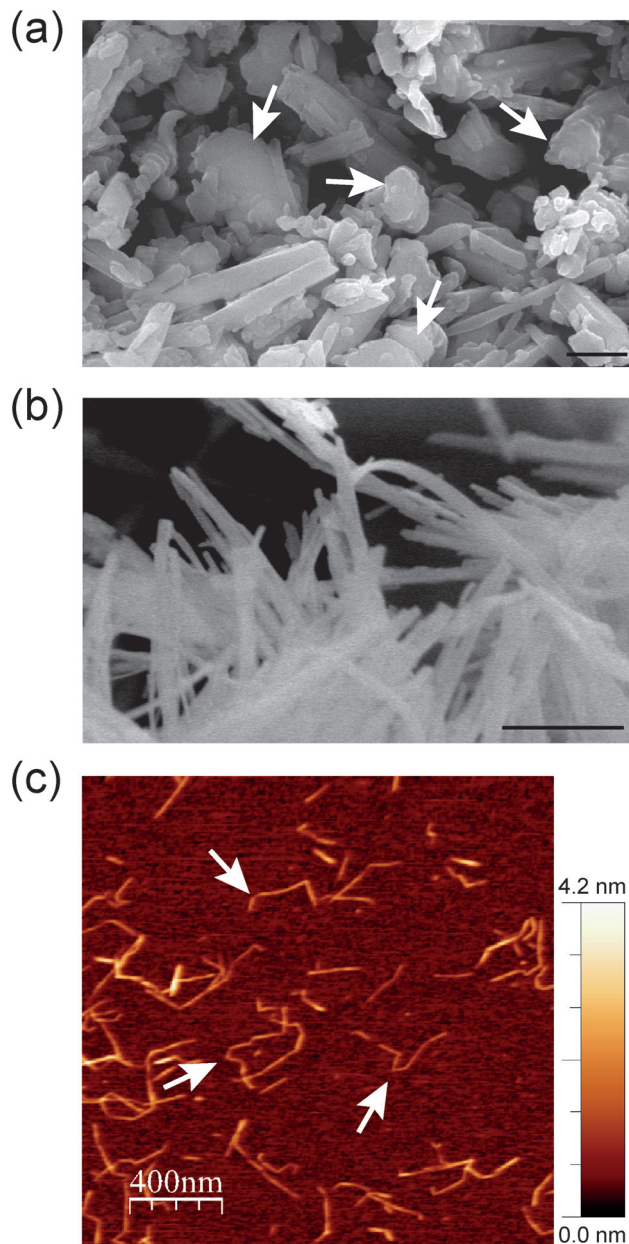


Fig. 2 SEM micrographs of (a) neat HNTs (white arrows represent the hexagonal kaolin sheets), (b) neat sepiolite and (c) the AFM image of the CNF (white arrows represent the fiber kinks). The scale bars in (a) and (b) refer to 500 nm.

have a preferred orientation within the hybrid nanopaper. Indeed, as the SEM images in Fig. 3 show, sepiolite seemed to be well accommodated within the plane of the film, and the fibers show an orientation that is probably induced by the interactions between the components.

The CNF-sepiolite interactions were investigated by IR spectroscopy to further elucidate their implication on the nematic ordering of the fibers. Fig. 5 shows the -OH stretching range ($3730\text{--}3670\text{ cm}^{-1}$) of the collected spectra of the individual pristine components and the HNT-SEP-CNF hybrid nanopaper, respectively. In particular, sepiolite has two bands at 3719



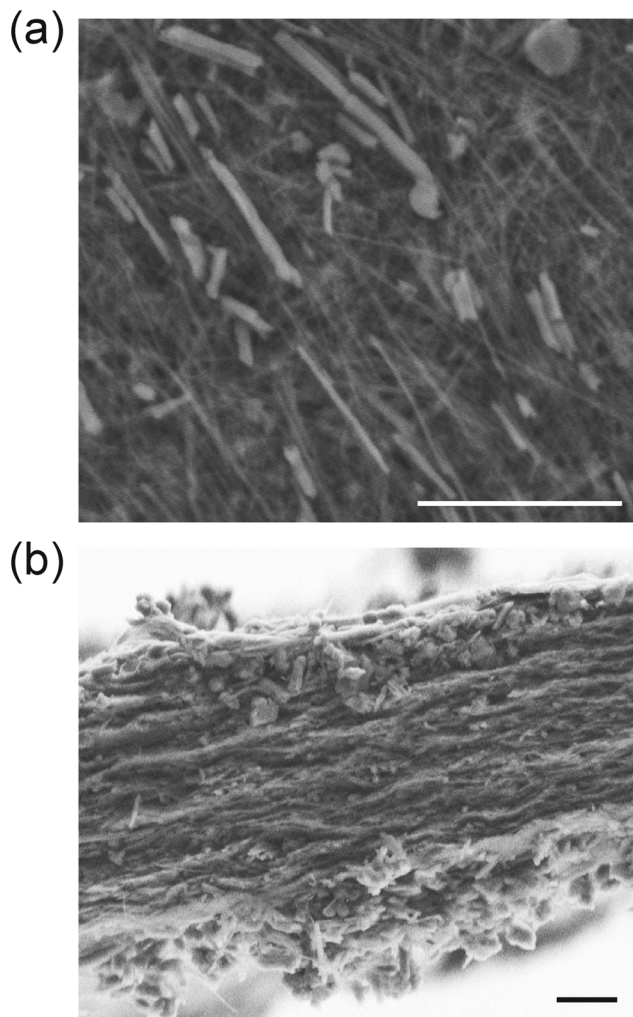


Fig. 3 SEM micrographs of (a) the surface and (b) the fracture cross-section of the 1:1:1 HNT-SEP-CNF hybrid nanopaper, respectively. The scale bars refer to 2 μm.

and 3680 cm^{-1} assigned to the $-\text{OH}$ stretching vibrations of silanol groups and hydroxyl groups bonded to magnesium atoms, respectively.³¹ The $\text{Mg}-\text{OH}$ band at 3680 cm^{-1} remains practically unchanged in the spectrum of the hybrid HNT-SEP-CNF nanopaper as the hydroxyl groups bonded to magnesium atoms are not accessible. However, the band related to the silanol groups (3719 cm^{-1}) disappears, indicating the perturbation of these groups probably due to the hydrogen bonding interaction between $\text{Si}-\text{OH}$ and the hydroxyl groups located on the surface of the CNF. In spite of this, certain interactions with the HNT clay may not be disregarded. Moreover, the two OH -stretching bands at 3695 and 3620 cm^{-1} related to the vibrations of the Al_2OH groups inside the lumen of halloysite⁷⁰ do not show relevant changes in the spectrum of the HNT-SEP-CNF hybrid nanopaper, suggesting the absence of interactions of the lumen with SEP and/or CNF. Thus, the H-bonding interactions between CNF and sepiolite that were conjectured to partake in the nematic ordering in the hybrid film are confirmed.

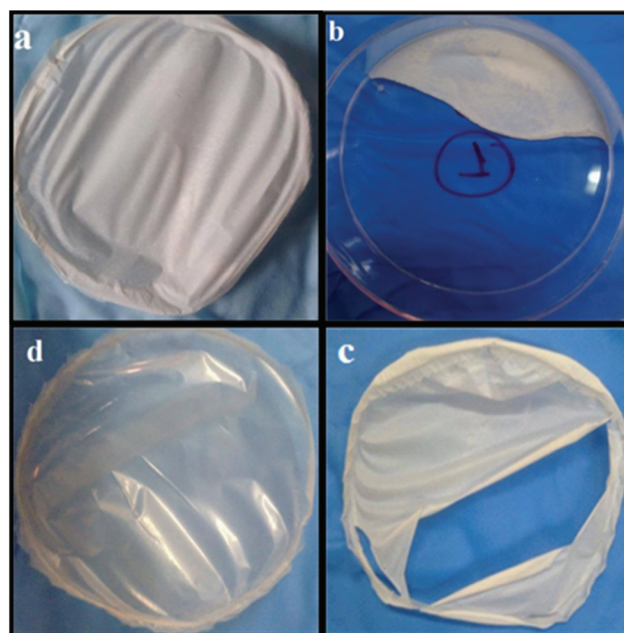


Fig. 4 Macroscopic aspect of various hybrid films prepared by combining HNT, SEP and CNF at different weight ratios: (a) 1:1:1 HNT-SEP-CNF nanopaper, (b) 1:1 HNT-SEP, (c) 1:1 HNT-CNF, and (d) 1:1 SEP-CNF.

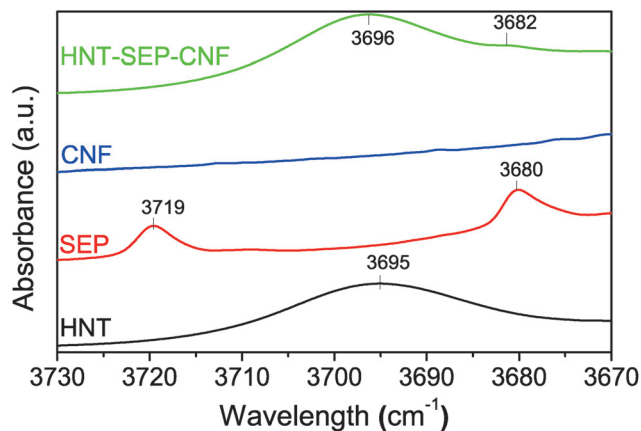


Fig. 5 FTIR spectra of the HNT, SEP, CNF and HNT-SEP-CNF hybrid nanopaper ($3730\text{--}3670\text{ cm}^{-1}$ range). The complete spectra are provided in Fig. S3.†

The mechanical properties of the HNT-SEP-CNF hybrid nanopaper were evaluated from the stress-strain measurements to estimate the Young's modulus (Fig. S4†). It is noteworthy that the incorporation of sepiolite decreased the Young's modulus of the CNF nanopaper from 3.8 GPa to 1.8 GPa. However, the incorporation of HNTs into the SEP-CNF significantly enhanced the mechanical properties of the nanopaper with an increase to 3.2 GPa. These variations in the mechanical properties can be explained considering that halloysite can act as a reinforcement agent as observed elsewhere in cellulose films.⁷¹



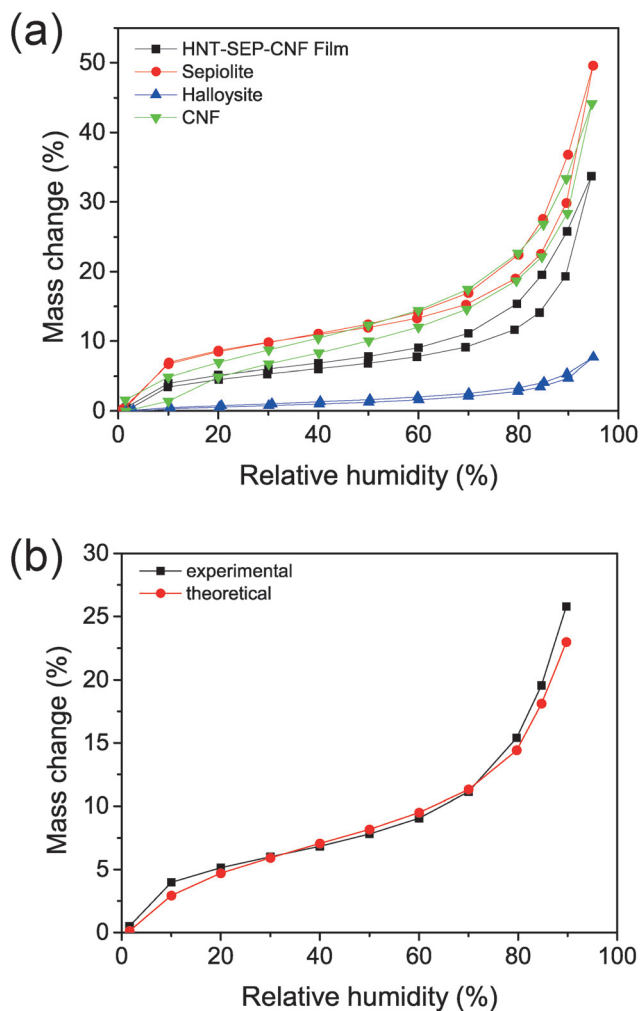


Fig. 6 Water sorption isotherms of (a) HNT (blue), sepiolite (red), CNF (green), and HNT-SEP-CNF (black) films. (b) Experimental vs. theoretical water sorption isotherms.

The wetting properties of the nanopapers were studied as they are relevant for topical drug delivery applications. Water sorption isotherms were recorded as shown in Fig. 6. The three individual components (*i.e.* SEP, CNF, and HNT) display different water sorption profiles (Fig. 6a). For instance, HNT adsorbs less water than sepiolite. Amongst other factors, this process is strongly influenced by both the specific surface area of the solids, *i.e.* 60 and 300 m² g⁻¹ in the case of halloysite and sepiolite, respectively, and the presence of surface groups.^{30,49} In particular, the external surface of HNT is constituted by hydrophobic Si-O-Si groups, whereas sepiolite displays hydrophilic Si-OH groups at the edges along the fiber length and the CNF presents a large number of -OH groups that are strongly hydrophilic. On the other hand, sepiolite and the CNF, the two fibrous components, show a similar mass change *vs.* relative humidity (% RH) value. Concerning the HNT-SEP-CNF hybrid nanopaper, the isotherm is between the isotherms of the HNT and SEP/CNF. A theoretical water adsorption isotherm was determined for the hybrid nanopaper

Table 1 Contact angle (θ_i), n and k_θ values of CNF, SEP-CNF and HNT-SEP-CNF films

	θ_i	n	k_θ (s ⁻ⁿ)
CNF	50 ± 1	0.48 ± 0.04	0.06 ± 0.01
SEP-CNF	31 ± 1	0.54 ± 0.09	0.03 ± 0.01
HNT-SEP-CNF	56 ± 5	0.27 ± 0.04	0.38 ± 0.09

by a simple numerical addition of the individual isotherms considering the 1 : 1 : 1 (w/w) ratio of HNT, SEP and CNF (Fig. 6b). This curve coincides with the experimental isotherm (Fig. 6a), which suggests that the wetting properties of the film are additive and not affected by the interactions between the individual components.

The surface wetting properties of the different materials were also studied by water contact angle measurements on the films. The data were analyzed by fitting the contact angle θ *vs.* time τ curve with the following equation:

$$\Theta = \theta_i \exp(-k_\theta \tau^n) \quad (2)$$

where θ_i is the contact angle at $\tau = 0$, n represents the fractional values ascribable to the occurrence of absorption and spreading and k_θ is the rate of the former or the latter process.⁷¹ The fitted data are reported in Table 1.

The contact angle value of the CNF nanopaper is 50°, whereas the value decreases to 31° in the case of CNF-SEP at a 1 : 1 weight ratio, confirming the strongly hydrophilic surface. It was also observed that the HNT-SEP-CNF 1 : 1 : 1 hybrid nanopaper displays a contact angle of 56°. This implies that the incorporation of halloysite notably decreases the wettability of HNT-SEP-CNF. The network of the self-assembled fibrils and nanotubes is also likely to display air-filled protrusions due to the increased surface roughness and thus giving rise to changes in the wettability of these materials. Indeed, similar observations were reported for polypropylene-HNT nanocomposites, in which the generation of a rough surface caused by the enrichment with HNT nanoparticles was ascribed to an improvement in the hydrophobic film properties.^{72,73} Moreover, the data fitting of the Θ, τ curves revealed that both the spreading and absorption mechanisms of water took place for the studied nanopapers, that is $n = 0$ and 1 for pure absorption and pure spreading, respectively. For instance, the n value was ≈ 0.5 for the pure CNF and SEP-CNF films and it decreased to 0.27 for the HNT-SEP-CNF nanopaper, reflecting a major role in the absorption mechanism of water into the material.

3.2. Uptake of salicylic acid and ibuprofen by HNT-SEP-CNF hybrid nanopapers

As mentioned above, the HNT-SEP-CNF hybrid nanopapers were evaluated as drug delivery systems (DDS) using two model drugs, SA and IBU, due to their widespread use in topical applications including injury cure. The SA loading into HNT was 8.4 wt% as deduced from the elemental analysis, which shows a similar value as reported for other halloysite-SA



systems.⁷⁴ The total amount of IBU loaded into HNT was 5.1 wt%. It is interesting to note that the SA loading at pH 8 to maximize the negative charge of the drug allowed a larger amount of SA to be adsorbed on HNT as compared with IBU loading values.

The FTIR spectra of SA, HNT and HNT-SA were collected to investigate the possible interactions of SA with HNT (Fig. S5a†). These data indicate that the interaction with HNT changes the π -electron density of the benzene ring of the salicylate, as inferred from the shift of the absorption bands of the C=C vibrations from 1597, 1485 and 1468 cm^{-1} to 1606, 1473 and 1463 cm^{-1} , respectively. In addition, it was found that the ν_{as} vibration of $-\text{COO}^-$ was shifted from 1582 to 1577 cm^{-1} , meanwhile the band at 1377 cm^{-1} of the ν_{s} vibration of $-\text{COO}^-$ splits into two components, *i.e.* 1387 and 1375 cm^{-1} .⁷⁴ Moreover, the stretching and bending vibrations of Ph-OH at 1248 cm^{-1} and 1319 cm^{-1} respectively, shift, which suggests that the phenolic group is involved in the interaction between the salicylate and ALOH groups inside the HNT lumen. For what concerns the IBU-loaded HNTs, the FTIR spectra (Fig. S5b and c†) show the appearance of the characteristic bands at 2956, 2925, 2869, 2849 and 1550 cm^{-1} of IBU.⁷⁵ This is attributed to the successful entrapment of IBU in the lumen of the nanotube.

The N_2 adsorption/desorption isotherms for pristine HNT, salicylate loaded HNT and ibuprofen loaded HNT (Fig. S6†) were collected in order to verify the entrapment of the molecules in the HNT lumen. After loading, the type IV isotherm persisted but an appreciable reduction in the BET surface area, pore surface area, and pore volume in comparison with pristine HNT was observed (Table 2).

After SA loading into HNT, the BET surface area dropped from 27.3 to 20.2 $\text{m}^2 \text{g}^{-1}$, the mesopore area decreased from 23.2 to 17.8 $\text{m}^2 \text{g}^{-1}$ and the mesopore volume was reduced from 0.062 to 0.054 $\text{cm}^3 \text{g}^{-1}$. This suggests that the SA inside the halloysite lumen produced a partial pore blockage accounting for the BET surface area reduction and the corresponding reduction in the mesopore area and volume parameters. The modification of these parameters is more noticeable for HNT-SA than HNT-IBU reflecting the higher SA uptake.

The release profiles for SA and IBU from the HNT and HNT-SEP-CNF nanopapers were collected to determine the release kinetics (Fig. 7).

The profiles show that more than 90% of salicylic acid was released from HNT within 60 min while less than 80% was released from the HNT-SEP-CNF hybrid nanopaper during the same period of time. Moreover, ibuprofen is released from

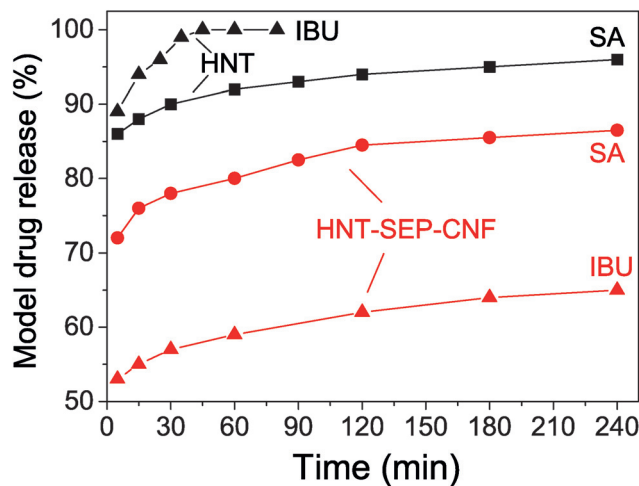


Fig. 7 Release profiles of salicylic acid (SA) and ibuprofen (IBU) from the loaded HNTs and loaded HNT-SEP-CNF hybrid nanopaper.

HNT at an even higher rate, while the release rate from the HNT-SEP-CNF film was considerably lower. Almost 60% of ibuprofen was released from the film within 60 min *vs.* 100% release from HNT. After 4 hours, only *ca.* 65% of IBU was released. These observations could be explained by invoking the very high solubility of the drugs (salicylate and ibuprofen sodium salts) in water. The solubility of IBU in water is 100 mg mL^{-1} while for SA it is 50 mg mL^{-1} . This may explain why IBU is released faster from HNT than SA. In contrast, in the HNT-SEP-CNF hybrid nanopaper, the release rate of the drug is lower possibly due to the multiple interactions with the halloysite, sepiolite and cellulose nanofibers. In this case, once the drugs are released from the lumen, the interactions with the other matrix components are important and determine the release kinetics. For instance, strong interactions have been reported to exist between IBU and the nanocellulose,⁷⁶ which could explain the slower IBU release kinetics from the HNT-SEP-CNF hybrid nanopaper as compared to SA. In addition, the openings of the nanotubes could be partially obstructed by the particular texture of the film and thus, sustained the drug release. Moreover, the particular diffusion mechanism of the drugs inside the nanotube lumen and through the nanocomposite matrix plays an important role. For instance, the particular position of the loaded drug inside the nanotubes, at the edges or at the center of the lumen, has been reported to deeply affect the release kinetics due to the diffusion path of the guest molecules which is faster in the first case and slower in the second case.⁷⁰

3.3. *In vitro* antibacterial assay

Based on the sustained SA release from the HNT-SEP-CNF hybrid nanopapers, the studies of antibacterial activity were performed to evaluate this new type of delivery system for topical applications. Therefore, the studies were carried out against the typically used Gram-negative *E. coli* and Gram-positive *S. aureus* bacteria under neutral and acidic (pH = 5.5) con-

Table 2 The BET surface area, pore surface area, S_{mes} , and pore volume, V_{mes} , of pristine HNT, SA loaded HNT and IBU loaded HNT

	S_{BET} ($\text{m}^2 \text{g}^{-1}$)	S_{mes} ($\text{m}^2 \text{g}^{-1}$)	V_{mes} ($\text{cm}^3 \text{g}^{-1}$)
HNTs	27.3	23.2	0.062
HNT + SA	20.2	17.8	0.054
HNT + IBU	24.6	21.9	0.057





Fig. 8 Inhibition zone of the salicylic acid loaded HNT–SEP–CNF hybrid nanopaper against Gram-positive *S. aureus* at pH = 5.5.

ditions by means of the disk diffusion method.⁵² The positive controls for salicylate are displayed in Fig. S6.†

It was observed that the SA loaded in HNT and then incorporated to the HNT–SEP–CNF nanopaper displays antimicrobial activity and shows an effect when it is used against *S. aureus* at pH = 5.5, as confirmed by the positive controls (Fig. S7d†).

The result of the trials is shown in Fig. 8, where the formation of the inhibition zone is clearly observable. Moreover, its average diameter is in the same order of magnitude of salicylic acid loaded pectin–HNT bionanocomposites⁷⁰ thus, confirming the activity of the drug loaded HNT–SEP–CNF hybrid nanopaper.

4. Conclusions

A new type of biohybrid material processed as a film was prepared by co-assembling nanotubular halloysite, fibrous sepilite, and cellulose nanofibers. The 1 : 1 : 1 (w/w) ratio of the three components was found to render homogeneous and self-supported films displaying reasonable mechanical properties and endorsing suitable characteristics for the proposed applications. Different characterization techniques confirm the short-range interactions between the organic and the inorganic components, mainly occurring through hydrogen bonding between the hydroxyl groups.

The incorporation of HNT allows controlling the textural and surface chemistry characteristics of the resulting film including its mechanical properties and the wetting behavior. For instance, we observed an increased Young's modulus value and a less hydrophilic surface for the HNT–SEP–CNF hybrid nanopaper compared to the SEP–CNF films. The interaction of HNT, SEP, and CNF renders multifunctional hybrid nanopapers that can be deployed for further functionalization in a wide range of applications. In this way, they were evaluated as drug delivery systems using salicylic acid and ibuprofen due to their conventional use in topical treatments. The results proved the effective encapsulation of the drugs into the positively charged HNT lumen and more sustained release kinetics

for the hybrid nanopaper as compared to the loaded neat halloysite. Furthermore, the evaluation of the antimicrobial activity studies against Gram-positive and Gram-negative bacteria proved the effective inhibition of *S. aureus* growth at pH = 5.5 confirming the interest of this new type of biohybrid material in controlled delivery applications. Besides, these nanopapers also offer interesting possibilities for further applications in view of the different chemical features and functional groups of the components.

Conflicts of interest

The authors declare no conflict of interest.

Acknowledgements

The authors thank the MINECO (Spain) and FEDER (EU) for financial support (project MAT2015-71117-R). LL and GDL acknowledge the University of Palermo for the “UOB21 Borse di studio finalizzate alla ricerca” grants. BW thanks the MINECO for the IJCI contract (IJCI-2015-23886). The authors also thank Ms Paloma Encinas from INIA and M. Mar Blanco-Gutierrez from the Veterinary Faculty of the Complutense University of Madrid for providing bacterial strains.

References

- 1 E. Ruiz-Hitzky, P. Aranda, M. Darder and G. Rytwo, *J. Mater. Chem.*, 2010, **20**, 9306–9321.
- 2 E. Ruiz-Hitzky, M. Darder, F. M. Fernandes, B. Wicklein, A. C. S. Alcântara and P. Aranda, *Prog. Polym. Sci.*, 2013, **38**, 1392–1414.
- 3 T. Hueckel and S. Sacanna, *ACS Nano*, 2018, **12**, 3533–3540.
- 4 E. Abdullayev and Y. Lvov, *J. Mater. Chem. B*, 2013, **1**, 2894–2903.
- 5 M. Catauro, E. Tranquillo, F. Barrino, I. Blanco, F. Dal Poggetto and D. Naviglio, *Materials*, 2018, **11**, 2270.
- 6 M. Faustini, L. Nicole, E. Ruiz-Hitzky and C. Sanchez, *Adv. Funct. Mater.*, 2018, **28**, 1704158.
- 7 E. Paineau, M.-E. M. Krapf, M.-S. Amara, N. V. Matskova, I. Dozov, S. Rouzière, A. Thill, P. Launois and P. Davidson, *Nat. Commun.*, 2016, **7**, 10271.
- 8 L. Lisuzzo, G. Cavallaro, S. Milioto and G. Lazzara, *New J. Chem.*, 2019, **43**, 10887–10893.
- 9 E. P. Rebitski, P. Aranda, M. Darder, R. Carraro and E. Ruiz-Hitzky, *Dalton Trans.*, 2018, **47**, 3185–3192.
- 10 E. P. Rebitski, G. P. Souza, S. A. A. Santana, S. B. C. Pergher and A. C. S. Alcântara, *Appl. Clay Sci.*, 2019, **173**, 35–45.
- 11 M. Djellali, P. Aranda and E. Ruiz-Hitzky, *Appl. Clay Sci.*, 2019, **171**, 65–73.
- 12 B. Huang, M. Liu and C. Zhou, *Carbohydr. Polym.*, 2017, **175**, 689–698.
- 13 G. Gorrasi, R. Pantani, M. Murariu and P. Dubois, *Macromol. Mater. Eng.*, 2014, **299**, 104–115.



- 14 Y. Fukushima and S. Inagaki, *J. Inclusion Phenom.*, 1987, **5**, 473–482.
- 15 F. Li, E. Mascheroni and L. Piergiovanni, *Packag. Technol. Sci.*, 2015, **28**, 475–508.
- 16 H. Zhu, Z. Fang, C. Preston, Y. Li and L. Hu, *Energy Environ. Sci.*, 2014, **7**, 269–287.
- 17 B. Wicklein, A. Kocjan, G. Salazar-Alvarez, F. Carosio, G. Camino, M. Antonietti and L. Bergström, *Nat. Nanotechnol.*, 2015, **10**, 277–283.
- 18 Y. Xue, Z. Mou and H. Xiao, *Nanoscale*, 2017, **9**, 14758–14781.
- 19 L. Shun and H. Jianguo, *Adv. Mater.*, 2016, **28**, 1143–1158.
- 20 B. Wicklein, D. Kocjan, F. Carosio, G. Camino and L. Bergström, *Chem. Mater.*, 2016, **28**, 1985–1989.
- 21 M. Pääkkö, M. Ankerfors, H. Kosonen, A. Nykänen, S. Ahola, M. Österberg, J. Ruokolainen, J. Laine, P. T. Larsson, O. Ikkala and T. Lindström, *Biomacromolecules*, 2007, **8**, 1934–1941.
- 22 T. Saito, S. Kimura, Y. Nishiyama and A. Isogai, *Biomacromolecules*, 2007, **8**, 2485–2491.
- 23 R. J. Moon, A. Martini, J. Nairn, J. Simonsen and J. Youngblood, *Chem. Soc. Rev.*, 2011, **40**, 3941–3994.
- 24 A. Hajian, S. B. Lindström, T. Pettersson, M. M. Hamed and L. Wågberg, *Nano Lett.*, 2017, **17**, 1439–1447.
- 25 B. Wicklein, A. M. Diem, A. Knöller, M. S. Cavalcante, L. Bergström, J. Bill and Z. Burghard, *Adv. Funct. Mater.*, 2017, 1704274.
- 26 C. Aulin, G. Salazar-Alvarez and T. Lindstrom, *Nanoscale*, 2012, **4**, 6622–6628.
- 27 K. Yao, S. Huang, H. Tang, Y. Xu, G. Buntkowsky, L. A. Berglund and Q. Zhou, *ACS Appl. Mater. Interfaces*, 2017, **9**, 20169–20178.
- 28 M. M. Gonzalez del Campo, M. Darder, P. Aranda, M. Akkari, Y. Huttel, A. Mayoral, J. Bettini and E. Ruiz-Hitzky, *Adv. Funct. Mater.*, 2017, 1703048.
- 29 M. Ghanadpour, B. Wicklein, F. Carosio and L. Wagberg, *Nanoscale*, 2018, **10**, 4085–4095.
- 30 E. Ruiz-Hitzky, *J. Mater. Chem.*, 2001, **11**, 86–91.
- 31 M. Akkari, P. Aranda, A. Mayoral, M. García-Hernández, A. B. H. Amara and E. Ruiz-Hitzky, *J. Hazard. Mater.*, 2017, **340**, 281–290.
- 32 J. L. Ahlrichs, C. Serna and J. M. Serratos, *Clays Clay Miner.*, 1975, **23**, 119–124.
- 33 F. M. Fernandes and E. Ruiz-Hitzky, *Carbon*, 2014, **72**, 296–303.
- 34 E. Ruiz-Hitzky, M. M. C. Sobral, A. Gómez-Avilés, C. Nunes, C. Ruiz-García, P. Ferreira and P. Aranda, *Adv. Funct. Mater.*, 2016, **26**, 7394–7405.
- 35 P. Aranda and E. Ruiz-Hitzky, *Chem. Rec.*, 2018, **18**, 1125–1137.
- 36 P. Pasbakhsh, G. J. Churchman and J. L. Keeling, *Appl. Clay Sci.*, 2013, **74**, 47–57.
- 37 Y. Lvov and E. Abdullayev, *Prog. Polym. Sci.*, 2013, **38**, 1690–1719.
- 38 A. Takahara and Y. Higaki, *RSC Smart Mater.*, 2017, 131–156.
- 39 E. Abdullayev, A. Joshi, W. Wei, Y. Zhao and Y. Lvov, *ACS Nano*, 2012, **6**, 7216–7226.
- 40 M. R. Dзамukova, E. A. Naumenko, Y. M. Lvov and R. F. Fakhrullin, *Sci. Rep.*, 2015, **5**, 10560.
- 41 L. Lisuzzo, G. Cavallaro, F. Parisi, S. Milioto and G. Lazzara, *Ceram. Int.*, 2019, **45**, 2858–2865.
- 42 G. Cavallaro, G. Lazzara, S. Milioto, F. Parisi and V. Sanzillo, *ACS Appl. Mater. Interfaces*, 2014, **6**, 606–612.
- 43 J. Tully, R. Yendluri and Y. Lvov, *Biomacromolecules*, 2016, **17**, 615–621.
- 44 H. Zhang, C. Cheng, H. Song, L. Bai, Y. Cheng, X. Ba and Y. Wu, *Chem. Commun.*, 2019, **55**, 1040–1043.
- 45 G. Cavallaro, I. Grillo, M. Gradzielski and G. Lazzara, *J. Phys. Chem. C*, 2016, **120**, 13492–13502.
- 46 G. Cavallaro, G. Lazzara, L. Lisuzzo, S. Milioto and F. Parisi, *Nanotechnology*, 2018, **29**, 325702.
- 47 F. Liu, L. Bai, H. Zhang, H. Song, L. Hu, Y. Wu and X. Ba, *ACS Appl. Mater. Interfaces*, 2017, **9**, 31626–31633.
- 48 B. Huang, M. Liu and C. Zhou, *Cellulose*, 2017, **24**, 2861–2875.
- 49 M. Du, B. Guo and D. Jia, *Polym. Int.*, 2010, **59**, 574–582.
- 50 G. Lazzara, G. Cavallaro, A. Panchal, R. Fakhrullin, A. Stavitskaya, V. Vinokurov and Y. Lvov, *Curr. Opin. Colloid Interface Sci.*, 2018, **35**, 42–50.
- 51 G. Cavallaro, G. Lazzara, S. Milioto, F. Parisi, V. Evtugyn, E. Rozhina and R. Fakhrullin, *ACS Appl. Mater. Interfaces*, 2018, **10**, 8265–8273.
- 52 G. Cavallaro, S. Milioto, F. Parisi and G. Lazzara, *ACS Appl. Mater. Interfaces*, 2018, **10**, 27355–27364.
- 53 H. Wan, H. Xiong, X. Liu, G. Chen, N. Zhang, H. Wang, R. Ma and G. Qiu, *Dalton Trans.*, 2018, **47**, 7522–7527.
- 54 M. M. Najafpour and E. Amini, *Dalton Trans.*, 2015, **44**, 15441–15449.
- 55 S. Sadjadi, M. Akbari, E. Monflier, M. M. Heravi and B. Leger, *New J. Chem.*, 2018, **42**, 15733–15742.
- 56 G. I. Fakhrullina, F. S. Akhatova, Y. M. Lvov and R. F. Fakhrullin, *Environ. Sci.: Nano*, 2015, **2**, 54–59.
- 57 G. Cavallaro, G. Lazzara and S. Milioto, *J. Phys. Chem. C*, 2012, **116**, 21932–21938.
- 58 G. Lo Dico, B. Wicklein, L. Lisuzzo, G. Lazzara, P. Aranda and E. Ruiz-Hitzky, *Beilstein J. Nanotechnol.*, 2019, **10**, 1303–1315.
- 59 R. Zurita, J. Puiggalí and A. Rodríguez-Galán, *Macromol. Biosci.*, 2006, **6**, 767–775.
- 60 R. Abdeen and N. Salahuddin, *Eur. J. Chem.*, 2013, 1–9.
- 61 M. Haraleti, K. Hosni and E. Srasra, *Surf. Eng. Appl. Electrochem.*, 2017, **53**, 360–370.
- 62 Ú. Fillat, B. Wicklein, R. Martín-Sampedro, D. Ibarra, E. Ruiz-Hitzky, C. Valencia, A. Sarrión, E. Castro and M. E. Eugenio, *Carbohydr. Polym.*, 2018, **179**, 252–261.
- 63 L. Ji, W. Qiao, Y. Zhang, H. Wu, S. Miao, Z. Cheng, Q. Gong, J. Liang and A. Zhu, *Mater. Sci. Eng., C*, 2017, **78**, 362–369.
- 64 L. Lisuzzo, G. Cavallaro, P. Pasbakhsh, S. Milioto and G. Lazzara, *J. Colloid Interface Sci.*, 2019, **547**, 361–369.



- 65 D. Yu, J. Wang, W. Hu and R. Guo, *Mater. Des.*, 2017, **129**, 103–110.
- 66 W. Yang, Z. Zhao, K. Wu, R. Huang, T. Liu, H. Jiang, F. Chen and Q. Fu, *J. Mater. Chem. C*, 2017, **5**, 3748–3756.
- 67 M. Zhao, F. Ansari, M. Takeuchi, M. Shimizu, T. Saito, L. A. Berglund and A. Isogai, *Nanoscale Horiz.*, 2018, **3**, 28–34.
- 68 A. N. Fernandes, L. H. Thomas, C. M. Altaner, P. Callow, V. T. Forsyth, D. C. Apperley, C. J. Kennedy and M. C. Jarvis, *Proc. Natl. Acad. Sci. U. S. A.*, 2011, **108**, E1195–E1203.
- 69 R. Shinoda, T. Saito, Y. Okita and A. Isogai, *Biomacromolecules*, 2012, **13**, 842–849.
- 70 M. Makaremi, P. Pasbakhsh, G. Cavallaro, G. Lazzara, Y. K. Aw, S. M. Lee and S. Milioto, *ACS Appl. Mater. Interfaces*, 2017, **9**, 17476–17488.
- 71 G. Cavallaro, D. I. Donato, G. Lazzara and S. Milioto, *J. Phys. Chem. C*, 2011, **115**, 20491–20498.
- 72 Q. Zhou, K. P. Pramoda, J.-M. Lee, K. Wang and L. S. Loo, *J. Colloid Interface Sci.*, 2011, **355**, 222–230.
- 73 A. Marmur, *Langmuir*, 2008, **24**, 7573–7579.
- 74 A. Spepi, C. Duce, A. Pedone, D. Presti, J.-G. Rivera, V. Ierardi and M. R. Tiné, *J. Phys. Chem. C*, 2016, **120**, 26759–26769.
- 75 H. Li, X. Zhu, H. Zhou and S. Zhong, *Colloids Surf., A*, 2015, **487**, 154–161.
- 76 G. Chantereau, M. Sharma, A. Abednejad, B. M. Neves, G. Sèbe, V. Coma, M. G. Freire, C. S. R. Freire and A. J. D. Silvestre, *ACS Sustainable Chem. Eng.*, 2019, **7**, 14126–14134.

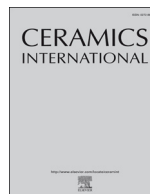




ELSEVIER

Contents lists available at ScienceDirect

Ceramics International

journal homepage: www.elsevier.com/locate/ceramint

Colloidal stability of halloysite clay nanotubes

Lorenzo Lisuzzo, Giuseppe Cavallaro, Filippo Parisi, Stefana Milioto, Giuseppe Lazzara*

Dipartimento di Fisica e Chimica, Università degli Studi di Palermo, Viale delle Scienze pad 17, 90128 Palermo, Italy



ARTICLE INFO

Keywords:

Halloysite nanotubes
Surfactants
Colloidal stability
Clay dispersion
Polymers
Biopolymers
Pickering emulsion

ABSTRACT

The colloidal stability of halloysite clay nanotubes dispersion is reviewed showing the strategy and the mechanism to obtain stable systems in water and apolar solvents. The selective modification of halloysite inner/outer surfaces can be achieved by exploiting electrostatic interactions. The adsorption of anionic surfactants onto the halloysite cavity allows generating inorganic cylindrical micelles that can be separated from the solvent. On the other hand, the functionalization of halloysite shell by positively charged surfactants drives to obtain stable water-in-oil emulsions. The interactions with ionic and nonionic polymers alters the dispersability of halloysite due to electrostatic and steric effects that are strongly dependent on the nanoarchitecture of the hybrid systems.

Modified nanotubes by selective interactions lead to the formation of colloidal systems with tuneable surface properties and controlled colloidal stability adjusted to the solvent polarity. These dispersions are perspectives nanocarriers for substances such as antioxidants, biocides, drugs and corrosion inhibitors, to be released in response to external stimuli.

1. Introduction

In recent years, nanoclays have been the object of particular interest for many scientists and researchers in chemistry, physics, engineering and biology due to their excellent properties as well as their sustainability [1–3]. For instance, they represent the starting point to the development of smart materials for drug delivery [4–9], food packaging [10–12], environmental remediation and wastewater treatment [13], cultural heritage [14–17] and additives for enhancing the performances of polymers [18,19]. Due to the large demand of applications, the physico-chemical properties of nanoparticles, and nanoclays particularly, have been manipulated in order to improve their stability in aqueous media [20,21]. Since the discovery of carbon nanotubes in 1991 [22], the tubular structure has been widely investigated in other types of particles including metal nanotubes [23,24], oxide nanotubes [25,26], semiconducting nanotubes [27], nitride nanotubes [28,29] and natural clay nanotubes, which have gained interest in the material science and nanotechnology for their large specific surface, high porosity and tunable surface chemistry.

This review will be focused on the strategies to prepare stable dispersions of halloysite clay nanotubes (HNTs) that are naturally-occurring two-layered aluminosilicate characterized by a hollow tubular structure with a spiral conformation (Fig. 1) and unit formula $(\text{Al}_2\text{Si}_2\text{O}_5(\text{OH})_4)_n\text{H}_2\text{O}$ [1]. The interlayer distance depends on the hydration state being 0.7 nm and 1 nm for $n = 0$ and $n = 2$ respectively

[1].

The HNTs size depends on the deposit and varies from 50 to 70 nm in external diameter, and from 10 to 20 nm diameter for the lumen [18,31]. The tubes' lengths range within 0.5–1.5 μm . The external surface of HNTs is composed of silicon oxygen tetrahedron meanwhile the internal lumen consists of alumina oxygen octahedrons [32], so the outer surface is distributed mainly with Si-O-Si group and the inner surface is composed of Al-OH [30,33]. Because of the multilayer structure, most of the hydroxyl groups exist within the lumen and only a few in the outer surface [34]. Considering the different chemistry in the inner/outer surface, the former is positively charged and the latter is negatively charged in water in a pH range between 2 and 8. Moreover, as a widely used environmentally friendly clay material, HNTs have a good biocompatibility [35] and they are non-toxic as evidenced by in vivo [36] and in vitro tests [37]. These characteristics make HNTs excellent vehicles for carrying numerous types of cargos, when negatively charged molecules are sacked into the tube's lumen and positive ones adsorbed on the tube's outer surface. The colloidal stability of HNTs is a key point that has been deeply investigated, in order to improve the nanoparticles manageability through the several possible uses that could be made [38]. For instance, when stable colloidal dispersions are reached, both a higher specific surface and a greater cavity area of halloysite nanotubes could be obtained and extensively used in nanocatalysis [39–45], nanotemplate [46] and biological controlled release [47–49]. This purpose was pursued by some different strategies of

* Corresponding author.

E-mail address: giuseppe.lazzara@unipa.it (G. Lazzara).

<https://doi.org/10.1016/j.ceramint.2018.07.289>

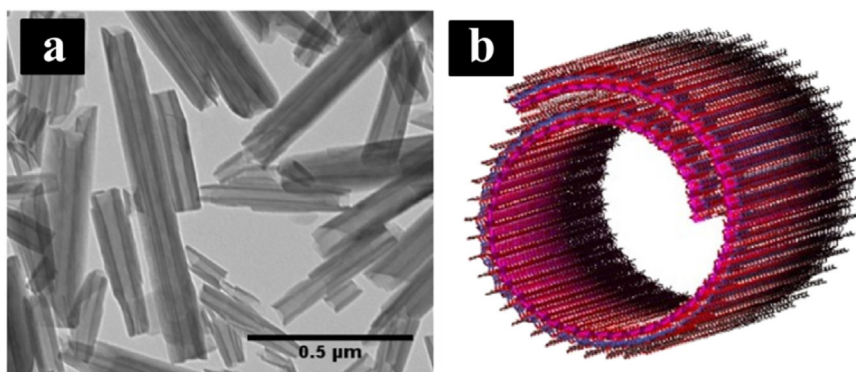


Fig. 1. TEM halloysite image (a) adapted with permission from [3], copyright 2015 Wiley Publ. Modeling of the halloysite spiral ordering (b) adapted with permission from [30], copyright 2015 American Chemical Society.

manipulation of the physico-chemical properties that range from the direct study into aqueous media by the selective functionalization of halloysite outer/inner surface with ionic molecules (surfactants, polymers and biomacromolecules) to the evaluation of HNTs in generating Pickering emulsions.

2. Halloysite nanotubes in water

Due to their high aspect ratios, the anisotropic nanoparticles can form liquid crystalline phases, such as those observed for carbon nanotubes (CNTs) [50–52], graphene oxide (GO) [53,54], cellulose [55], which are recognized as key potential precursors for the fluid phase processing of particles into aligned materials with outstanding properties. Firstly, Luo et al. [56] have studied the liquid crystalline phase of HNTs in aqueous dispersions. It has been observed that the liquid crystalline phase starts to form at the HNTs concentration of 1 wt%, and a full liquid crystalline phase is achieved at the HNTs concentration of 25 wt%. Rheological measurements indicate a typical shear flow behavior for the HNT aqueous dispersions with concentrations above 20 wt% and the sol–gel transition occurs at the HNT concentration of 37 wt% [56]. Furthermore, the HNTs aqueous dispersions exhibit pH-induced gelation with more intense birefringence when hydrochloric acid (HCl) is added. These findings could facilitate the large-scale alignments of HNTs in the fluid phase and open the way to make the long-range ordered structures of HNT-based functional materials, offering the opportunities to uncover the complex phase transition behaviors for HNT dispersions with particular topologies [56]. The sedimentation behavior of halloysite in water is rather peculiar and a simple percolation model can explain it. It has been already observed in 1952 [57] that halloysite aqueous dispersions settle down with a large sedimentation volume. Recently, [58] this peculiarity has been explained on the basis of geometric considerations allowing to predict the nanotubes volume fraction in the sedimentation volume (Φ) by considering the contact distance as:

$$\Phi = \pi R^2/L^2 \quad (1)$$

where R and L are the external radius and the length of the nanotubes [58]. A scheme of the sedimentation behavior with optical image is presented in Fig. 2.

3. Effect of surfactants on halloysite colloidal stability in polar and apolar solvents

Amphiphilic molecules are typically used to stabilize nanoparticles dispersions due to their surface active features. Regarding halloysite nanotubes, the choice of surfactant in terms of the headgroup charge is a key factor and it has a profound effect on their colloidal stability. Such a peculiarity is due to the charge separation in the inner and outer surface of halloysite.

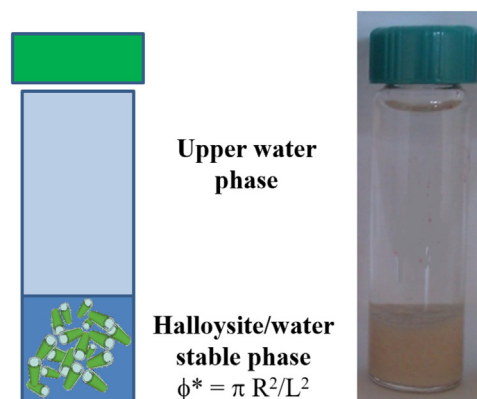


Fig. 2. Scheme for the sedimentation volume of halloysite nanotubes. Halloysite concentration in the stable phase was $\Phi = 0.03$.

3.1. Anionic surfactants selective functionalization

It has been demonstrated that the adsorption of anionic surfactants (e.g. sodium alkanates) occurs into the HNTs lumen and it increases the net negative charge of the nanotubes enhancing the electrostatic repulsions and consequently the dispersion stability [59,60]. It is noteworthy that the change of ζ potential, that becomes more negative, predicts a better colloidal stability of the hybrid materials compared to the pristine nanotubes because of the low tendency to aggregate and the sedimentation is strongly slowed down by the surfactants [60] (Fig. 3).

Moreover, it was observed that the colloidal stability of modified HNTs is not strictly correlated to the loading degree of the anionic surfactants into the HNT inner lumen as soon as the inner surface is fully covered.

However, the very high surfactant content (close to 10%) indicates the formation of self-organized structures in the cavity, for example double-layers that maintain the counter-ions and do not contribute to the charge increase of the nanoparticle and consequently to its electrostatic stabilization [60].

These findings are consistent with the DLVO theory that establishes that the stability of a colloidal suspension depends on the balance between attractive van der Waals forces and electrostatic repulsions caused by the double layer surrounding each particle [61]. Therefore, both ζ -potential and width of the electric double layer contribute to the total repulsive force. This theory also envisages that a large ionic strength generates a screening of the electrostatic repulsions because of the reduction of the double layer [60].

Moreover, the structures of pristine halloysite nanotubes and ones functionalized by anionic surfactants (sodium dodecanoate and sodium dodecyl sulfate) were investigated by small angle neutron scattering

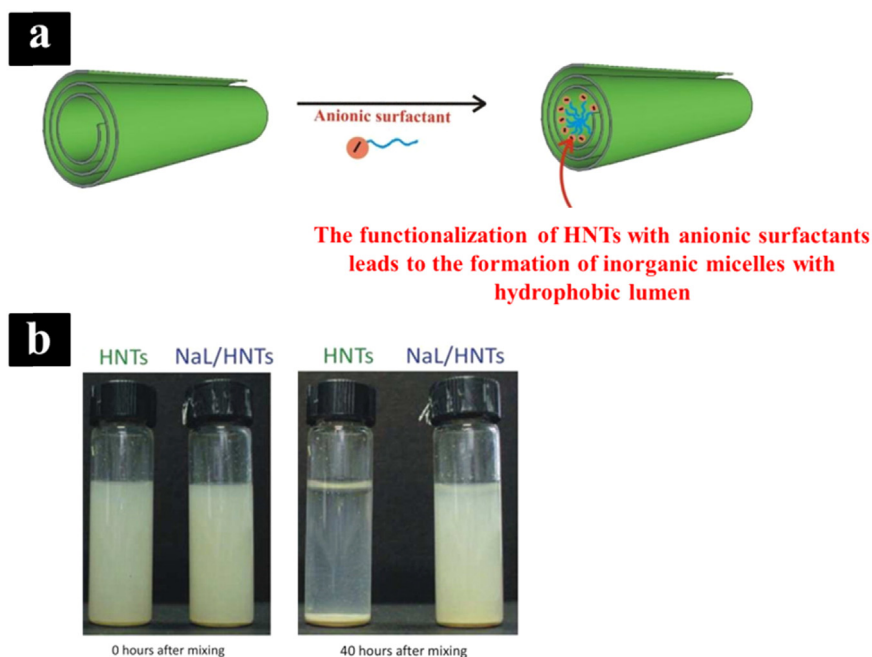


Fig. 3. Scheme of HNTs functionalization with anionic surfactants (a) and photographs of pristine halloysite and nanotubes functionalized with sodium dodecanoate (NaL) in water (b) adapted with permission from [30,59], copyright 2015 American Chemical Society.

(SANS) [62]. These experiments evidenced the structural organization of the surfactants adsorbed onto the HNT cavity and the influence of their headgroup, which affects the surfactant organization and, consequently, the hydrophobic character of the HNT lumen and the net charge [62]. In particular, it was noted that only the carboxylate group promotes the formation of organized structures, such as densely packed multilayers of sodium dodecanoate within the halloysite cavity, as seen from a correlation peak in SANS curves [62].

Finally, the solubilization capacity of these functionalized nanotubes toward hydrophobic compounds has been demonstrated. Accordingly, the surfactant/HNTs hybrids can be considered as inorganic micelles useful for the solubilization of pollutants and delivery of compounds from different origin [59,60,62]. As sketched in Fig. 4, surface tension experiments highlighted the removal capacity of sodium dodecanoate/HNTs composite towards n-decane. In particular the jump of surface tension to the value for pure water value indicates the oil removal from the interface. It should be noted that pristine HNT was not suitable for oil incorporation while the hydrophobization of the lumen allowed the solubilization of liquid n-decane.

Literature [63] reports a similar methodology where uniform and dispersed halloysite nanotubes were obtained using sodium dodecyl sulfate (SDS). The results indicated that SDS was adsorbed on the HNTs, which could enhance the dispersibility by the electrostatic effect; in fact, the zeta potential of dispersed HNTs became larger than that of the raw ones within the pH ranging from 2.5 to 11.9. The difference is higher under alkaline conditions, due to the adsorption of SDS molecules by electrostatic forces between surfactant molecules and HNTs, leading to ion exchange at the alumina surface [64]. It was also observed that there is no obvious difference between the zeta potential at different concentration of SDS (1.22 g/L and 1.48 g/L), which suggests that the well dispersion effect does not depend on the more content of dispersant confirming the saturation effect. Therefore, the zeta potential of SDS/HNTs is always more negative than HNTs, and the high zeta potential is a condition of good colloidal stability of SDS/HNTs.

It was found that also perfluoroalkylated anionic surfactants, when adsorbed at the inner surface, formed kinetically stable dispersions due to the enhanced electrostatic repulsions exercised between the particles and these systems can be used as non-foaming oxygen nanocontainers

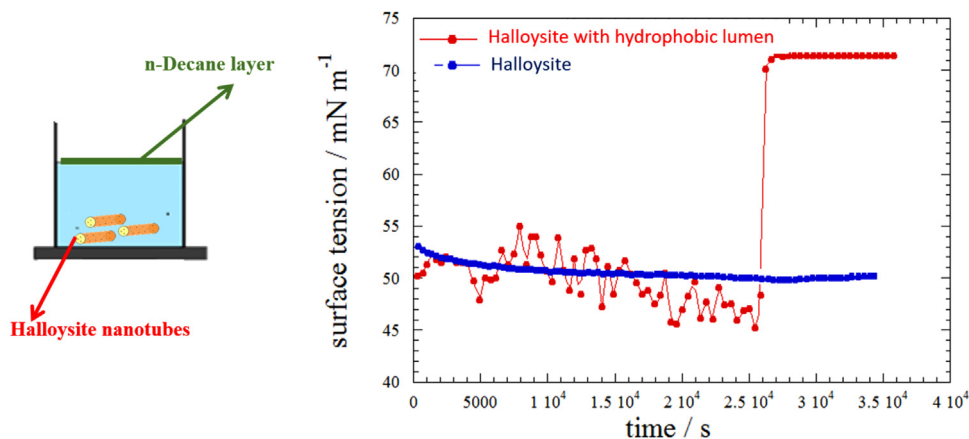


Fig. 4. Surface tension as a function of time for pristine halloysite and halloysite functionalized with sodium tetradecanoate dispersions in the presence of an n-Decane film on top of the aqueous phase. Adapted with permission from [60], copyright 2014 American Chemical Society.

in aqueous media [58]. Interestingly, the oxygen release from these hybrids can be tuned by specific external stimuli [58].

The determination of the translational diffusion coefficient and the charge of the hybrid materials showed that the concentration effect was negligible and the functionalized HNTs did not aggregate in water but they diffuse as single nanotubes [58]. To definitely rule out the presence of aggregates and to evidence eventual particle–particle interactions, the specific volume, the isentropic compressibility of HNT and HNT/surfactants dispersed in water and the pair interaction parameters were determined. Data reflected that the nanoparticle–nanoparticle electrostatic interactions are enhanced in the hybrid material in agreement with the ζ -potential results.

Above all, the sedimentation of the clay nanotubes assumes a crucial role in order to understand the colloidal stability and the sedimentation volume is a key parameter that, at least in water, is controlled by repulsive forces between particles [65]. For instance, the electrostatic repulsions are caused by the double layer surrounding each particle and by the particle charge. Therefore, if the particles repel to each other they remain independent until reaching the closest packing, which will represent the concentration in the sedimentation volume. If the particles do not strongly repel to each other, they are sticking together generating a smaller sedimentation volume [58]. The presence of anionic surfactants strongly affects the concentration of the sedimented phase, which corresponds to the critical value above which the dispersion is stable because the highest packing of the nanotubes is reached and shorter distances between the nanoparticles are hindered by the electrostatic repulsions.

As concerns the hybrid HNT/anionic surfactants, ζ -potential data evidenced an increase in the net charge and, therefore, the particle – particle repulsive interactions shift to longer range increasing the closest average distance between the functionalized nanoparticles. Moreover, it was revealed that each mole of adsorbed anionic surfactant neutralizes an equivalent number of positive charges of the inner lumen thus generating a linear increase in the net negative charge of HNT and therefore longer range interactions [61].

3.2. Cationic surfactant selective functionalization

Literature reports another easy strategy to obtain stable colloidal dispersions and it deals with the preparation of inorganic reverse micelles in non-aqueous media based on halloysite nanotubes and cationic surfactants, such as alkyltrimethylammonium bromides [66]. It is known that generally, a “reverse micelle” structure possesses a hydrophilic core and a hydrophobic shell that delineates a nanoscale droplet of aqueous phase from a nonpolar medium [67]. Because of their positive headgroup, the cationic surfactants are selectively adsorbed onto the HNTs external surface endowing to the formation of tubular nanoparticles with a hydrophobic shell and a hydrophilic cavity. The effect of the hydrophilic/hydrophobic balance on the properties of the obtained hybrid materials and their colloidal stability was studied in solvents with different polarity (water, 1-octanol, chloroform, and hexane) [66] (Fig. 5).

The first evidence is that the charge of the modified HNTs is strongly dependent on the hydrocarbon length chain of the surfactant. In particular, the ζ potential of the hybrids increases with the tails length of the adsorbed alkyltrimethylammonium bromide.

This allowed asserting that the enhancement of the surfactants hydrophobic character improves the adsorption efficiency due to stronger tail – tail hydrophobic interaction evidenced by FTIR [59] and, consequently, the neutralization of the HNTs negative sites thus determining an inversion of the HNTs charge. Dynamic Light Scattering in chloroform evidenced that the hybrid materials present a faster dynamic behavior compared to the pristine HNTs, in agreement with the enhancement of the repulsive interactions between the nanoparticles. In other words, the very large hydrodynamic radius value for pristine HNTs in chloroform indicates the aggregation of nanotubes in this

solvent whereas the presence of the surfactant confers hydrophobicity to the HNTs outer surface, and consequently, the colloidal stability of the nanotubes in nonpolar solvents is increased [66]. Briefly, the reported procedure allows to fabricate eocompatible reverse micelles with different dispersibility in organic solvents and tunable hydrophobic/hydrophilic interface that might be suitable for industrial or biological applications and to generate an aqueous nano-pool in organic media. Recently, this feature was used to confine hydrogel based on alginate inside the halloysite lumen generating a drug delivery system with sustained release sensitive to chemical stimuli (Fig. 6).

4. Effect of biopolymers on halloysite colloidal stability in water

Another promising strategy for the preparation of stable colloidal dispersions is represented by the adsorption of biopolymers via non-covalent interactions with a resulting improvement in the biocompatibility of HNTs.

It is reported a facile and green method for preparing a supramolecular complex of amylose and HNT in solid state using just mechanical force [68]. The wrapping of amylose onto the HNTs external surface induced the formation of modified nanotubes with a peculiar core-shell structure. The stability of HNTs and amylose-HNTs in DMSO/H₂O dispersions was studied for 24 h. Pure HNTs fastly precipitated due to the high density and the long tubular structure of halloysite [69] whereas the amylose-HNT dispersion showed an excellent stability being that any sedimentation was observed within 24 h. This behavior can be related to the high affinity between the polymer and the solvent mixture. Surprisingly, the stability of the hybrid system was maintained over a period of two weeks. This was probably dependent on the interaction between amylose and the outer surface of HNT [68].

Recent literature [70] reports studies on the adsorption of three biopolymers (anionic pectin, non-ionic hydroxypropyl cellulose HPC and cationic chitosan) onto halloysite nanotubes in water using isothermal titration calorimetry (ITC) to determine the thermodynamic parameters. ITC data show that the non-ionic HPC has the stronger tendency to adsorb onto halloysite surfaces while chitosan and pectin have a comparable affinity. Moreover, HPC presents the largest loading amount at saturation onto the nanotubes. The entropic contribution for the polymer adsorption is always negative demonstrating the loss of configuration freedom upon adsorption. In addition, the combination of turbidimetry and ζ -potential experiments provided the stability and the surface change properties of functionalized nanoparticles at two different pH values in order to understand the influence of the polymer and HNT charge density on the settling process of the nanotubes. Briefly, they found that the dispersion stability is dependent on particle dimensions, charge, viscosity of the medium, and interactions between components (HNTs/polymer). As expected, the addition of the nonionic HPC hardly alters the ζ -potential values and, on the other hand, the addition of charged biopolymers shifted the ζ -potential values toward negative and positive values for pectin and chitosan, respectively [70] (Fig. 7). Moreover, the changes induced in the ζ -potential values reflect the protonation equilibria of the biopolymer. Besides, HPC is the more efficient polymer in retarding the sedimentation. The ζ -potential trends for chitosan- and pectin-based mixtures show that an electrostatic mechanism of nanotube stabilization exists. As a general feature, chitosan is efficient in stabilizing HNT dispersions under acidic pH, whereas pectin is recommended for the same purpose at basic pH values. In particular, pectin should adsorb within the HNT lumen onto the positively charged surface of alumina, altering the overall HNT charge toward more negative values. The opposite occurs for chitosan, which is selectively adsorbed on the outer silica surface. HPC is in a stretched conformation at the interface, and therefore its adsorption could be considered very efficient in creating a steric barrier around the nanotubes against agglomeration and precipitations. Finally, the stability of the dispersions is controlled by the interactions (electrostatic and steric) between the dispersed particles [70].



Fig. 5. Scheme of HNTs functionalization with cationic surfactants (a) and partition of pristine and functionalized HNTs between the oil and the aqueous phases (b) adapted with permission from [66], copyright 2015 American Chemical Society.

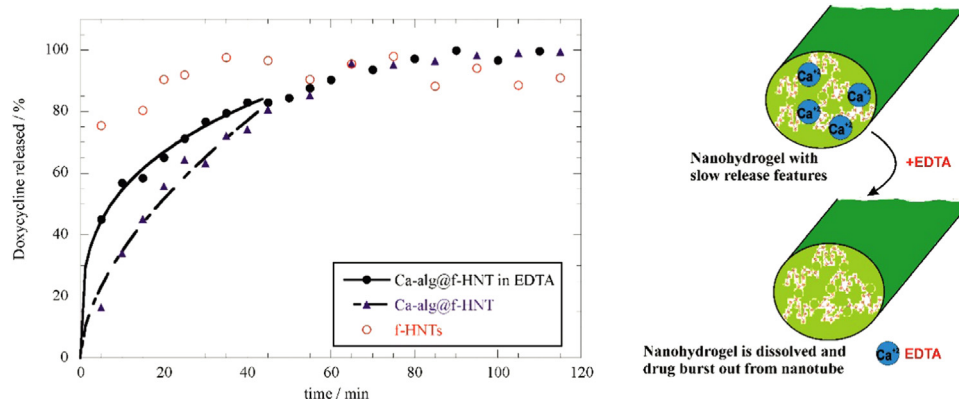


Fig. 6. Release profile of doxycycline from halloysite with hydrophobic shell, and confined hydrogel inside the halloysite lumen (Ca-alg@f-HNT) in water and in EDTA aqueous solution. Adapted with permission from [9], copyright 2018 American Chemical Society.

The biopolymer charge is also a key aspect in the thermal stability of dried nanocomposites [11]. As thermogravimetric analysis data show (Fig. 8), a peculiar effect in the high temperature range is observed. The mass lost at 700–800 °C are attributed to the dehydroxylation of alumina groups of HNT. DTG thermoanalytical curve of alginate/HNT does not show the dehydroxylation process in agreement with the idea that ionic exchange involving alginate COO⁻ groups and Al-OH groups generates significant structural changes that cancels out the signal. The positively charged chitosan and non-ionic polymer did not show such a peculiarity. These results confirm that thermogravimetric analysis is a powerful tool in the investigation of thermal response, ie temperature delay of decomposition for composite materials [68–71].

Besides bio-derived macromolecules, the effect onto the colloidal stability has been studied also taking into account the functionalization with other types of polymers, for example the temperature responsive poly(N-isopropylacrylamide) [72,73]. Meanwhile PNIPAAm was grafted onto the external surface of modified HNT-NH₂ by an amine bond, it was found that PNIPAAm-NH₂ selectively adsorb onto the external surface by exploiting electrostatic interactions at pH = 6. More interestingly the physico-chemical properties of the modified nanotubes in the polymer/HNT are deeply changed in comparison with the pristine nanoclay, thus evidencing a transferring of the thermo-responsiveness

from polymers to halloysite in the hybrid system [72]. Since the dispersion are stable under the Lower critical solution temperature (LCST) and unstable above it, this allowed to prepare very versatile systems where the temperature of the colloidal stability can be controlled in order to have external-stimuli triggering solubilization and delivery of hydrophobic compounds. The PNIPAAm/HNT system was loaded with curcumin providing a biocompatible and thermosensitive system for targeted release of active species in the intestine [73].

Lee et al. [74] reported the synthesis of HNT-based supramolecular complexes by the wrapping of DNA to the surface of halloysite. It is observed that pristine HNTs are insoluble in water, but they become highly water dispersible after interacting with DNA. It is reported that the interaction between DNA and HNTs induces a reorientation of the phosphate groups in DNA and an association of the phosphates in DNA with the outer surface of the nanotubes, which is composed of silica. Thus, π - π interaction is supposed to be a critical force to determine the interaction between DNA and the outer surface of HNTs [74]. Most likely, this interpretation should be revised being that the enhanced colloidal stability is due to the neutralization of the inner positive charge that drives to an increase of the total net negative ζ -potential enhancing the particle – particle repulsions.

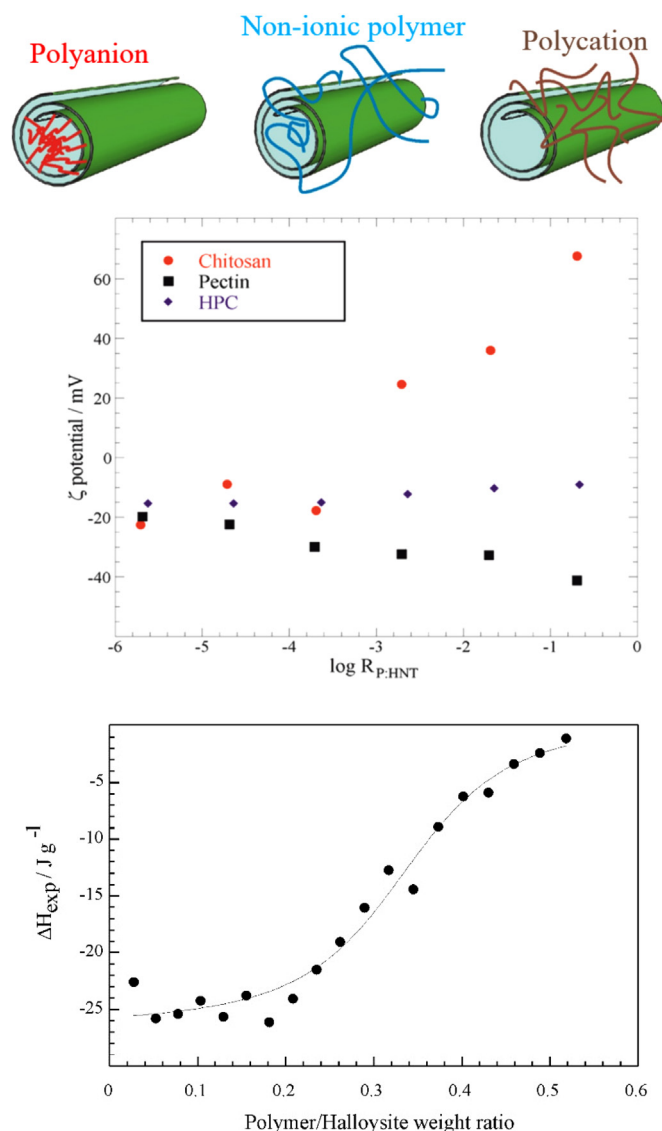


Fig. 7. Top: Scheme of adsorption site based on electrostatic interactions between polymers and halloysite surfaces and ζ -Potential values for HNT/biopolymers dispersions as a function of the polymer/halloysite weight ratio. Bottom: ITC curve for HPC titration into HNTs dispersion. Adapted with permission from [70] copyright 2015 American Chemical Society.

5. Pickering emulsion

Emulsions are dispersions of one liquid in another immiscible liquid in the form of small droplets. Typically, these systems are stabilized by the addition of emulsifiers that can be either surfactants, or solid particles. For instance it is known that interfacially-active solid particles can act as emulsifiers for stabilizing oil-in-water, as reported by the pioneering studies of Ramsden and Pickering [75], from which the name derives. In recent years, several experimental and theoretical studies have been carried out on solids-stabilized emulsions to understand the factors that affect the stability and the structure of the interface [76,77] for application in food and materials science.

Owoseni et al. [78] reported the halloysite effect in stabilizing oil-in-water emulsions. On this basis, HNTs can be considered as interfacially-active vehicles for delivering oil spill treatment. They evidenced that the increase of HNTs concentration leads to the formation of more stable emulsions. The formation of a rigid and protective interfacial film by the adsorption of HNTs at the oil–water interface provides steric hindrance to drop coalescence [79] (Fig. 9). Since

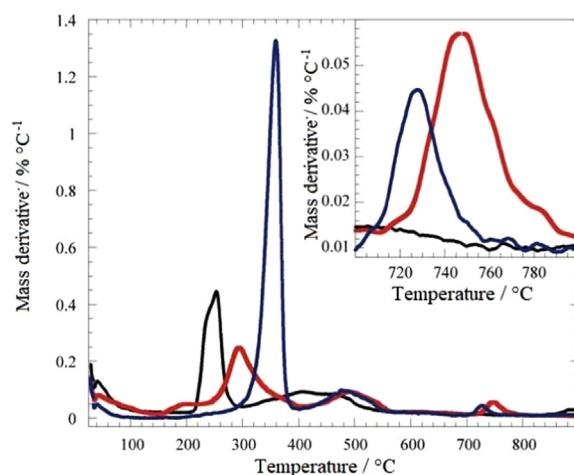


Fig. 8. DTG curves of the polymers (blue for methylcellulose, black for alginate, red for chitosan) containing 50 wt% of HNT. Adapted with permission from [11] copyright 2016 American Chemical Society. (For interpretation of the references to color in this figure legend, the reader is referred to the web version of this article.)

surfactants and interfacially-active particles can act synergistically to stabilize the emulsion, HNT were loaded and it was observed that the adsorption of surfactant molecules at the emulsions interface serves to lower the interfacial tension while the adsorption of particles provides a steric barrier to drop coalescence [78,80].

Similar observations were found by von Klitzing et al [81]. They prepared hydrophobized halloysite nanotubes for model petroleum and dodecene emulsification demonstrating the suitability of these systems for catalysis. They observed that an increase in halloysite concentration drives to denser packing at the oil/water interface, which stabilizes the droplets against coalescence allowing their architectural control. The oil-in-water emulsions allowed an efficient hydroformylation reaction using an aqueous Rh-catalyst. This gave efficient dodecene conversion to tridecanal with a simple aqueous catalyst separation from the product [81].

Besides, these systems were studied also for oil spill bioremediation exploiting the bacterial proliferation on HNTs [82]. It was observed that the oil/water interface is roughened and the oil degrading microorganisms are linked to these oil droplets better than to the ones without halloysite. The presence of halloysite enhances the metabolic activity demonstrating that HNTs-based dispersant systems are environmentally friendly and promising formulations to achieve ‘bioremediation’ through degradation of spilled crude oil [82].

6. Conclusions and perspectives

In this review, we summarized the current strategies that are followed in order to create stable colloidal dispersions of halloysite clay nanotubes. In particular, they range from their own liquid crystalline behavior in water to the selective functionalization of inner/outer surface by using differently charged molecules such as surfactants, polymers, biopolymers. Several advantages rise up from these methods, such as the possibility to obtain highly stable systems, reverse micelles, Pickering emulsions that can be applied for pollutants removal, oil spill, catalysis and controlled drug release.

Moreover, it is well known that the sample of halloysite could contain impurities (kaolinite above all) and could present high polydispersity in sizes. In this regards, this review represents a relevant background for designing separation and purification routes. In fact, one of the crucial challenges for further research in halloysite could be the “selective sedimentation” of nanoparticles of different length/radius in order to obtain halloysite samples with a reduced polydispersion

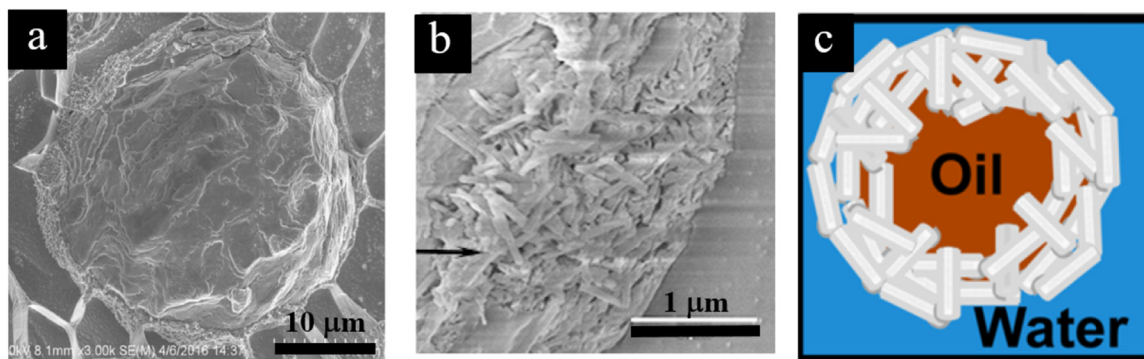


Fig. 9. Cryo-SEM images of HNT emulsions with oil showing halloysite on oil-water interface (a, b) adapted with permission from [82] copyright 2018 Elsevier and (c), scheme of the Pickering emulsion droplet adapted with permission from [78] copyright 2014 American Chemical Society.

degree.

Acknowledgments

The authors acknowledge University of Palermo for financial support.

Conflicts of interest

The authors declare that they have no conflicts of interest to this work.





References

- [1] G. Lazzara, G. Cavallaro, A. Panchal, R. Fakhrullin, A. Stavitskaya, V. Vinokurov, Y. Lvov, An assembly of organic-inorganic composites using halloysite clay nanotubes, *Curr. Opin. Colloid Interface Sci.* 35 (2018) 42–50, <https://doi.org/10.1016/j.cocis.2018.01.002>.
- [2] G. Cavallaro, L. Chiappisi, P. Pasbakhsh, M. Gradzielski, G. Lazzara, A structural comparison of halloysite nanotubes of different origin by small-angle neutron scattering (SANS) and electric birefringence, *Appl. Clay Sci.* 160 (2018) 71–80, <https://doi.org/10.1016/j.clay.2017.12.044>.
- [3] Y. Lvov, W. Wang, L. Zhang, R. Fakhrullin, Halloysite clay nanotubes for loading and sustained release of functional compounds, *Adv. Mater.* 28 (2016) 1227–1250, <https://doi.org/10.1002/adma.201502341>.
- [4] M. Massaro, G. Lazzara, S. Milioto, R. Noto, S. Riela, Covalently modified halloysite clay nanotubes: synthesis, properties, biological and medical applications, *J. Mater. Chem. B* 5 (2017) 2867–2882, <https://doi.org/10.1039/C7TB00316A>.
- [5] Y.M. Lvov, M.M. DeVilliers, R.F. Fakhrullin, The application of halloysite tubule nanoclay in drug delivery, *Expert Opin. Drug Deliv.* 13 (2016) 977–986, <https://doi.org/10.1517/17425247.2016.1169271>.
- [6] R.F. Fakhrullin, Y.M. Lvov, Halloysite clay nanotubes for tissue engineering, *NanoMed* 11 (2016) 2243–2246, <https://doi.org/10.2217/nmm-2016-0250>.
- [7] M. Liu, Y. Zhang, C. Wu, S. Xiong, C. Zhou, Chitosan/halloysite nanotubes bionanocomposites: structure, mechanical properties and biocompatibility, *Int. J. Biol. Macromol.* 51 (2012) 566–575, <https://doi.org/10.1016/j.ijbiomac.2012.06.022>.
- [8] M. Liu, C. Wu, Y. Jiao, S. Xiong, C. Zhou, Chitosan-halloysite nanotubes nanocomposite scaffolds for tissue engineering, *J. Mater. Chem. B* 1 (2013) 2078–2089, <https://doi.org/10.1039/C3TB20084A>.
- [9] G. Cavallaro, G. Lazzara, S. Milioto, F. Parisi, V. Evtugyn, E. Rozhina, R. Fakhrullin, Nanohydrogel formation within the halloysite lumen for triggered and sustained release, *ACS Appl. Mater. Interfaces* 10 (2018) 8265–8273, <https://doi.org/10.1021/acsami.7b19361>.
- [10] G. Biddeci, G. Cavallaro, F. Di Blasi, G. Lazzara, M. Massaro, S. Milioto, F. Parisi, S. Riela, G. Spinelli, Halloysite nanotubes loaded with peppermint essential oil as filler for functional biopolymer film, *Carbohydr. Polym.* 152 (2016) 548–557, <https://doi.org/10.1016/j.carbpol.2016.07.041>.
- [11] V. Bertolino, G. Cavallaro, G. Lazzara, M. Merli, S. Milioto, F. Parisi, L. Sciascia, Effect of the biopolymer charge and the nanoclay morphology on nanocomposite materials, *Ind. Eng. Chem. Res.* 55 (2016) 7373–7380, <https://doi.org/10.1021/acs.iecr.6b01816>.
- [12] G. Gorrasi, R. Pantani, M. Murariu, P. Dubois, PLA/halloysite nanocomposite films: water vapor barrier properties and specific key characteristics, *Macromol. Mater. Eng.* 299 (2014) 104–115, <https://doi.org/10.1002/mame.201200424>.
- [13] Y. Zhao, E. Abdullayev, A. Vasiliev, Y. Lvov, Halloysite nanotubule clay for efficient water purification, *J. Colloid Interface Sci.* 406 (2013) 121–129, <https://doi.org/10.1016/j.jcis.2013.05.072>.
- [14] G. Cavallaro, A.A. Danilushkina, V.G. Evtugyn, G. Lazzara, S. Milioto, F. Parisi, E.V. Rozhina, R.F. Fakhrullin, Halloysite nanotubes: controlled access and release by smart gates, *Nanomaterials* 7 (2017) 199, <https://doi.org/10.3390/nano7080199>.
- [15] G. Cavallaro, G. Lazzara, S. Milioto, F. Parisi, F. Ruisi, Nanocomposites based on esterified colophony and halloysite clay nanotubes as consolidants for waterlogged archaeological woods, *Cellulose* 24 (2017) 3367–3376, <https://doi.org/10.1007/s10570-017-1369-8>.
- [16] G. Cavallaro, G. Lazzara, S. Milioto, F. Parisi, V. Sparacino, Thermal and dynamic mechanical properties of beeswax-halloysite nanocomposites for consolidating waterlogged archaeological woods, *Polym. Degrad. Stab.* 120 (2015) 220–225, <https://doi.org/10.1016/j.polymdegradstab.2015.07.007>.
- [17] G. Cavallaro, G. Lazzara, S. Milioto, F. Parisi, Halloysite nanotubes as sustainable nanofiller for paper consolidation and protection, *J. Therm. Anal. Calorim.* 117 (2014) 1293–1298, <https://doi.org/10.1007/s10973-014-3865-5>.
- [18] M. Makaremi, P. Pasbakhsh, G. Cavallaro, G. Lazzara, Y.K. Aw, S.M. Lee, S. Milioto, Effect of morphology and size of halloysite nanotubes on functional pectin bionanocomposites for food packaging applications, *ACS Appl. Mater. Interfaces* 9 (2017) 17476–17488, <https://doi.org/10.1021/acsami.7b04297>.
- [19] G. Gorrasi, Dispersion of halloysite loaded with natural antimicrobials into pectins: characterization and controlled release analysis, *Carbohydr. Polym.* 127 (2015) 47–53, <https://doi.org/10.1016/j.carbpol.2015.03.050>.
- [20] G. Cavallaro, G. Lazzara, S. Milioto, Aqueous phase/nanoparticles interface: hydroxypropyl cellulose adsorption and desorption triggered by temperature and inorganic salts, *Soft Matter* 8 (2012) 3627–3633, <https://doi.org/10.1039/C2SM07021A>.
- [21] R. De Lisi, M. Gradzielski, G. Lazzara, S. Milioto, N. Muratore, S. Prévost, Aqueous laponite clay dispersions in the presence of poly(ethylene oxide) or poly(propylene oxide) oligomers and their triblock copolymers, *J. Phys. Chem. B* 112 (2008) 9328–9336, <https://doi.org/10.1021/jp8024073>.
- [22] S. Iijima, Helical microtubules of graphitic carbon, *Nature* 354 (1991) 56.
- [23] J. Sun, J. Wang, Z. Li, Z. Yang, S. Yang, Controllable synthesis of 3D hierarchical bismuth compounds with good electrochemical performance for advanced energy storage devices, *RSC Adv.* 5 (2015) 51773–51778, <https://doi.org/10.1039/C5RA09760F>.
- [24] G. Yang, X. Yang, C. Yang, Y. Yang, A reagentless amperometric immunosensor for human chorionic gonadotropin based on a gold nanotube arrays electrode, *Colloids Surf. Physicochem. Eng. Asp.* 389 (2011) 195–200, <https://doi.org/10.1016/j.colsurfa.2011.08.027>.
- [25] Y. Lai, Y. Huang, H. Wang, J. Huang, Z. Chen, C. Lin, Selective formation of ordered arrays of octacalcium phosphate ribbons on TiO₂ nanotube surface by template-assisted electrodeposition, *Colloids Surf. B Biointerfaces* 76 (2010) 117–122, <https://doi.org/10.1016/j.colsurfb.2009.10.023>.
- [26] S. Xu, J. Ng, X. Zhang, H. Bai, D.D. Sun, Adsorption and photocatalytic degradation of Acid Orange 7 over hydrothermally synthesized mesoporous TiO₂ nanotube, *Colloids Surf. Physicochem. Eng. Asp.* 379 (2011) 169–175, <https://doi.org/10.1016/j.colsurfa.2010.11.032>.
- [27] W.L. Zhang, H.J. Choi, Fabrication of semiconducting polyaniline-wrapped halloysite nanotube composite and its electrorheology, *Colloid Polym. Sci.* 290 (2012) 1743–1748, <https://doi.org/10.1007/s00396-012-2719-6>.
- [28] M. Emanet, R. Fakhrullin, M. Çulha, Boron nitride nanotubes and layer-by-layer polyelectrolyte coating for yeast cell surface engineering, *ChemNanoMat* 2 (2016) 426–429, <https://doi.org/10.1002/cnma.201600044>.
- [29] S. Kalay, Y. Stetsyshyn, V. Lobaz, K. Harhay, H. Ohar, M. Çulha, Water-dispersed thermo-responsive boron nitride nanotubes: synthesis and properties, *Nanotechnology* 27 (2016) 035703.
- [30] F. Ferrante, R. Amratta, G. Lazzara, Modeling of the halloysite spiral nanotube, *J. Phys. Chem. C* 119 (2015) 16700–16707, <https://doi.org/10.1021/acs.jpcc.5b04281>.
- [31] P. Pasbakhsh, G.J. Churchman, J.L. Keeling, Characterisation of properties of various halloysites relevant to their use as nanotubes and microfibre fillers, *Appl. Clay Sci.* 74 (2013) 47–57, <https://doi.org/10.1016/j.clay.2012.06.014>.
- [32] Y. Yang, Y. Chen, F. Leng, L. Huang, Z. Wang, W. Tian, Recent advances on surface modification of halloysite nanotubes for multifunctional applications, *Appl. Sci.* 7 (2017), <https://doi.org/10.3390/app7121215>.
- [33] M. Massaro, R. Amorati, G. Cavallaro, S. Guernelli, G. Lazzara, S. Milioto, R. Noto, P. Poma, S. Riela, Direct chemical grafted curcumin on halloysite nanotubes as

- dual-responsive prodrug for pharmacological applications, *Colloids Surf. B Biointerfaces* 140 (2016) 505–513, <https://doi.org/10.1016/j.colsurfb.2016.01.025>.
- [34] R.L. Frost, H.F. Shurvell, Raman microprobe spectroscopy of halloysite, *Clays Clay Miner.* 45 (1997) 68.
- [35] M. Kryuchkova, A. Danilushkina, Y. Lvov, R. Fakhruullin, Evaluation of toxicity of nanoclays and graphene oxide in vivo: a *Paramecium caudatum* study, *Environ. Sci. Nano* 3 (2016) 442–452, <https://doi.org/10.1039/C5EN00201J>.
- [36] G.I. Fakhruullina, F.S. Akhatova, Y.M. Lvov, R.F. Fakhruullin, Toxicity of halloysite clay nanotubes in vivo: a *Caenorhabditis elegans* study, *Environ. Sci. Nano* 2 (2015) 54–59, <https://doi.org/10.1039/C4EN00135D>.
- [37] Y. Lvov, E. Abdullayev, Functional polymer–clay nanotube composites with sustained release of chemical agents, *Prog. Polym. Sci.* 38 (2013) 1690–1719, <https://doi.org/10.1016/j.progpolymsci.2013.05.009>.
- [38] G. Cavallaro, G. Lazzara, S. Milioto, Dispersions of nanoclays of different shapes into aqueous and solid biopolymeric matrices. extended physicochemical study, *Langmuir* 27 (2011) 1158–1167, <https://doi.org/10.1021/la103487a>.
- [39] E. Abdullayev, K. Sakakibara, K. Okamoto, W. Wei, K. Ariga, Y. Lvov, Natural tube clay template synthesis of silver nanorods for antibacterial composite coating, *ACS Appl. Mater. Interfaces* 3 (2011) 4040–4046, <https://doi.org/10.1021/am200896d>.
- [40] Y. Zhang, H. Yang, Co3O4 nanoparticles on the surface of halloysite nanotubes, *Phys. Chem. Miner.* 39 (2012) 789–795, <https://doi.org/10.1007/s00269-012-0533-9>.
- [41] Y. Liu, J. Zhang, H. Guan, Y. Zhao, J.-H. Yang, B. Zhang, Preparation of bimetallic Cu-Co nanocatalysts on poly (diallyldimethylammonium chloride) functionalized halloysite nanotubes for hydrolytic dehydrogenation of ammonia borane, *Appl. Surf. Sci.* 427 (2018) 106–113, <https://doi.org/10.1016/j.apsusc.2017.08.171>.
- [42] Y. Liu, H. Guan, J. Zhang, Y. Zhao, J.-H. Yang, B. Zhang, Polydopamine-coated halloysite nanotubes supported AgPd nanoalloy: an efficient catalyst for hydrolysis of ammonia borane, *Int. J. Hydrog. Energy* 43 (2018) 2754–2762, <https://doi.org/10.1016/j.ijhydene.2017.12.105>.
- [43] Y. Zhao, W. Kong, Z. Jin, Y. Fu, W. Wang, Y. Zhang, J. Liu, B. Zhang, Storing solar energy within Ag-Paraffin@Halloysite microspheres as a novel self-heating catalyst, *Appl. Energy* 222 (2018) 180–188, <https://doi.org/10.1016/j.apenergy.2018.04.013>.
- [44] S. Sadjadi, M.M. Heravi, M. Malmir, Pd@HNTs-CDNS-g-C3N4: a novel heterogeneous catalyst for promoting ligand and copper-free Sonogashira and Heck coupling reactions, benefits from halloysite and cyclodextrin chemistry and g-C3N4 contribution to suppress Pd leaching, *Carbohydr. Polym.* 186 (2018) 25–34, <https://doi.org/10.1016/j.carbpol.2018.01.023>.
- [45] V.A. Vinokurov, A.V. Stavitskaya, Y.A. Chudakov, E.V. Ivanov, L.K. Shrestha, K. Ariga, Y.A. Darrat, Y.M. Lvov, Formation of metal clusters in halloysite clay nanotubes, *Sci. Technol. Adv. Mater.* 18 (2017) 147–151, <https://doi.org/10.1080/14686996.2016.1278352>.
- [46] M. Du, B. Guo, D. Jia, Newly emerging applications of halloysite nanotubes: a review, *Polym. Int.* 59 (2010) 574–582.
- [47] N.G. Veerabadran, D. Mongayt, V. Torchilin, R.R. Price, Y.M. Lvov, Organized shells on clay nanotubes for controlled release of macromolecules, *Macromol. Rapid Commun.* 30 (2009) 99–103, <https://doi.org/10.1002/marc.200800510>.
- [48] M.R. Dzumukova, E.A. Naumenko, Y.M. Lvov, R.F. Fakhruullin, Enzyme-activated intracellular drug delivery with tubule clay nanoformulation, *Sci. Rep.* 5 (2015) 10560.
- [49] W. Wei, R. Minullina, E. Abdullayev, R. Fakhruullin, D. Mills, Y. Lvov, Enhanced efficiency of antiseptics with sustained release from clay nanotubes, *RSC Adv.* 4 (2014) 488–494, <https://doi.org/10.1039/C3RA45011B>.
- [50] W. Song, I.A. Kinloch, A.H. Windle, Nematic liquid crystallinity of multiwall carbon nanotubes, *Science* 302 (2003), <https://doi.org/10.1126/science.1089764> 1363–1363.
- [51] F. Tardani, L. Gentile, G.A. Ranieri, C. La Mesa, Shear orientation in nematic carbon nanotube dispersions: a combined NMR investigation, *J. Phys. Chem. C* 117 (2013) 8556–8562, <https://doi.org/10.1021/jp4015349>.
- [52] R. Wang, J. Sun, L. Gao, Liquid-crystal phase reinforced carbon nanotube fibers, *J. Phys. Chem. C* 114 (2010) 4923–4928, <https://doi.org/10.1021/jp100108m>.
- [53] Z. Xu, C. Gao, Aqueous liquid crystals of graphene oxide, *ACS Nano* 5 (2011) 2908–2915, <https://doi.org/10.1021/nn200069w>.
- [54] Z. Xu, C. Gao, Graphene chiral liquid crystals and macroscopic assembled fibres, *Nat. Commun.* 2 (2011) 571.
- [55] Y. Habibi, L.A. Lucia, O.J. Rojas, Cellulose nanocrystals: chemistry, self-assembly, and applications, *Chem. Rev.* 110 (2010) 3479–3500, <https://doi.org/10.1021/cr900339w>.
- [56] Z. Luo, H. Song, X. Feng, M. Run, H. Cui, L. Wu, J. Gao, Z. Wang, Liquid crystalline phase behavior and sol–gel transition in aqueous halloysite nanotube dispersions, *Langmuir* 29 (2013) 12358–12366, <https://doi.org/10.1021/la402836d>.
- [57] I. McDowall, W. Vose, Sedimentation of halloysite, *Nature* 170 (1952), <https://doi.org/10.1038/170368a0> 368–368.
- [58] G. Cavallaro, G. Lazzara, S. Milioto, G. Palmisano, F. Parisi, Halloysite nanotube with fluorinated lumen: non-foaming nanocontainer for storage and controlled release of oxygen in aqueous media, *J. Colloid Interface Sci.* 417 (2014) 66–71, <https://doi.org/10.1016/j.jcis.2013.11.026>.
- [59] G. Cavallaro, G. Lazzara, S. Milioto, Exploiting the colloidal stability and solubilization ability of clay nanotubes/ionic surfactant hybrid nanomaterials, *J. Phys. Chem. C* 116 (2012) 21932–21938, <https://doi.org/10.1021/jp307961q>.
- [60] G. Cavallaro, G. Lazzara, S. Milioto, F. Parisi, V. Sanzillo, Modified halloysite nanotubes: nanoarchitectures for enhancing the capture of oils from vapor and liquid phases, *ACS Appl. Mater. Interfaces* 6 (2014) 606–612, <https://doi.org/10.1021/am404693r>.
- [61] B.V. Derjaguin, L.D. Landau, Theory of the stability of strongly charged lyophobic sols and of the adhesion of strongly charged particles in solutions of electrolytes, *Acta Physicochim.* 14 (1941) 733–762.
- [62] G. Cavallaro, I. Grillo, M. Gradzielski, G. Lazzara, Structure of hybrid materials based on halloysite nanotubes filled with anionic surfactants, *J. Phys. Chem. C* 120 (2016) 13492–13502, <https://doi.org/10.1021/acs.jpcc.6b01282>.
- [63] H. Lum, J. Ouyang, H. Yang, Enhancing dispersion of halloysite nanotubes via chemical modification, *Phys. Chem. Miner.* 41 (2014) 281–288, <https://doi.org/10.1007/s00269-013-0646-9>.
- [64] C. Aguzzi, P. Cerezo, C. Viseras, C. Caramella, Use of clays as drug delivery systems: possibilities and limitations, *Appl. Clay Sci.* 36 (2007) 22–36, <https://doi.org/10.1016/j.clay.2006.06.015>.
- [65] H. Freundlich, A.D. Jones, Sedimentation volume, dilatancy, thixotropic and plastic properties of concentrated suspensions, *J. Phys. Chem.* 40 (1935) 1217–1236, <https://doi.org/10.1021/j150378a012>.
- [66] G. Cavallaro, G. Lazzara, S. Milioto, F. Parisi, Hydrophobically modified halloysite nanotubes as reverse micelles for water-in-oil emulsion, *Langmuir* 31 (2015) 7472–7478, <https://doi.org/10.1021/acs.langmuir.5b01181>.
- [67] N.M. Correa, J.J. Silber, R.E. Riter, N.E. Levinger, Nonaqueous polar solvents in reverse micelle systems, *Chem. Rev.* 112 (2012) 4569–4602, <https://doi.org/10.1021/cr200254q>.
- [68] P.R. Chang, Y. Xie, D. Wu, X. Ma, Amylose wrapped halloysite nanotubes, *Carbohydr. Polym.* 84 (2011) 1426–1429, <https://doi.org/10.1016/j.carbpol.2011.01.038>.
- [69] M.H. Shamsi, D.V. Geckeler, The first biopolymer-wrapped non-carbon nanotubes, *Nanotechnology* 19 (2008) 075604.
- [70] V. Bertolino, G. Cavallaro, G. Lazzara, S. Milioto, F. Parisi, Biopolymer-targeted adsorption onto halloysite nanotubes in aqueous media, *Langmuir* 33 (2017) 3317–3323, <https://doi.org/10.1021/acs.langmuir.7b00600>.
- [71] A. Rotaru, I. Nicolaescu, P. Rotaru, C. Neaga, Thermal characterization of humic acids and other components of raw coal, *J. Therm. Anal. Calorim.* 92 (2008) 297–300, <https://doi.org/10.1007/s10973-007-8816-y>.
- [72] G. Cavallaro, G. Lazzara, S. Milioto, F. Parisi, Steric stabilization of modified nanoclays triggered by temperature, *J. Colloid Interface Sci.* 461 (2016) 346–351, <https://doi.org/10.1016/j.jcis.2015.09.046>.
- [73] G. Cavallaro, G. Lazzara, M. Massaro, S. Milioto, R. Noto, F. Parisi, S. Riela, Biocompatible poly(*n*-isopropylacrylamide)-halloysite nanotubes for thermo-responsive curcumin release, *J. Phys. Chem. C* 119 (2015) 8944–8951, <https://doi.org/10.1021/acs.jpcc.5b00991>.
- [74] Y. Lee, G.-E. Jung, S.J. Cho, K.E. Geckeler, H. Fuchs, Cellular interactions of doxorubicin-loaded DNA-modified halloysite nanotubes, *Nanoscale* (2013), <https://doi.org/10.1039/C3NR02665E>.
- [75] S.U. Pickering, CXCVI. Emulsions, *J. Chem. Soc. Trans.* 91 (1907) 2001–2021, <https://doi.org/10.1039/CT9079102001>.
- [76] B.P. Binks, S.O. Lumsdon, Influence of particle wettability on the type and stability of surfactant-free emulsions, *Langmuir* 16 (2000) 8622–8631, <https://doi.org/10.1021/la000189s>.
- [77] D.R. Ingram, C. Kotsmar, K.Y. Yoon, S. Shao, C. Huh, S.L. Bryant, T.E. Milner, K.P. Johnston, Superparamagnetic nanoclusters coated with oleic acid bilayers for stabilization of emulsions of water and oil at low concentration, *J. Colloid Interface Sci.* 351 (2010) 225–232, <https://doi.org/10.1016/j.jcis.2010.06.048>.
- [78] O. Owoseni, E. Nyankson, Y. Zhang, S.J. Adams, J. He, G.L. McPherson, A. Bose, R.B. Gupta, V.T. John, Release of surfactant cargo from interfacially-active halloysite clay nanotubes for oil spill remediation, *Langmuir* 30 (2014) 13533–13541, <https://doi.org/10.1021/la503687b>.
- [79] D.E. Tambe, M.M. Sharma, Factors controlling the stability of colloid-stabilized emulsions: I. An experimental investigation, *J. Colloid Interface Sci.* 157 (1993) 244–253, <https://doi.org/10.1006/jcis.1993.1182>.
- [80] R. Aveyard, B.P. Binks, J.H. Clint, Emulsions stabilised solely by colloidal particles, *Adv. Colloid Interface Sci.* 100–102 (2003) 503–546, [https://doi.org/10.1016/S0001-8686\(02\)00069-6](https://doi.org/10.1016/S0001-8686(02)00069-6).
- [81] R. von Klitzing, D. Stehl, T. Pogrzeba, R. Schomäcker, R. Minullina, A. Panchal, S. Konnova, R. Fakhruullin, J. Koetz, H. Möhwald, Y. Lvov, Halloysites stabilized emulsions for hydroformylation of long chain olefins, *Adv. Mater. Interfaces* (2016), <https://doi.org/10.1002/admi.201600435> 1600435-n/a.
- [82] A. Panchal, L.T. Swientoniewski, M. Omarova, T. Yu, D. Zhang, D.A. Blake, V. John, Y.M. Lvov, Bacterial proliferation on clay nanotube pickering emulsions for oil spill bioremediation, *Colloids Surf. B Biointerfaces* 164 (2018) 27–33, <https://doi.org/10.1016/j.colsurfb.2018.01.021>.

Review

Stability of Halloysite, Imogolite, and Boron Nitride Nanotubes in Solvent Media

Lorenzo Lisuzzo ¹ , Giuseppe Cavallaro ¹, Giuseppe Lazzara ^{1,*} , Stefana Milioto ¹,
Filippo Parisi ¹  and Yuriy Stetsyshyn ² 

¹ Dipartimento di Fisica e Chimica, Università degli Studi di Palermo, 90128 Palermo, Italy; lorenzo.lisuzzo@unipa.it (L.L.); giuseppe.cavallaro@unipa.it (G.C); stefana.milioto@unipa.it (S.M.); filippo.pariasi@unipa.it (F.P.)

² Department of Organic Chemistry, Lviv Polytechnic National University, 79013 Lviv, Ukraine; yrstecushun@ukr.net

* Correspondence: giuseppe.lazzara@unipa.it; Tel.: +39 09123897962

Received: 28 May 2018; Accepted: 27 June 2018; Published: 30 June 2018



Featured Application: The review is focused on the stabilization of nanotubular materials in solvent media. This aspect is a key starting point for any application of nanotube-based formulations for pharmaceutical and industrial applications.

Abstract: Inorganic nanotubes are attracting the interest of many scientists and researchers, due to their excellent application potential in different fields. Among them, halloysite and imogolite, two naturally-occurring aluminosilicate mineral clays, as well as boron nitride nanotubes have gained attention for their proper shapes and features. Above all, it is important to reach highly stable dispersion in water or organic media, in order to exploit the features of this kind of nanoparticles and to expand their applications. This review is focused on the structural and morphological features, performances, and ratios of inorganic nanotubes, considering the main strategies to prepare homogeneous colloidal suspensions in various solvent media as special focus and crucial point for their uses as nanomaterials.

Keywords: colloidal stability; nanoparticle dispersion; halloysite; imogolite; boron nitrides; nanotubes

1. Introduction

Since carbon nanotubes were discovered in 1991 [1], the nanotube structure has garnered interest and has been widely researched in other types of particles, like metal nanotubes [2,3], oxide nanotubes [4,5], boron nitride nanotubes [6,7] and nanotubular clays, to study the characteristics of tunable chemistry, surface area, and porosity.

The need to reach homogeneous particles dispersion in different solvent media represents one of the main conditions for the use and applicability of those systems [8]. With this aim, this review will be focused on the colloidal stability of inorganic nanotubes, as well as on the most used strategies to prepare well-dispersed suspensions. In particular, these aspects will be investigated for halloysite nanotubes (HNTs) [8], imogolite nanotubes (INTs) [9], and boron nitride nanotubes (BNNTs) [10].

Halloysite nanotubes are composed of a silicon oxygen tetrahedron and alumina oxygen octahedrons forming a kaolinite-like sheet that rolls up, giving the clay its own hollow tubular structure (Figure 1a) [11,12]. Since the lumen and the external surface are chemically different, they are positive and negative in water, respectively, in the 2–8 pH range [13]. HNT size varies with respect to the natural origin, ranging from 0.5 to 1.5 μm in length, within 50–70 nm for the outer nanotube diameter

and 10–20 nm for the internal diameter [14]. Moreover, they have biocompatibility [15] and show no toxicity in vivo [16] and in vitro [17]. These characteristics make HNTs excellent smart materials for the most diverse applications—for example: food packaging [18–20], drug delivery [21–26], environment remediation and wastewater treatment [27], cultural heritage [28–32], and additives for enhancing the performances of polymers [14,33].

Imogolite, firstly observed in volcanic soils, is another natural aluminosilicate whose shape is nanotubular, with an external diameter of about 2 nm; its length can be expressed in micrometers [34]. INTs are always arranged into bundles, so it is not possible to observe a single nanotube, but rather a network of bundles (Figure 1b) [35]. Their structure, proposed by Cradwick in 1972, is very similar to halloysite, namely a layer of orthosilicate tetrahedra overlapping a layer with an aluminum in a dioctahedral configuration [36]. INTs are considered the clay counterpart of carbon nanotubes, and they are very similar if dimensions, aspect ratios, and rigidity are considered [9]. Moreover, imogolite nanotubes are easily synthesized using hydrothermal techniques, without purification steps to do post-synthesis, and they form stable colloidal suspensions in aqueous solvents [34,37].

The good monodispersity of INTs has motivated researchers to investigate their formation process. Preparation routes for imogolite were developed very quickly. For instance, the possibility of controlling their structure and chemical nature makes them very interesting nano-platforms for various applications [37].

BNNTs were predicted in 1994 [38], and first prepared by Chopra et al. [39] in 1995 as carbon nanotube inorganic analogs, by alternating boron and nitrogen instead of carbon, almost without changing the atomic spacing of the graphite-like sheet [10,38]. The key parameters that influence both the length and size of BNNTs are temperature, catalyst, and boron precursor, as well as duration of the heating process [10]. The external diameter varies from 4 to 300 nm, usually reaching 30–100 nm, and the tubes' lengths are in the range of 500 nm to 1 mm, usually 5–10 μm [10]. Moreover, by changing the condition of synthesis, a single-walled BNNT, a double-walled BNNT, or a multi-walled BNNT can be prepared [40]. Although they are very similar to CNTs, BNNTs show greater mechanical (Young's modulus of 1.2 TPa) [41], and excellent chemical [42] and electrical properties [43]. One of the critical points for the applications of BNNTs, as well for CNTs, is their very poor dispersibility in water and apolar media. Being hydrophobic, BNNTs tend to aggregate and precipitate in about 1 h in aqueous media [44]. Therefore, they can be exploited in the biological field after an appropriate noncovalent [45,46] or covalent [47] modification, which can increase their dispersibility in water. BNNTs were used as smart materials [7], drug [47] and gene delivery systems [48], biomaterials [49], sensory systems [50], as well as hydrogen storage [51].

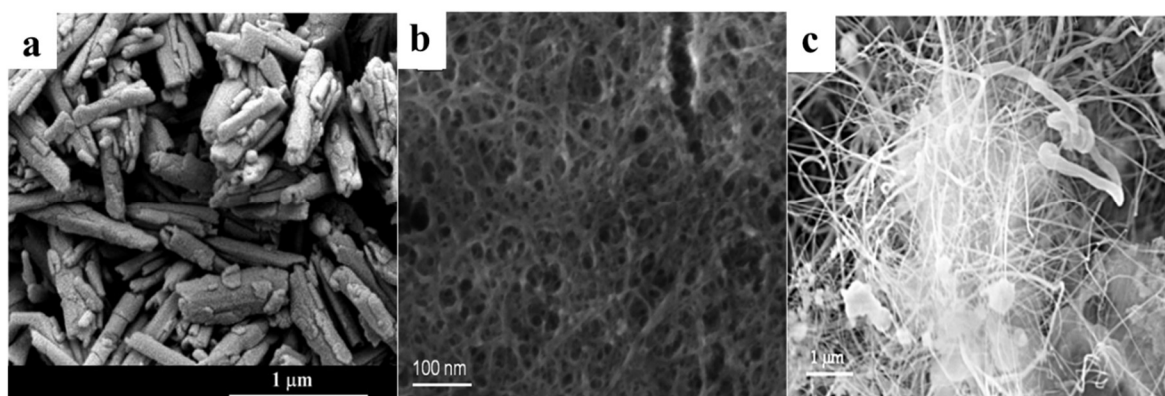


Figure 1. SEM images of (a) halloysite, (b) imogolite and (c) boron nitride nanotubes. Adapted from References [7,35,52].

2. Halloysite Nanotubes

2.1. Colloidal Stability in Water

The colloidal stability of HNTs is a crucial aspect that has been investigated with the aim of improving nanoparticle use and range through several possible applications [8]. HNTs' aqueous dispersions can form liquid crystalline phases when high concentrations are approached [53]. Moreover, the transition can be controlled by pH, providing an interesting system for obtaining birifrangent materials under controlled chemical stimuli [53]. In light of that, different strategies for the manipulation of chemico-physical properties into aqueous media are pursued by the most appropriate functionalization of halloysite internal or external surfaces by electrostatic interactions with differently charged surfactants or polyelectrolytes.

Bertolino et al. [54] reported studies on the adsorption of three biopolymers that possess a different charge—namely positive chitosan, neutral hydroxypropyl cellulose (HPC), and negative pectin—onto halloysite nanotube surfaces in an aqueous environment. It was found that the dispersion stability depends on the charge of particles and their dimensions, as well on the viscosity and inter-particle interactions. For instance, the ζ -potential values are not deeply modified by adding the nonionic HPC; meanwhile they are shifted toward more positive or more negative values by the addition of charged biopolymers, namely chitosan and pectin, respectively [54]. Generally, ζ -potential experiments are conducted to evaluate the surface properties and stability of functionalized nanoparticles, in order to understand if the charge density of both HNTs and polymers can influence the precipitation process. It was observed that HPC strongly delays sedimentation; meanwhile, chitosan and pectin stabilize nanotube dispersion at acidic and basic conditions, respectively. Pectin interacts with the HNTs' positive lumen and it decreases the HNTs' negative net charge. Chitosan, however, interacts on the outer surface. The HPC mechanism is completely different, because it is adsorbed and it creates a steric barrier that avoids agglomeration and settling [54].

Lee et al. [55] reported the preparation of HNT-based supramolecular complexes by the wrapping of DNA onto halloysite. It was observed that HNTs become highly dispersible in water after their interaction with DNA, because the phosphate groups of DNA are re-orientated and can interact with the silica groups on the external surface of HNTs. Most likely, the enhanced colloidal stability is due to the neutralization of the inner positive charge, leading to an increase of the net negative ζ -potential and particle–particle repulsions. These findings are confirmed by more recent studies on anionic surfactants and bio-polyanions (pectins) [54,56].

The effect on the colloidal stability of halloysite nanotubes has been also studied, considering the functionalization with thermosensitive polymers, namely poly(*N*-isopropylacrylamide) (PNIPAM) [57,58]. It was observed that PNIPAM interacted with the external surface of HNT and PNIPAM-NH₂ (amine terminated poly(*N*-isopropylacrylamide)) was adsorbed onto the external surface. Moreover, halloysite nanotubes changed their properties within the polymer/HNTs in comparison with the neat clay, thus indicating a transferring of the thermos-responsiveness from polymers to halloysite in the hybrid system [57]. Furthermore, since the dispersions were stable only under the “critical temperature”, this allowed for preparing systems where the temperature can be tuned in order to have external stimuli-responsive solubilization and delivery, providing a biocompatible and thermosensitive material for the targeted release of active species [58].

Amphiphilic molecules are often used to stabilize nanoparticle dispersions, exploiting their functional groups. The choice of the surfactant in terms of the headgroup charge is a key factor, and it has an important effect on the colloidal stability of halloysite because of its differently charged surfaces.

For instance, it has been demonstrated that the adsorption of surfactants that are negatively charged (e.g., sodium alkanoates) onto the internal surface of the nanotubes increases their overall negative charge, and thus enhances both electrostatic repulsions and colloidal stability (Figure 2) [56,59].

The change of the ζ potential, which becomes more negative, predicts a better dispersibility of the hybrid materials in comparison with the neat clay. The sedimentation process is strongly slowed down by the surfactants [59].

According to the DLVO (Derjaguin-Landau-Verwey-Overbeek) theory, colloidal stability is influenced by the balance between attractive and repulsive van der Waals forces coming from the double layer that surrounds each particle [60], meaning that experimental results are consistent with the theory.

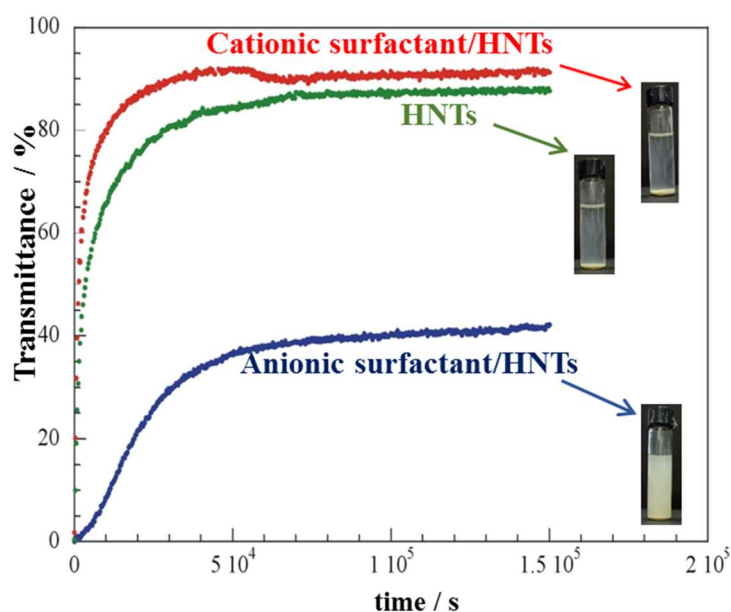


Figure 2. Halloysite nanotubes (HNTs) and surfactant-functionalized HNT dispersions (1 wt %) in water: photographs and transmittance as a function of time. Adapted from [56].

Moreover, the structure of neat HNTs and negatively charged surfactant-functionalized nanotubes were studied by small angle neutron scattering [52]. The importance of both the structural organization of the surfactants and their headgroup was shown. In particular, it was noted that sodium dodecanoate is organized in a densely packed, multilayer structure within the halloysite cavity, and is promoted by the carboxylate groups, as seen from a correlation peak in SANS (Small Angle Neutron Scattering) [52].

Finally, these inorganic, micelles-like hybrid materials can be used to solubilize and deliver species of a different nature in water, thus exploiting their sustainable and biocompatible properties [52,56,59].

It was also found that perfluoroalkylated surfactants, when adsorbed at the internal surface, created stable suspensions, and these systems can be exploited as nanocontainers of non-foaming oxygen in aqueous media for gas delivery by external stimuli [61].

More interestingly, it was shown that the concentration effect was negligible and that the hybrid materials did not associate; however, nanotubes diffuse as single particles [61].

Lun et al. [62] reported a method where sodium dodecyl sulfate (SDS) was used to prepare uniform and stable halloysite nanotubes dispersions. The ζ -potential values of an HNTs/SDS system became more negative than those of the neat clay, indicating that SDS is adsorbed on the inner surface, enhancing the dispersibility by electrostatic effect. It was observed that the dispersibility is not effected by the content of the dispersant, thus confirming the saturation effect.

2.2. Colloidal Stability in Organic Media

Another crucial aspect is the preparation of stable colloidal dispersions of halloysite nanotubes in organic media. Chang et al. [63] prepared a complex of amylose and HNT by co-assembly in a

solid state. In particular, it was found that the amylose interacts with the outer surface of HNTs, wrapping them. The stability of pristine nanotubes and amylose-HNT dispersions in DMSO/H₂O were observed for 24 h, and the precipitation of HNT occurred at 0 h [63]; whereas, since the solution of DMSO/H₂O is a good dispersant for the organic moiety, the amylose-HNT was well dispersed in the solution, and no precipitation was found for 24 h [64]. This was most likely due to the interactions between amylose and the external surface of HNTs [63]. Literature also reports another strategy to obtain stable colloidal suspensions, which is the preparation of inorganic reverse micelles in non-aqueous media based on halloysite nanotubes and cationic surfactants [65]. It is known that a reverse micelle is constituted by a hydrophobic shell and a hydrophilic cavity, which create an aqueous nano-droplet in a nonpolar medium. Cationic surfactants interact with the negative outer surface of HNTs, thus creating nanoparticles with a hydrophobic jacket and a hydrophilic cavity. The action of the colloidal stability of the obtained hybrid materials was investigated in solvents with different polarity [65]. Firstly, it was observed that the length chain of the surfactant strongly influences the charge of modified HNTs. For instance, when the tail length increases, the same happens to the ζ potential of the hybrid materials, due to the strong hydrophobic interaction between tails, as evidenced by FTIR [56]. Moreover, the hybrids present faster dynamics compared to the neat nanotubes, as evidenced by DLS (Dynamic Light Scattering) measurements in chloroform, thus reflecting the enhancement of electrostatic repulsions. The external surface of nanotubes is more hydrophobic, due to the presence of the surfactant, resulting in an increase of the colloidal stability of the nanotubes in nonpolar solvents [65]. In a few words, this procedure allows the fabricating of eco-compatible reverse micelles with different dispersibility in organic media and tunable hydrophobic/hydrophilic interfaces, thus available for industrial or biological applications.

3. Imogolite

Concerning imogolite nanotubes, although their formation mechanism has been extensively investigated and described in recent literature [66], their stability in aqueous suspension was not deeply investigated. On the other hand, Paineau et al. [9] firstly observed that INTs show a liquid-crystal phase, columnar in particular, at low concentrations ($\approx 0.3\%$) with low visco-elasticity and that is aligned under an electric field.

As expected, INT suspensions form a nematic phase at lower concentrations [67]. Contrarily, the columnar phase, which can be seen in suspensions of other rod-like particles, was only observed at large volume fractions (10–70%) [68–70]. Meanwhile the columnar phase of INTs is presented at concentrations that are two orders of magnitude lower (Figure 3) [9].

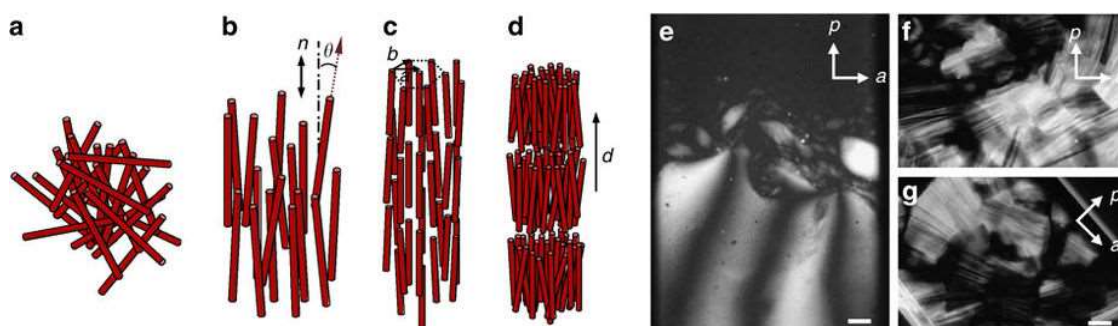


Figure 3. Schemes of (a) isotropic, (b) nematic, (c) columnar, and (d) smectic phases in imogolite suspensions. Photographs of (e) both isotropic and nematic phases in sedimented spindle-shaped nematic droplets; and (f, g) the columnar phase, obtained with single-walled Si-imogolite nanotube (INT) suspensions. Scale bar, 200 nm. Adapted from [9].

Such a difference is most likely due to the high aspect ratio of imogolite, which favors the nematic phase [67]. The large intensity of the electrostatic repulsions between charged linear objects is strongly evidenced by the ordered positions of the charged INT, which stabilizes the columnar phase at very low concentrations [9].

These results could present important implications for the physics of suspensions of charged rod-shaped nanoparticles, and could be used for the preparation of ordered nanocomposites, as well for biophysics, in order to understand the behavior of rod-like biopolymers suspensions.

Moreover, it was observed that imogolite forms sediments at an alkaline pH, even if the net charge is highly negative, and this leads to fibrous particle aggregation to form thick bundles [71]. To clarify this aspect, Ma and Karube [72] measured the charge features of INT by calculating the intensity of the electric field at the external surface, considering the model of imogolite structure and the Gauss' law.

It was calculated that the field intensity, due to the charge at the external surface of INTs, is half that at the internal surface. It was impossible to explain the flocculation, because the cation exchange capability (CEC) of imogolite was high under alkaline conditions. For instance, assuming cation distribution inside the tube, or inner cation exchange, the measured CEC would correspond to the negative charge at the inner surface, and the electric field intensity at the external surface would become half that at the internal surface [72]. This means that the electric field, due to the negative charges, would be balanced by the counter-ions that entered the tube, and the external surface would be neutral, thus explaining that imogolite flocculates at alkaline pH and its dispersed at the point of zero net charge, or at pH = 6.0 [72].

4. Boron Nitride Nanotubes

To improve dispersion stability, numerous methods to functionalize BNNTs were used [10,45,73]. These methods can be organized into three groups: (1) noncovalent, (2) covalent modifications, and (3) alternation in BNNTs (fabrication of defect sites, insertion of the amino groups, and transformation of the amino groups) (Figure 4).

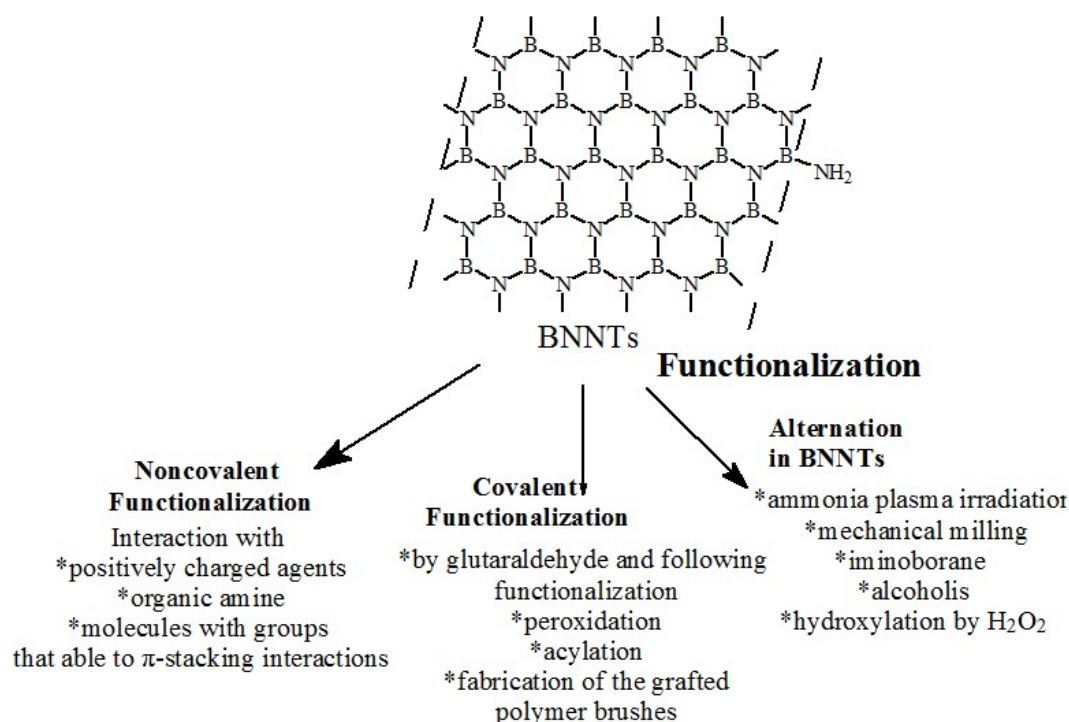


Figure 4. Different approaches for functionalization of the boron nitride nanotubes (BNNTs).

Noncovalent reactions are the most frequently used approach for the surface functionalization of BNNTs [73]. However, only positively charged agents (e.g., poly-L-lysine and poly-ethyleneimine), organic amines, or chemical species able to make π -stacking and hydrophobic interactions showed good results [73]. Synthetic structures with aromatic rings (2-naphthalenecarboxylic acid, 9-anthracenecarboxylic acid, 1-pyrenecarboxylic acid, 1-aminopyrene, and 1-hydroxypyrene) [74] and polymers containing aromatic subunits, polyaniline, poly(p-phenyleneethynylene), polythiophene, poly(xylydienetetrahydrothiophene) and poly(sodium styrene sulfonate) [73,75] interacted with the sidewall of BNNTs via π - π stacking and created stable dispersions. It was shown that poly(p-phenylene) derivatives have the most interesting potential to disperse BNNTs among studied polymers [75].

Another simple way to prepare stable colloidal dispersions of BNNTs in organic solution or aqueous media is to obtain boron nitride nanotubes with NH_3 or organic amines [76] or amino acids (glycine), and coat them subsequently with biopolymers [77]. The glycine has two roles: its amine group interacts with the B-sites of nanotubes, binding with them; meanwhile, its carboxylic acid group is an ionic site for anchoring polyelectrolytes. Unexpectedly, BNNTs were effectively dispersed in water using arabic gum (hydrophilic polymer), where the hydrophobic part of the polymers had strong hydrophobic interactions with BNNTs and the hydrophilic part was exposed to interactions with water molecules [78]. Other examples of the fabrication of the stable BNNT dispersions are modification of the BNNTs, using peptides [79], nucleotide [80], DNA [81], doxorubicin and folate [82], and lipids [83]. The most stable dispersions in water were obtained for the flavin mononucleotide, a derivative of vitamin B₂ containing an aromatic structure interacting with BNNT via π - π stacking [80]. In addition, flavin mononucleotide-functionalized BNNTs showed high visible light emission, and were stable for different pH and temperature values. A new approach to disperse the BNNTs was recently demonstrated [6], in this case via a layer-by-layer deposition of hydroxylated BNNTs with polyelectrolytes onto *Saccharomyces cerevisiae* cells.

Different methods of covalent modification of BNNTs have been developed to create colloidal dispersions in both aqueous media and organic solvents. This functionalization can be done by exploiting the $-\text{NH}_2$ and $-\text{OH}$ groups of boron atoms [46,84–86]. Covalent modification of the hydroxylated BNNTs with glutaraldehyde, followed by functionalization with oligonucleotides [87] and carbohydrates [88] are described. Zettl developed a new functionalization route by linking stearoyl chloride with amino groups onto BNNTs [84]. A similar approach was realized with hydroxylated BNNTs esterified by perfluorobutyric acid or a thioglycolic acid [88]. Another easy approach for covalent derivatization of nanotubes with organic peroxides was proposed [89], and the functionalized BNNTs were able to form the stable dispersion in chloroform.

Nowadays, one of the most interesting procedures for nanomaterial functionalization is to prepare grafted polymer brushes [7,90] (Figure 5a). In this route, the nanotubes are covalently functionalized with polymer brushes through surface polymerization. In particular, BNNTs were covalently modified with hydrophobic polystyrene or polyglycidyl methacrylate polymer brushes [90]. The modified nanotubes displayed high dispersibility in a large number of organic media. In the work of Kalay et al. [7], BNNTs functionalized with the thermo-responsive poly(*N*-isopropylacrylamide) (PNIPAM) were fabricated, and were dispersible in water (Figure 5b). It was also shown that the hydrodynamic radius of these systems decreased two-fold at around 32 °C (Figure 5c). In addition, BNNTs were functionalized by other grafted polymer brushes, similar to other works [91,92].

The modification of nanotubes on their amine groups is widely used, because the amine groups exist at the ends and as defects of BNNTs. Moreover, other $-\text{NH}_2$ groups were also created on the nanotube surfaces with ammonia plasma irradiation [84]. Amine-functionalized BNNTs after sonication in chloroform exhibit significantly better dispersibility than pristine BNNTs. Other mechanisms of functionalization by amine groups use mechanical milling of the boron nitride nanosheets [93] or iminoborane, which increases the defects density due to cleavage of B–N bonds and

to the expansion of BN rings [94]. In addition, a prospective method to create stable dispersion in water is the hydroxylation of BNNTs in H_2O_2 solution for 48 h at 110 °C [86,87].

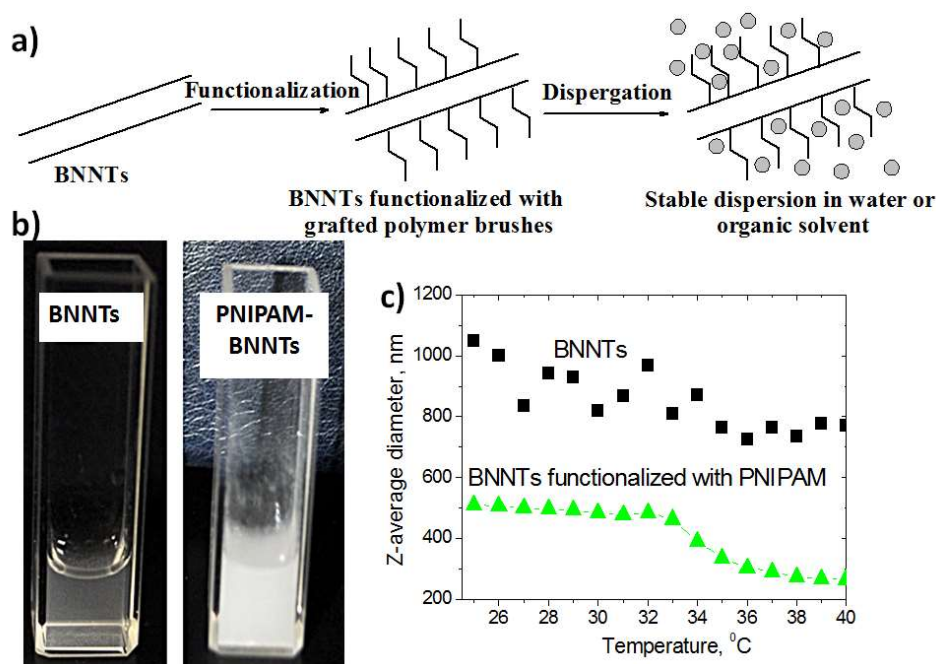


Figure 5. Fabrication of stable dispersion of the functionalized BNNTs (a), supernatants obtained after the water suspensions of native and PNIPAM-functionalized BNNT centrifugation (b), and Z-average diameters of the neat and PNIPAM-functionalized BNNTs at different temperatures (c). Adapted from [7].

5. Conclusions and Perspectives

It is clear the importance of nanotubular inorganic structures for their characteristics of high surface ratios, porosity, and tunable chemistry. Halloysite, imogolite, and boron nitride nanotubes are among the prospective tubular materials for industrial applications. In particular, they are considered safe materials for living organisms. Although they present a similar morphology, their chemical structure and properties are different. Chemical composition of HNTs and INTs are very similar; the surface chemistry is dominated by hydroxyl groups that make them hydrophilic. In the contrast, native BNNTs are superhydrophobic, and cannot be dispersed in most organic solvents or in aqueous media. BNNTs show greater mechanical properties (Young's modulus of 1.22 TPa) than HNTs and INTs (Young's modulus of 140–390 GPa). Another interesting aspect is the pH effect on surface charge. The dielectric properties of aluminum and silicon oxides in HNTs and INTs are different. Because these nanotubes undergo ionization in aqueous media in an opposite way, they generate tubes with oppositely charged inner and outer surfaces. Information on BNNT ionization is limited; in relation to chemical structure, we can assume that BNNTs can be ionized at a low pH, but this aspect should be investigated in detail. In addition, HNTs and INTs can be easily modified using hydroxyl groups on the outer surface, while BNNTs are chemically inert enough.

In this review, we report the main aspects of the colloidal stability of hollow-shaped nanoparticles in both aqueous and organic media, as well as the main strategies to prepare homogeneous and stable suspensions ranging from selective functionalization with charged molecules like polymers, biopolymers, and surfactants to pH dependence in water. These are crucial points for the preparation of a new class of smart hybrid nanomaterials with a wide class of applications, like drug delivery, catalysis, food packaging, environmental treatment, and cultural heritage.

Author Contributions: Writing-Original Draft Preparation, L.L., G.C., F.P., Y.S.; Writing-Review & Editing, G.L.; Supervision, S.M.

Funding: The work was financially supported by the University of Palermo.

Conflicts of Interest: The authors declare that they have no conflicts of interest with this work.

References

1. Iijima, S. Helical microtubules of graphitic carbon. *Nature* **1991**, *354*, 56–58. [[CrossRef](#)]
2. Sun, J.; Wang, J.; Li, Z.; Yang, Z.; Yang, S. Controllable synthesis of 3D hierarchical bismuth compounds with good electrochemical performance for advanced energy storage devices. *RSC Adv.* **2015**, *5*, 51773–51778. [[CrossRef](#)]
3. Yang, G.; Yang, X.; Yang, C.; Yang, Y. A reagentless amperometric immunosensor for human chorionic gonadotrophin based on a gold nanotube arrays electrode. *Colloids Surf. Physicochem. Eng. Asp.* **2011**, *389*, 195–200. [[CrossRef](#)]
4. Lai, Y.; Huang, Y.; Wang, H.; Huang, J.; Chen, Z.; Lin, C. Selective formation of ordered arrays of octacalcium phosphate ribbons on TiO₂ nanotube surface by template-assisted electrodeposition. *Colloids Surf. B Biointerfaces* **2010**, *76*, 117–122. [[CrossRef](#)] [[PubMed](#)]
5. Xu, S.; Ng, J.; Zhang, X.; Bai, H.; Sun, D.D. Adsorption and photocatalytic degradation of Acid Orange 7 over hydrothermally synthesized mesoporous TiO₂ nanotube. *Colloids Surf. Physicochem. Eng. Asp.* **2011**, *379*, 169–175. [[CrossRef](#)]
6. Emanet, M.; Fakhrullin, R.; Çulha, M. Boron Nitride Nanotubes and Layer-By-Layer Polyelectrolyte Coating for Yeast Cell Surface Engineering. *Chem. Nano. Mat.* **2016**, *2*, 426–429. [[CrossRef](#)]
7. Kalay, S.; Stetsyshyn, Y.; Lobaz, V.; Harhay, K.; Ohar, H.; Çulha, M. Water-dispersed thermo-responsive boron nitride nanotubes: Synthesis and properties. *Nanotechnology* **2016**, *27*, 035703. [[CrossRef](#)] [[PubMed](#)]
8. Lazzara, G.; Cavallaro, G.; Panchal, A.; Fakhrullin, R.; Stavitskaya, A.; Vinokurov, V.; Lvov, Y. An assembly of organic-inorganic composites using halloysite clay nanotubes. *Curr. Opin. Colloid Interface Sci.* **2018**, *35*, 42–50. [[CrossRef](#)]
9. Paineau, E.; Krapf, M.-E.M.; Amara, M.-S.; Matskova, N.V.; Dozov, I.; Rouzière, S.; Thill, A.; Launois, P.; Davidson, P. A liquid-crystalline hexagonal columnar phase in highly-dilute suspensions of imogolite nanotubes. *Nat. Commun.* **2016**, *7*, 10271. [[CrossRef](#)] [[PubMed](#)]
10. Kalay, S.; Yilmaz, Z.; Sen, O.; Emanet, M.; Kazanc, E.; Çulha, M. Synthesis of boron nitride nanotubes and their applications. *Beilstein J. Nanotechnol.* **2015**, *6*, 84–102. [[CrossRef](#)] [[PubMed](#)]
11. Massaro, M.; Amorati, R.; Cavallaro, G.; Guernelli, S.; Lazzara, G.; Milioto, S.; Noto, R.; Poma, P.; Riela, S. Direct chemical grafted curcumin on halloysite nanotubes as dual-responsive prodrug for pharmacological applications. *Colloids Surf. B Biointerfaces* **2016**, *140*, 505–513. [[CrossRef](#)] [[PubMed](#)]
12. Ferrante, F.; Armata, N.; Lazzara, G. Modeling of the Halloysite Spiral Nanotube. *J. Phys. Chem. C* **2015**, *119*, 16700–16707. [[CrossRef](#)]
13. Yang, Y.; Chen, Y.; Leng, F.; Huang, L.; Wang, Z.; Tian, W. Recent Advances on Surface Modification of Halloysite Nanotubes for Multifunctional Applications. *Appl. Sci.* **2017**, *7*, 1215. [[CrossRef](#)]
14. Makaremi, M.; Pasbakhsh, P.; Cavallaro, G.; Lazzara, G.; Aw, Y.K.; Lee, S.M.; Milioto, S. Effect of Morphology and Size of Halloysite Nanotubes on Functional Pectin Bionanocomposites for Food Packaging Applications. *ACS Appl. Mater. Interfaces* **2017**, *9*, 17476–17488. [[CrossRef](#)] [[PubMed](#)]
15. Kryuchkova, M.; Danilushkina, A.; Lvov, Y.; Fakhrullin, R. Evaluation of toxicity of nanoclays and graphene oxide in vivo: A Paramecium caudatum study. *Environ. Sci. Nano* **2016**, *3*, 442–452. [[CrossRef](#)]
16. Fakhrullina, G.I.; Akhatova, F.S.; Lvov, Y.M.; Fakhrullin, R.F. Toxicity of halloysite clay nanotubes in vivo: A Caenorhabditis elegans study. *Environ. Sci. Nano* **2015**, *2*, 54–59. [[CrossRef](#)]
17. Lvov, Y.; Abdullayev, E. Functional polymer–clay nanotube composites with sustained release of chemical agents. *Prog. Polym. Sci.* **2013**, *38*, 1690–1719. [[CrossRef](#)]
18. Biddeci, G.; Cavallaro, G.; Di Blasi, F.; Lazzara, G.; Massaro, M.; Milioto, S.; Parisi, F.; Riela, S.; Spinelli, G. Halloysite nanotubes loaded with peppermint essential oil as filler for functional biopolymer film. *Carbohydr. Polym.* **2016**, *152*, 548–557. [[CrossRef](#)] [[PubMed](#)]

19. Bertolino, V.; Cavallaro, G.; Lazzara, G.; Merli, M.; Milioto, S.; Parisi, F.; Sciascia, L. Effect of the Biopolymer Charge and the Nanoclay Morphology on Nanocomposite Materials. *Ind. Eng. Chem. Res.* **2016**, *55*, 7373–7380. [[CrossRef](#)]
20. Gorrasi, G.; Pantani, R.; Murariu, M.; Dubois, P. PLA/Halloysite Nanocomposite Films: Water Vapor Barrier Properties and Specific Key Characteristics. *Macromol. Mater. Eng.* **2014**, *299*, 104–115. [[CrossRef](#)]
21. Massaro, M.; Lazzara, G.; Milioto, S.; Noto, R.; Riela, S. Covalently modified halloysite clay nanotubes: Synthesis, properties, biological and medical applications. *J. Mater. Chem. B* **2017**, *5*, 2867–2882. [[CrossRef](#)]
22. Lvov, Y.M.; DeVilliers, M.M.; Fakhrullin, R.F. The application of halloysite tubule nanoclay in drug delivery. *Expert Opin. Drug Deliv.* **2016**, *13*, 977–986. [[CrossRef](#)] [[PubMed](#)]
23. Fakhrullin, R.F.; Lvov, Y.M. Halloysite clay nanotubes for tissue engineering. *Nanomedicine* **2016**, *11*, 2243–2246. [[CrossRef](#)] [[PubMed](#)]
24. Liu, M.; Zhang, Y.; Wu, C.; Xiong, S.; Zhou, C. Chitosan/halloysite nanotubes bionanocomposites: Structure, mechanical properties and biocompatibility. *Int. J. Biol. Macromol.* **2012**, *51*, 566–575. [[CrossRef](#)] [[PubMed](#)]
25. Liu, M.; Wu, C.; Jiao, Y.; Xiong, S.; Zhou, C. Chitosan-halloysite nanotubes nanocomposite scaffolds for tissue engineering. *J. Mater. Chem. B* **2013**, *1*, 2078–2089. [[CrossRef](#)]
26. Cavallaro, G.; Lazzara, G.; Milioto, S.; Parisi, F.; Evtugyn, V.; Rozhina, E.; Fakhrullin, R. Nanohydrogel Formation within the Halloysite Lumen for Triggered and Sustained Release. *ACS Appl. Mater. Interfaces* **2018**, *10*, 8265–8273. [[CrossRef](#)] [[PubMed](#)]
27. Zhao, Y.; Abdullayev, E.; Vasiliev, A.; Lvov, Y. Halloysite nanotubule clay for efficient water purification. *J. Colloid Interface Sci.* **2013**, *406*, 121–129. [[CrossRef](#)] [[PubMed](#)]
28. Cavallaro, G.; Danilushkina, A.A.; Evtugyn, V.G.; Lazzara, G.; Milioto, S.; Parisi, F.; Rozhina, E.V.; Fakhrullin, R.F. Halloysite Nanotubes: Controlled Access and Release by Smart Gates. *Nanomaterials* **2017**, *7*, 199. [[CrossRef](#)] [[PubMed](#)]
29. Cavallaro, G.; Lazzara, G.; Milioto, S.; Parisi, F.; Ruisi, F. Nanocomposites based on esterified colophony and halloysite clay nanotubes as consolidants for waterlogged archaeological woods. *Cellulose* **2017**, *24*, 3367–3376. [[CrossRef](#)]
30. Cavallaro, G.; Lazzara, G.; Milioto, S.; Parisi, F.; Sparacino, V. Thermal and dynamic mechanical properties of beeswax-halloysite nanocomposites for consolidating waterlogged archaeological woods. *Polym. Degrad. Stab.* **2015**, *120*, 220–225. [[CrossRef](#)]
31. Cavallaro, G.; Lazzara, G.; Milioto, S.; Parisi, F. Halloysite nanotubes as sustainable nanofiller for paper consolidation and protection. *J. Therm. Anal. Calorim.* **2014**, *117*, 1293–1298. [[CrossRef](#)]
32. Cavallaro, G.; Lazzara, G.; Milioto, S.; Parisi, F. Halloysite Nanotubes for Cleaning, Consolidation and Protection. *Chem. Rec.* **2018**. [[CrossRef](#)] [[PubMed](#)]
33. Gorrasi, G. Dispersion of halloysite loaded with natural antimicrobials into pectins: Characterization and controlled release analysis. *Carbohydr. Polym.* **2015**, *127*, 47–53. [[CrossRef](#)] [[PubMed](#)]
34. Thill, A.; Maillet, P.; Guiose, B.; Spalla, O.; Belloni, L.; Chaurand, P.; Auffan, M.; Olivi, L.; Rose, J. Physico-chemical Control over the Single- or Double-Wall Structure of Aluminogermanate Imogolite-like Nanotubes. *J. Am. Chem. Soc.* **2012**, *134*, 3780–3786. [[CrossRef](#)] [[PubMed](#)]
35. Rotoli, B.M.; Guidi, P.; Bonelli, B.; Bernardeschi, M.; Bianchi, M.G.; Esposito, S.; Frenzilli, G.; Lucchesi, P.; Nigro, M.; Scarcelli, V.; et al. Imogolite: An Aluminosilicate Nanotube Endowed with Low Cytotoxicity and Genotoxicity. *Chem. Res. Toxicol.* **2014**, *27*, 1142–1154. [[CrossRef](#)] [[PubMed](#)]
36. Cradwick, P.D.G.; Farmer, V.C.; Russell, J.D.; Masson, C.R.; Wada, K.; Yoshinaga, N. Imogolite, a Hydrated Aluminium Silicate of Tubular Structure. *Nat. Phys. Sci.* **1972**, *240*, 187–189. [[CrossRef](#)]
37. Amara, M.-S.; Paineau, E.; Bacia-Verloop, M.; Krapf, M.-E.M.; Davidson, P.; Belloni, L.; Levard, C.; Rose, J.; Launois, P.; Thill, A. Single-step formation of micron long (OH)₃Al₂O₃Ge(OH) imogolite-like nanotubes. *Chem. Commun.* **2013**, *49*, 11284–11286. [[CrossRef](#)] [[PubMed](#)]
38. Rubio, A.; Corkill, J.L.; Cohen, M.L. Theory of graphitic boron nitride nanotubes. *Phys. Rev. B* **1994**, *49*, 5081–5084. [[CrossRef](#)]
39. Chopra, N.G.; Luyken, R.J.; Cherrey, K.; Crespi, V.H.; Cohen, M.L.; Louie, S.G.; Zettl, A. Boron Nitride Nanotubes. *Science* **1995**, *269*, 966–967. [[CrossRef](#)] [[PubMed](#)]
40. Madani, M.S.; Monajjemi, M.; Aghaei, H. The Double Wall Boron Nitride Nanotube: Nano-Cylindrical Capacitor. *Orient. J. Chem.* **2017**, *33*, 1213–1222. [[CrossRef](#)]

41. Chopra, N.G.; Zettl, A. Measurement of the elastic modulus of a multi-wall boron nitride nanotube. *Solid State Commun.* **1998**, *105*, 297–300. [[CrossRef](#)]
42. Zhi, C.; Bando, Y.; Tang, C.; Xie, R.; Sekiguchi, T.; Golberg, D. Perfectly dissolved boron nitride nanotubes due to polymer wrapping. *J. Am. Chem. Soc.* **2005**, *127*, 15996–15997. [[CrossRef](#)] [[PubMed](#)]
43. Terao, T.; Zhi, C.; Bando, Y.; Mitome, M.; Tang, C.; Golberg, D. Alignment of Boron Nitride Nanotubes in Polymeric Composite Films for Thermal Conductivity Improvement. *J. Phys. Chem. C* **2010**, *114*, 4340–4344. [[CrossRef](#)]
44. Ciofani, G.; Danti, S.; Ricotti, L.; D'Alessandro, D.; Moscato, S.; Berrettini, S.; Mattoli, V.; Menciasci, A. Boron nitride nanotubes: Production, properties, biological interactions and potential applications as therapeutic agents in brain diseases. *Curr. Nanosci.* **2011**, *7*. [[CrossRef](#)]
45. Gao, Z.; Zhi, C.; Bando, Y.; Golberg, D.; Serizawa, T. Chapter 2—Functionalization of boron nitride nanotubes for applications in nanobiomedicine. In *Boron Nitride Nanotubes in Nanomedicine*; Elsevier Inc.: New York, NY, USA, 2016; pp. 17–40.
46. Ciofani, G.; Genchi, G.G.; Liakos, I.; Athanassiou, A.; Dinucci, D.; Chiellini, F.; Mattoli, V. A simple approach to covalent functionalization of boron nitride nanotubes. *J. Colloid Interface Sci.* **2012**, *374*. [[CrossRef](#)] [[PubMed](#)]
47. Li, X.; Hanagata, N.; Wang, X.; Yamaguchi, M.; Yi, W.; Bando, Y.; Golberg, D. Multimodal luminescent-magnetic boron nitride nanotubes@NaGdF(4):Eu structures for cancer therapy. *Chem. Commun.* **2014**, *50*, 4371–4374. [[CrossRef](#)] [[PubMed](#)]
48. Ferreira, T.H.; Hollanda, L.M.; Lancellotti, M.; de Sousa, E.M.B. Boron nitride nanotubes chemically functionalized with glycol chitosan for gene transfection in eukaryotic cell lines. *J. Biomed. Mater. Res. Part A* **2015**, *103*, 2176–2185. [[CrossRef](#)] [[PubMed](#)]
49. Şen, Ö.; Çulha, M. Boron nitride nanotubes included thermally cross-linked gelatin-glucose scaffolds show improved properties. *Colloids Surf. B* **2016**, *138*, 41–49. [[CrossRef](#)] [[PubMed](#)]
50. Yu, Y.; Chen, H.; Liu, Y.; Li, L.H.; Chen, Y. Humidity sensing properties of single Au-decorated boron nitride nanotubes. *Electrochem. Commun.* **2013**, *30*, 29–33. [[CrossRef](#)]
51. Leela, A.; Reddy, M.; Tanur, A.E.; Walker, G.C. Synthesis and hydrogen storage properties of different types of boron nitride nanostructures. *Int. J. Hydrogen Energy* **2010**, *35*, 4138–4143. [[CrossRef](#)]
52. Cavallaro, G.; Grillo, I.; Gradzielski, M.; Lazzara, G. Structure of Hybrid Materials Based on Halloysite Nanotubes Filled with Anionic Surfactants. *J. Phys. Chem. C* **2016**, *120*, 13492–13502. [[CrossRef](#)]
53. Luo, Z.; Song, H.; Feng, X.; Run, M.; Cui, H.; Wu, L.; Gao, J.; Wang, Z. Liquid Crystalline Phase Behavior and Sol-Gel Transition in Aqueous Halloysite Nanotube Dispersions. *Langmuir* **2013**, *29*, 12358–12366. [[CrossRef](#)] [[PubMed](#)]
54. Bertolino, V.; Cavallaro, G.; Lazzara, G.; Milioto, S.; Parisi, F. Biopolymer-Targeted Adsorption onto Halloysite Nanotubes in Aqueous Media. *Langmuir* **2017**, *33*, 3317–3323. [[CrossRef](#)] [[PubMed](#)]
55. Lee, Y.; Jung, G.-E.; Cho, S.J.; Geckeler, K.E.; Fuchs, H. Cellular interactions of doxorubicin-loaded DNA-modified halloysite nanotubes. *Nanoscale* **2013**. [[CrossRef](#)] [[PubMed](#)]
56. Cavallaro, G.; Lazzara, G.; Milioto, S. Exploiting the Colloidal Stability and Solubilization Ability of Clay Nanotubes/Ionic Surfactant Hybrid Nanomaterials. *J. Phys. Chem. C* **2012**, *116*, 21932–21938. [[CrossRef](#)]
57. Cavallaro, G.; Lazzara, G.; Milioto, S.; Parisi, F. Steric stabilization of modified nanoclays triggered by temperature. *J. Colloid Interface Sci.* **2016**, *461*, 346–351. [[CrossRef](#)] [[PubMed](#)]
58. Cavallaro, G.; Lazzara, G.; Massaro, M.; Milioto, S.; Noto, R.; Parisi, F.; Riela, S. Biocompatible Poly(*N*-isopropylacrylamide)-halloysite Nanotubes for Thermoresponsive Curcumin Release. *J. Phys. Chem. C* **2015**, *119*, 8944–8951. [[CrossRef](#)]
59. Cavallaro, G.; Lazzara, G.; Milioto, S.; Parisi, F.; Sanzillo, V. Modified Halloysite Nanotubes: Nanoarchitectures for Enhancing the Capture of Oils from Vapor and Liquid Phases. *ACS Appl. Mater. Interfaces* **2014**, *6*, 606–612. [[CrossRef](#)] [[PubMed](#)]
60. Derjaguin, B.V.; Landau, L.D. Theory of the Stability of Strongly Charged Lyophobic Sols and of the Adhesion of Strongly Charged Particles in Solutions of Electrolytes. *Acta Physicochim.* **1941**, *14*, 733–762. [[CrossRef](#)]
61. Cavallaro, G.; Lazzara, G.; Milioto, S.; Palmisano, G.; Parisi, F. Halloysite nanotube with fluorinated lumen: Non-foaming nanocontainer for storage and controlled release of oxygen in aqueous media. *J. Colloid Interface Sci.* **2014**, *417*, 66–71. [[CrossRef](#)] [[PubMed](#)]

62. Lun, H.; Ouyang, J.; Yang, H. Enhancing dispersion of halloysite nanotubes via chemical modification. *Phys. Chem. Miner.* **2014**, *41*, 281–288. [[CrossRef](#)]
63. Chang, P.R.; Xie, Y.; Wu, D.; Ma, X. Amylose wrapped halloysite nanotubes. *Carbohydr. Polym.* **2011**, *84*, 1426–1429. [[CrossRef](#)]
64. Shamsi, M.H.; Geckeler, D.V. The first biopolymer-wrapped non-carbon nanotubes. *Nanotechnology* **2008**, *19*, 075604. [[CrossRef](#)] [[PubMed](#)]
65. Cavallaro, G.; Lazzara, G.; Milioto, S.; Parisi, F. Hydrophobically Modified Halloysite Nanotubes as Reverse Micelles for Water-in-Oil Emulsion. *Langmuir* **2015**, *31*, 7472–7478. [[CrossRef](#)] [[PubMed](#)]
66. Du, P.; Yuan, P.; Thill, A.; Annabi-Bergaya, F.; Liu, D.; Wang, S. Insights into the formation mechanism of imogolite from a full-range observation of its sol-gel growth. *Appl. Clay Sci.* **2017**, *150*, 115–124. [[CrossRef](#)]
67. Kanji, K.; Nobuo, D.; Yuzuru, H.; Hiroshi, I. Lyotropic mesophase of imogolite, 1. Effect of polydispersity on phase diagram. *Makromol. Chem.* **1986**, *187*, 2883–2893. [[CrossRef](#)]
68. Livolant, F.; Leforestier, A. Condensed phases of DNA: Structures and phase transitions. *Prog. Polym. Sci.* **1996**, *21*, 1115–1164. [[CrossRef](#)]
69. Vroege, G.J.; Thies-Weesie, D.M.E.; Petukhov, A.V.; Lemaire, B.J.; Davidson, P. Smectic Liquid-Crystalline Order in Suspensions of Highly Polydisperse Goethite Nanorods. *Adv. Mater.* **2006**, *18*, 2565–2568. [[CrossRef](#)]
70. Ramos, L.; Fabre, P. Swelling of a lyotropic hexagonal phase by monitoring the radius of the cylinders. *Langmuir* **1997**, *13*, 682–685. [[CrossRef](#)]
71. Karube, J. Hysteresis of the Colloidal Stability of Imogolite. *Clays Clay Miner.* **1998**, *46*, 583–585. [[CrossRef](#)]
72. Ma, Y.L.; Karube, J. Imogolite flocculation under alkaline conditions. *Soil Sci. Plant Nutr.* **2013**, *59*, 125–129. [[CrossRef](#)]
73. Gao, Z.; Zhi, C.; Bando, Y.; Golberg, D.; Serizawa, T. Noncovalent Functionalization of Boron Nitride Nanotubes in Aqueous Media Opens Application Roads in Nanobiomedicine. *Nanobiomedicine* **2014**, *1*, 7. [[CrossRef](#)]
74. Kim, D.; Sawada, T.; Zhi, C.Y.; Bando, Y.; Golberg, D.; Serizawa, T. Dispersion of Boron Nitride Nanotubes in Aqueous Solution by Simple Aromatic Molecules. *J. Nanosci. Nanotechnol.* **2014**, *14*, 3028–3033. [[CrossRef](#)] [[PubMed](#)]
75. Gao, Z.; Fujioka, K.; Sawada, T.; Zhi, C.; Bando, Y.; Golberg, D.; Aizawa, M.; Serizawa, T. Noncovalent functionalization of boron nitride nanotubes using water-soluble synthetic polymers and the subsequent preparation of superhydrophobic surfaces. *Polym. J.* **2013**, *45*, 567–570. [[CrossRef](#)]
76. Wu, X.; An, W.; Zeng, X.C. Chemical functionalization of boron-nitride nanotubes with NH₃ and amino functional groups. *J. Am. Chem. Soc.* **2006**, *128*, 12001–12006. [[CrossRef](#)] [[PubMed](#)]
77. Lau, Y.T.R.; Yamaguchi, M.; Li, X.; Bando, Y.; Golberg, D.; Winnik, F.M. Facile and mild strategy toward biopolymer-coated boron nitride nanotubes via a glycine-assisted interfacial process. *J. Phys. Chem. C* **2013**, *117*, 19568–19576. [[CrossRef](#)]
78. Gao, Z.; Zhi, C.; Bando, Y.; Golberg, D.; Komiyama, M.; Serizawa, T. Efficient disentanglement of boron nitride nanotubes using water-soluble polysaccharides for protein immobilization. *RSC Adv.* **2012**, *2*, 6200–6208. [[CrossRef](#)]
79. Gao, Z.; Zhi, C.; Bando, Y.; Golberg, D.; Serizawa, T. Isolation of individual boron nitride nanotubes via peptide wrapping. *J. Am. Chem. Soc.* **2010**, *132*, 4976–4977. [[CrossRef](#)] [[PubMed](#)]
80. Gao, Z.; Zhi, C.; Bando, Y.; Golberg, D.; Serizawa, T. Noncovalent functionalization of disentangled boron nitride nanotubes with flavin mononucleotides for strong and stable visible-light emission in aqueous solution. *ACS Appl. Mater. Interfaces* **2011**, *3*, 627–632. [[CrossRef](#)] [[PubMed](#)]
81. Zhi, C.; Bando, Y.; Wang, W.; Tang, C.; Kuwahara, H.; Golberg, D. DNA-mediated assembly of boron nitride nanotubes. *Chem. Asian J.* **2007**, *2*, 1581–1585. [[CrossRef](#)] [[PubMed](#)]
82. Emanet, M.; Şen, Ö.; Çulha, M. Evaluation of boron nitride nanotubes and hexagonal boron nitrides as nanocarriers for cancer drugs. *Nanomedicine* **2017**, *12*, 797–810. [[CrossRef](#)] [[PubMed](#)]
83. Lee, C.; Zhang, D.; Yap, Y. Functionalization, Dispersion, and Cutting of Boron Nitride Nanotubes in Water. *J. Phys. Chem. C* **2012**, *116*, 1798–1804. [[CrossRef](#)]
84. Ikuno, T.; Sainsbury, T.; Okawa, D.; Frechet, J.M.J.; Zettl, A. Amine-functionalized boron nitride nanotubes. *Solid State Commun.* **2007**, *142*, 643–646. [[CrossRef](#)]

85. Zhi, C.; Bando, Y.; Tang, C.; Honda, S.; Sato, K.; Kuwahara, H.; Golberg, D. Covalent functionalization: Towards soluble multiwalled boron nitride nanotubes. *Angew. Chem. Int. Ed.* **2005**, *44*, 7932–7935. [[CrossRef](#)] [[PubMed](#)]
86. Emanet, M.; Şen, Ö.; Çobandede, Z.; Çulha, M. Interaction of carbohydrate modified boron nitride nanotubes with living cells. *Colloids Surf. B* **2015**, *134*, 440–446. [[CrossRef](#)] [[PubMed](#)]
87. Şen, Ö.; Çobandede, Z.; Emanet, M.; Bayrak, Ö.F.; Çulha, M. Boron nitride nanotubes for gene silencing. *Biochim. Biophys. Acta Gen. Subj.* **2017**, *1861*, 2391–2397. [[CrossRef](#)] [[PubMed](#)]
88. Zhi, C.Y.; Bando, Y.; Terao, T.; Tang, C.C.; Kuwahara, H.; Golberg, D. Chemically activated boron nitride nanotubes. *Chem. Asian J.* **2009**, *4*, 1536–1540. [[CrossRef](#)] [[PubMed](#)]
89. Lin, S.; Ashrafi, B.; Laqua, K.; Kim, S. Nanotubes with peroxides and their application in polycarbonate composites. *New J. Chem.* **2017**, *41*, 7571–7577. [[CrossRef](#)]
90. Ejaz, M.; Rai, S.C.; Wang, K.; Zhang, K.; Zhou, W.; Grayson, S.M. Surface-initiated atom transfer radical polymerization of glycidyl methacrylate and styrene from boron nitride nanotubes. *J. Mater. Chem. C* **2014**, *2*, 4073–4079. [[CrossRef](#)]
91. Stetsyshyn, Y.; Raczowska, J.; Lishchynskiy, O.; Bernasik, A.; Kostruba, A.; Harhay, K.; Ohar, H.; Marzec, M.M.; Budkowski, A. Temperature-Controlled Three-Stage Switching of Wetting, Morphology, and Protein Adsorption. *ACS Appl. Mater. Interfaces* **2017**, *9*, 12035–12045. [[CrossRef](#)] [[PubMed](#)]
92. Raczowska, J.; Stetsyshyn, Y.; Awsiuk, K.; Zemła, J.; Kostruba, A.; Harhay, K.; Marzec, M.; Bernasik, A.; Lishchynskiy, O.; Ohar, H.; Budkowski, A. Temperature-responsive properties of poly(4-vinylpyridine) coatings: Influence of temperature on the wettability, morphology, and protein adsorption. *RSC Adv.* **2016**, *6*, 87469–87477. [[CrossRef](#)]
93. Lin, Y.; Williams, T.V.; Cao, W.; Elsayed-Ali, H.E.; Connell, J.W. Defect functionalization of hexagonal boron nitride nanosheets. *J. Phys. Chem. C* **2010**, *114*, 17434–17439. [[CrossRef](#)]
94. Sundaram, R.; Scheiner, S.; Roy, A.K.; Kar, T. B=N bond cleavage and BN ring expansion at the surface of boron nitride nanotubes by iminoborane. *J. Phys. Chem. C* **2015**, *119*, 3253–3259. [[CrossRef](#)]



© 2018 by the authors. Licensee MDPI, Basel, Switzerland. This article is an open access article distributed under the terms and conditions of the Creative Commons Attribution (CC BY) license (<http://creativecommons.org/licenses/by/4.0/>).